Ultrathin Films of Metal Oxides, Nitrides and Sulfides Obtained by Atomic Layer Deposition and Other Means

A Thesis Submitted for the Degree of

Doctor of Philosophy

By

Sreedhara M. B.

Chemistry and Physics of Materials Unit
Jawaharlal Nehru Centre for Advanced Scientific Research
(A Deemed University)
Bangalore - 560064 (India)

April 2018

To
My Teacher

C. N. R. Rao

DECLARATION

I hereby declare that the matter embodied in this thesis entitled **"Ultrathin Films of Metal Oxides, Nitrides and Sulfides Obtained by Atomic Layer Deposition and Other Means"** is the result of investigations carried out by me under the supervision of **Prof. C. N. R. Rao, FRS** at the Chemistry and Physics of Materials Unit, JNCASR, Bangalore, India and that it has not been submitted elsewhere for the award of any degree or diploma.

In keeping with the general practice in reporting scientific observations, due acknowledgement has been made whenever the work described is based on the findings of other investigators.

(Sreedhara M. B.)

CERTIFICATE

I hereby certify that the matter embodied in this thesis entitled **"Ultrathin Films of Metal Oxides, Nitrides and Sulfides Obtained by Atomic Layer Deposition and Other Means"** has been carried out by Mr. Sreedhara M. B. at the Chemistry and Physics of Materials Unit, Jawaharlal Nehru Centre for Advanced Scientific Research, Bangalore, India under my supervision and it has not been submitted elsewhere for the award of any degree or diploma.

Prof. C. N. R. Rao

(Research Supervisor)

ACKNOWLEDGEMENTS

First and foremost, I express my sincere and heartfelt gratitude and profound respect to my research supervisor ***Prof. C. N. R. Rao, FRS,*** for introducing me to the fascinating fields of two dimensional materials and atomic layer deposition. His enthusiasm, dedication and relentless pursuit of science even in his eighties are truly inspiring and motivating. I shall remain ever indebted to him for bearing with me throughout the course of the work. He has not only been instrumental in shaping up my research, my career but my entire personality, my outlook towards life as a whole. I consider myself extremely lucky to receive all the love and care that he has bestowed me with. With his fathomless patience, unfailing support, critical suggestions and iron will, nothing was ever a hurdle in this journey. I do not have words to thank him; I express my immense gratitude to him.

I thank Prof. Umesh V. Waghmare, Prof. G. U. Kulkarni, Prof. U. Ramamurty, Prof. Aninda Bhattacharyya, Prof. Ranjan Datta, Prof. S. K. Pati, Dr. Jay Ghatak, Dr. Subhra Gope, Dr. Kouser, Mr. Santhosh, Mr, Badri Vishal, Mr. Abhishek and Mr. Bharat for their fruitful ***scientific collaborations*** and all their insightful discussions.

I thank Dr. A. Govindaraj for helping me in innumerable ways and I have been extremely benefited with his scientific skills.

I thank my ***course work instructors***: Prof. G. U. Kulkarni, Prof. A. Sundaresan, Prof. S. Balasubramanian, Prof. S. M. Shivaprasad, and Prof. Ranjan Datta

I thank past and present ***Chairman of CPMU*** for allowing me to use department instrumentation facilities.

I thank all ***the faculty members of CPMU and NCU*** and I thank Prof. S. N. Bhat for giving me an opportunity to be part of the POCE programme.

I thank all my ***beloved labmates***: Dr. Matte, Dr. Nitesh, Dr. Maitra, Dr. Moses, Dr. Vasu, Dr. Naidu, Dr. Saha, Dr. Gopal, Dr. Kumar, Dr. Dey, Dr. Manjunath, Dr. Chithaiah, Dr. Prasad Dr. Goapal, Dr. Pramoda, Dr. Lingampalli, Dr. Jana, Dr. Vishnoi, Dr. Magesh, Govind. A. Roy, Uttam, Chhetri, Manaswee. Monis, Manjunatha, Rajesh, Amit, Rohit, Swaraj and Reetendra.

I thank the timely help of the ***technical staff*** members: Ms. N. R. Selvi, Dr. Jay Mrs. Usha and Mr. Kannan, Mr. Vasu, Dr. Basavaraju and Mr. Mahesh, Mr. Anil, Mr. Prajwal, Mr. Jagadeesh, Mr. Shivakumar, Mr. Srinath and Mr. Sanjit. I thank Mrs. Shashi, Mrs. Sudha, Mr. Gowda and Mr. Victor for their help in various aspects.

I thank the faculty members of department of Chemistry, ***Tumkur University***, and faculty members of ***Governament Science College, Tumkur*** for their support and guidance.

I thank all the staff members associated with ***Admin, Academic, Library, CPMU, NCU, ICMS, Hostel, Gardening, Dhanvantari*** and other depts.

I thank the ***Dept. of science and technology (India)*** for funding, JNCASR and IISc for extending research facilities.

I thank the ***Council of Scientific and Industrial Research (CSIR),*** India for the fellowship. I also thank ***SSL-RAK-CAM*** for funding and fellowship.

I thank all my ***batch mates and friends***: Sanjay, Dheeraj, Satya, Sunil, Manoj, Swathi, Papri, Shivakumar and all seniors for their lovable company and support. I thank ***my masters and bachelors friends*** for their support.

My special thanks to ***Mrs. Indumati Rao*** and ***Mr. Sanjay Rao*** for their warmth affection and excellent hospitality they extended during several occasions.

Last but not least, I thank my ***dearest parents*** and specially ***brother Shivu, sister Pavithra*** and wife ***Archana*** for their support, love and care.

PREFACE

Two-dimensional ultrathin films with atomic thickness and infinite planar lengths have gained tremendous importance due to their unique properties compared to other nanostructures and to their bulk counterparts. Over the last two decades there has been tremendous development in 2D structures with fundamentally new properties of materials. The present study mainly focuses on the synthesis (or deposition), characterization of ultrathin films of oxides, sulfides and nitrides and their selected properties related to energy storage and electronic devices. Thesis is divided into three parts, wherein **Part I** deals with ultrathin nanosheets of oxide materials, their structure, properties and their use in energy related applications. **Part II** deals with the nanosheets of nitride materials, their properties and use in energy related devices. **Part III** emphasises on atomic layer deposition of ultrathin films of inorganic oxides and sulfides, their detailed characterization and selected properties in energy and sensing applications.

Part I is divided into four chapters of which **Chapter I.1** gives a brief overview of the ultrathin nanosheets of layered and non layered materials and their unique properties. **Chapter I.2** discusses the facile synthesis and characterization of few-layer nanosheets of MoO_3, their photochemical properties and supercapacitor performance. This study also showcases the results of MoO_3-graphene composites as potential anode materials for Na ion batteries. **Chapter I.3** describes the synthesis characterization of nanosheets of Aurivillius family of oxides and their properties. **Chapter I.4** describes the effect of N-substitution on the metal insulator transition of V_2O_3.

Part II contains two chapters of which **Chapter II.1** describes the synthesis and characterization of borocarbonitride nanosheets of various compositions obtained via solid state reaction. Applications of theses nanosheets as supercapacitor electrodes and active oxygen reduction reaction catalyst are also examined. This study also outlines the mechanical properties of BCN-reinforced polymer nanocomposites. **Chapter II.2** discusses the synthesis and characterization of GaN, VN and MoN nanosheets from their respective layered oxide or sulfide nanosheets.

Part III is divided in to four chapters with **Chapter III.1** giving a brief overview of atomic layer deposition and its unique advantages over other techniques. **Chapter III.2** describes the growth and characterization p-type epitaxial thin films of anatase TiO_2 and their use in diode applications. **Chapter III.3** discusses the growth and in detail characterization of V_2O_5 epitaxial film and their responses to relative humidity. **Chapter III.4** describes the growth and detailed characterization of MoS_2 nanowall networks and their performance in Na and Li-ion batteries. The study also shows an efficient way to fabricate the battery electrodes and how to improve their performance without conducting and binder additives.

TABLE OF CONTENTS

Part-I. Ultrathin Nanosheets of Layered and Non-Layered Materials

Chapter I.1. Two-dimensional nanosheets of layered and non-layered materials: A brief overview

Chapter I.2. Synthesis, characterization, and selected properties of few-layer nanosheets of MoO_3

Chapter I.3. Few-layer nanosheets of the Aurivillius family of oxides

Chapter I.4. Effect of nitrogen substitution in V_2O_3 films on the metal–insulator transition

PART II. Nanosheets of Borocarbonitrides and Other Metal Nitrides

Chapter II.1. Nanosheets of 2D-borocarbonitrides: synthesis, characterization and selected properties

Chapter II.2. Synthesis and Characterization of Few-layer Nanosheets of GaN and Other Metal Nitrides

PART III. Atomic Layer Deposition (ALD) of Ultrathin Films of Metal Oxides and Sulfides

Chapter III.4. Atomic layer deposition of epitaxial MoS_2 nanowall networks and their Performance in thin film Na-ion batteries

Part I

Ultrathin Nanosheets of Layered and Non-Layered Metal Oxides

Chapter I.1

Two-dimensional Nanosheets of Layered and Non-layered Materials: A brief overview

SUMMARY

Two-dimensional (2D) nanosheets, which possess atomic or molecular thickness and infinite planar lengths are emerging as conceptually new class of thinnest functional nanomaterials. The emergence of graphene and its fascinating properties triggered the research community towards single and few-layer ultrathin nanosheets. Over the last two decades there is tremendous development in the 2D materials research having witnessed several fundamentally new properties of materials. Recent developments in the methods for manipulating them have provided new possibilities and applications for 2D systems. A noteworthy feature is that unlike Graphene, many of the dichalcogenides are semiconductors with direct band gap. This chapter includes a summary of the preparation methods of ultrathin nanosheets of layered and non-layered materials and their electronic structures and possible applications in energy storage and conversion with particular emphasis on supercapacitors and batteries. The unique advantages offered by nanosheets over other dimensionalities has been highlighted. Chapter also gives a perspective on the advantages offered by this class of materials, their heterostructures and composites for energy and electronic devices.

1. Introduction

Materials at nanoscale

Nanoscale materials are defined as materials where at least one dimension is in the nanometer scale approximately 1-100 nm. The reduction in the spatial dimension, in a particular crystallographic direction within a structure leads to changes in fundamental properties of the material. The changes which occur in electronic properties due to quantum size effects influence the physical properties and they can be altered by tuning the dimensionality.[1-4] The properties of a material at mesoscopic scale are governed not only by nature of its chemical bonds but also by its dimensionality and shape.[5, 6] The application of nanomaterials can be traced even before the development of modern science and technology. In 1857, Michael Faraday published a paper on how metal nanoparticles affect the color of church windows. The real burst of nanotechnology happened in the late 1990s when sophisticated instrumentation became available to characterize the nanomaterials. The basic understanding of nanostructured materials from fundamental principles to their use in novel applications created a new paradigm of material design. As a result of exotic properties exhibited by materials at the nanoscale, the nanotechnology initiative was established worldwide in last decade.[7-9] The term nanotechnology describes the ability to manipulate matter at the atomic and molecular level and exploiting their properties as compared to those associated with bulk. In the emerging field of science and technology, nanotechnology made a profound economic impact in diverse sectors ranging from semiconductor manufacturing, energy harvesting, healthcare and agriculture in a very short span of time. Nanotechnology has become the ultimate frontier to change material properties, with the most efficient length scale for fabrication and manufacturing.

2. Two-dimensional nanosheets

Engineering of nanostructures to create functional materials is considered to be ‘holy-grail’ of nanotechnology. The main goal is to generate materials, systems and devices with fundamentally new properties and functions by manipulating their nanoscale

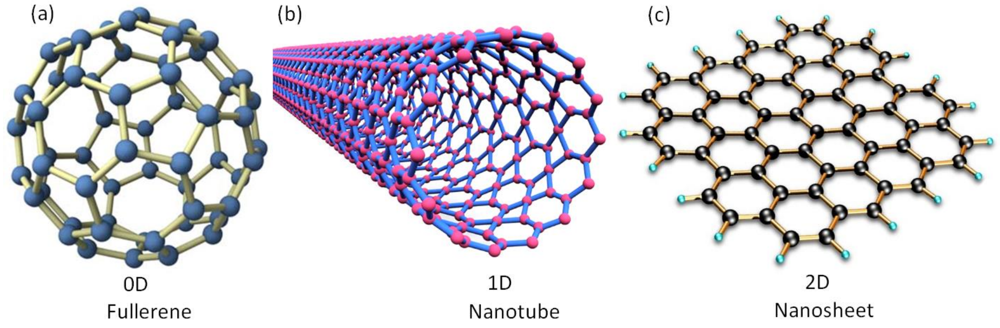

Figure 1. Classification of nanomaterials based on their dimensionality.

structures. One of the recent class of nanostructures has shown great potential to reach the expectation are two-dimensional (2D) nanosheets. Atomically thin nanosheets of materials with only a few atoms of thickness and very large lateral dimensions are conceptually new class of materials.[10-15] These 2D nanosheets or ultrathin films are confined in one direction and have two dimensions outside the nanoscale regime. **Figure 1** shows classification of nanomaterials based on their dimensionality (0D fullerene, 1D nanotubes and 2D nanosheets) by which they have confined. The term nanosheets were used by Sasaki to define the unilamellar structures of layered protonic titanates of few nm thickness with several micron lateral dimension.[16] In an ideal case nanosheets are single monolayers of respective bulk material but they often manifested with flakes of incomplete exfoliation or few-layers or stacked monolayers. Although traditional layered materials have a long history, the isolation of graphene from graphite by micromechanical cleavage give the first experimental evidence for stable existence of monolayer nanosheets.[17, 18] The experimental discovery of free-standing graphene challenged the theoretical views on 2D materials and showcased the research community about potential application and stability of nanosheets.[19] Since then graphene has been widely explored in diverse applications ranging from hybrid materials, energy storage, and optoelectronic devices.[20-23] Nevertheless, graphene is a gapless material composed of one kind of atoms which limits its versatility in the current technology.[17] Henceforth, the nanosheets which offer vast diversity of composition and functionalities became the forefront of the advanced materials research. In this context variety of atomically thin nanosheets of transition metal dichalcogenides (TMDCs),[13, 24-26] transition metal oxides (TMOs), elemental two-dimensional nanosheets of phosphorene, germanene, graphene analogues such as boron nitride and borocarbonitrides (BCN) have been successfully investigated in the last few years.[15] These ultrathin nanosheets possess fascinating properties including extremely high surface area, rich electrochemical active sites,[27, 28] structural stability and flexibility, which could provide promising opportunities to satisfy the requirements for next-generation electronic devices and other emerging sectors.[29]

The 2D nanostructure can be obtained from two types of parent compounds; they basically differ in their crystal structure, namely, layered and non-layered materials. The layered materials consist of 2D flakes with strong in-plane chemical bonds and held by weak van der Waals forces in out-of-plane. Since the discovery of graphene, the layered materials emerged as diverse source nanosheets whose properties can be easily manipulated by delaminating into individual layers.[30, 31] The non-layered solids possess atomic organization and bond strength in three dimensions in contrast to layered materials. It is well-known that layered materials can be easily exfoliated into individual layers by breaking the van der Waals forces by chemical or physical means.[19, 31-34] However, for non-layered materials it is very difficult to prepare or delaminate into atomically thin nanosheets due to strong chemical bond in third dimension.[35, 36] In this context wet-chemical synthesis and conversion of atomically thin nanosheets of the layered-structure into nanosheets of completely new material with non-layered structure emerged as promising approach.[37]

2D nanosheets with atomic thickness and infinite planar lengths emerged as important class new materials due to their exotic properties.[35] The remarkable properties exhibited by nanosheets of non-layered oxides, sulphides as well as nitrides stimulate interest towards planer nanosheets of any kind of materials. In the recent

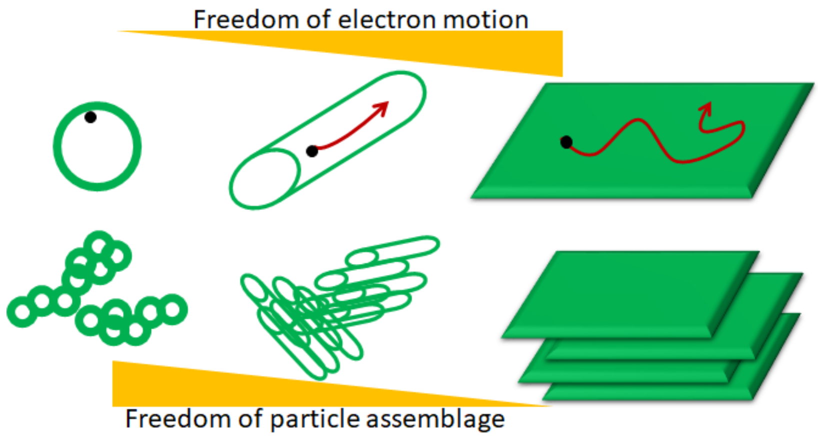

Figure 2. Schematic representation of the characteristics of 0D, 1D, 2D nanostructures, arrows indicates freedom of electrons transportation.

years, the 2D nanosheets morphology has gained tremendous attention of research community irrespective of their bulk structure because the potential they offer to study the fundamental physics and underlining phenomenon at the nanoscale. What's more nice with a 2D nanosheets is that they are much easier to manipulate compared to other types of nanomaterials like 0D fullerene, nanoparticles and 1D nanotube and nanowires.[17, 38] Nanosheets offer several lucrative features which promote their use in device fabrication, composites, catalysis and other sectors.

3. Unique advantages of 2D nanosheets

- Nanosheets provide an ideal platform to study fundamental physical properties of the material that are rarely seen in bulk materials
- 2D nanosheets offer exciting opportunities to fabricate the devices for various applications due to the ultra-small thickness and infinite lateral dimensions
- The charge carriers are strongly confined in a 2D plane which leads to unusual physical phenomena such as 2D electron gas (2DEG) and quantum Hall effect (QHE)
- As they can be exfoliated which drastically increases the surface area, the surfaces of 2D nanosheets are larger than those of 0D and 1D particles, in contrast, the assembling (agglomeration) is more restricted compared to 0D and 1D nanostructures (**Figure 2**)
- Nanosheets provide more degree of freedom for a free movement of electron which results in unique fascinating features
- Few-layer nanosheets offer the Nano spaces along z direction which can be expandable to gain an additional degree of freedom
- 2D nanosheets act as building blocks to construct 3D nanostructures for advanced electrochemical and device architecture
- 2D layered materials already proved that they can be synthesized in industrial scale and can be roll-to-roll processable
- The 2D crystals enable easy access to mobile carries and exhibit substantial carrier mobility which displays fundamental phenomenon of QHE
- The 2D nanosheets can be easily rolled into 0D and 1D nanostructures or restacked into 3D (**Figure 3**), which could result in new properties

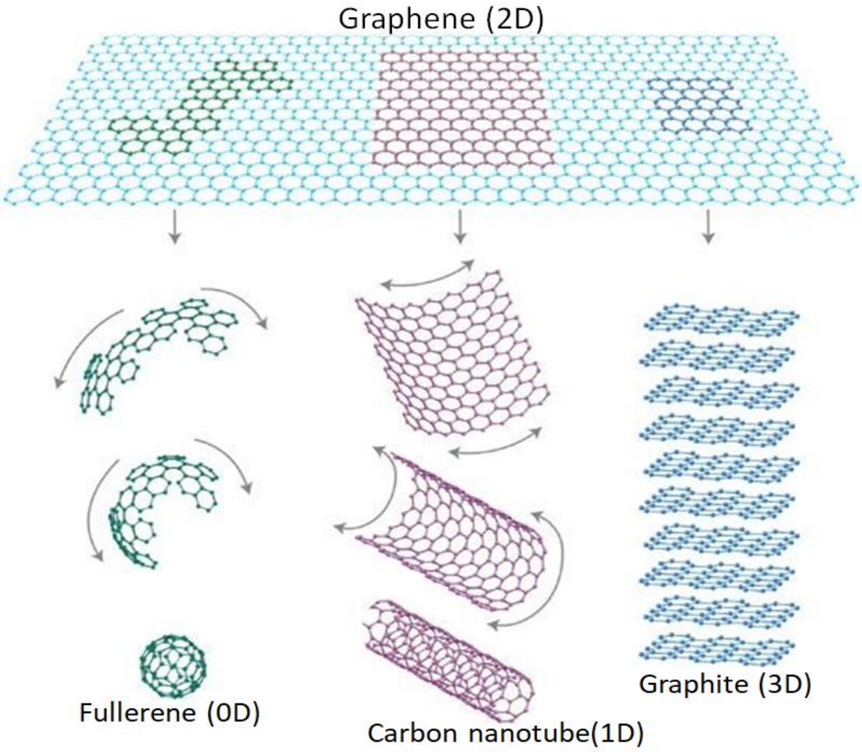

Figure 3. 2D Nanosheets are building block of nanomaterials of all other dimensionalities. Nanosheets can be wrapped into 0D or 1D or stacked into 3D. Reproduced with permission from ref.[17]

- ❖ In 2D nanosheets, atoms are exposed to surfaces, which gives the opportunity to tailor the properties through functionalization which also indeed helpful to create new hybrid materials[38]
- ❖ The anisotropic morphology of nanosheets is beneficial to obtain hybrid heterostructure by stacking layer by layer for specific application
- ❖ 2D nanosheets already proved to be potential materials in wide range of applications from electronics, optical devices, energy storage, flexible devices, agriculture and healthcare etc.
- ❖ As the nanosheets resemble the thin films, the properties of them can be easily transferred on a chip by fabrication.

Figure 4 illustrates the various unique advantages of 2D nanosheets which can be tuned for the various purposes.

The current chapter gives the literature overview of the 2D nanosheets of layered materials such as graphene, boron nitride, TMDCs, TMOs and the nanosheets of non-layered materials. This includes the discussion of structure, chemical entities as well as outlining the fundamental physical and electronic properties. The various methods and strategies involved in the exfoliation of bulk materials and bottom-up

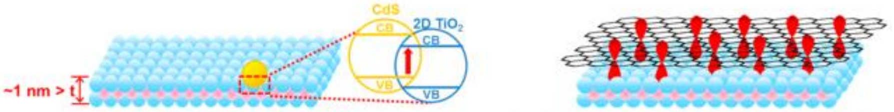

1. A creation of novel physicochemical properties attributed to the hybridization with the subnanometer thickness-nanosheet

2. A formation of strong interaction between inorganic nanosheet and graphene attributed to the common 2D morphology

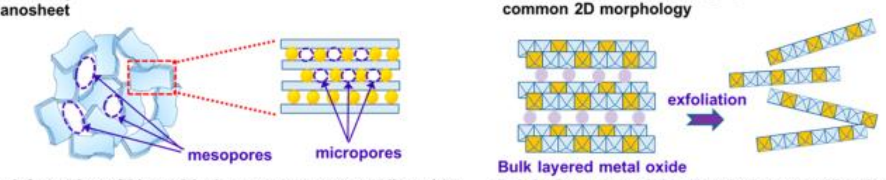

3. A formation of hierarchical porous structure attributed to the two types of the nanosheets-stacking

4. A facile tuning of the chemical composition for the inorganic nanosheet via the substitution–exfoliation reaction

5. A use of mixed colloidal suspension as effective precursor for the synthesis of nanohybrid attributed to the mixability of the inorganic nanosheet and rG-O

6. A modification of surface property by the anchoring of the functional groups on the large surface of the nanosheet

Figure 4. Schematic illustration of unique advantages of 2D nanosheets. Reproduced with permission from ref.[38]

approach to prepare the atomically thin layers have been briefly summarized in each section. The potential application in energy storage, catalysis, electronic device, battery and supercapacitor has also been touched upon.

4. Nanosheets of layered materials

Layered van der Waals materials exhibit strong in-plane covalent bonding within the layers and van der Waals forces between them. For example, graphite which consists of graphene layers along crystallographic c-direction. Layered materials emerged as largely untapped source of 2D nanosheets with exotic electronic properties. Layered materials offered a platform for chemists to develop intercalation chemistry to obtain kinetically stable products that cannot be prepared by other approaches. Layered compounds helped physicists to discover and understand novel phenomena at reduced dimensionality. The recent discovery of two-dimensional topological insulating state is a remarkable milestone in condensed matter physics is due to layered structure. After the tremendous success of graphene research, a huge library of layered compounds has been studied (**Table 1**). The layered compounds with semiconducting and insulating properties become more interesting due to technological interest. Some of the well-studied layered materials till data with widespread electronics are graphene, semiconducting metal chalcogenides such as MoS_2, WS_2,

Table 1. Library of 2D layered materials whose nanosheets are known. Reproduced with permission from ref.[138]

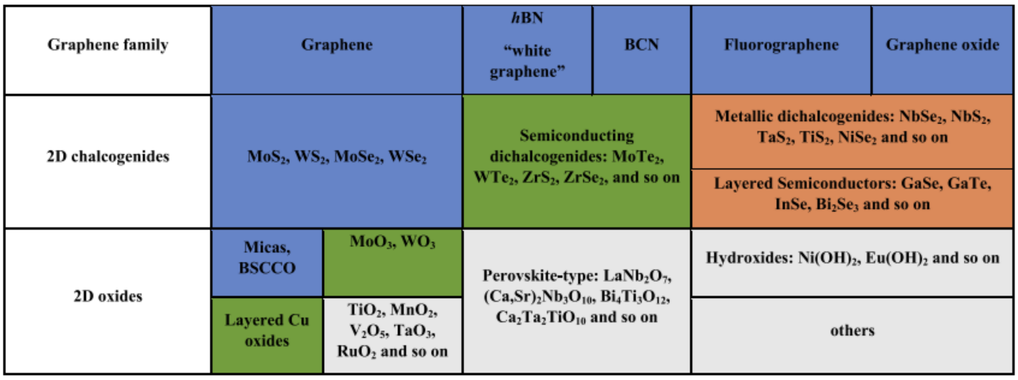

Graphene family	Graphene		*h*BN "white graphene"	BCN	Fluorographene	Graphene oxide
2D chalcogenides	MoS_2, WS_2, $MoSe_2$, WSe_2		Semiconducting dichalcogenides: $MoTe_2$, WTe_2, ZrS_2, $ZrSe_2$, and so on		Metallic dichalcogenides: $NbSe_2$, NbS_2, TaS_2, TiS_2, $NiSe_2$ and so on Layered Semiconductors: GaSe, GaTe, InSe, Bi_2Se_3 and so on	
2D oxides	Micas, BSCCO	MoO_3, WO_3	Perovskite-type: $LaNb_2O_7$, $(Ca,Sr)_2Nb_3O_{10}$, $Bi_4Ti_3O_{12}$, $Ca_2Ta_2TiO_{10}$ and so on		Hydroxides: $Ni(OH)_2$, $Eu(OH)_2$ and so on	
	Layered Cu oxides	TiO_2, MnO_2, V_2O_5, TaO_3, RuO_2 and so on			others	

metal oxides like MoO_3, V_2O_5 and insulating boron nitride. Layered compounds have proved their applicability in many promising application such as catalysis, supercapacitor, FETs, batteries, electrocatalysis and many more. In this section, we briefly discuss the structure and electronic properties of some well-known layered compounds and their academic as well as technological interest.

5. Graphene

Graphene is a single layer mono atomically thick sheet of sp^2 carbon atoms which are tightly arranged in honeycomb lattice. Graphene is considered as mother of all graphitic forms, which can be wrapped into 0D fullerene, 1D nanotubes and can be restacked into 3D graphite. The graphene was first isolated and characterized by Manchester group by A. K. Geim and K. S. Novoselov which lead to win the Nobel prize in 2010.[17, 39] The graphene obtained by micromechanical cleavage of highly oriented pyrolytic graphite (HOPG) displayed good crystalline quality and ballistic conduction.[17, 40] Graphene has attracted a lot of attention of research community because of its unique electronic properties such as very high carrier mobility, quantum Hall effect at room temperature.[41] It is known that graphene is a 2D semi-metal with a tiny overlap between valence and conduction bands.[18] Graphene exhibits a strong ambipolar electric field effect with very high concentrations of electrons and holes, up to $10^{13}/cm^2$ and room-temperature mobilities of ~10,000 $cm^2/V.s$. Furthermore, properties such as high elasticity,[41] unusual magnetic properties,[42, 43] extremely high surface area, gas adsorption makes it more exciting for numerous applications.[40, 44] In general graphene refers to single layer of sp^2 carbon atoms while bi and few-layers

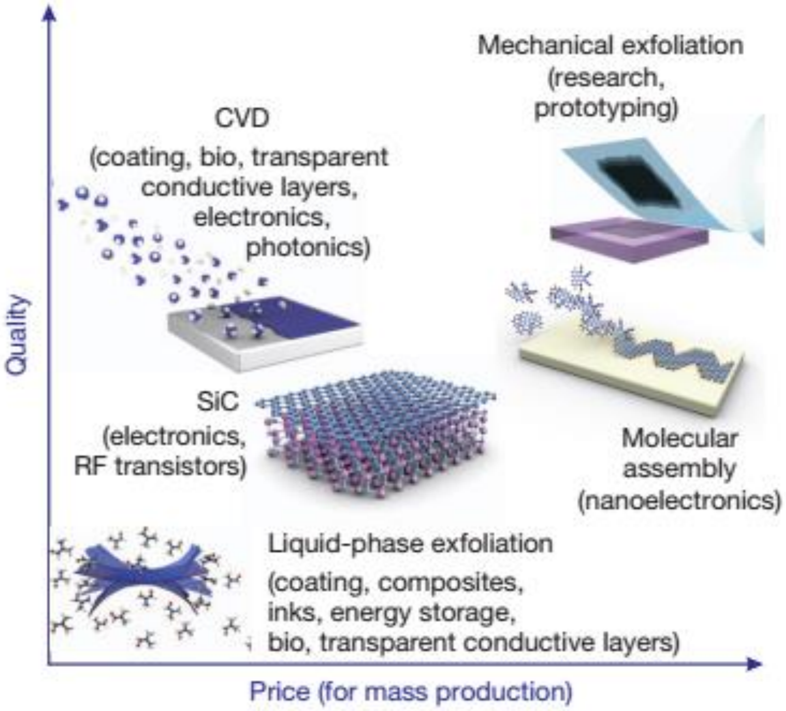

Figure 5. Comparision of synthetic procedures of nanosheets with respect to quality of the sample and mass production. Reproduced with permission from ref.[40]

graphene have been investigated due to drastic changes in the properties with number of layers.[45-47]

Properties and application of graphene depends on the process by which graphene is synthesized.[48, 49] Hence fabrication process of graphene plays a crucial role to have the optimum properties. To date no single method yields graphene exhibiting the optimum properties in more than one applications; therefore, several synthetic routes have been explored.[50-60] There are mainly two synthetic methods: physical methods[50, 52, 54, 61, 62] and chemical methods.[55-60, 63, 64] The physical methods includes mainly micromechanical exfoliation, chemical vapour deposition (CVD) and Arc discharge method. **Figure 5** shows the quality of graphene obtained by various chemical and physical methods. Micro-mechanical cleavage of HOPG using adhesive tape produce single- and few-layer graphene. Although the method produce very good quality graphene with several µm lateral dimension, the throughput of the method is very poor. Hence this method is only interesting to academicians to study the fundamental phenomenon but not suitable for mass production. The CVD growth process of graphene[50, 51] generally utilize the metal surfaces as a support and hydrocarbon as precursors at very high temperature. This method produces bulk amount of graphene with good quality which can be used in many electrochemical applications. Even though CVD method produces bulk quantity of graphene, controlling single layer and uniformity still remain a major challenge. Epitaxial growth of graphene on silicon carbide[52, 54, 62] is very promising method to synthesize uniform wafer scale graphene. But the technique is not feasible for large-scale production due to cost-effectiveness since it involves high vacuum, high temperature and single crystal substrate. Arc discharge method[61, 65] produces crystalline graphene with high thermal stability but lack of selectivity in producing number of layers with uniform size. Many chemical methods have been employed to obtain single and few-layer graphene. Chemical reduction of graphene oxide (GO) to graphene is considered to be efficient methods for low-cost and large-scale production. The quality of graphene obtained by the above process will be very poor since it involves several chemical modifications. Intercalation of guest molecules between the sheets and subsequent separation of the layers [57, 63] provides enormous potential for obtaining high quality graphene. Unzipping of carbon nanotubes by plasma etching[58, 66] and oxidative treatment[67] are also interesting but the method suffers from low throughput.

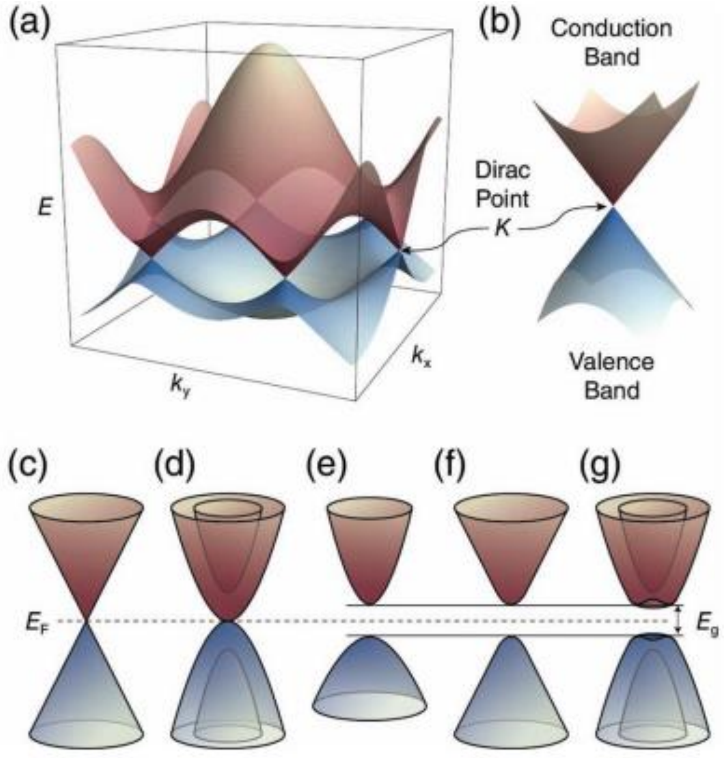

Figure 6. (a) Electronic band structure of graphene (b) linear dispersion showing Dirac cones. (c-e) Comparision of band structures in monolayer graphene(c), bi-layer graphene (d), typical direct bandgap semiconductor (e), opening of the bandgap in monolayer graphene (f), bilayer graphene (g). Reproduced with permission from ref.[83]

Single layer graphene with high quality can be obtained from physical methods, most of the chemical methods often yields few-layer graphene.[44]

Graphene is a stable material with the crystal energy similar to diamond. Graphene exhibit peculiar electronic structure with the density of states being zero at Fermi level.[68] Graphene shares two atoms per unit cell giving rise to conical points where Fermi level is crossed by electronic bands (**Figure 6**). The energy of electron within the Brillouin zone is linearly dependent on wave vector. Due to this linear or conical dispersion relation, single layer graphene mimic the relativistic particles described using Dirac equation.[69, 70] The Dirac equation is a direct consequence of the crystal symmetry of graphene. The interaction of electrons moving around the carbon atoms with the periodic potential of honeycomb lattice gives rise to quasi-particles and these carriers are called as Dirac fermions and corners of the Brillouin zone are called as Dirac points (Figure 6). The cones at Dirac points are centered at the high-symmetry K points in the Brillouin zone of the hexagonal lattice and have been explored towards valleytronics applications recently. Because of linear dispersion, the quasiparticles in graphene are expected to behave differently from those in metals and semiconductors. Graphene exhibit strong ambipolar electric field effect such that the carrier type can be tuned continuously between n and p-type.[17] A half-integer quantum Hall effect has been observed in single layer graphene at low temperatures, where Hall conductivity follows the equidistance steps of uninterrupted ladder through Dirac point.[18] A room temperature half-integer QHE has also been observed in single-layer graphene. Extremely low spin-orbit interaction in graphene makes it an ideal spin carrier for spintronics.[71, 72] The electronic structure of graphene can be engineered by chemical or structural modification to use in many optoelectronic applications. Single-layer graphene is capable of detecting individual gas molecule such as NH_3, CO, and NO_2.[73] The adsorbed molecules causes the change in charge carrier concentration leading to the resistance change. In the case of bi-layer graphene, the approximation predicts a gapless state with parabolic bands, instead of conical bands.[74] Detailed considerations revealed a small band overlap at larger energies. Thus, bi-layer graphene can be treated as a gapless semiconductor. The charge carriers have finite mass and bi-layer graphene exhibits an equally anomalous quantum Hall effect and it remains metallic at the neutrality point.[75] The gate voltage changes the carrier concentration and induces an asymmetry between the two layers, resulting in a semiconducting gap in bilayer graphene.[76-78]

Graphene shows excellent in-plane mechanical properties due to strong 2D honeycomb lattice. Several experimental studies revealed that graphene is a novel nanomaterial with excellent mechanical properties.[41] With 0.35 nm thickness Young's modulus of graphene can reach >130 GPa with 2D plane strength of 42 Nm.[79] Due to its elastic modulus and long mean free path of electrons, graphene shows extraordinary thermal behavior properties. Thermal conductivity of graphene can reach up to 3000–6000 W.[80] The optical properties of graphene is not so exciting due to its zero band gap. Single-layer graphene is colourless, it transmit completely hence graphene cannot be seen without a substrate. The light absorption intensity of graphene appear to have linear relationship with number of layers but it has no relation with frequency of light.[81] Single layer graphene shows 97.7% transmittance and 2.3% absorption respectively.[82] Graphene shows non-linear optical behaviour with infrared radiations. The defects, shape and quality of graphene have large influence on the optical performance since they alter the electronic structure. Graphene also shows paramagnetic properties under certain condition even though it does not have d or f electrons. The methods adopted for production play a crucial role in determining the properties of resultant graphene.[40, 44]

The 2D nanosheets of materials are promising architecture for electronic applications compared to their bulk counterpart. The dangling bonds present on the surface of 3D material act as electron traps and reduces the performance of the devices. The nanosheets act as 2D pristine surfaces and the electrons are confined in atomically thin space which allows easy control of charge carriers leading to excellent device characteristics. The high carrier mobility and mechanical strength of graphene make it extremely useful in flexible electronics. The high optical transparency and good conductivity of graphene enable its use in touchscreen displays, organic light emitting diodes, e-papers etc. Few-layer graphene is considered to be one of the excellent material for energy storage and conversion application due to its high surface area and layered structure. Fabrication of FETs using graphene crystals as an active component can significantly contribute for next-generation electronics. Graphene-based thin film transistor and other electronic devices has been summarized in many reviews.[83, 84] Even though graphene looks promising material for flexible electronics, there is needs to overcome various technological issues in order to have graphene in practical devices.[85] Some of the important technological issues are large-area integration, crystallinity, quality and thickness uniformity with minimal defects.[86] Deposition of graphene on insulating substrate have high priority and impact for both fundamental studies and technological applications.[86, 87]

Few-layer graphene nanosheets possess extraordinary surface to volume ratio and have been widely explored for energy storage and catalysis applications.[88] The nanosheets produced by physical methods are highly suitable for electronic applications and for fundamental studies and they found less interesting in energy storage and catalysis. The few-layer graphene obtained by chemical methods, particularly by liquid phase exfoliation are useful for the energy storage applications, although the process introduces lot of defects which cannot be removed completely.[32, 89] Graphene related materials have been used as an active or conductive component in many energy storage devices. The chemical exfoliation method enables the functionalization of graphene which facilitates the easy preparation of composite materials. The reduced surface of graphene shows electrical double layer capacitance (EDLC) behaviour whereas graphene with oxygen functionalities show pseudocapacitance behaviour (**Figure 7**). The pseudocapacitance varies according to oxygen functionalities on surface. Few-layer graphene also act as excellent anode materials for lithium and sodium ion batteries.[90-93] Energy density and power density

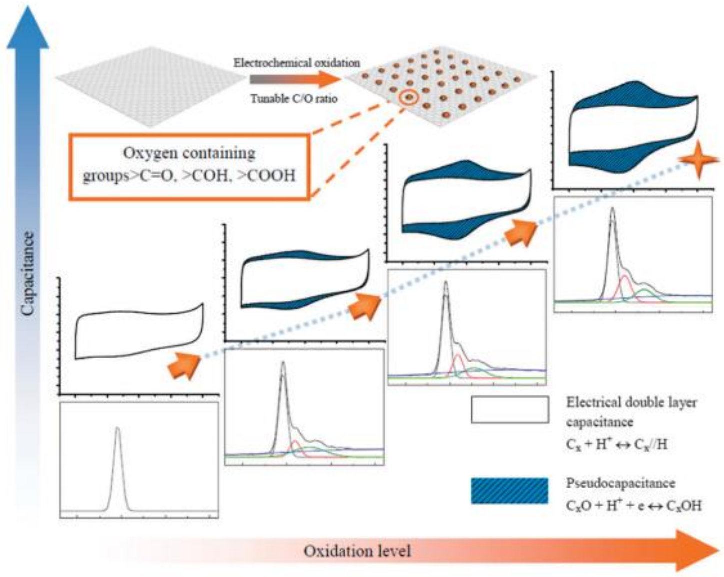

Figure 7. Introduction of pseudocapacitance in addition to EDLC by surface functionalities on graphene. Faradic capacitance increases with number of surface functionalities. Reproduced with permission from ref.[94]

of these devices are strongly dependent on microstructural properties, the methodological electrode structural design and synthetic method. Several efforts have been made to achieve excellent electrochemical energy storage and deliver it rapidly and efficiently. However, still much effort is required in the rational design of structure and chemistry of graphene to reach theoretical limit and use graphene in energy storage devices.[94, 95] The high thermal conductivity of graphene may help in dissipating the heat generated during high current loads which also results in intrinsic safety of the device.[40] Graphene-based materials have been used in a variety of catalytic reactions such as oxygen reduction reaction,[96] hydrogen generation and CO_2 activation. Even though the pristine graphene with no band gap is catalytically not much interesting, the little perturbation in structure, chemical doping and the introduction of defects can increase its activity by several folds.[97]

6. Boron nitride

Boron nitride is the structural analogue of graphene with hexagonal unit consisting of alternating B and N atoms. BN also known as white graphene and the lightest among all group III-V compounds and show resemblance with graphite and diamond in terms of number of electrons between the neighboring atoms. BN exist in the various crystal structure, the layered structure exists in hexagonal honeycomb lattice and rhombohedral form.[98] The cubic form (c-BN) which is similar to diamond and is the second hardest material known to date. Unlike graphene, BN exhibit the strong ionic character of B–N bond because of the significant difference in electronegativity of nitrogen and boron. The ionic character in B–N bonds and localized electronic structure makes BN insulating and possess large band gap.[99] In h-BN, the layers are stacked on top of each other with an interlayer spacing of 3.31 Å with van der Waals forces along c-direction with in-plane B bonded to N atoms. Even though BN is electronically insulator, it shows excellent thermal conductivity which approaches as high as 600 $Wm^{-1}K^{-1}$ in single layer BN.

The rise of graphene and the subsequent research progress on single and few-layer nanosheets intrigued the existence and properties of 2D BN nanosheets.[100] Soon after the exfoliation of graphene, single-layer BN nanosheets are mechanically peeled from BN single crystals. BN exist in various low dimensional nanostructures such as

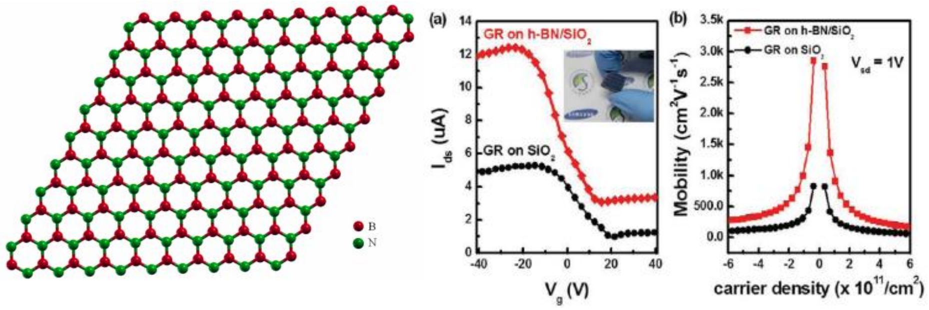

Figure 8. Structure of BN, FET characteristics of graphene device with BN as a gate dielectric in comparison with SiO_2 dielectric. Reproduced with permission from ref.[104]

Fullerenes, nanotubes, nanoribbons and nanosheets. Among the several nanostructures, nanotubes and nanosheets have received much attention. Various methods have been reported for the synthesis of single and few-layer BN, growth of few nanometers thick BN films through CVD process[101] and large-scale production of BN nanosheets through solid state reactions are noteworthy.[102] BN films have been deposited on Si substrates by microwave assisted plasma CVD without the use of any catalyst.[103] Atomically thin BN films grown by magnetron sputtering show negligible leakage current, demonstrating high-quality thin film for dielectrics.[102] BN is a very stable and excellent dielectric material for electronic devices. Recently, atomically thin BN deposited by vacuum methods found to be better gate material for graphene-based FETs, which also reveals BN is better dielectric than SiO_2 (**Figure 8**).[104, 105] Further BN nanosheets can be utilized as filler material in nanocomposite to influence the mechanical properties, thermally robust catalytic properties, sensing substrates, chemically inert super-hydrophobic films and so on.[99]

7. Borocarbonitrides

Borocarbonitrides ($B_xC_yN_z$) are layered materials with properties expected to be intermediate between gapless graphene and insulating BN. Electronic devices based on graphene are of interest due to fascinating physical properties, such as quantum Hall effect and massless Dirac Fermions. The main limitation of graphene is absence of bandgap which limits its versatility in electronic applications. Recent studies have shown chemical doping of graphene with hetero atoms alter the electronic properties with specific charge carriers (holes and electrons).[106] Theoretical calculations have shown that random doping of graphene with boron or nitrogen can open a small gap in the Dirac points. To be precise, graphene sheets containing B and N at different composition may exhibit exotic electronic properties. Borocarbonitrides with the general formula of $B_xC_yN_z$ constitute a new family of 2D materials, whose composition can be varied over a wide range.[106] These materials are generally nanosheets containing graphene and BN domains along with BCN rings.[107] If the ratio of B, N and C is 1:1:1, the composition would be BCN. Structure of BCN contain hexagonal networks of B−C, B−N, C−N, and C−C bonds but no B−B and N-N bonds. The structural similarities between graphene and BN nanosheets allow them to form in-plane hybrids with continuously tunable C:BN composition, which alters the electronic characteristics. Single and few-layer BCN containing hybridized bonds of B, C and N have shown good electronic and optical properties which are very distinct from those of graphene and BN. B, N-doped graphene films can be synthesized using a thermal catalytic CVD method. BCN can be prepared in large scale using activated carbon, boric acid and urea through solid state reaction. A significant breakthrough on the controlled CVD preparation and characterization of epitaxial BCN nanosheets has recently been reported.[108] BCN nanosheets could also be prepared by either doping BN structures with C or replacing C atoms in graphene with B and N.[109] The properties of BCN mainly depends on its composition and the domain sizes of BN and graphene. BCN nanosheets and other morphologies shows composition dependent luminescence properties.[110, 111]

BCN nanosheets are most promising candidates for several applications owing high chemical heterogeneity, tunable band gap and surface areas. BCN nanosheets would be expected to exhibit novel distinct properties compared to graphene and BN. The various applications including supercapacitors, oxygen reduction reaction, hydrogen evolution reaction, batteries and transistors have been studied.[112] It is noteworthy that energy and electrochemical devices fabricated using BCN are superior compared to those of graphene and other layered materials such as MoS_2.[113, 114] Tunability of the band gap is a significant feature that can be exploited for several optoelectronic and semiconductor devices. The composition and band gap of BCN are yet to be fully examined to generate materials with desirable features. Furthermore, it may be necessary to determine some of the properties of BCN with respect to composition, morphology and number of layers. It would be most worthwhile to study the electronic and optical properties of BCN with a wide range of compositions. The rigorous theoretical calculations may help in understanding of chemical heterogeneity, domain structure and composition of these materials and the resulting properties.[113]

8. Nanosheets of transition metal dichalcogenides (TMDs)

Graphene is the most popular 2D material due to its fascinating properties, but the absence of a bandgap limits its applications in electronic devices. This has given rise to interest of researchers in layered materials with semiconducting properties.[115] The inorganic transition metal dichalcogenides (TMDCs) with semiconducting character with the general formula of MX_2, where M is a transition metal atom (M= Mo, W, Ti and so on) and X is a chalcogen atom (X= S, Se or Te) are the better alternatives.[14] TMDs are layered solids with the stacks of strongly bonded layers with weak interlayer van der Waals forces. Monolayer of TMDs consist of three atomic layers in which metal atoms are sandwiched between chalcogen atoms. Bulk TMDs are widely studied materials over last few decades because of formulation of materials with distinct electronic structure. The layered structure of TMDs allow for the exfoliation bulk solid into single and few-layer nanosheets. The single and few-layer nanosheets of these materials exhibit distinct fundamental properties compared to their bulk counterparts,[116] making them potentially interesting class of materials for wide range of applications.[115] The layer dependent properties of TMDs gained tremendous attention, for instance, several semiconducting TMDs shows transition of indirect bandgap in bulk to direct bandgap in monolayer.[116] TMDs are stable under ambient condition unlike other semiconducting materials such as phosphorene. The semiconducting TMDs display remarkable features such as layer dependent electrostatic coupling, photoswitching, band gap and so on.[115] The unique features and favorable electronic and mechanical properties, which make potentially interesting candidates for fundamental studies and for applications in electronics, spintronics, energy harvesting.[25] Several methods have been developed for the production of TMDs, the quality and properties of the layers dependent on the method employed. The ease of exfoliation into single and few-layers, large-scale production by chemical means and high surface area drew the attention towards large-scale applications. The specific surface area and larger interlayer spacing of these materials make them useful in energy storage applications.[26, 36]

TMDs exist mainly in two structural forms based on the coordination of the transition metal atoms, trigonal prismatic (2H) and octahedral (1T) phase. Molybdenum sulphide (MoS_2) is the well-studied material in TMDs family till date because of its robustness and fascinating properties. MoS_2 occurs in nature as crystalline mineral molybdenite with hexagonal symmetry. The structural phases can also be defined based on different stacking orders of the three atomic planes (X–M–X) forming the individual layers. The 2H phases correspond to an ABA stacking in which chalcogen atoms in different atomic planes occupy the same position, whereas in 1T phases follows ABC stacking order (**Figure 9a**). In 2H-phase, each metal atom puts six coordination in two tetrahedrons, the hexagonal symmetry can be seen in the top view, and therefore, X–M–X arrangement in z-direction is considered as monolayer. In 1T-phase, a trigonal chalcogen layer on the top and 180° rotated structure at the bottom in a single layer and results in hexagonal arrangement of chalcogen atoms in the top view.[115]

Considerable efforts have been devoted to synthesise uniform atomic layers of single and few-layer nanosheets TMDs using various top-down and bottom-up approaches. The most common methods are chemical intercalation, mechanical exfoliation, liquid phase exfoliation and chemical vapor deposition (CVD). Atomically thin layers of TMDs can be peeled off from the single crystal by micromechanical cleavage. Mechanical exfoliation is an effective method to produce the single layer with high quality and good crystallinity, which are suitable to study the fundamental properties and fabrication of devices. Liquid phase exfoliation methods of TMDs are promising method to obtain the large quantities of the material, which also provides the additional opportunity to obtain the hybrid materials and composites by simple mixing. The single and few-layer suspension can be used to deposit thin films for electronic applications.[31, 117] The intercalation of guest species such as n-butyllithium and organic molecules allows layers to exfoliate in solvents. The intercalation of TMDs with lithium and subsequent exfoliation in water has been successfully demonstrated, these methods found renewed interest recently. These exfoliation methods produces large quantity of samples compared to other chemical methods but the obtained single and few-layer differ in their properties. For example the exfoliation of 2H MoS_2 with n-butyllithium changes the electronic structure from semiconducting to metallic with change in crystal structure from 2H to 1T. The electrochemical intercalation of lithium and exfoliation is demonstrated for several TMDs materials including MoS_2, WS_2, TiS_2, TaS_2, which allows faster and precise control over the intercalation. The liquid phase exfoliation in organic solvents by ultrasonication gives the few hundred nanometer flakes. The chemical methods create the defects in the materials and leaves many foreign species on surfaces which may affect the device properties. However, the applications which require a large quantity of samples such as composites, catalysis and energy storage, the chemical exfoliation methods are preferred.[13, 14]

Recently, attempts have been made to obtain high-quality TMD films with wafer-scale uniformity and precise control of thickness using atomic layer deposition (ALD), CVD, sputtering and pulsed laser deposition (PLD) methods.[118, 119] These vacuum deposition methods are effective to achieve large area growth with good quality crystalline films for device applications. CVD is most commonly employed technique for the deposition of atomically thin films of MoS_2 and WS_2.[120] These methods employ metal and chalcogen precursor, heated to high temperature and deposited on the substrates. MoS_2 has been deposited successfully using MoO_3 and sulfur powder as initial precursors (**Figure 9c**). A slight modification in the method also helps to control the thickness of the film, a thin layer of Mo deposited on a substrate or substrate dip coated in the solution of $(NH_4)_2MoS_4$, heated in the sulfur

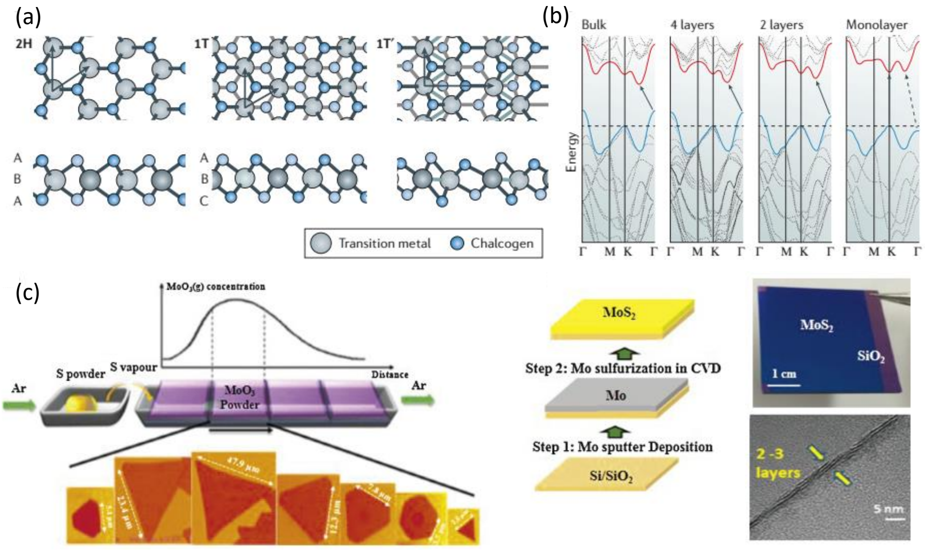

Figure 9. Schematic representation of 2H and 1T crystal phases of MoS_2. (b) Band structure of MoS_2 and corresponding changes from bulk to monolayer. (c) Schematic illustration of CVD process of MoS_2. Reproduced with permission from ref.[115]

vapour yields ultrathin MoS_2 films. Even though CVD emerged as an adequate method to deposit thin films, it is challenging to obtain growth of single and bilayers uniformly over large area. More recently ALD has been employed for the deposition of MoS_2 which allows precise control of thickness down to monolayer with wafer scale uniformity. Ultrathin films of MoS_2 has been deposited by ALD using $MoCl_5$ or MoF_6 or $Mo(CO)_6$ and H_2S as Mo and S precursor respectively.

The electronic structure of TMDs are largely determined by the crystal structure; the monolayer consists of X-M-X sandwich with in-plane covalent bonding. Despite the structural similarities TMDs exhibit broad range of electronic properties due to the diversity of chemical composition and coordination geometry of the metal atom. TMDs of group VI metal such as MoX_2 and WX_2 are semiconductors in thermodynamically stable 2H phase whereas NbX_2 and TaX_2 are metallic. The semiconducting property of these materials draw the attention towards electronic and optical devices. Another interesting factor of the TMDs is change in band structure with number of layers, monolayer MoS_2 shows the direct band gap which turns into indirect band gap in multilayers (**Figure 9b**).[121, 122] The direct bandgap has significant implication in the optoelectronic, photonic and sensing devices.[123, 124] The TMDs semiconducting gap is almost similar to the bandgap of silicon and it makes them suitable for transistors digital electronics.[87, 125, 126] MoS_2 based FET displayed the

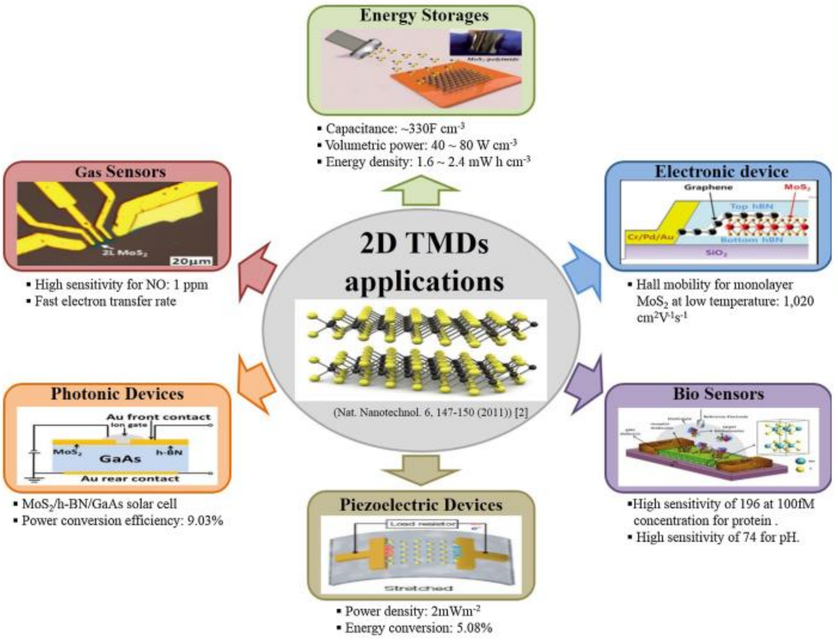

Figure 10. Applications of TMDs nanosheets in various fields such as optoelectronics, sensors, energy devices and so on. Reproduced with permission from ref.[118]

mobility of 200 cm^{2}VS^{-1} with the current on-off ratio of 10^8 at room temperature.[14] Few-layer nanosheets of TMDs possess high surface area which enables their use in energy storage devices and catalysis (**Figure 10**).[127]

Few-layer nanosheets of TMDs received significant attention as electrode material in supercapacitor and batteries due to their larger interlayer spacing compared to graphene and excellent electrochemical properties.[128, 129] The layered structure offers more storage sites with facile path for diffusion of ions into the bulk of the material and maintains structural stability while charging and discharging. Supercapacitor electrode fabricated with MoS_2 as an active electrode material shows electrical double layer capacitance due to stacked nanosheet morphology and huge pseudocapacitance due to different oxidation states of Mo.[118] The specific capacitance of MoS_2 depends mainly on the flake size, number of layers and defects present in the material. Several efforts have been made to increase the capacitance of MoS_2 by using various synthetic methods by tuning the surface morphology, increasing the interlayer spacings and so on. The edge-oriented vertically aligned MoS_2 with larger van der Walls gaps emerged as the superior geometry for energy storage.[118] The sponge-like vertically aligned MoS_2 nanosheets demonstrated for

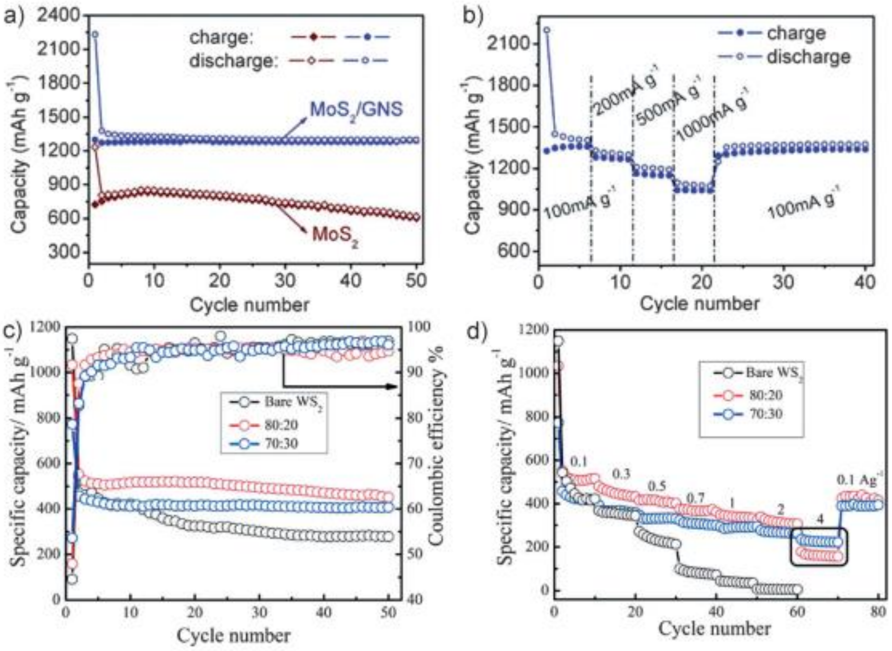

Figure 11. (a) Galvanostatic cycling behaviors of MoS_2 and MoS_2-graphene composites. (b) Cycling behaviors of MoS_2-graphene at different current densities. (c) Galvanostatic cyclic performance and coulombic efficiencies of WS_2 and WS_2-graphene composites (d) specific capacities at various discharge currents. Reproduced with permission from ref.[134]

flexible supercapacitor with high areal capacitance. The chemically derived 1T metallic MoS_2 nanosheets exhibit better electrical conductance than 2H MoS_2, thereby displaying excellent capacitance of 400 to 700 Fcm^{-3}.[130] The low electrical conductivity and cycle stability of 2H MoS_2 can be offset by preparing its composites with graphene.[128] MoS_2-graphene based composites exhibit outstanding electrochemical performance with good cyclic stability over several cycles.[118] Few-layer MoS_2 nanosheets as an active electrode material in Li-ion battery display first discharge capacity of 800 $mAhg^{-1}$ and maintain stable capacity of 750 $mAhg^{-1}$ over several cycles whereas bulk MoS_2 show drastic fade in capacity.[131] Various synthetic strategies and structural modifications have been employed to improve the stability and capacity of MoS_2 batteries. The highest capacity of 2200 $mAhg^{-1}$ has been observed in the first discharge cycle with a stable reversible capacity of 1290 $mAhg^{-1}$ up to 50 cycles for the MoS_2-graphene composites.[132] Similarly, pristine WS_2 nanosheets show the reversible charging capacity of 780 $mAhg^{-1}$ with good cyclic stability at a current density of 47 mAg^{-1}.[133] WS_2-graphene composites also exhibit excellent lithiation capacity with good rate capability and excellent cyclic stability (**Figure 11**).[134, 135] The rapid progress in the TMDs research proved that atomically thin layers of these materials have a potential impact on the future electronics and energy storage devices.

9. Nanosheets of transition metal oxides (TMOs)

Layered metal oxide nanosheets forms an important class of 2D materials and are significant by virtue of their properties and practical importance. Along with graphene and TMDs, inorganic nanosheets of oxides received considerable attention since oxides constitute the richest class of materials with a wide range of properties.[134] These oxide nanosheets have distinct differences and advantages compared with graphene and TMDs due to their potential to be used as insulators, semiconductors, and even conductors. Single and few-layer oxide nanosheets have the potential to be used as dielectric alternatives in next-generation nanoelectronics.[136] Inorganic nanosheets derived from layered transition metal oxides have tunable properties with diverse chemical composition and crystal structure.[137] As oxides, they are very stable in ambient condition and also exhibit high chemical and thermal stability. Similar to other atomically thin layers of TMDs, the properties of thin oxide nanosheets are expected to differ from those of their bulk owing to quantum confinement. Among numerous oxides TiO_2, MoO_3, WO_3 and many perovskite oxides such as BSCCO are delaminated from their bulk.[138] Indeed, monolayer oxide nanosheets often have lower dielectric constants and larger bandgaps than their bulk counterparts. However, most of the studies on single and few-layer nanosheets of metal oxides are limited to their synthesis and microscopic characterization. The fundamental properties, layer dependent studies of isolated nanosheets are yet to be studied in detail. The oxide nanosheets also show wide range of electronic and optical properties, the nanosheets based on Ti, Ta, Nb, etc. show semiconducting properties while Mn, Mo, W oxide nanosheets exhibit redox reactivity.

Single and few-layer metal oxide nanosheets can be obtained by various chemical and physical methods.[139] The exfoliation by osmotic swelling was first employed by Sasaki, emerged as a significant method. Various non-layered oxide films have been prepared in recent years, the early report of the preparation of single layers of titanates by delamination of layered titanates deserves special mention.[16] An important strategy employed for delamination is to use intercalating agents such as tetrabutylammonium ions or long-chain amines. The dielectric properties of layered titanate nanosheets have been investigated in detail, and nanosheets show relatively high dielectric constant. Another interesting class of layered oxides are layered

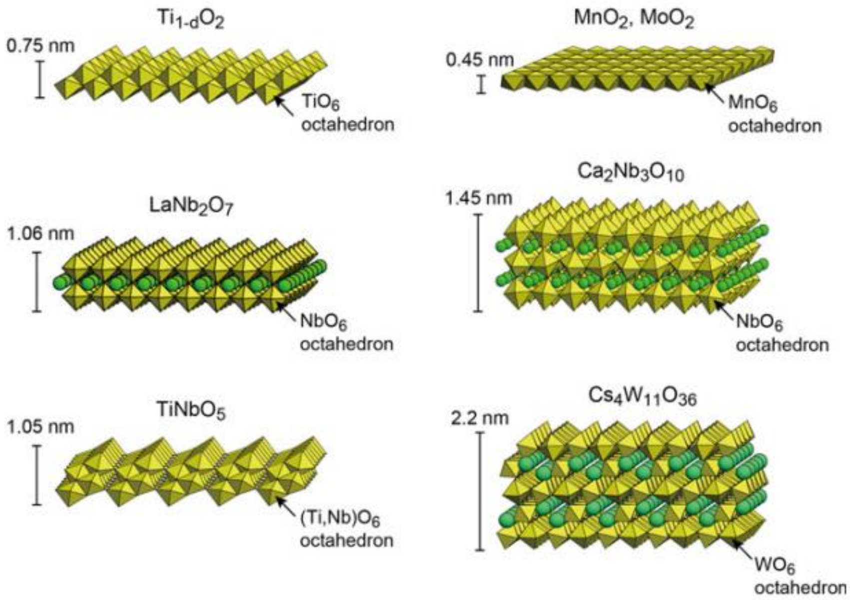

Figure 12. Structures of selected oxide nanosheets. Reproduced with permission from ref.[136]

perovskite oxides with interesting magnetic, dielectric and other properties.[140] Of these oxides, Aurivillius family with the general formula (Bi_2O_2) $(A_{m-1}B_mO_{3m+1})$ and the Ruddlesdon–Popper family with the general formula $A_{m+1}M_mO_{3m+1}$ received significant attention. The exfoliation of various members of these family of oxides have been reported and they possess interesting ferroelectric and magnetic properties.[141] Some materials with Ruddlesden–Popper family ($SrLaTi_2TaO_{10}$, $Ca_2Ta_2TiO_{10}$) and Aurivillius family ($Bi_4Ti_3O_{12}$, $Bi_4Ti_3FeO_{15}$) of oxides have been delaminated into single and few-layers.[142] The important aspect of these nanosheets is that they consist of perovskite building blocks with a high molecular polarizability. $Ca_2Nb_3O_{10}$ nanosheets have extensively been investigated as high-k nanodielectrics and their multilayer films exhibited insulating properties even at thicknesses below 10 nm.[141] The high permittivity high capacitor density of oxide nanosheets make them potential targets for capacitor applications.[143] A common feature of the oxide nanosheet films is the size-effect-free characteristic of dielectric responses. The multilayer films of $Ti_{0.87}O_2$, Ti_2NbO_7, nanosheets showed stable dielectric responses even at few nm thickness. In $Ca_2Nb_3O_{10}$, multilayer films maintained a constant permittivity value with negligible dielectric loss. **Figure 12** show the structures of single layer sheets of perovskite oxides of $LaNb_2O_7$ and $(CaSr)_2Nb_3O_{10}$.[134] Osada and Sasaki have extensively reviewed the layered oxide nanosheets structures and their dielectric properties.[136, 144] Recent interests on room temperature ferromagnetic semiconductors have stimulated research on nanosheet based ferromagnets. There have been several studies reported on magnetic properties of oxide nanosheets. Ferromagnetic properties in oxide nanosheets were first observed in $Ti_{0.8}Co_{0.2}O_2$, layers of layered titanate. The magnetic properties of layered titanates can be tuned by doping with Fe and Co impurities. The variation of the dielectric constant with the number of layers is a valuable feature for the fabrication of devices. Similarly, layer-dependent magnetic properties could be used in spintronics. There are several studies to be carried out on single- and few-layer nanosheets of metal oxides.[136] The layer-dependent properties of layered rare-earth manganites could be investigated in regard to their magnetic and electrical properties. The layer dependent superconducting properties of BSCCO and YBCO could be studied. Various useful properties have been developed by stacking oxide nanosheets into hybrid materials or multilayer heterostructures. Nanodevices can be fabricated through the selection of nanosheets with desired properties and combining them with precise control over their lateral arrangement. The high-k nanocapacitors, field-effect transistors (FETs), ferroelectrics, magnetic superlattices, energy storage devices have been successfully demonstrated.[145]

Single and few-layered nanosheets of simple oxides such as MoO_3 and V_2O_5 have been studied extensively for their electrochemical supercapacitor performances and battery chemistries.[146, 147] The layered structure of MoO_3 exists in orthorhombic structure with P_{nma} space group. Single layer nanosheet of MoO_3 is composed of double layer of linked distorted MoO_6 octahedra with the edge-sharing along [001] direction and corner-sharing along [100] direction. In vertical direction the octahedral layers are held together by van der Waal forces, thus allow easy exfoliation of bulk material into individual layers. α-MoO_3 exhibit p-type semiconducting nature with the optical band gap of 3 eV, the band structure is indirect in nature. Single layer MoO_3 has been mechanically exfoliated, the thickness of the single layer is found to 1.4 nm. Several methods including liquid phase exfoliation, CVD and sol-gel have been employed for the production of few-layer nanosheets of MoO_3. The layered structure of MoO_3 makes it versatile and highly tunable material for catalytic, optical, electronic, and energy systems. The properties and potential applications of MoO_3 based oxides have been thoroughly reviewed. [148] The layered MoO_3 exhibit excellent electrochromic and photochromic properties. MoO_3 also emerged as potential material for the degradation of organic pollutant under light. Hetero-structuring and band gap narrowing has been tried to tune the properties of MoO_3. Layered $MoO_{3,}$ owing to its excellent redox properties, emerged as a potential candidate as electrode material for batteries and supercapacitors. The battery characteristics of MoO_3 has been extensively studied for both anode and cathode material.[148] The composites based MoO_3 and graphene show good electrochemical stability and excellent capacity approaches nearly to its theoretical capacity. The composites of MoO_3 nanosheets with various conducting carbonaceous structure exhibit excellent supercapacitor electrode performances. Similarly V_2O_5 nanosheets also exhibit good supercapacitor and battery performances.[149] The layer dependent properties of these nanosheets is yet to study and which may yield new interesting phenomenon. Various oxide based heterostructure could be obtained by employing suitable synthetic strategies to achieve stable devices architectures for future electronics.

10. Nanosheets of non-layered materials

Ultrathin 2D nanomaterials display many unconventional physical, optical and electronic properties because of strong confinement of charge carriers in two dimension and high specific surface area.[38] 2D nanostructure shows great potential as active material in electronic devices, energy storage, catalysis and also provides a very good platform to study fundamental properties such as charge density, two-dimensional electron gas, quantum Hall effect etc.[17] The research on nanosheets of layered materials has achieved huge success since the discovery of graphene. Layered materials such as Graphite, TMDs, TMOs with weak forces between the layers became a diverse source of 2D nanosheets.[15, 30] However their species are limited after all, several functional materials with superior properties exist in bulk crystals with atomic bonding in three dimensions, showing the non-layered nature of the materials.[12] For instance, group III-V semiconductors show both high carrier mobility and direct bandgap. Taking the 2D geometry consideration and inspired by plenty of emergent properties displayed by ultrathin films of layered materials, it would be natural attempt to anticipate that, 2D nanosheets of non-layered materials may bring up some unique physical and chemical properties that cannot be attained from their bulk counterparts. The nanosheets of non-layered material with strong fundamental properties in the bulk and 2D characteristic could lead to several exotic functions. As a consequence, 2D

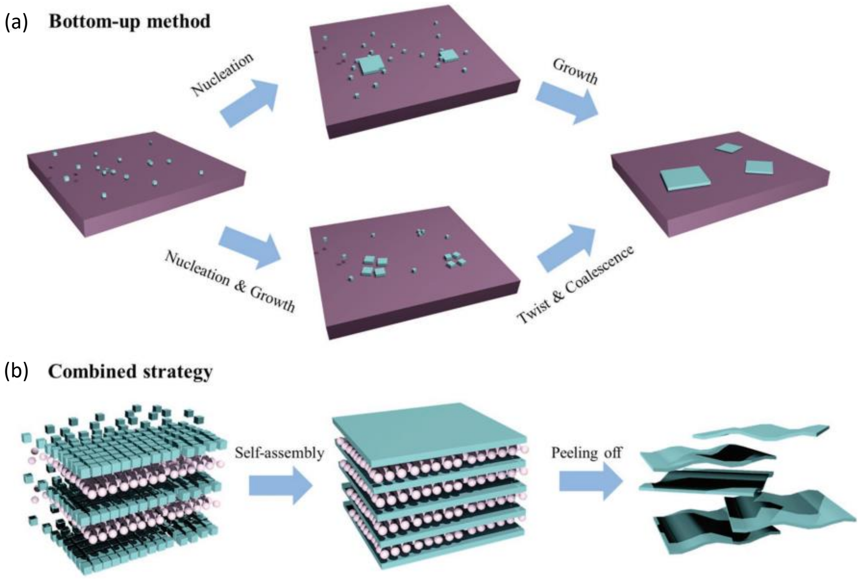

Figure 13. Synthetic strategies for the nanosheets of non-layered materials. Reproduced with permission from ref.[36]

nanostructures of non-layered materials received significant attention in recent days and it might have some beneficial effects on emerging applications.[36] Another important aspect is the surface of 2D non-layered materials filled with dangling bonds which are absent in the nanosheets of layered materials, make the surface highly active for catalysis and sensing. However synthesis of free-standing 2D nanostructure has been limited to the exfoliation of layered materials. Lack of a robust synthetic mechanism for the bottom-up synthesis of nanosheets of non-layered solids has become an obstacle to explore the physical and chemical properties and advanced applications. The development of controlled synthetic methods to prepare ultrathin nanosheets of non-layered materials is important. Several bottom-up synthetic strategies have been approached to achieve the anisotropic growth (**Figure 13**), namely wet chemical method, template-assisted synthesis, self-assembly of low dimensional nanocrystals and surfactant-assisted synthesis to name a few.[37, 150] The wet chemistry methods of synthesis emerged as a potential method to reproduce the nanosheets on non-layered materials in large scale.[35, 37, 151] The ultrathin 2D nanosheets of various non-layered materials, including metals (Au, Pd, Pt etc.), metal oxides (TiO_2, ZnO, CeO_2, SnO_2, Fe_2O_3 etc.), metal chalcogenides (CuS, SnSe, ZnS,

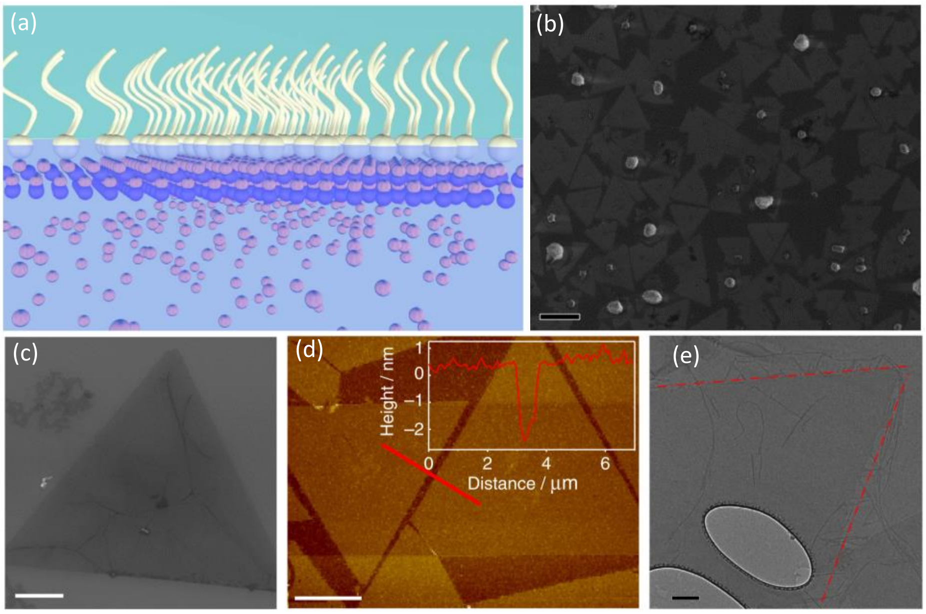

Figure 14. (a) Schematic representation of the formation of ZnO nanosheets directed by surfactant monolayer. (b) SEM image of the nanosheets on a Si/SiO_2 substrate (scale bar 10 µm). (c) SEM image showing a typical nanosheet with an equiangular triangle shape (scale bar 5 µm). (d) AFM topography image of typical nanosheets with flat surfaces on a Si substrate (scale bar 5 µm). (e) TEM image of a corner of a ZnO nanosheet (scale bar 200 nm). Reproduced with permission from ref.[35]

CdSe etc.) and metal nitride (GaN, VN etc.) have been successfully synthesized in recent days.[12, 37] Most of these nanosheets of non-layered materials are obtained by wet chemical synthetic route.[152] As expected, the synthesized unique 2D geometry of these non-layered materials show some unique advantages in comparison with their counterparts and hold great promise in a variety of applications, such as catalysis, supercapacitors, batteries photodetectors and so on. [153] In this connection, synthesis of large area single crystalline ZnO nanosheets by surfactant-assisted solution-based technique is noteworthy. **Figure 14** shows the ZnO nanosheets obtained by above process and interestingly these sheets exhibit p-type conductivity whereas, bulk ZnO inherently exhibit n-type.[35] The research on 2D nanosheets of non-layered materials is still in its infant stage and the most of the focus is paid towards material synthesis hitherto. There are only limited studies on the fundamental properties and device applications. There are still lot more materials whose atomically thin sheets have not been known. Another promising direction in this field is the fabrication of functional heterostructure or hybrid nanomaterials based on the 2D nanosheets of non-layered materials.

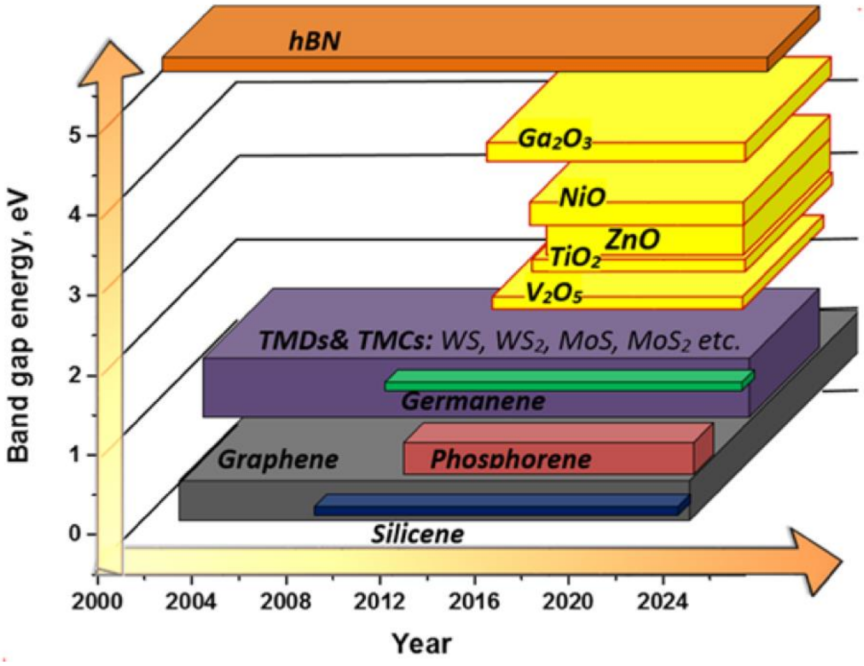

Figure 15. Evolution of the family of 2D materials as a function of time and their respective band gap values. The yellow slabs indicate the expected 2D metal oxides contribution. Reproduced with permission from ref.[154]

11.Summary and outlook

Owing to their novel properties, 2D nanosheets of various layered materials have demonstrated promising applications in electronics, catalysis, energy conversion and storage. Graphene and MoS_2 have been particularly prominent amongst the 2D materials in terms of the variety of novel properties with potential applications. Recently, 2D materials such as phosphorene, silicene and germanene have received much attention due to their semiconducting properties. The 2D materials constitute the materials with a range of properties from best conductor graphene to insulating BN, along with some narrow band gap semiconductors. The current library of 2D materials is incomplete with respect to their bandgap due to lack of materials which can fill the bridge between ~ 2.3 to 6 eV (**Figure 15**). To make rapid progress in technology, bridging this gap is very necessary. The mentioned barrier of band gap energy range (~2.3– 6 eV) can be successfully overcome not only by existing 2D non-graphene materials, but also by a forthcoming group of metal oxides, metal nitrides and other nanosheets of non-layered materials. This thesis deals entirely with the ultrathin layers of metal oxides, nitrides and sulfides prepared by different means including atomic layer deposition. Many properties of these materials with potential applications have been examined.

12. References

[1] M.-C. Daniel, D. Astruc, *Chem. Rev.* **2004**, *104*, 293-346.

[2] W. P. Halperin, *Rev. Mod. Phys.* **1986**, *58*, 533-606.

[3] N. Satoh, T. Nakashima, K. Kamikura, K. Yamamoto, *Nat. Nanotechnol.* **2008**, *3*, 106.

[4] Y. Wang, N. Herron, *J. Phys. Chem.* **1991**, *95*, 525-532.

[5] S. Zeng, D. Baillargeat, H.-P. Ho, K.-T. Yong, *Chem. Soc. Rev.* **2014**, *43*, 3426-3452.

[6] I. Shalish, H. Temkin, V. Narayanamurti, *Phys. Rev. B* **2004**, *69*, 245401.

[7] M. C. Roco, *J. Nanopart. Res.* **2011**, *13*, 427-445.

[8] W. P. McCray, *History and Technology* **2005**, *21*, 177-203.

[9] K. A. Dunphy Guzmán, M. R. Taylor, J. F. Banfield, *Environ. Sci. Technol.* **2006**, *40*, 1401-1407.

[10] X. Zhang, Y. Xie, *Chem. Soc. Rev.* **2013**, *42*, 8187-8199.

[11] Y. Sun, S. Gao, F. Lei, C. Xiao, Y. Xie, *Acc. Chem. Res.* **2015**, *48*, 3-12.

[12] L. Peng, P. Xiong, L. Ma, Y. Yuan, Y. Zhu, D. Chen, X. Luo, J. Lu, K. Amine, G. Yu, *Nat. Commun.* **2017**, *8*, 15139.

[13] M. Chhowalla, H. S. Shin, G. Eda, L.-J. Li, K. P. Loh, H. Zhang, *Nat. Chem.* **2013**, *5*, 263.

[14] Q. H. Wang, K. Kalantar-Zadeh, A. Kis, J. N. Coleman, M. S. Strano, *Nat. Nanotechnol.* **2012**, *7*, 699.

[15] M. Xu, T. Liang, M. Shi, H. Chen, *Chem. Rev.* **2013**, *113*, 3766-3798.

[16] T. Sasaki, M. Watanabe, H. Hashizume, H. Yamada, H. Nakazawa, *J. Am. Chem. Soc.* **1996**, *118*, 8329-8335.

[17] A. K. Geim, K. S. Novoselov, *Nat. Mater.* **2007**, *6*, 183.

[18] K. S. Novoselov, A. K. Geim, S. V. Morozov, D. Jiang, M. I. Katsnelson, I. V. Grigorieva, S. V. Dubonos, A. A. Firsov, *Nature* **2005**, *438*, 197.

[19] K. S. Novoselov, A. K. Geim, S. V. Morozov, D. Jiang, Y. Zhang, S. V. Dubonos, I. V. Grigorieva, A. A. Firsov, *Science* **2004**, *306*, 666.

[20] A. K. Geim, *Science* **2009**, *324*, 1530.

[21] A. H. Castro Neto, F. Guinea, N. M. R. Peres, K. S. Novoselov, A. K. Geim, *Rev. Mod. Phys.* **2009**, *81*, 109-162.

[22] Y. Zhang, L. Zhang, C. Zhou, *Acc. Chem. Res.* **2013**, *46*, 2329-2339.

[23] Y. Zhu, S. Murali, W. Cai, X. Li, J. W. Suk, J. R. Potts, R. S. Ruoff, *Adv. Mater*. **2010**, *22*, 3906-3924.

[24] P. Yu, W. Fu, Q. Zeng, J. Lin, C. Yan, Z. Lai, B. Tang, K. Suenaga, H. Zhang, Z. Liu, *Adv. Mater*. **2017**, *29*, 1701909-n/a.

[25] X. Duan, C. Wang, A. Pan, R. Yu, X. Duan, *Chem. Soc. Rev.* **2015**, *44*, 8859-8876.

[26] M. Chhowalla, Z. Liu, H. Zhang, *Chem. Soc. Rev.* **2015**, *44*, 2584-2586.

[27] Y. Sun, S. Gao, F. Lei, Y. Xie, *Chem. Soc. Rev.* **2015**, *44*, 623-636.

[28] J. Di, C. Yan, A. D. Handoko, Z. W. Seh, H. Li, Z. Liu, *Mater. Today*. **2018,** *DOI: 10.1016/j.mattod.2018.01.034*

[29] Y. Sun, S. Gao, Y. Xie, *Chem. Soc. Rev.* **2014**, *43*, 530-546.

[30] C. Tan, X. Cao, X.-J. Wu, Q. He, J. Yang, X. Zhang, J. Chen, W. Zhao, S. Han, G.-H. Nam, M. Sindoro, H. Zhang, *Chem. Rev.* **2017**, *117*, 6225-6331.

[31] J. N. Coleman, M. Lotya, A. O'Neill, S. D. Bergin, P. J. King, U. Khan, K. Young, A. Gaucher, S. De, R. J. Smith, I. V. Shvets, S. K. Arora, G. Stanton, H.-Y. Kim, K. Lee, G. T. Kim, G. S. Duesberg, T. Hallam, J. J. Boland, J. J. Wang, J. F. Donegan, J. C. Grunlan, G. Moriarty, A. Shmeliov, R. J. Nicholls, J. M. Perkins, E. M. Grieveson, K. Theuwissen, D. W. McComb, P. D. Nellist, V. Nicolosi, *Science* **2011**, *331*, 568.

[32] V. Nicolosi, M. Chhowalla, M. G. Kanatzidis, M. S. Strano, J. N. Coleman, *Science* **2013**, *340*.

[33] M. Yi, Z. Shen, *J. Mater. Chem. A* **2015**, *3*, 11700-11715.

[34] K. Manna, H.-N. Huang, W.-T. Li, Y.-H. Ho, W.-H. Chiang, *Chem. Mater.* **2016**, *28*, 7586-7593.

[35] F. Wang, J.-H. Seo, G. Luo, M. B. Starr, Z. Li, D. Geng, X. Yin, S. Wang, D. G. Fraser, D. Morgan, Z. Ma, X. Wang, *Nat. Commun.* **2016**, *7*, 10444.

[36] F. Wang, Z. Wang, T. A. Shifa, Y. Wen, F. Wang, X. Zhan, Q. Wang, K. Xu, Y. Huang, L. Yin, C. Jiang, J. He, *Adv. Funct. Mater.* **2017**, *27*, 1603254.

[37] C. Tan, H. Zhang, *Nat. Commun.* **2015**, *6*, 7873.

[38] I. Y. Kim, Y. K. Jo, J. M. Lee, L. Wang, S.-J. Hwang, *J. Phys. Chem. Lett.* **2014**, *5*, 4149-4161.

[39] K. K. Banger, Y. Yamashita, K. Mori, R. L. Peterson, T. Leedham, J. Rickard & H. Sirringhaus, *Nat. Mater.* **2010**, *10*, 1.

[40] K. S. Novoselov, V. I. Fal′ko, L. Colombo, P. R. Gellert, M. G. Schwab, K. Kim, *Nature Rev* **2012**, *490*, 192.

[41] C. Lee, X. Wei, J. W. Kysar, J. Hone, *Science* **2008**, *321*, 385.

[42] H. S. S. R. Matte, K. S. Subrahmanyam, C. N. R. Rao, *J. Phys. Chem. C* **2009**, *113*, 9982-9985.

[43] Y. Wang, Y. Huang, Y. Song, X. Zhang, Y. Ma, J. Liang, Y. Chen, *Nano Lett.* **2009**, *9*, 220-224.

[44] C. N. R. Rao, A. K. Sood, R. Voggu, K. S. Subrahmanyam, *J. Phys. Chem. Lett.* **2010**, *1*, 572-580.

[45] K. R. Paton, E. Varrla, C. Backes, R. J. Smith, U. Khan, A. O'Neill, C. Boland, M. Lotya, O. M. Istrate, P. King, T. Higgins, S. Barwich, P. May, P. Puczkarski, I. Ahmed, M. Moebius, H. Pettersson, E. Long, J. Coelho, S. E. O'Brien, E. K. McGuire, B. M. Sanchez, G. S. Duesberg, N. McEvoy, T. J. Pennycook, C. Downing, A. Crossley, V. Nicolosi, J. N. Coleman, *Nat. Mater.* **2014**, *13*, 624.

[46] S. Stankovich, D. A. Dikin, G. H. B. Dommett, K. M. Kohlhaas, E. J. Zimney, E. A. Stach, R. D. Piner, S. T. Nguyen, R. S. Ruoff, *Nature* **2006**, *442*, 282.

[47] A. C. Ferrari, J. C. Meyer, V. Scardaci, C. Casiraghi, M. Lazzeri, F. Mauri, S. Piscanec, D. Jiang, K. S. Novoselov, S. Roth, A. K. Geim, *Phys. Rev. Lett.* **2006**, *97*, 187401.

[48] S. Guo, S. Dong, *Chem. Soc. Rev.* **2011**, *40*, 2644-2672.

[49] M. Pumera, *Chem. Soc. Rev.* **2010**, *39*, 4146-4157.

[50] X. Li, W. Cai, J. An, S. Kim, J. Nah, D. Yang, R. Piner, A. Velamakanni, I. Jung, E. Tutuc, S. K. Banerjee, L. Colombo, R. S. Ruoff, *Science* **2009**, *324*, 1312.

[51] N. G. Shang, P. Papakonstantinou, M. McMullan, M. Chu, A. Stamboulis, A. Potenza, S. S. Dhesi, H. Marchetto, *Adv. Funct. Mater.* **2008**, *18*, 3506-3514.

[52] D. Deng, X. Pan, H. Zhang, Q. Fu, D. Tan, X. Bao, *Adv. Mater.* **2010**, *22*, 2168-2171.

[53] A. Srivastava, C. Galande, L. Ci, L. Song, C. Rai, D. Jariwala, K. F. Kelly, P. M. Ajayan, *Chem. Mater.* **2010**, *22*, 3457-3461.

[54] C. Berger, Z. Song, T. Li, X. Li, A. Y. Ogbazghi, R. Feng, Z. Dai, A. N. Marchenkov, E. H. Conrad, P. N. First, W. A. de Heer, *J. Phys. Chem. B* **2004**, *108*, 19912-19916.

[55] D. Li, M. B. Müller, S. Gilje, R. B. Kaner, G. G. Wallace, *Nat. Nanotechnol.* **2008**, *3*, 101.

[56] H.-L. Guo, X.-F. Wang, Q.-Y. Qian, F.-B. Wang, X.-H. Xia, *ACS Nano* **2009**, *3*, 2653-2659.

[57] M. Lotya, Y. Hernandez, P. J. King, R. J. Smith, V. Nicolosi, L. S. Karlsson, F. M. Blighe, S. De, Z. Wang, I. T. McGovern, G. S. Duesberg, J. N. Coleman, *J. Am. Chem. Soc.* **2009**, *131*, 3611-3620.

[58] L. Jiao, L. Zhang, X. Wang, G. Diankov, H. Dai, *Nature* **2009**, *458*, 877.

[59] M. Zhou, Y. Wang, Y. Zhai, J. Zhai, W. Ren, F. Wang, S. Dong, *Chem. Eur. J* **2009**, *15*, 6116-6120.

[60] X. Yang, X. Dou, A. Rouhanipour, L. Zhi, H. J. Räder, K. Müllen, *J. Am. Chem. Soc.* **2008**, *130*, 4216-4217.

[61] Z.-S. Wu, W. Ren, L. Gao, J. Zhao, Z. Chen, B. Liu, D. Tang, B. Yu, C. Jiang, H.-M. Cheng, *ACS Nano* **2009**, *3*, 411-417.

[62] S. Shivaraman, R. A. Barton, X. Yu, J. Alden, L. Herman, M. V. S. Chandrashekhar, J. Park, P. L. McEuen, J. M. Parpia, H. G. Craighead, M. G. Spencer, *Nano Lett.* **2009**, *9*, 3100-3105.

[63] P. K. Ang, S. Wang, Q. Bao, J. T. L. Thong, K. P. Loh, *ACS Nano* **2009**, *3*, 3587-3594.

[64] H. Qian, F. Negri, C. Wang, Z. Wang, *J. Am. Chem. Soc.* **2008**, *130*, 17970-17976.

[65] K. S. Subrahmanyam, L. S. Panchakarla, A. Govindaraj, C. N. R. Rao, *J. Phys. Chem. C* **2009**, *113*, 4257-4259.

[66] L. Jiao, L. Zhang, L. Ding, J. Liu, H. Dai, *Nano Res.* **2010**, *3*, 387-394.

[67] A. Hirsch, *Angew. Chem. Int. Ed.* **2009**, *48*, 6594-6596.

[68] P. Miro, M. Audiffred, T. Heine, *Chem. Soc. Rev.* **2014**, *43*, 6537-6554.

[69] M. I. Katsnelson, K. S. Novoselov, A. K. Geim, *Nat. Phys.* **2006**, *2*, 620.

[70] F. D. M. Haldane, *Phys. Rev. Lett.* **1988**, *61*, 2015-2018.

[71] W. Han, R. K. Kawakami, M. Gmitra, J. Fabian, *Nat. Nanotechnol.* **2014**, *9*, 794.

[72] D. Pesin, A. H. MacDonald, *Nat. Mater.* **2012**, *11*, 409.

[73] F. Schedin, A. K. Geim, S. V. Morozov, E. W. Hill, P. Blake, M. I. Katsnelson, K. S. Novoselov, *Nat. Mater.* **2007**, *6*, 652.

[74] K. S. Novoselov, E. McCann, S. V. Morozov, V. I. Fal’ko, M. I. Katsnelson, U. Zeitler, D. Jiang, F. Schedin, A. K. Geim, *Nat. Phys.* **2006**, *2*, 177.

[75] B. Partoens, F. M. Peeters, *Phys. Rev. B* **2006**, *74*, 075404.

[76] E. McCann, *Phys. Rev. B* **2006**, *74*, 161403.

[77] E. V. Castro, K. S. Novoselov, S. V. Morozov, N. M. R. Peres, J. M. B. L. dos Santos, J. Nilsson, F. Guinea, A. K. Geim, A. H. C. Neto, *Phys. Rev. Lett.* **2007**, *99*, 216802.

[78] C. N. R. Rao, A. K. Sood, K. S. Subrahmanyam, A. Govindaraj, *Angew. Chem. Int. Ed.* **2009**, *48*, 7752-7777.

[79] J. Wang, F. Ma, M. Sun, *RSC Adv.* **2017**, *7*, 16801-16822.

[80] A. A. Balandin, *Nat. Mater.* **2011**, *10*, 569.

[81] K. S. Kim, Y. Zhao, H. Jang, S. Y. Lee, J. M. Kim, K. S. Kim, J.-H. Ahn, P. Kim, J.-Y. Choi, B. H. Hong, *Nature* **2009**, *457*, 706.

[82] R. R. Nair, P. Blake, A. N. Grigorenko, K. S. Novoselov, T. J. Booth, T. Stauber, N. M. R. Peres, A. K. Geim, *Science* **2008**, *320*, 1308.

[83] N. O. Weiss, H. Zhou, L. Liao, Y. Liu, S. Jiang, Y. Huang, X. Duan, *Adv. Mater.* **2012**, *24*, 5782-5825.

[84] D. Akinwande, N. Petrone, J. Hone, *Nat. Commun.* **2014**, *5*, 5678.

[85] X. Li, X. Wang, L. Zhang, S. Lee, H. Dai, *Science* **2008**, *319*, 1229.

[86] Z. Zhu, I. Murtaza, H. Meng, W. Huang, *RSC Adv.* **2017**, *7*, 17387-17397.

[87] M. Chhowalla, D. Jena, H. Zhang, *Nat Rev Mater* **2016**, *1*, 16052.

[88] R. Raccichini, A. Varzi, S. Passerini, B. Scrosati, *Nat. Mater.* **2014**, *14*, 271.

[89] Y. Hernandez, V. Nicolosi, M. Lotya, F. M. Blighe, Z. Sun, S. De, I. T. McGovern, B. Holland, M. Byrne, Y. K. Gun'Ko, J. J. Boland, P. Niraj, G. Duesberg, S. Krishnamurthy, R. Goodhue, J. Hutchison, V. Scardaci, A. C. Ferrari, J. N. Coleman, *Nat. Nanotechnol.* **2008**, *3*, 563.

[90] G. Kucinskis, G. Bajars, J. Kleperis, *J. Power Sources* **2013**, *240*, 66-79.

[91] G. Zhou, F. Li, H.-M. Cheng, *Energy Environ. Sci.* **2014**, *7*, 1307-1338.

[92] J. Xu, M. Wang, N. P. Wickramaratne, M. Jaroniec, S. Dou, L. Dai, *Adv. Mater.* **2015**, *27*, 2042-2048.

[93] Y. Yan, Y.-X. Yin, Y.-G. Guo, L.-J. Wan, *Adv. Energy Mater.* **2014**, *4*, 1301584.

[94] K. Chen, S. Song, F. Liu, D. Xue, *Chem. Soc. Rev.* **2015**, *44*, 6230-6257.

[95] Y. Gogotsi, *ACS Nano* **2014**, *8*, 5369-5371.

[96] D. Higgins, P. Zamani, A. Yu, Z. Chen, *Energy Environ. Sci.* **2016**, *9*, 357-390.

[97] D. Deng, K. S. Novoselov, Q. Fu, N. Zheng, Z. Tian, X. Bao, *Nat. Nanotechnol.* **2016**, *11*, 218.

[98] A. Pakdel, Y. Bando, D. Golberg, *Chem. Soc. Rev.* **2014**, *43*, 934-959.

[99] A. Nag, K. Raidongia, K. P. S. S. Hembram, R. Datta, U. V. Waghmare, C. N. R. Rao, *ACS Nano* **2010**, *4*, 1539-1544.

[100] D. Golberg, Y. Bando, Y. Huang, T. Terao, M. Mitome, C. Tang, C. Zhi, *ACS Nano* **2010**, *4*, 2979-2993.

[101] L. Song, L. Ci, H. Lu, P. B. Sorokin, C. Jin, J. Ni, A. G. Kvashnin, D. G. Kvashnin, J. Lou, B. I. Yakobson, P. M. Ajayan, *Nano Lett.* **2010**, *10*, 3209-3215.

[102] P. Sutter, J. Lahiri, P. Zahl, B. Wang, E. Sutter, *Nano Lett.* **2013**, *13*, 276-281.

[103] Z. Liu, L. Song, S. Zhao, J. Huang, L. Ma, J. Zhang, J. Lou, P. M. Ajayan, *Nano Lett.* **2011**, *11*, 2032-2037.

[104] K. H. Lee, H.-J. Shin, J. Lee, I.-y. Lee, G.-H. Kim, J.-Y. Choi, S.-W. Kim, *Nano Lett.* **2012**, *12*, 714-718.

[105] C. R. Dean, A. F. Young, I. Meric, C. Lee, L. Wang, S. Sorgenfrei, K. Watanabe, T. Taniguchi, P. Kim, K. L. Shepard, J. Hone, *Nat. Nanotechnol.* **2010**, *5*, 722.

[106] N. kumar, K. Moses, K. Pramoda, S. N. Shirodkar, A. K. Mishra, U. V. Waghmare, A. Sundaresan, C. N. R. Rao, *J. Mater. Chem. A* **2013**, *1*, 5806-5821.

[107] L. Ci, L. Song, C. Jin, D. Jariwala, D. Wu, Y. Li, A. Srivastava, Z. F. Wang, K. Storr, L. Balicas, F. Liu, P. M. Ajayan, *Nat. Mater.* **2010**, *9*, 430.

[108] L. Qin, J. Yu, S. Kuang, C. Xiao, X. Bai, *Nanoscale* **2012**, *4*, 120-123.

[109] W.-Q. Han, H.-G. Yu, Z. Liu, *Appl. Phys. Lett.* **2011**, *98*, 203112.

[110] M. O. Watanabe, S. Itoh, T. Sasaki, K. Mizushima, *Phys. Rev. Lett.* **1996**, *77*, 187-189.

[111] L.-W. Yin, Y. Bando, D. Golberg, A. Gloter, M.-S. Li, X. Yuan, T. Sekiguchi, *J. Am. Chem. Soc.* **2005**, *127*, 16354-16355.

[112] S. Wang, L. Zhang, Z. Xia, A. Roy, D. W. Chang, J.-B. Baek, L. Dai, *Angew. Chem. Int. Ed.* **2012**, *51*, 4209-4212.

[113] C. N. R. Rao, K. Gopalakrishnan, *ACS Appl. Mater. Interfaces* **2017**, *9*, 19478-19494.

[114] M. B. Sreedhara, K. Gopalakrishnan, B. Bharath, R. Kumar, G. U. Kulkarni, C. N. R. Rao, *Chem. Phys. Lett.* **2016**, *657*, 124-130.

[115] S. Manzeli, D. Ovchinnikov, D. Pasquier, O. V. Yazyev, A. Kis, *Nat Rev Mater* **2017**, *2*, 17033.

[116] A. Splendiani, L. Sun, Y. Zhang, T. Li, J. Kim, C.-Y. Chim, G. Galli, F. Wang, *Nano Lett.* **2010**, *10*, 1271-1275.

[117] Z. Zeng, Z. Yin, X. Huang, H. Li, Q. He, G. Lu, F. Boey, H. Zhang, *Angew. Chem. Int. Ed.* **2011**, *50*, 11093-11097.

[118] W. Choi, N. Choudhary, G. H. Han, J. Park, D. Akinwande, Y. H. Lee, *Mater. Today* **2017**, *20*, 116-130.

[119] Y. Shi, H. Li, L.-J. Li, *Chem. Soc. Rev.* **2015**, *44*, 2744-2756.

[120] Q. Ji, Y. Zhang, Y. Zhang, Z. Liu, *Chem. Soc. Rev.* **2015**, *44*, 2587-2602.

[121] G.-B. Liu, D. Xiao, Y. Yao, X. Xu, W. Yao, *Chem. Soc. Rev.* **2015**, *44*, 2643-2663.

[122] K. F. Mak, C. Lee, J. Hone, J. Shan, T. F. Heinz, *Phys. Rev. Lett.* **2010**, *105*, 136805.

[123] K. F. Mak, J. Shan, *Nat. Photonics* **2016**, *10*, 216.

[124] Z. Yu, Z. Y. Ong, Y. Pan, T. Xu, Z. Wang, L. Sun, J. Wang, G. Zhang, Y. W. Zhang, Y. Shi, X. Wang, in *2016 IEEE International Nanoelectronics Conference (INEC)*, **2016**, pp. 1-2.

[125] D. J. Late, B. Liu, H. S. S. R. Matte, V. P. Dravid, C. N. R. Rao, *ACS Nano* **2012**, *6*, 5635-5641.

[126] H. Schmidt, F. Giustiniano, G. Eda, *Chem. Soc. Rev.* **2015**, *44*, 7715-7736.

[127] D. Voiry, J. Yang, M. Chhowalla, *Adv. Mater.* **2016**, *28*, 6197-6206.

[128] Y. M. Chen, X. Y. Yu, Z. Li, U. Paik, X. W. Lou, *Sci. Adv.* **2016**, *2*.

[129] M. Pumera, Z. Sofer, A. Ambrosi, *J. Mater. Chem. A* **2014**, *2*, 8981-8987.

[130] M. Acerce, D. Voiry, M. Chhowalla, *Nat. Nanotechnol.* **2015**, *10*, 313.

[131] G. Du, Z. Guo, S. Wang, R. Zeng, Z. Chen, H. Liu, *Chem. Commun.* **2010**, *46*, 1106-1108.

[132] K. Chang, W. Chen, *Chem. Commun.* **2011**, *47*, 4252-4254.

[133] R. Bhandavat, L. David, G. Singh, *J. Phys. Chem. Lett.* **2012**, *3*, 1523-1530.

[134] C. N. R. Rao, H. S. S. Ramakrishna Matte, U. Maitra, *Angew. Chem. Int. Ed.* **2013**, *52*, 13162-13185.

[135] K. Shiva, H. S. S. Ramakrishna Matte, H. B. Rajendra, A. J. Bhattacharyya, C. N. R. Rao, *Nano Energy* **2013**, *2*, 787-793.

[136] R. Ma, T. Sasaki, *Adv. Mater.* **2010**, *22*, 5082-5104.

[137] M. A. Bizeto, A. L. Shiguihara, V. R. L. Constantino, *J. Mater. Chem.* **2009**, *19*, 2512-2525.

[138] A. K. Geim, I. V. Grigorieva, *Nature* **2013**, *499*, 419.

[139] H.-J. Kim, M. Osada, Y. Ebina, W. Sugimoto, K. Tsukagoshi, T. Sasaki, *Sci. Rep.* **2016**, *6*, 19402.

[140] M. Osada, T. Sasaki, *Adv. Mater.* **2012**, *24*, 210-228.

[141] M. Osada, T. Sasaki, *Dalton Trans.* **2018**, *47*, 2841-2851.

[142] R. Ma, T. Sasaki, *Acc. Chem. Res.* **2015**, *48*, 136-143.

[143] K. Hyung-Jun, O. Minoru, S. Takayoshi, *Jpn. J. Appl. Phys.* **2016**, *55*, 1102A1103.

[144] M. Osada, T. Sasaki, *J. Mater. Chem.* **2009**, *19*, 2503-2511.

[145] P. Xiong, R. Ma, N. Sakai, T. Sasaki, *ACS Nano* **2018**, *12*, 1768-1777.

[146] N. A. Chernova, M. Roppolo, A. C. Dillon, M. S. Whittingham, *J. Mater. Chem.* **2009**, *19*, 2526-2552.

[147] D. Hanlon, C. Backes, T. M. Higgins, M. Hughes, A. O’Neill, P. King, N. McEvoy, G. S. Duesberg, B. Mendoza Sanchez, H. Pettersson, V. Nicolosi, J. N. Coleman, *Chem. Mater.* **2014**, *26*, 1751-1763.

[148] I. A. de Castro, R. S. Datta, J. Z. Ou, A. Castellanos-Gomez, S. Sriram, T. Daeneke, K. Kalantar-zadeh, *Adv. Mater.* **2017**, *29*, 1701619.

[149] Y. Li, J. Yao, E. Uchaker, J. Yang, Y. Huang, M. Zhang, G. Cao, *Adv. Energy Mater.* **2013**, *3*, 1171-1175.

[150] X. Xiao, H. Song, S. Lin, Y. Zhou, X. Zhan, Z. Hu, Q. Zhang, J. Sun, B. Yang, T. Li, L. Jiao, J. Zhou, J. Tang, Y. Gogotsi, *Nat. Commun.* **2016**, *7*, 11296.

[151] C. Zhao, H. Zhang, W. Si, H. Wu, *Nat. Commun.* **2016**, *7*, 12543.

[152] Z. Sun, T. Liao, Y. Dou, S. M. Hwang, M.-S. Park, L. Jiang, J. H. Kim, S. X. Dou, *Nat. Commun.* **2014**, *5*, 3813.

[153] Y. Dou, L. Zhang, X. Xu, Z. Sun, T. Liao, S. X. Dou, *Chem. Soc. Rev.* **2017**, 46, 7338-7373.

[154] K. Shavanova, Y. Bakakina, I. Burkova, I. Shtepliuk, R. Viter, A. Ubelis, V. Beni, N. Starodub, R. Yakimova, V. Khranovskyy, *Sensors* **2016**, *16*, 223.

Chapter I.2

Synthesis, Characterization and Selected Properties of Few-layer Nanosheets of MoO_3

SUMMARY*

Nanosheets of MoO_3 consisting of only a few layers have been prepared by four methods including oxidation of MoS_2 nanosheets, intercalation with LiBr and ultrasonication of bulk MoO_3. Besides showing blue-shift of the optical absorption band compared to the bulk sample, few-layer MoO_3 exhibits enhanced photocatalytic activity. In combination with a borocarbonitride, few-layer MoO_3 shows good performance characteristics as a supercapacitor electrode. Ultrathin nanosheets of MoO_3 synthesized starting from MoS_2 nanosheets have been chemically tagged with optimum amounts of reduced graphene oxide (rGO) leading to formation of a MoO_3-rGO composites. The MoO_3-rGO composite exhibits remarkable electrochemical stability, cyclability and high rate capability over a wide range of operating currents in Na-ion batteries. MoO_3-rGO composites enable buffering of volume changes during repeated cycling and offers facile pathways for Na-ion and electron transport in MoO_3.

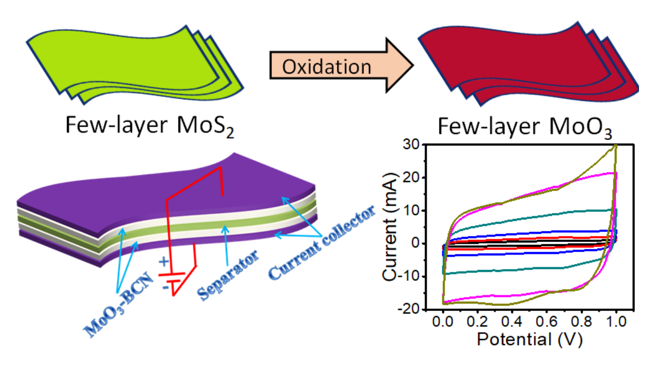

---

*Papers based on this study have appeared in Chemistry-An Asian Journal (2013) Journal of Materials Chemistry A (2016).

1. Introduction

After the advent of graphene[1] there has been extensive research on two-dimensional layered structures of inorganic materials such as MoS_2.[2] These studies have revealed interesting results on the structure and properties of these sheet nanostructures. Metal oxides with layered structures are known.[3] Single- or few-layer nanostructures of some of the layered oxides have been generated by mechanical exfoliation.[4] Single-layer of layered titanates can be prepared by delamination employing intercalation.[5] Such ultrathin oxide layers are of importance as dielectric materials.[6] One of the most well-known layered oxides is MoO_3, which exists in three polymorphs, namely the thermodynamically stable orthorhombic α-MoO_3, monoclinic β-MoO_3 and low-temperature metastable hexagonal h-MoO_3. The stable α-MoO_3 structure involves stacking of MoO_6 octahedra bilayer sheets along the [010] direction (**Figure 1**). Some of the nanostructured morphologies of MoO_3 have been reported.[7] Two-dimensional inorganic nanosheets[5, 8] are attracting attention due to their diverse range of applications such as electrochromic,[9] photochromic,[10] gas sensing,[11] photocatalysis,[12] photovoltaic[13] field emission[14] devices as well as in transistors,[15] capacitors,[16] dielectrics,[7a, 17] and Li-ion batteries.[18] Few-layer nanosheets morphology of MoO_3 with high surface area expected to show good photocatalytic activity and energy storage properties.

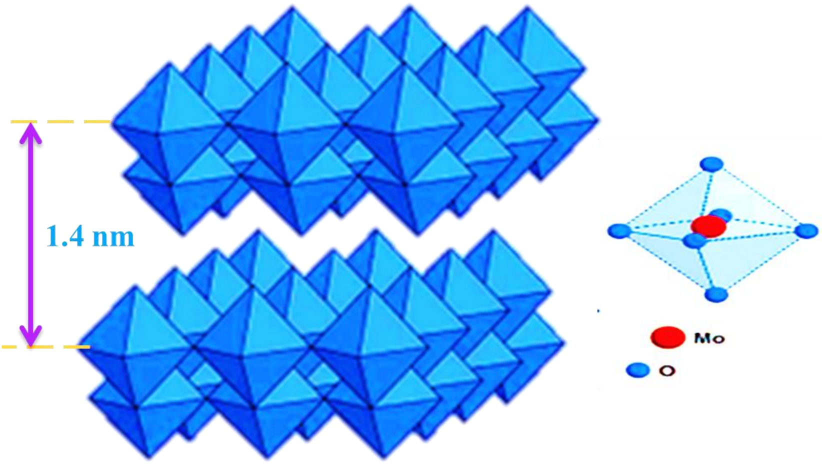

Figure 1. The layered structure of α-MoO_3.

Few-layer MoO_3 as potential anode for batteries

Demand for the rechargeable batteries is on the rise for vehicular transportation as well as for large stationary energy storage applications such as integration with the electricity grid as well as renewables such as solar, wind and electric power grid.[19] Rechargeable batteries based on lithium such as the lithium-ion batteries have been already demonstrated as very promising energy storage system for various portable applications because of their high specific energy and power density.[20] However, the global natural resources of lithium are very limited and hence for widespread usage rechargeable battery technologies based on lithium will be very cost intensive. This short-coming has motivated many researchers worldwide to shift emphasis from lithium to sodium based rechargeable batteries. Sodium is the fourth most abundant element in the Earth's crust and expected to be more cost effective compared to lithium and lithium-based batteries. However, these advantages are easily offset by the inferior electrochemical properties of sodium compared to lithium. The energy density of Na cannot reach that of the Li, as Na is more than three times heavier than Li. Additionally, the standard electrochemical potential of Na (2.71 V) is lower than Li (3.04V) with respect to standard hydrogen electrode (SHE).[21] Larger size of Na-ion (ionic radius=1.02 Å) compared to Li-ion (0.76 Å) leads to slower diffusion kinetics and large volume change leading to gradual pulverization of the electrode material. Thus, there are several challenges that need to be overcome for the development of high performance sodium-ion batteries (NaBs).[22]

Graphite, which is the anode in commercial lithium-ion batteries, has been shown to be generally unsuitable for Na-ion batteries.[23] In fact, other forms of carbon and even non-carbonaceous materials have been demonstrated as more suitable anode materials for sodium-ion batteries. Nanostructures of these materials have been demonstrated as anode material in NaBs.[24] In this context, nanostructures of two-dimensional materials especially extended carbon structures (e.g. graphene-based), oxides and sulphides are very promising owing to their attractive physical properties which are useful for diverse fields such as electronics, catalysis and biological applications. These have also been extensively used in lithium and sodium ion batteries.[25] Orthorhombic α-MoO_3, has a layered structure consisting of double-layers of MoO_6 octahedra linked by edge and corner sharing along (001) and (100) axes and by weak van der Waals forces along (010) direction. Owing to this attractive structure and chemical stability, α-MoO_3 has been demonstrated as a potential alternative anode for lithium-ion batteries. The theoretical lithium storage capacity value of MoO_3 is very high equal to 1117 $mAhg^{-1}$,[26] being three times higher than that of graphite (372 $mAhg^{-1}$).[27] As Na^+ intercalation properties are very similar to Li^+, MoO_3 will expectedly be equally promising for NaBs. However, the poor electronic conductivity of MoO_3 and sluggish kinetics of ions may detrimentally affect its electrochemical performance especially in NaBs. To enhance the kinetics of Na^+ in MoO_3, lower dimension nanostructures are expected to be very promising. In this context, several well-defined MoO_3 nanostructures, e.g. nanoparticles,[28] nanorods,[29] nanobelts,[30] and nanosheets[31] have been developed. The nanosheet morphology with larger van der Waal layer spacing is more interesting due to their high surface area and the ability to store the charge between the layers.

2. Scope of the present investigations

Dimensionality plays a crucial role in determining the properties of the materials. The remarkable properties of graphene shown that the two-dimensional nanosheets are of great importance in electronic applications. Since then, layered materials became a diverse source of nanosheets whose properties would be useful in energy and electronic applications. Exfoliation of these layered materials into single and few-layer nanosheets, their scalability and precise fabrication into useful devices are challenges in this field. The successor to graphene, inorganic 2D transition metal dichalcogenides (TMDCs) have been explored extensively in recent times due to their exotic properties and potential applications. In this context, ultrathin nanosheets of two-dimensional van der Waal layered transition metal oxides (TMOs) are fundamentally and technologically intriguing. In contrast to graphene and TMDCs, TMOs are chemically versatile and stable under moderate conditions. Our focus in the present study is to synthesize and characterize nanosheets of MoO_3 and explore its photocatalytic and energy storage properties. We have studied the photodegradation of methylene blue by nanosheets of MoO_3 in comparison with bulk MoO_3. We have also examined supercapacitor applications of MoO_3 nanosheets in combination with a borocarbonitride, $B_xC_yN_z$, since latter is known to exhibit excellent electrode properties in supercapacitors.[32a]

Sodium ion batteries have recently drawn significant attention because, unlike Li, Na is a ubiquitous and earth-abundant element. Demand for large-scale energy storage for grid applications has revived the interest of NaBs. Most of the research on NaBs electrode materials has focused mainly on cathodes, efforts on anode material are less explored yet, here we focus on a possibility of new anode material for NaBs. Graphite, as the most common anode for commercial LIBs, has a long-range-ordered layered structure, with theoretical reversible capability of 372 $mAhg^{-1}$ and long cycle life. However, the electrochemical sodiation/desodiation capacity of graphite is very low. The interlayer distance of graphite (3.4 Å) is too small to accommodate the large Na ion. Results suggests that there materials having long-range-ordered layered structures with larger interlayer distances (>3.7 Å) are desired for electrochemical sodiation/desodiation.[32b] Layered MoO_3 is a promising anode material for NaBs owing to its high theoretical capacity, larger interlayer spacing and stability. Unfortunately, its practical application is still hindered by its low conductivity and large volume expansion during Na^+ intercalation and de-intercalation. Due to poor electronic conductivity of MoO_3 and sluggish nature of Na ions, it is still a big challenge to enhance significantly the electrochemical performance of MoO_3 in NaBs. We present here, a composite comprising of ultrathin nanosheets of few-layer MoO_3 and reduced graphene oxide (rGO) as a potential high rate capability anode for NaBs. The electrochemical performance of the few-layer MoO_3-rGO composites is studied vis-à-vis the few-layer MoO_3 (i.e. without any rGO). The motivation here is to develop a MoO_3-based anode material providing fast Na^+ diffusion pathways and displaying high electronic conductivity. All these factors will eventually lead to a NaB anode with a high degree of cyclability at widely varying current densities.

3. Experimental Section

Materials

All the chemicals used for the synthesis are highly pure and purchased from commercial sources. Molybdic acid (Sigma-aldrich, >85% MoO_3 basis), thiourea (SD Fine Chem Ltd, India) , boric acid (SD Fine Chem Ltd, India, 99 %) KOH (SD Fine

Chem Ltd, India, 85.5 %), LiBr (Alfa aesar, 99%), DMF (Spectrochem, India, 99.9 %), activated charcoal (SD Fine Chem Ltd), water (Millipore) and H_2SO_4 (Spectrochem, India, 98%), natural Graphite (Alfa Aesar, 4000 mesh), $KMnO_4$ (SD Fine Chem Ltd, India, 99 %), $NaNO_3$ (SD Fine Chem Ltd, India, 85.5 %), H_2O_2 (Alfa Aesar, 30%), EC and DEC (Sigma-Aldrich) $NaPF_6$ (Sigma-Aldrich, 99,9%) are used without any further purification.

Synthesis

The synthetic procedures for preparing few-layer MoO_3 Nanosheets:

Method-1: Few-layer MoS_2 was synthesised by using the literature method.[2a] In this method, we react molybdic acid with an excess of thiourea (1:48) in N_2 atmosphere at 873 K for 5h. Few-layer MoO_3 was obtained by heating few-layer MoS_2 in air at 1 °C/min to 723 K for 3 h.

Method-2: Graphene oxide (GO) was synthesised by the modified Hummers method.[33] GO and molybdenum pentachloride were dispersed in DMF and the mixture stirred at room temperature for 24 h. The GO-Mo complex collected after centrifugation was dried at 60 °C. For obtaining the few-layer MoO_3, the GO-Mo complex was heated in air at 550 °C for 3 h.

Method-3: Bulk MoO_3 (0.2 g) and lithium bromide (0.1 g) were refluxed in diethyl ether at 60 °C in a round bottom flask with water cool condenser for 24 h. The product obtained was washed and centrifuged. Finally, we have added water for exfoliation to obtain few-layer MoO_3.

Method-4: Bulk MoO_3 (25 mg) and 50 ml DMF were taken in a 100 ml beaker and sonicated for 2 h using a probe sonicator (Imeco Ultrasonics, 20 kHz, 230 V). The unexfoliated MoO_3 was allowed to settle for 10 min after sonication. The dispersion was centrifuged at 8000 rpm for 10 min and the top solution decanted and used for characterization.

Characterization

The crystal structure is determined by powder X-ray diffraction (PXRD) in Bruker D8 Discover diffractometer with Cu-Kα radiation with accelerating voltage 40 kV and current 30 mA. The nanosheets are imaged using scanning electron microscopy Nova

NanoSEM 600 FESEM with Energy Dispersive X-ray Analysis (EDX) system (FEI Company). Transmission electron microscopy (TEM) images are recorded with a JEOL JEM 3010 microscope, fitted with a Gatan CCD camera operating at an accelerating voltage of 300 kV. Atomic force microscope (AFM) imaging in tapping mode is carried out in a Bruker Innova instrument. Raman spectra are recorded in the backscattering geometry using a 632 nm HeNe laser with a Jobin Yvon LabRam HR spectrometer. Electronic absorption spectra were recorded on Perkin Elmer Lambda 650 UV-Vis Spectrometer and an X-ray photoelectron (XP) spectrum was recorded with an Omicron nanotechnology spectrometer. Thermogravimetric analyses (TGA) of MoO_3-rGO composites were carried out in oxygen atmosphere with Metler Toledo TGA-850 TG analyzer. Infrared spectra are recorded in Bruker FTIR spectrometer in ATR mode. The cyclic voltammogram is obtained in CH Instrument (CH 403), while the galvanostatic charge/discharge cycling are obtained on Neware Battery Cycler using TC53 software at different C-rates.

Photocatalytic measurements

Photodegradation of Methylene blue (MB) was followed using absorption spectroscopy. In a typical experiment, 40 mL of 2.5×10^{-5} M aqueous MB solution and 25 mg few- layer MoO_3 were placed in a 50 mL quartz vessel and sonicated for 10 min followed by 10 min stirring in dark to allow sufficient mixing. Under continuous stirring, photoreaction vessel was exposed to the UV irradiation produced by a 120 W high-pressure mercury lamp with wavelength 267 nm which was positioned 20 cm away from the reaction vessel. The concentration of photo reacted MB was recorded at regular time intervals by monitoring the changes in the absorption maximum of the UV-Vis absorption spectra of MB at 664 nm. The samples were collected after the photoreaction were centrifuged for 5 min to remove the photocatalyst before UV-Vis measurements. For carrying out the recycling test of the photocatalyst, five consecutive cycles were carried out. After each cycle, the catalyst was centrifuged and washed thoroughly with water and ethanol, followed by drying at 100 °C for an hour.

Few-layer MoO_3-BCN composites for supercapacitor electrode

Synthesis of borocarbonitride nanosheets:

A borocarbonitride with high carbon content was synthesized by the urea method as reported earlier.[34] 0.1 g of H_3BO_3, 0.5 g of activated charcoal and 2.4 g urea were taken in 50 mL water and sonicated for 15 min. The water was slowly evaporated to obtain a slurry. The slurry was transferred to a quartz boat and heated at 900 ^oC for 10 h in N_2 atmosphere followed by ammonia treatment at 930 ^oC for 3 h. Based on X-ray photoelectron spectroscopy, the composition was found to be $B_1C_7N_2$.

The synthetic procedures for preparing few-layer MoO_3–BCN composite:

Few-layer MoO_3-BCN composites were prepared by mixing equal weight of MoO_3 and BCN using a small amount of ethanol and homogenised by ultrasonication. The electrodes for electrochemical measurements were prepared by mixing the few-layer MoO_3-BCN composite with carbon black as a conducting matrix and a PVDF as a binder. The sample obtained was again dispersed in small amount of ethanol and ground for 1 hour followed by ultra-sonication for 10 min to obtain a homogeneous mixture.

Electrochemical capacitance measurements:

As prepared MoO_3-BCN composite was drop cast on the gold coated stainless steel current collector having the mass of the active material at each electrode as 2 mg. For cyclic voltammetry and galvanostatic charge/discharge measurements, symmetrical electrochemical capacitors (MoO_3-BCN/separator/ MoO_3-BCN) were separated by a fibrous glass separator and measurements were performed in a two-electrode cell using 0.5 M Li_2SO_4 as the aqueous electrolyte. All the electrochemical measurements were carried measured by using PG262A potentiostat/galvanostat, (Technoscience Ltd, Bangalore, India).

Few-layer MoO_3-rGO composites for Na ion batteries

Preparation of graphene oxide:

Graphene oxide (GO) is prepared by the modified Hummers method.[35] In a typical synthesis concentrated H_2SO_4 (75 ml) is slowly added to a beaker containing synthetic graphite powder (1.5 g) which is kept in ice bath. $NaNO_3$ (1.5 g) is then added slowly and the mixture is stirred for 15 min until it becomes uniform. Following slow addition of 10 g of $KMnO_4$, the mixture is transferred to a oil bath maintained at temperature 40 °C and stirred for an hour. To the resulting dark brown product, 75 ml of water is added and the mixture is stirred at 75 °C. Finally, 15 ml of H_2O_2 (30 %) in 150 ml of deionized water is added to the reaction mixture. The color of the suspension changes from brown to yellow. As obtained GO suspension is centrifuged, washed several times and dialyzed in deionized water for 24 h.[33] The dialyzed product is freeze-dried under vacuum in a lyophilizer.

Preparation of few-layer MoO_3 nanosheets and its composites with reduced graphene oxide (rGO):

Few-layer MoO_3 nanosheets (about 2-3 sheets) are synthesized by oxidation of few-layer MoS_2 at 500 °C for 15 min in air.[13a] MoO_3-rGO composites are prepared using a hydrothermal method. Briefly, few-layer MoO_3 is dispersed in the GO suspension with the corresponding weight ratio of 5%, 10% and 20%. The dispersion is stirred and sonicated for 1 h until a homogeneous mixture is obtained. As formed few-layer MoO_3-GO suspension is transferred into teflon lined autoclave and heated to 180 °C for 4 h. In the course of reaction the GO is reduced on MoO_3 nanosheets and forms MoO_3-rGO nanocomposite (**Scheme 1**). The as-obtained MoO_3-rGO composite is freeze-dried under vacuum in lyophilizer for 24 h and is used for further characterizations and battery testing.

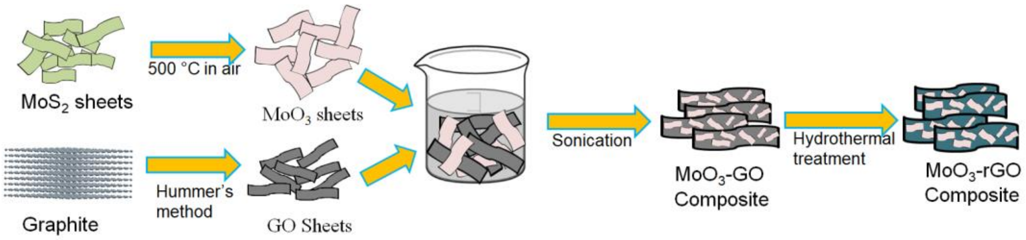

Scheme 1. Schematic representation of the synthesis of few-layer MoO_3 nanosheets and MoO_3-rGO nanocomposites.

Electrode preparation and electrochemical measurement of NaBs:

The electrochemical stability of few-layer MoO_3 and MoO_3-rGO composites are tested for sodium-ion battery applications. Sodium metal is used as both reference and counter electrode. The working electrode is fabricated by 95 wt% of active material and 5 wt % polyvinylidene fluoride (PVdF) as a binder in N-methyl-2-pyrrolidene (NMP) solution. Slurry is uniformly distributed on the copper current collector and dried at 120 °C for 12 h in a vacuum oven. Swagelok^{TM} type half cells are assembled in argon-filled glove box (H_2O < 0.1 ppm). 1 M $NaPF_6$ in ethylene carbonate, propylene carbonate, and diethyl carbonate in the volume ratio 0.45:0.45:0.1 is employed as an electrolyte. Galvanostatic charge/discharge cycling (Arbin) studies are carried out at various current densities in the voltage ranging from (0.05-3) V ($Na|Na^+$). Cyclic voltammogram (CV) are performed at a scan rate of 0.005 mVs^{-1}. The ac-impedance (Alpha, Novocontrol) measurements are performed at the charged state (2 V) in the frequency range from 100 kHz to 0.1 Hz with alternating potential amplitude of 5 mV. All the electrochemical experiments are performed at room temperature.

4. Results and Discussion

Characteristics of few-layer MoO_3 nanosheets

Ultrathin sheets of MoO_3 prepared (i) by the oxidation of few-layer MoS_2 (Method 1), (ii) by using graphene oxide as a template (Method 2), (iii) by LiBr intercalation in bulk MoO_3 (Method 3) and (iv) by ultrasonication of bulk MoO_3 in liquid DMF (Method 4) were characterized by various methods. In **Figure 2**, we show the XRD patterns of bulk MoO_3 and few-layer MoO_3 obtained by methods 1-3. The diffraction

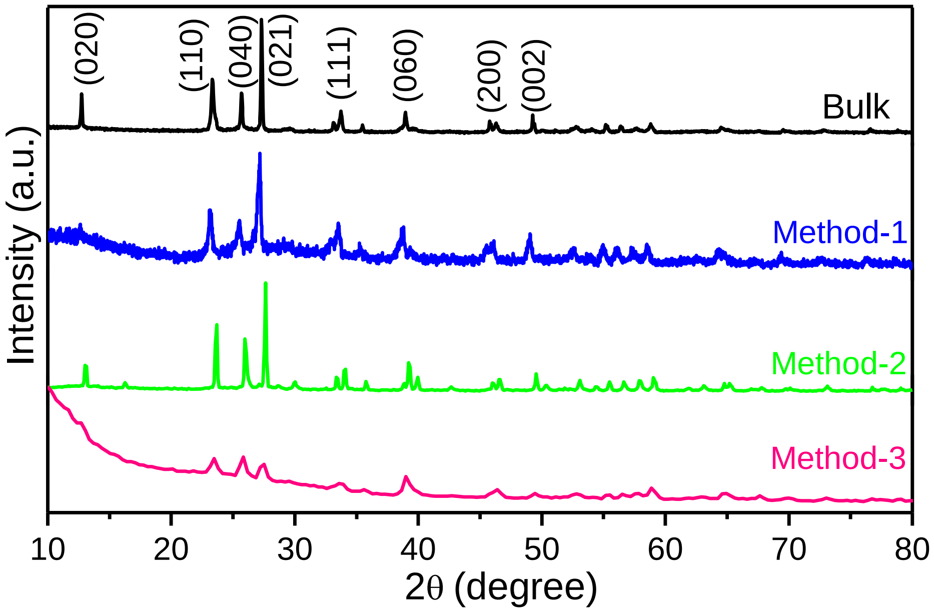

Figure 2. Comparison of XRD patterns of bulk and few-layer MoO_3 obtained from different methods 1-3 respectively.

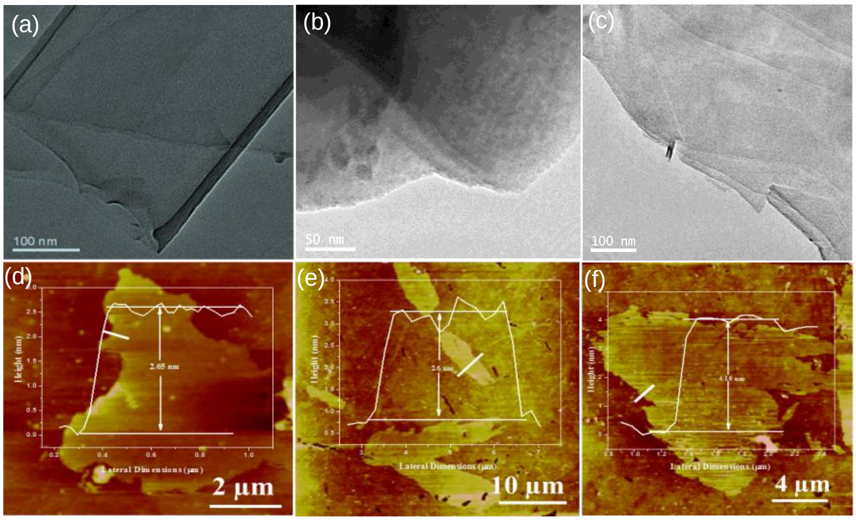

Figure 3. (a-c) TEM images of few-layer MoO_3 obtained from methods (1-3) respectively (d-f) are the AFM images of few-layer MoO_3 obtained by methods (1-3) respectively.

patterns are readily indexed on the orthorhombic structure with the space group P_{bnm} (JCPDS file No. 05-0508). The XRD reflections of few-layer MoO_3 are quite broad and less intense compared to the bulk sample due to less stacking in the c-direction. This is specially there in the case of the products from methods 1 and 3. **Figure 3**a-c present TEM images of the nanosheets which confirm the two-dimensional morphology of the sheets. The sheets are transparent, indicating the thickness to be only a few nanometers.

The AFM image and the corresponding height profile of the few-layer MoO_3 obtained from method 1 are shown in Figure 3d. We see the layer thickness to be 2.65 nm with lateral dimensions of several µm. The AFM image of the few-layer MoO_3

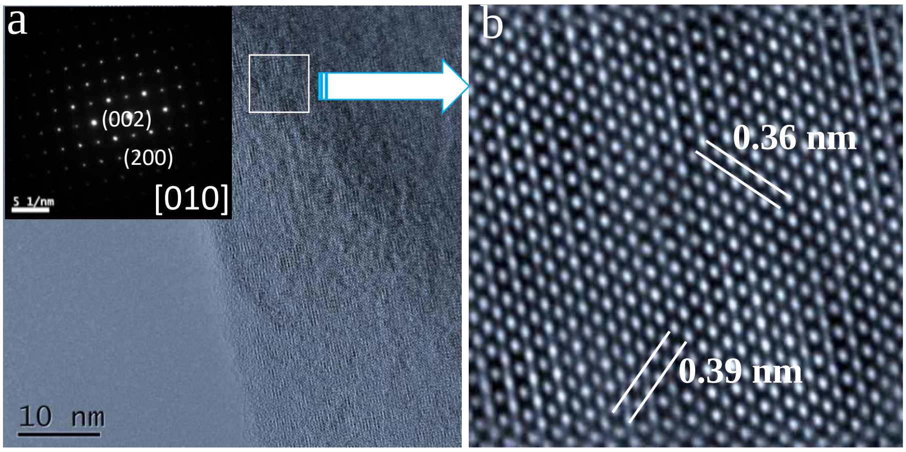

Figure 4. a) TEM images, inset SAED patterns b) HRTEM image of few-layer MoO_3 obtained by method 1.

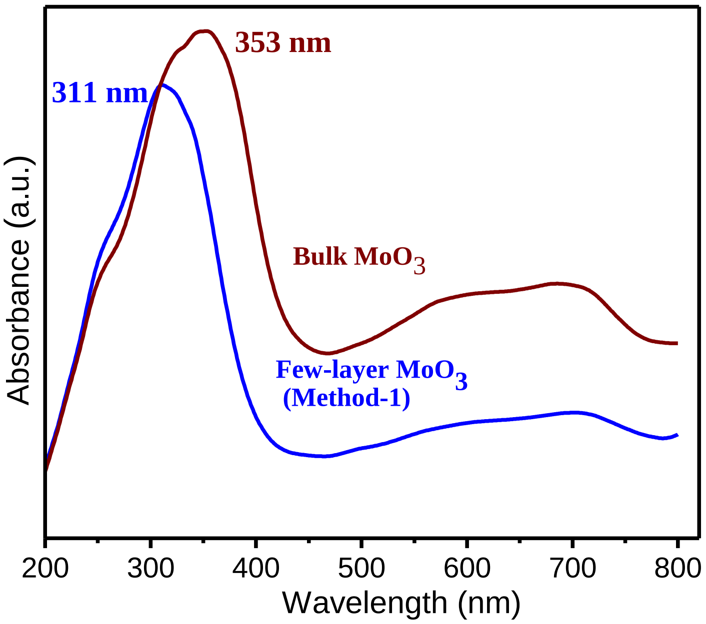

Figure 5. UV-Vis absorption spectra of bulk MoO_3 and few-layer MoO_3 obtained by method 1.

obtained from method 3 has a height profile of 2.55 nm with lateral dimensions of 4.75 µm. The AFM studies reveal that the nanosheets of MoO_3 obtained generally possess 2-4 layers. The sample prepared by liquid phase exfoliation of bulk MoO_3 in DMF (method 4) showed a smaller layer thickness.

High-resolution TEM images were obtained from an FEI Titan (cube) 80–300 kV aberration-corrected transmission electron microscope. The HRTEM images shown in **Figure 4** reveal layer spacings 0.36 and 0.39 nm corresponding to the (001) and (100) planes of respectively. The selected area electron diffraction (SAED) along the [010] direction (see inset Figure 4a) shows layers has ordered orthorhombic lattice structure with zone axis along (010).These results reveal that nanosheets grow along (001) and (100) directions normal to (010) direction consistent with XRD results.[36] We have recorded the optical absorption spectrum of few-layer MoO_3 prepared by method 1 in comparison with that of bulk MoO_3. We show the spectra in **Figure 5**. We see the absorption maximum shift from 353 nm to 311 nm in the few-layer sample. The corresponding change in band gap is from 2.75 eV to 3.1 eV.

Photocatalytic properties

The photocatalytic activity of bulk MoO_3 and few-layer MoO_3 prepared by different methods were investigated by studying the kinetics of photodegradation of methylene blue (MB) dye under UV irradiation. MB is a cationic organic pollutant discharged by many textile and paint industries, has a maximum absorbance of light

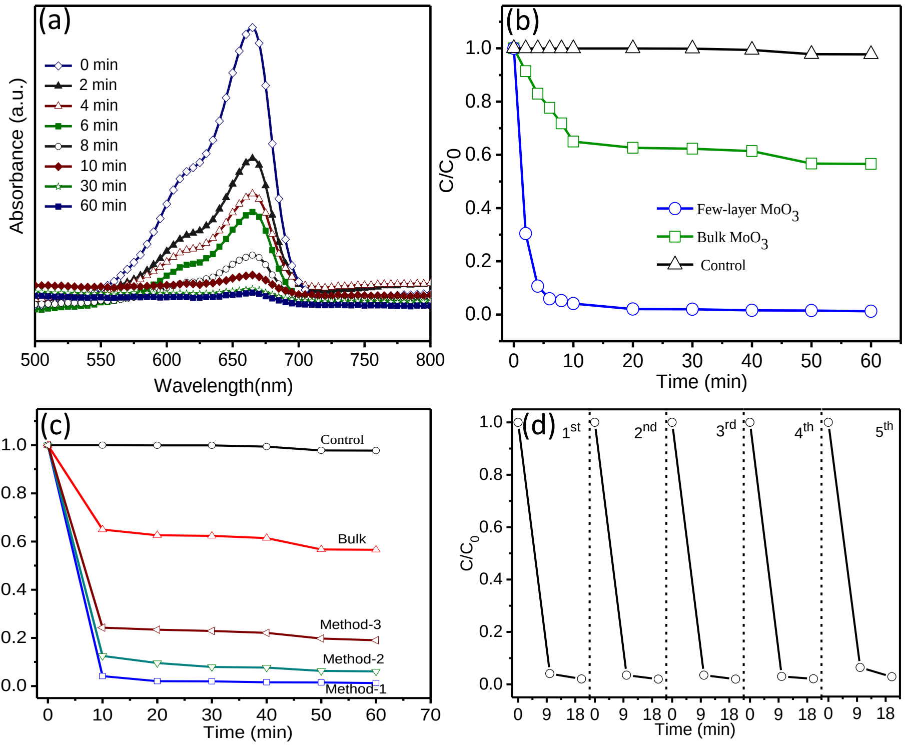

Figure 6. (a) Effect of few-layer MoO_3 on absorption spectra of MB as a function of irradiation time. (b, c) Photocatalytic degradation of MB with variation of normalized concentration with the irradiation time in the presence of bulk MoO_3 and few-layer MoO_3. (d) Stability in the photocatalytic activity of few-layer MoO_3 on MB photodegradation under UV light irradiation measured by reusing same catalyst over 5 times under similar conditions.

around 664 nm. **Figure 6** (a) shows time-dependent changes in the absorbance of MB on irradiation by UV light. It shows an exponential decrease in the concentration of the dye molecule as a function of irradiation time, following Langmuir-Hinshelwood kinetics. We have monitored the changes in the concentration of MB at 664 nm as a function of irradiation time in the presence of bulk and few-layer MoO_3 (Figures 6 b & c). The photodegradation is faster with few-layer MoO_3 than bulk MoO_3. Self-degradation of MB under similar conditions without any photocatalyst shows negligible degradation. The kinetics of the photodegradation reaction could be fitted to pseudo first-order reaction kinetics at low dye concentrations by fitting with the equation, ln $(C_0/C) = kt$ where k is the apparent rate constant. The values of k for bulk MoO_3 and few-layer MoO_3 (Method-1) are 0.00594 min^{-1} and 0.07689 min^{-1} respectively. The k for few-layer MoO_3 is much higher than that for bulk MoO_3 indicating a higher rate of degradation of MB. We also calculated the percentage degradation of MB as a function of irradiation time using the equation,

$$\%\ degradation = \frac{(A_0 - A_t)}{A_0} \times 100$$

Here, A_0 is the absorbance at time t = 0 min and A_t is the absorbance at given time interval t. We find that 98% degradation is achieved with few-layer MoO_3 within 10 min, while bulk MoO_3 shows only 35% degradation in this period. The percentage degradation was negligible in the control experiment. We have examined the recycling behaviour of few-layer MoO_3 for the degradation of MB up to 5 cycles by reusing the same catalyst with fresh MB solution under similar conditions. We have observed that few-layer MoO_3 exhibits satisfactory photostability with the photocatalytic efficiency reducing only by 1.6% after 5 cycles (Figure 6d).

Supercapacitor performances

We have investigated the electrochemical properties of MoO_3 by examining its use in supercapacitor with a borocarbonitride. We have recently found that nitrogen-doped graphene and BCN specially the latter to be exhibit excellent electrode material for supercapacitors.[32a] To evaluate electrochemical properties of MoO_3 and to measure the specific capacitance, the supercapacitor cells were fabricated as reported by Conway.[37] We performed cyclic voltammogram (CV) and galvanostatic charge discharge measurements on fabricated BCN and MoO_3-BCN electrode materials in a 0.5M Li_2SO_4 aqueous electrolyte by using disc type two electrode system. This cell

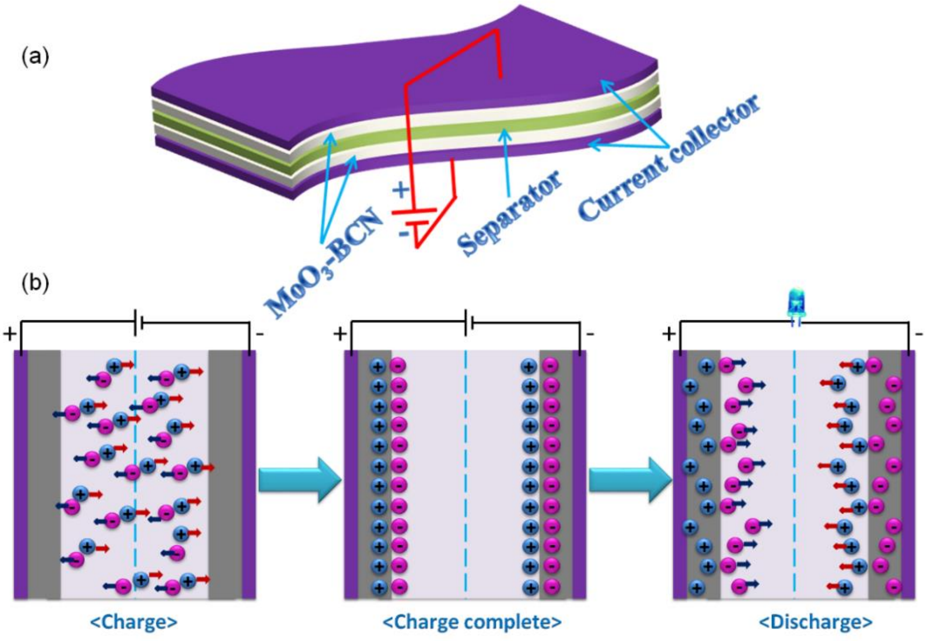

Scheme 2. (a) Schematic representation of cross-sectional view of fabricated MoO_3-BCN supercapacitor electrode, (b) mechanism of charge-discharge state of a supercapacitor.

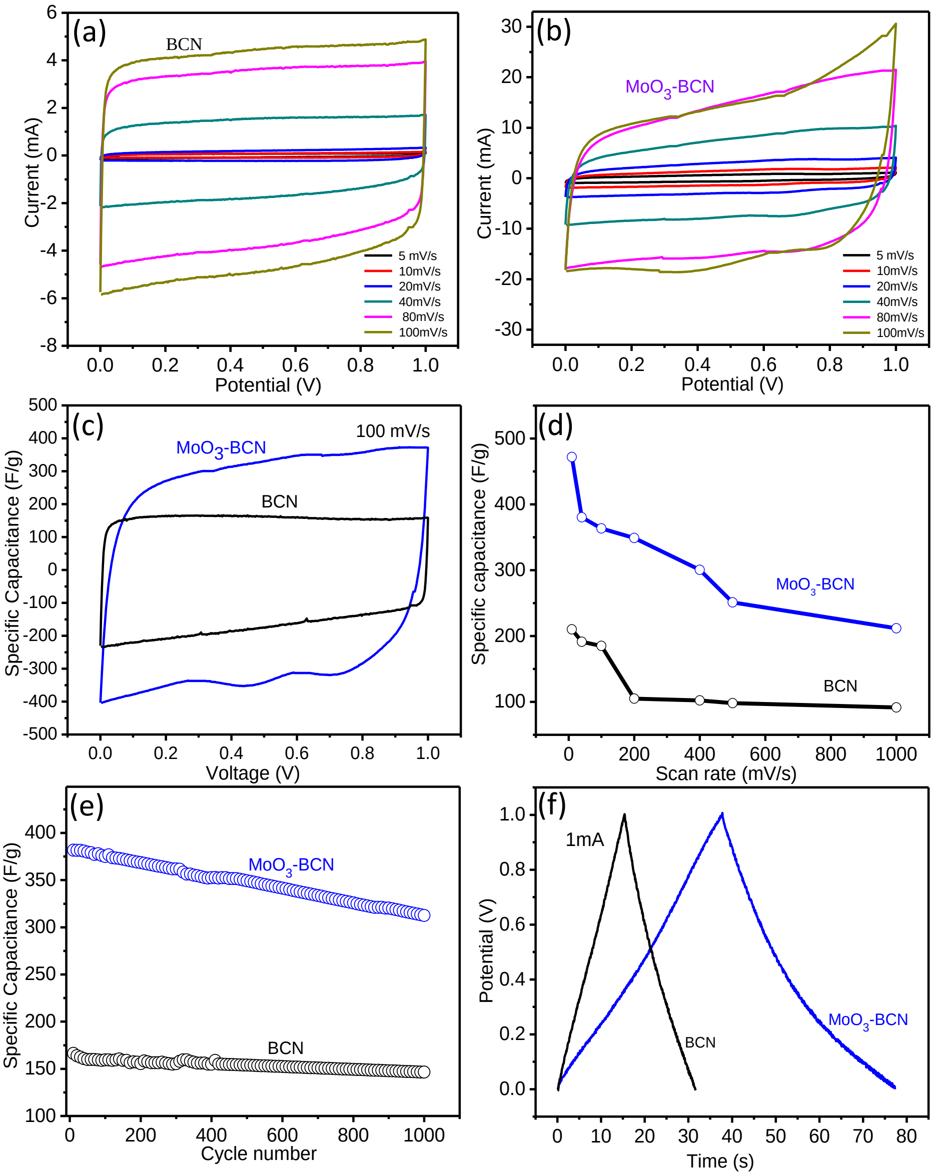

Figure 7. (a, b) Cyclic voltammetry curves for BCN and few-layer MoO_3-BCN supercapacitor at different scan rates, (c) comparison of BCN and few-layer MoO_3-BCN electrodes at the scan rate 100 mV/s. (d) Variation of specific capacitance as a function of scan rate, (e) cyclic stability of the BCN and MoO_3-BCN supercapacitor over 1000 cycles. (f) Galvanostatic charge/discharge curves for BCN and few-layer MoO_3-BCN at current density 1 A/g.

typically consists of two electrodes, two current collectors and porous glassy separator which conduct only ions (**Scheme 2**). The CV of these electrodes was measured within the potential window 0 to 1 V with all possible scan rates. The two-electrode test cell configuration was used because it provides the most accurate measure of a material's performance for electrochemical capacitors.[38]

The cell capacitance (C in F) from the cyclic voltammogram measurements was calculated from the equation

$$C = {}^{i}/_{s}$$

Where ‘i’ is the current from the CV at corresponding potential V and ‘s’ is the scan rate.

The specific capacitance (C_{sp} in F/g) is the capacitance per unit mass of one electrode which is given by equation

$$C_{sp} = {}^{2C}/_{m}$$

Where ‘C’ is the measured capacitance of two electrodes and ‘m’ is the mass of active material at each electrode.

The specific capacitance was also calculated from constant current discharge curves using bellow equation

$$C_{sp} = 2i/(m \times dV/dt)$$

Where ‘i’ is the discharge current and dV/dt is the slope of discharge curve which can be taken as

$$\frac{dV}{dt} = \frac{(V_{max} - 0.5\,V_{max})}{(T_2 - T_1)}$$

The CV curves exhibit good rectangular shape at all scan rates (**Figure**s **7**a & b) which indicates typical capacitive property of electrical double layer capacitors (EDLCs). Figure 7 (c) shows the comparison of supercapacitor performance of BCN and few-layer MoO_3-BCN electrodes at 100 mV/s. Few-layer MoO_3-BCN electrodes delivers the higher capacitance than pristine MoO_3 and BCN. Figure 7(d) shows that the specific capacitance of the samples decreases with increase in the scan rate as expected. The specific capacitance of BCN at the scan rates 500, 400, 200, 100, 40 and 10 mV/s are found to be 98, 102, 105, 158, 171 and 183 F/g respectively whereas for few-layer MoO_3-BCN at the scan rates 500, 400, 200, 100, 40 and 10 mV/s are 251, 300, 349, 363,380,and 471 F/g respectively.

Cyclic performance and excellent cyclic stability are the key factors in determining the supercapacitor for commercial applications. The cyclic stability of the both the samples have been measured (Figure 7e) and we found that it has good cyclic stability over 1000 cycles. The percentage of capacitance retention of BCN and MoO_3-

BCN are found to be 88% and 82% over 1000 cycles. Figure 7(f) shows the galvanostatic charge/discharge curves for both the samples at the current density of 1 A/g which clearly indicates that both the curves are linear and symmetrical. We have also measured the galvanostatic charge/discharge curves at different current density and number of cycles, it shows that the curves are linear and symmetrical. Thus we found that the incorporation of few-layer MoO_3 in BCN has beneficial effects.

Few-layer MoO_3-rGO sodium-ion batteries

Schematic representation of the adopted synthetic procedures for the few-layer MoO_3 and its composites with rGO are shown in **Scheme 1**. As the MoO_3-(10%)-rGO composite displayed the best half-cell electrochemical performance among the various MoO_3-(*x*%)-rGO compositions, all structural and electrochemical performances discussed here are with regard MoO_3-(10%)-rGO sample only. The phase and composition of bulk and few-layer α-MoO_3 are characterized by powder X-ray diffraction. **Figure 8**a shows the PXRD patterns of few-layer and bulk MoO_3. All the diffraction lines can be indexed to orthorhombic α-MoO_3 with space group P_{bnm}, and lattice constants a = 3.962 Å, b = 13.858 Å, c = 3.697 Å (JCPDS file No. 05-0508).

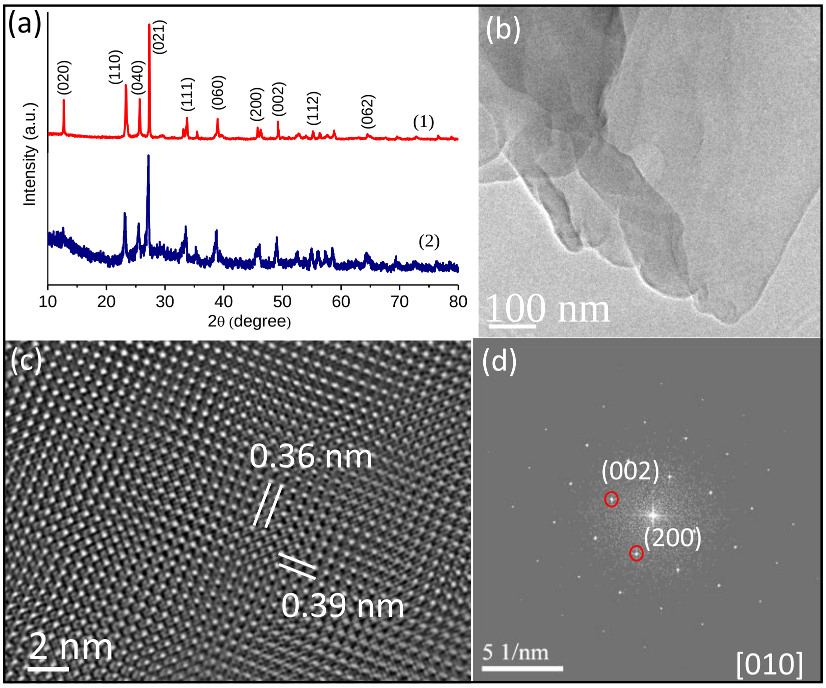

Figure 8. (a) PXRD patterns (1) bulk samples of MoO_3 and (2) few-layer MoO_3. (b) Bright field TEM images of few-layer MoO_3 nanosheets (c) High-resolution TEM image with lattice spacing of few-layer MoO_3. (d) Selected area electron diffraction (SAED) pattern of few-layer MoO_3 along [010].

The lines are less intense and broader in the case of few-layer MoO_3 compared to the bulk thus, convincingly strongly confirming the few-layer MoO_3. The intensity of (*0l0*) lines in the case of few-layer MoO_3 is very low indicating lesser degree of stacking in this direction. The findings from XRD thus confirm the synthesis strategy involving the oxidation of MoS_2 nanosheets at 500 °C under a laboratory air atmosphere to MoO_3. Under these conditions oxygen deficiencies can be ruled out as there are copious amounts of oxygen available for uptake to fill up any oxygen deficiencies.

The 2D morphology of few-layer MoO_3 nanosheets is visualized in TEM as shown in Figure 8b. These nanosheets are transparent indicating that there exist only thin layers with the thickness of few nanometers and with a large lateral dimension in the µm range. Figure 8c shows the high-resolution TEM image obtained on FEI Titan (cube) (80–300) kV aberration-corrected transmission electron microscope. Nanosheets shows the layer spacing to be 0.36 and 0.39 nm corresponding to *(001)* and *(100)* planes of MoO_3 respectively. The selected area electron diffraction (SAED) along [010] direction (Figure 8d) consists of highly ordered homogeneous diffraction pattern which signifies that nanosheets are ordered in the orthorhombic lattice and grow along the (100) and (001) normal to the (010). This finding is thus, consistent with XRD results. **Figure 9** (a, b) shows the FESEM images of few-layer MoO_3. The

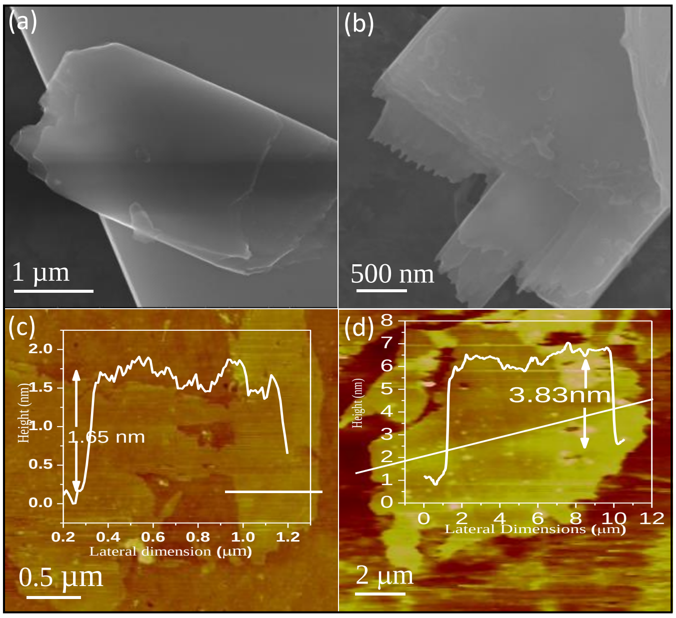

Figure 9. FESEM (a, b) and AFM (c, d) images with corresponding high profile of few- layer MoO_3.

nanosheets appear to possess a quadrilateral sheet-like shape with a lateral dimension of (1-4) µm. Further, some nanosheets partially overlap with each other. To ascertain the thickness and number of layers, AFM is very suitable due to its high spatial resolution. AFM images of MoO_3 nanosheets on Si substrate and with the corresponding height profile resolved in the tapping mode is shown in Figure 9(c) and (d). The sheets are observed to be very thin with thickness of 1.6 and 3.8 nm. This corresponds to 1 to 3 bilayers (thickness of single bilayer nanosheet ≈ 1.4 nm) [39] of MoO_3 along (*0l0*) direction with lateral dimensions of 1 and 10 µm.

The composition and thermal stability of MoO_3-rGO composites are studied by thermogravimetric analysis (**Figure 10**a). All samples are preheated to 100 °C in oven to remove adsorbed moisture prior to the measurement. The measurements are carried out under O_2 flow (20 ml min^{-1}) from 30 to 950 °C at the rate of 3 °C min^{-1}. Few-layer MoO_3 show no weight loss and is highly stable between 300 to 600 °C. The composites on the other hand, show weight loss of 5%, 10% and 18% from 200 to 450 °C. The weight loss is due to rGO reaching the deflagration point and decomposing to

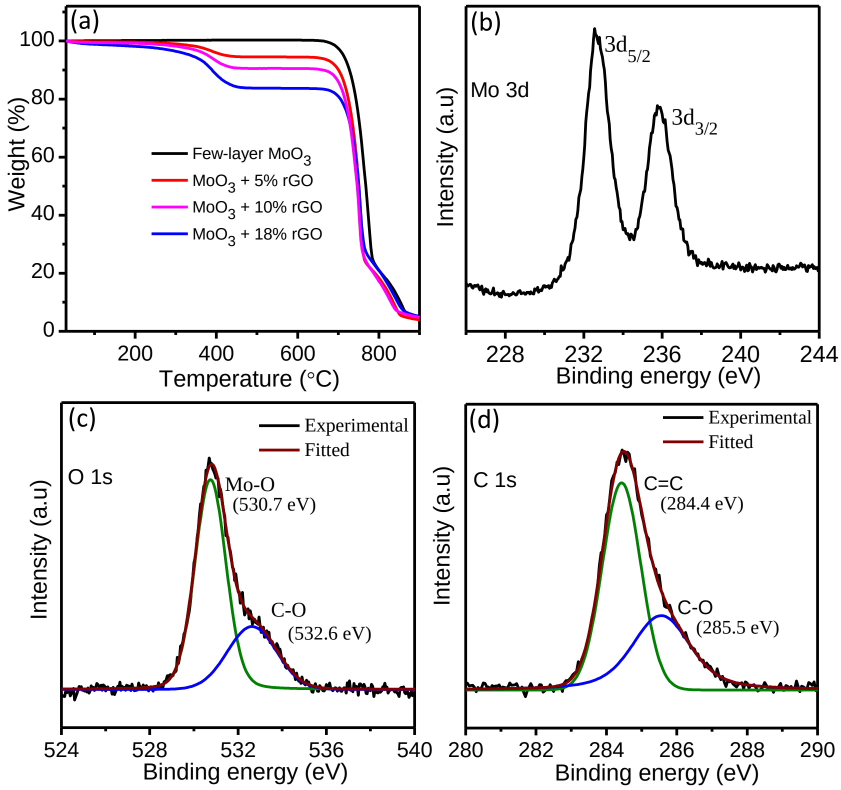

Figure 10. (a) Thermogravimetric analysis of few-layer MoO_3 and MoO_3-rGO composites showing the weight loss. Core-level x-ray photoelectron spectra of (b) Mo 3d (c) O 1s and (d) C 1s of 10% few-layer MoO_3-rGO composite.

carbon soot. Weight loss at temperatures above 700 °C corresponds to decomposition of MoO_3 which is observed in all cases. XPS analyses are carried out to ascertain the elemental compositions and bonding characteristics between few-layer MoO_3 and rGO in the composites. Core-level XP spectra of MoO_3-rGO composite are shown in Figure 10 (b-d). The peak centered at 232.5 and 235.8 eV corresponds to Mo $^{(VI)}$ $3d_{5/2}$ and $3d_{3/2}$ (Figure 3b) and is in good agreement with the MoO_3 binding energies. Oxygen 1s core-level signal (Figure 10c) is deconvoluted into two peaks: 530.7 and 532.65 eV corresponding to Mo-O bond of MoO_3 and C-O bond respectively. High-resolution spectra of carbon 1s (Figure 10d) are also deconvoluted into two peaks, one centered at 284.4 and the other at 285.5 eV corresponding to C=C and C-O bonds respectively. XPS study thus, confirms that MoO_3 is bonded to rGO through the Mo-O-C linkage at the interface.[40] Elemental mappings of MoO_3-rGO composite obtained using energy-dispersive X-ray spectroscopy (EDAX) in FESEM is shown in **Figure 11**. Mapping reveals homogeneity of the composite which is supported via the uniform distribution of molybdenum, oxygen and carbon. FESEM and TEM images also reveal the uniformity and homogeneity of the MoO_3-rGO composites (**Figure 12**). The SAED pattern of the composites (Figure 12d) shows spots as well as ring pattern. The spots correspond to orthorhombic α-MoO_3 and the rings correspond to graphene. MoO_3-rGO composites are further characterized by Raman (**Figure 13**a) and FTIR Figure 13b) spectroscopy shows characteristic bands corresponding to both

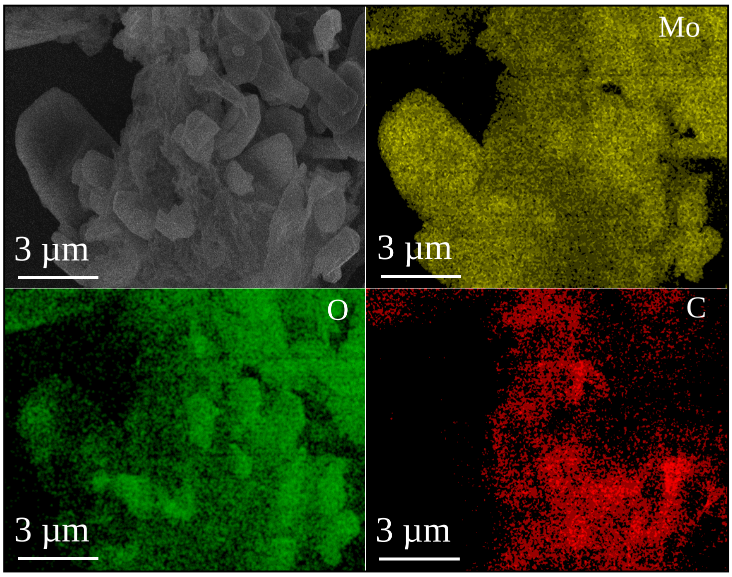

Figure 11. EDAX elemental mapping of MoO_3-rGO composite. Mo (yellow), O (green) and C (red).

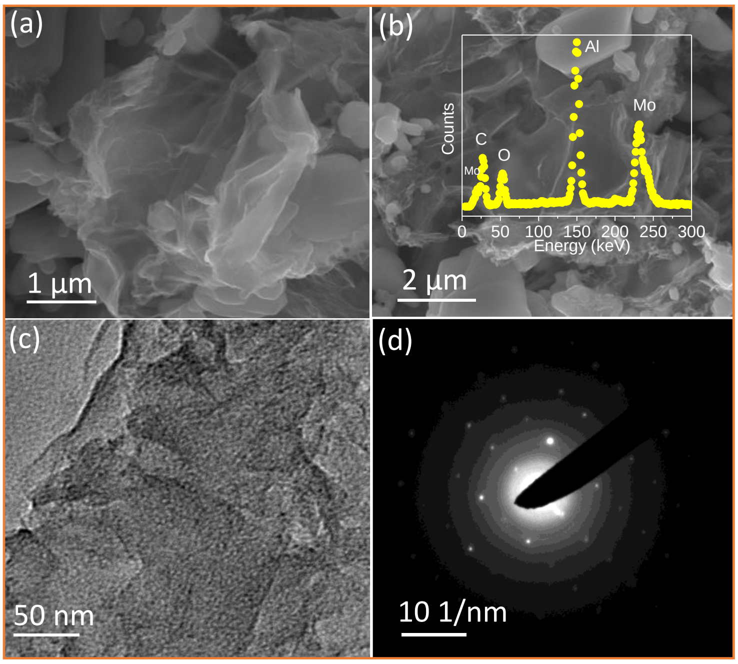

Figure 12. (a, b) FESEM images of few-layer MoO_3-rGO composite (10 wt%). Inside of (b) shows EDAX spectra corresponding Mo, O and C. (c, d) TEM images of few-layer MoO_3-rGO composite and corresponding electron diffraction patterns.

MoO_3 as well as graphene.

Figure 14a shows representative charge and discharge profiles of the MoO_3-(10 wt%)-rGO composite at current density of C/20 (0.09 mA) for the 1st, 2nd, 5th, 10th, 50th and 100th cycles in the voltage range 0.1-3.0 V. All capacities reported for the composite are calculated based on the total weight of MoO_3 and rGO. Although the MoO_3-(10 wt%)-rGO composite shows a high 1st cycle discharge capacity of 1061.2 mAhg^{-1}, the corresponding 1st cycle charge capacity is only 934.4 mAhg^{-1}. This

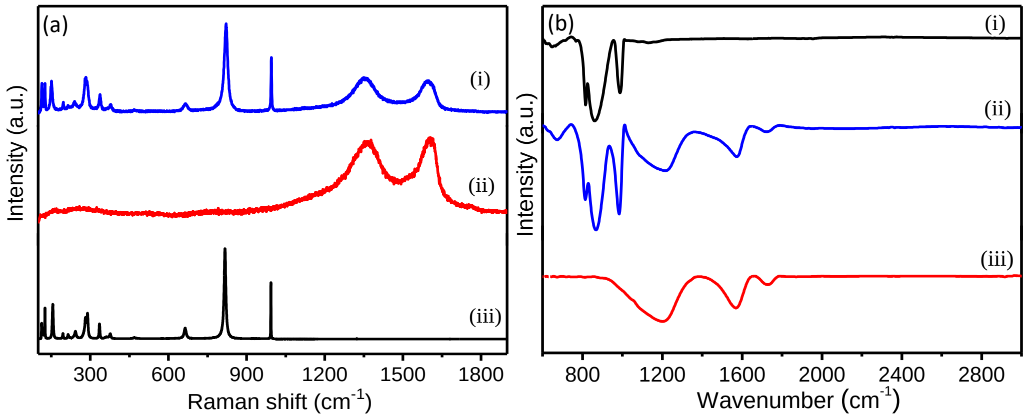

Figure 13. (a) Raman spectra of (i) MoO_3-rGO composite (10 wt%), (ii) rGO and (iii) few-layer MoO_3. (b) Fourier transform infrared spectrum of (i) few-layer MoO_3, (ii) few-layer MoO_3-rGO composite (10 wt%) and (iii) rGO.

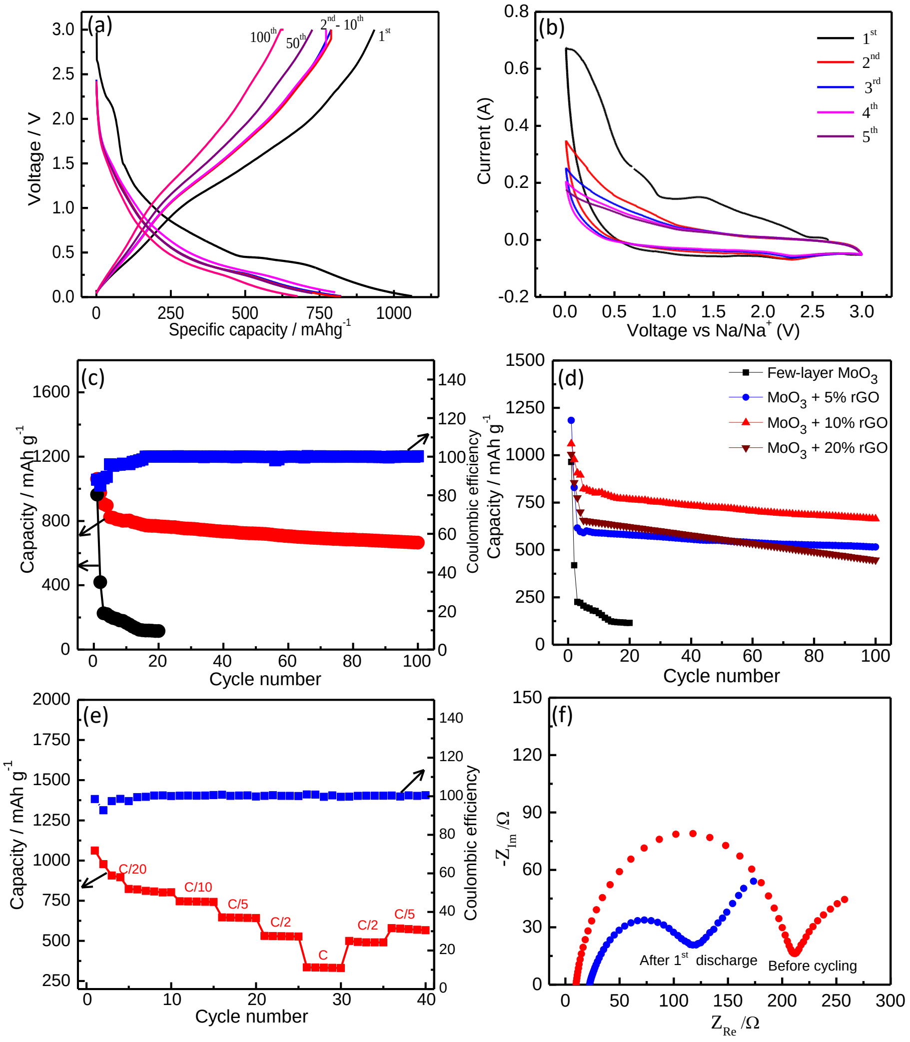

Figure 14. (a) Charge-discharge curves for few-layer MoO$_3$-(10%)-rGO at current rate 0.2 C (0.09 mA) (b) Cyclic voltammetry for few-layer MoO$_3$-rGO composite (10 wt%). (c) Na-discharge capacity and the corresponding Coulombic efficiency for MoO$_3$-(10%)-rGO, (d) Na-discharge specific capacity of few-layer MoO$_3$-rGO composites (5-20 wt%) and few-layer MoO$_3$. (e) Rate performance of MoO$_3$-(10%)-rGO and (f) Nyquist plots of imaginary and real parts of electrochemical impedance for MoO$_3$ before and after 1st discharge.

amounts to a 1st cycle coulombic efficiency of 88%. The loss in charge capacity can be attributed to the disconnection between the MoO$_3$ nanosheets which can result from some degree of disintegration of the nanosheets caused due to the volume changes associated with the alloying reaction.[41] During the first discharge, the potential drops rapidly until it reaches the plateaus at around 2.2 V (narrow) and 0.5 V (wide). Following the wide plateau at 0.5 V the voltage decreases continuously to 0.01 V. Similar voltage profiles were also previously reported in case of lithium intercalation.[42] The sodium-ion intercalation reaction can be divided into two regions: region–1 (i.e., above 1.5 V) can be attributed to the insertion of Na$^+$ ions into the interlayer spacing between the Mo–O octahedron layers. As the potential decreases to the region 2 (i.e., below 1.5 V), a wide plateau develops at about 0.5 V followed by a sloping profile (below 0.3 V). The wide plateau is due to the Na^+ uptake for the complete conversion reaction and sloped profile is due to the formation of solid electrolyte interface (SEI). The overall reaction for few-layer MoO_3 nanosheets with sodium can be expressed as:

(Voltage > 1.5 V): $MoO_3 + xNa^+ + xe^- \rightarrow Na_xMoO_3$ ($x \approx 1.2$)

(Voltage < 0.5V): $Na_xMoO_3 + (6 - x)Na^+ + (6 - x)e^- \rightarrow Mo + 3Na_2O$

During the 1st cycle of sodium insertion, the few-layer nanosheets of MoO_3 undergo an irreversible structural change from α-phase to an amorphous phase followed by a by a conversion reaction to form Na_2O and Mo metal.[26] Preliminary investigation using *ex-situ* XRD of the electrode material following the 1st discharge cycling shows lines corresponding to both Mo and Na_2O (**Figure 15**). On charging, a plateau at about 1.1 V is observed. Following this plateau, the profile does not exhibit any plateaus and in general, the profile displays a fairly steep slope. The charging profile remains nearly the same till the 100th cycle with the expected decrease in the total capacity. On the contrary, the plateau at around 0.5 V becomes narrower from the 1st to the 2nd discharge profile and remains the nearly identical till the 100th cycle. The observations from the galvanostatic cycling is in correspondence with the cyclic voltammetry results (Figure 14b).[41] The cycling behaviour of few-layer MoO_3 and MoO_3-(10 wt%)-rGO composites with Na/Na^+ are illustrated in the Figure 7c. Compared to the

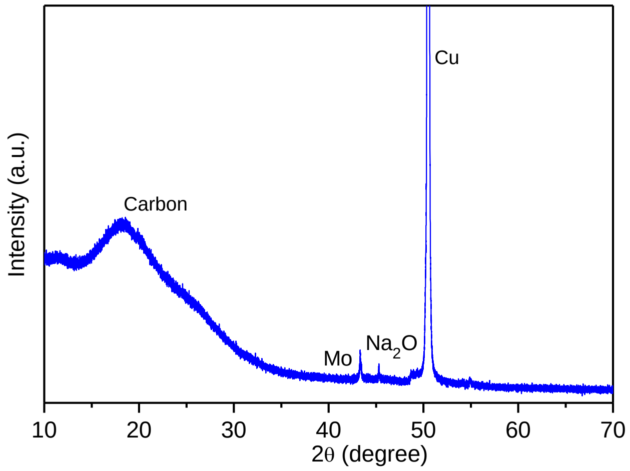

Figure 15. *Ex-situ* XRD of the MoO_3-rGO electrode after first discharge.

few-layer MoO_3 and few-layer MoO_3-(10 wt%)-rGO composite shows much higher specific capacity and excellent cyclability. This is also true for other rGO fractions in MoO_3 (Figure 14d). The remarkable electrochemical performance of MoO_3-(10 wt%)-rGO compared to MoO_3 is attributed to a combination of both the MoO_3 nanostructuring as well as due to the presence of rGO. The rGO forms a 3D network of electrical conduits between the MoO_3 nanosheets which provide facile electron pathways for the electrochemical reaction to occur efficiently and also transport charge to the current collector. In the present study, 10 wt% of rGO is found to be the optimum amount for reversible cyclability over 100 cycles of charge and discharge.

In addition to the requirement of an efficient electron percolation process, MoO_3 in nanosheet morphology is observed to be highly effective in optimizing the large volume change observed during repeated sodium intercalation and de-intercalation.[43] The spatial configuration of the MoO_3 nanosheets with optimum amount of rGO minimizes the cracks and the loses of electronic contact between electroactive material. With repeated cycling the coulombic efficiency increased to 99.8% in the 15th cycle and remained stable at this value till 100 cycles. The capacity also showed a similar trend and at the end of 100 cycles is 665 $mAhg^{-1}$. The MoO_3-(10 wt%)-rGO composite also showed very good rate capability in the current density range C/20- 1 C. At 1 C, the MoO_3-(10 wt%)-rGO showed a capacity of 330 $mAhg^{-1}$. With decrease in the value of the current, the capacities are again retained (Figure 14e). The electrochemical impedance spectroscopy (EIS) measurements (Figure 14f) also clearly shows that the charge transfer resistance decreases following the first discharge.

5. Conclusions

It is possible to prepare few-layer MoO_3 by several methods. These nanosheets have a higher band gap than bulk MoO_3 and exhibit higher catalytic activity for the photodegradation of methylene blue. It is also noteworthy that composites of few-layer MoO_3 with borocarbonitride possess good characteristics as electrode supercapacitors. It is likely that many other applications will be found for few-layer MoO_3.

We have also demonstrated successfully that few-layer MoO_3-rGO composites have considerable potential as a high performance anode material for Na-ion battery. The optimal 3D configuration of 2D-MoO_3 and rGO is essentially due to Mo-O-C linkages between MoO_3 and rGO. The spatial configuration not only aids in suppressing the mechanical instabilities of MoO_3 taking place during repeated cycling but also provides facile transport pathways for both electrons and Na-ions leading to an efficient and stable electrochemical reaction. The amount of rGO in the composite is crucial, as this directly ascertains the structural stability and electrochemical performance of the MoO_3-rGO composite. The novel design of a 3D-composite comprising of a 2D-electroactive compound and its integration with an optimum amount of extended carbon structure (1D, 2D) is expected to pave way for design of many more 2D-electroactive materials based 3D-composites for prospective applications in sodium-ion batteries.

6. References

[1] a) A. K. Geim, *Science* **2009**, *324*, 1530-1534; b) A. K. Geim, K. S. Novoselov, *Nat. Mater.* **2007**, *6*, 183-191; c) C. N. R. Rao, A. K. Sood, K. S. Subrahmanyam, A. Govindaraj, *Angew. Chem. Int. Ed.* **2009**, *48*, 7752-7777; d) C. N. R. Rao, H. S. S. R. Matte, K. S. Subrahmanyam, *Acc. Chem. Res.* **2012**, *46*, 149-159.

[2] a) H. S. S. Ramakrishna Matte, A. Gomathi, A. K. Manna, D. J. Late, R. Datta, S. K. Pati, C. N. R. Rao, *Angew. Chem. Int. Ed.* **2010**, *49*, 4059-4062; b) D. J. Late, B. Liu, H. S. S. R. Matte, C. N. R. Rao, V. P. Dravid, *Adv. Funct. Mater.* **2012**, *22*, 1894-1905.

[3] C. N. R. Rao, B. Raveau, *Transition Metal Oxides,Wiley-VCA, Weinheim* **1998**.

[4] K. S. Novoselov, D. Jiang, F. Schedin, T. J. Booth, V. V. Khotkevich, S. V. Morozov, A. K. Geim, *Proc. Natl. Acad. Sci.* **2005**, *102*, 10451-10453.

[5] T. Sasaki, M. Watanabe, *J. Am. Chem. Soc.* **1998**, *120*, 4682-4689.

[6] M. Osada, T. Sasaki, *Adv. Mater.* **2012**, *24*, 210-228.

[7] a) R. Naouel, H. Dhaouadi, F. Touati, N. Gharbi, *Nano-Micro Letters* **2011**, *3*, 6; b) L. Mai, F. Yang, Y. Zhao, X. Xu, L. Xu, B. Hu, Y. Luo, H. Liu, *Mater. Today* **2011**, *14*, 346-353; c) I. Shakir, J. H. Choi, M. Shahid, Z. Ali, D. J. Kang, *J. Mater. Chem.* **2012**, *22*, 20549-20553; d) L. X. Song, J. Xia, Z. Dang, J. Yang, L. B. Wang, J. Chen, *CrystEngComm* **2012**, *14*, 2675-2682; e) S. Hu, X. Wang, *J. Am. Chem. Soc.* **2008**, *130*, 8126-8127; f) L. Cai, P. M. Rao, X. Zheng, *Nano Lett.* **2011**, *11*, 872-877; g) M. E. Kurtoglu, T. Longenbach, Y. Gogotsi, *J. Mater. Chem.* **2011**, *21*, 7931-7936; h) A. M. Taurino, A. Forleo, L. Francioso, P. Siciliano, M. Stalder, R. Nesper, *Appl. Phys. Lett.* **2006**, *88*, 152111-152113; i) N. A. Dhas, K. S. Suslick, *J. Am. Chem. Soc.* **2005**, *127*, 2368-2369; j) S. Balendhran, S. Walia, H. Nili, J. Z. Ou, S. Zhuiykov, R. B. Kaner, S. Sriram, M. Bhaskaran, K. Kalantar-zadeh, *Adv. Funct. Mater.* **2013**, *23*, 39523970.

[8] K. Kalantar-zadeh, J. Tang, M. Wang, K. L. Wang, A. Shailos, K. Galatsis, R. Kojima, V. Strong, A. Lech, W. Wlodarski, R. B. Kaner, *Nanoscale* **2010**, *2*, 429-433.

[9] Y. A. Yang, Y. W. Cao, B. H. Loo, J. N. Yao, *J. Phys. Chem. B* **1998**, *102*, 9392-9396.

[10] a) J. N. Yao, K. Hashimoto, A. Fujishima, *Nature* **1992**, *355*, 624-626; b) J. N. Yao, Y. A. Yang, B. H. Loo, *J. Phys. Chem. B* **1998**, *102*, 1856-1860.

[11] D. D. Yao, J. Z. Ou, K. Latham, S. Zhuiykov, A. P. O'Mullane, K. Kalantar-zadeh, *Cryst. Growth Des.* **2012**, *12*, 1865-1870.

[12] Y. Chen, C. Lu, L. Xu, Y. Ma, W. Hou, J.-J. Zhu, *CrystEngComm* **2010**, *12*, 3740-3747.

[13] K. Gesheva, A. Szekeres, T. Ivanova, *Sol. Energy Mater. Sol. Cells* **2003**, *76*, 563-576.

[14] J. Zhou, N. S. Xu, S. Z. Deng, J. Chen, J. C. She, Z. L. Wang, *Adv. Mater.* **2003**, *15*, 1835-1840.

[15] S. Balendhran, J. Deng, J. Z. Ou, S. Walia, J. Scott, J. Tang, K. L. Wang, M. R. Field, S. Russo, S. Zhuiykov, M. S. Strano, N. Medhekar, S. Sriram, M. Bhaskaran, K. Kalantar-zadeh, *Adv. Mater.* **2013**, *25*, 109-114.

[16] a) W. Tang, L. Liu, S. Tian, L. Li, Y. Yue, Y. Wu, K. Zhu, *Chem. Commun.* **2011**, *47*, 10058-10060; b) T. Brezesinski, J. Wang, S. H. Tolbert, B. Dunn, *Nat. Mater.* **2010**, *9*, 146-151.

[17] M. Rapos, J. H. Calderwood, *J. Phys. D: Appl. Phys.* **1975**, *8*, 299.

[18] a) Y. B. Li, Y. Bando, D. Golberg, K. Kurashima, *Appl. Phys. Lett.* **2002**, *81*, 5048-5050; b) P. Meduri, E. Clark, J. H. Kim, E. Dayalan, G. U. Sumanasekera, M. K. Sunkara, *Nano Lett.* **2012**, *12*, 1784-1788.

[19] J. B. Goodenough, K.-S. Park, *J. Am. Chem. Soc.* **2013**, *135*, 1167-1176.

[20] A. S. Arico, P. Bruce, B. Scrosati, J.-M. Tarascon, W. van Schalkwijk, in *Nat. Mater.* **2005**, *4*, 366-377.

[21] V. Palomares, P. Serras, I. Villaluenga, K. B. Hueso, J. Carretero-Gonzalez, T. Rojo, *Energy Environ. Sci.* **2012**, *5*, 5884-5901.

[22] S. P. Ong, V. L. Chevrier, G. Hautier, A. Jain, C. Moore, S. Kim, X. Ma, G. Ceder, *Energy Environ. Sci.* **2011**, *4*, 3680-3688.

[23] S.-W. Kim, D.-H. Seo, X. Ma, G. Ceder and K. Kang, *Adv. Energy Mater.* **2012**, *2*, 710–721.

[24] a) D. Kundu, E. Talaie, V. Duffort, L. F. Nazar, *Angew. Chem. Int. Ed.* **2015**, *54*, 3431-3448; b) N. Yabuuchi, K. Kubota, M. Dahbi, S. Komaba, *Chem. Rev.*

2014, *114*, 11636-11682; c) M. H. Han, E. Gonzalo, G. Singh, T. Rojo, *Energy Environ. Sci.* **2015**, *8*, 81-102.

[25] a) Q. H. Wang, K. Kalantar-Zadeh, A. Kis, J. N. Coleman, M. S. Strano, *Nat. Nanotechnol.* **2012**, *7*, 699-712; b) K. S. Novoselov, V. I. Falko, L. Colombo, P. R. Gellert, M. G. Schwab, K. Kim, *Nature* **2012**, *490*, 192-200; c) S. Balendhran, S. Walia, H. Nili, J. Z. Ou, S. Zhuiykov, R. B. Kaner, S. Sriram, M. Bhaskaran, K. Kalantar-zadeh, *Adv. Funct. Mater.* **2013**, *23*, 3952-3970; d) M. Chhowalla, H. S. Shin, G. Eda, L.-J. Li, K. P. Loh, H. Zhang, *Nat. Chem.* **2013**, *5*, 263-275. e) B. Qu, C. Ma, G. Ji, C. Xu, J. Xu, Y. S. Meng, T. Wang, J. Y. Lee, *Adv. Mater.* **2014**, *26*, 3854-3859; f) L. David, R. Bhandavat, G. Singh, *ACS Nano* **2014**, *8*, 1759-1770.

[26] S. Hariharan, K. Saravanan, P. Balaya, *Electrochem. Commun.* **2013**, *31*, 5-9.

[27] Y. Wen, K. He, Y. Zhu, F. Han, Y. Xu, I. Matsuda, Y. Ishii, J. Cumings, C. Wang, *Nat. Commun.* **2014**, *5, 4033*.

[28] A. C. Dillon, L. A. Riley, Y. S. Jung, C. Ban, D. Molina, A. H. Mahan, A. S. Cavanagh, S. M. George, S. H. Lee, *Thin Solid Films* **2011**, *519*, 4495-4497.

[29] a) F. F. Ferreira, T. G. Souza Cruz, M. C. A. Fantini, M. H. Tabacniks, S. C. de Castro, J. Morais, A. de Siervo, R. Landers, A. Gorenstein, *Solid State Ionics* **2000**, *136–137*, 357-363; b) L. Noerochim, J.-Z. Wang, D. Wexler, Z. Chao, H.-K. Liu, *J. Power Sources* **2013**, *228*, 198-205.

[30] a) U. K. Sen, S. Mitra, *RSC Adv.* **2012**, *2*, 11123-11131; b) M. F. Hassan, Z. P. Guo, Z. Chen, H. K. Liu, *J. Power Sources* **2010**, *195*, 2372-2376.

[31] M. B. Sreedhara, H. S. S. R. Matte, A. Govindaraj, C. N. R. Rao, *Chem. Asian J.* **2013**, *8*, 2430-2435.

[32] a) K. Gopalakrishnan, K. Moses, A. Govindaraj, C. N. R. Rao, *Solid State Commun.* **2013,** *175***,** 43-50; b) Y. Wen, K. He, Y. Zhu, F. Han, Y. Xu, I. Matsuda, Y. Ishii, J. Cumings, C. Wang, *Nat. Commun.***2014**, *5*, 4033.

[33] a) K. S. Subrahmanyam, S. R. C. Vivekchand, A. Govindaraj, C. N. R. Rao, *J. Mater. Chem.* **2008**, *18*, 1517-1523; b) W. S. Hummers, R. E. Offeman, *J. Am. Chem. Soc.* **1958**, *80*, 1339-1339; c) H. C. Schniepp, J.-L. Li, M. J. McAllister, H. Sai, M. Herrera-Alonso, D. H. Adamson, R. K. Prud'homme, R. Car, D. A. Saville, I. A. Aksay, *J. Phys. Chem. B* **2006**, *110*, 8535-8539.

[34] N. Kumar, K. S. Subrahmanyam, P. Chaturbedy, K. Raidongia, A. Govindaraj, K. P. S. S. Hembram, A. K. Mishra, U. V. Waghmare, C. N. R. Rao, *ChemSusChem* **2011**, *4*, 1662-1670.

[35] W. S. Hummers, R. E. Offeman, *J. Am. Chem. Soc.* **1958**, *80*, 1339-1339.

[36] a) L. Fang, Y. Shu, A. Wang, T. Zhang, *J. Phys. Chem. C* **2007**, *111*, 2401-2408; b) Q. P. Ding, H. B. Huang, J. H. Duan, J. F. Gong, S. G. Yang, X. N. Zhao, Y. W. Du, *J. Cryst. Growth* **2006**, *294*, 304-308.

[37] B. E. Conway, *Electrochemical Spercapacitors*, *Springer*, **1999**.

[38] M. D. Stoller, R. S. Ruoff, *Energy Environ. Sci.* **2010**, *3*, 1294-1301.

[39] K. Kalantar-zadeh, J. Tang, M. Wang, K. L. Wang, A. Shailos, K. Galatsis, R. Kojima, V. Strong, A. Lech, W. Wlodarski, R. B. Kaner, *Nanoscale* **2010**, *2*, 429-433.

[40] K. Zhou, W. Zhou, X. Liu, Y. Sang, S. Ji, W. Li, J. Lu, L. Li, W. Niu, H. Liu and S. Chen, *Nano Energy* **2015**, *12*, 510–520.

[41] M. E. Spahr, P. Novák, O. Haas, R. Nesper, *J. Power Sources* **1995**, *54*, 346-351.

[42] a) S.-H. Lee, Y.-H. Kim, R. Deshpande, P. A. Parilla, E. Whitney, D. T. Gillaspie, K. M. Jones, A. H. Mahan, S. Zhang, A. C. Dillon, *Adv. Mater.* **2008**, *20*, 3627-3632; b) Y. S. Jung, S. Lee, D. Ahn, A. C. Dillon, S.-H. Lee, *J. Power Sources* **2009**, *188*, 286-291.

[43] X. Li, J. Xu, L. Mei, Z. Zhang, C. Cui, H. Liu, J. Ma, S. Dou, *J. Mater. Chem. A* **2015**, *3*, 3257-3260.

Chapter I.3

Few-layer Nanosheets of the Aurivillius Family of Oxides

SUMMARY*

Nanosheets containing few-layers of ferroelectric Aurivillius family of oxides, $Bi_2A_{n-1}B_nO_{3n+3}$ (where A= Bi^{3+}, Ba^{2+} etc. and B= Ti^{4+}, Fe^{3+} etc.) with n= 3, 4, 5, 6 and 7 have been prepared by the reaction with n-butyllithium, followed by exfoliation in water. The few-layer samples have been characterized by Tyndall cones, atomic force microscopy, optical spectroscopy and other techniques. The few-layer species have a thickness corresponding to a fraction of the *c*-parameter along which axis the perovskite layers are stacked. Magnetization measurements have been carried out on the few-layer samples containing iron. Significant changes in the optical spectra and magnetic properties are found in the few-layer species compared to the bulk samples. Few-layer species of the Aurivillius family of oxides may find uses as thin layer dielectrics in photovoltaics and other applications.

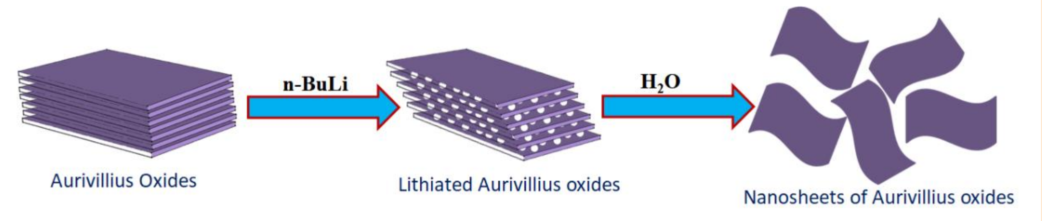

*A paper based on this work has appeared in Journal of Solid State Chemistry (2015).

1. Introduction

Since the discovery of graphene,[1] there has been intense interest in the exfoliation of layered materials to prepare single- or few-layered nanosheets since such species possess unique properties of value.[2, 3] There has been considerable effort made to exfoliate layered metal dichalcogenides such as MoS_2 and WS_2 and some inorganic layered compounds.[2, 3] It is indeed desirable to prepare few-layer species of various important layered inorganic materials and examine their properties. In this contest, exfoliating layered metal oxides into individual flakes by liquid phase exfoliation or mechanical means assumes importance. Recently, few-layer MoO_3 has been prepared by Li intercalation and ultrasonication.[4] The exfoliated layered oxides possessing high surface area and distinct electronic properties may have potential applications in catalysis, supercapacitors, gas storage and sensor technologies.[4-6] One of the well-known families of layered materials is that of Aurivillius oxides, a class of layered perovskites with strong covalent bonding in the molecular layer and van der Waals interaction between the layers.[7-9] These layered oxides form a homologous series of compounds with the general formula $Bi_2A_{n-1}B_nO_{3n+3}$ built from regular intergrowths of fluorite-like $(Bi_2O_2)^{2+}$ layers alternating with $(A_{n-1}B_nO_{3n+1})^{2-}$ perovskite layers along the (00*l*) direction. Generally, A= Bi^{3+}, La^{3+}, Sr^{2+} and B= Fe^{3+}, Ti^{4+}, in these materials and there are 'n' perovskite layers in one formula unit. Some of Aurivillius oxides containing iron exhibit strong antiferromagnetic ordering with the Néel temperature increasing with the increasing number of perovskite layers.[10] The strong antiferromagnetic interaction is due to Fe-O-Fe superexchange interaction in the perovskite layers which dominates over the diamagnetic interaction in the Bi_2O_2 layers.[10, 11] The Aurivillius oxides also exhibit ferroelectricity and other interesting properties.[9, 12-14] The ability to exfoliate layers of the Aurivillius oxides by intercalation of guest species into the van der Waals gap allows us to engineer their properties which may be useful in practical applications. Preparation of layered titanates by delamination has been reported.[15] It is likely that exfoliated nanosheets of the layered oxides may provide new venues for engineering and designing useful materials, specially by depositing the nanosheets on appropriate substrates.

2. Scope of the present investigations

After the discovery of graphene, atomically thin 2D nanosheets of transition metal dichalcogenides (TMDCs) and transition metal oxides (TMOs) received much attention due to their rich properties. Efforts on the exfoliation of 2D nanosheets are generally limited to binary oxides and sulfides and there is not much attention paid towards ternary and quaternary perovskite layered oxides. One family of oxides with rich electrical and magnetic properties is the Aurivillius family of oxides with the general formula $Bi_2A_{n-1}B_nO_{3n+3}$. We have exfoliated several members of Aurivillius oxides (n= 3, 4, 5, 6 and 7) by chemical Li intercalation using n-butyllithium followed by reaction in water and characterized the few-layer materials thus produced. Nanosheets of these materials are characterized by Tyndall effect and other methods.

3. Experimental Section

Materials

All the chemicals used for synthesis are highly pure and purchased from commercial sources. Bi_2O_3 (99.9% Sigma-Aldrich), Fe_2O_3 (99.9% Sigma-Aldrich) and TiO_2 (99.9% Sigma-Aldrich), n-BuLi in hexane (1.6 M, Acros), water (Millipore) and H_2SO_4 (Spectrochem, India, 98%) are used without any further purification.

Synthesis

Synthesis of Aurivillius oxides and their exfoliation:

Aurivillius compounds of the general formula $Bi_{n+1}Fe_{n-3}Ti_3O_{3n+3}$ (n = 3, 4, 5, 6 and 7) were synthesised by the solid-state method. Required amounts of pure Bi_2O_3, Fe_2O_3 and TiO_2 were finely ground (with 5 wt% excess Bi_2O_3 to compensate for the volatilization) pressed into a 12 mm circular pellet by applying pressure and heated in several steps to get the desired phase. The heating sequence for $Bi_4Ti_3O_{12}$ and $Bi_{n+1}Fe_{n-3}Ti_3O_{3n+3}$ are 800 ^{o}C/8 h and 800-1000 ^{o}C/24-48 h (for n = 4, 24 h; n = 5, 32 h; n = 6, 40 h and n = 7, 48 h) at a rate of 5 ^{o}C/min. After every 8 h, the pellet was cooled to room temperature ground, pressed into a pellet and heated again to get the pure phase. In order to prepare single or few-layer samples we exfoliated compounds by lithium intercalation and de-intercalation.[16, 17] This was carried out by the reaction between 3 mmol-excess n-BuLi in hexane with ground Aurivillius oxide powder in a N_2 atmosphere, n-BuLi was added drop by drop to well ground powder at 0 °C and the mixture slowly brought to room temperature and stirred for 72 h. The lithiated products were washed several times to remove the excess n-BuLi. The products were black in colour it is due to the partial reduction of bismuth and titanium. The exfoliation was done by oxidative lithium deintercalation by treating the lithiated Aurivillius oxides with deionized water under ultrasonication for 4 h followed by dialysis in a stream of deionized water for 48 h. The product was thoroughly washed and centrifuged until the pH of supernatant became 7. This method leads to exfoliation of layers as could be observed by the gradual color change from black to the expected color of the compound. During the exfoliation reaction the Li goes to solution as LiOH with the evolution of hydrogen from water thereby favouring the formation of few-layers.

Characterization

Powder X-ray diffraction (PXRD) patterns were recorded in Bruker D8 Discover diffractometer and Rigaku-99 diffractometer using Cu Kα radiation. Atomic force microscopy (AFM) was performed on an Innova atomic force microscope. Transmission electron microscopy (TEM) images were recorded using JEOL JEM 3010 microscope, fitted with a Gatan CCD camera operating at an accelerating voltage of 300 kV. Electronic absorption spectra were recorded in a Perkin-Elmer Lambda 900 UV/Vis/NIR spectrometer in the diffuse reflectance mode. Magnetic measurements were carried out in SQUID VSM (Quantum Design,U.S.).

4. Results and Discussion

Characteristics of few-layer Auruvillis oxide nanosheets

We have examined bulk as well as few-layer samples of a few members of the Aurivillius family of oxides including $Bi_4Ti_3O_{12}$ and the n = 4,5,6,7 members of the $Bi_{n+1}Fe_{n-3}Ti_3O_{3n+3}$ family. **Figure 1** shows structure of $Bi_4Ti_3O_{12}$ and $Bi_5Ti_3FeO_{15}$. The fluorite-like $(Bi_2O_2)^{2+}$ layers alternating with $(A_{n-1}B_nO_{3n+1})^{2-}$ perovskite layers along the (00*l*) direction. Li intercalation in these oxides with n-BuLi reaction, followed by

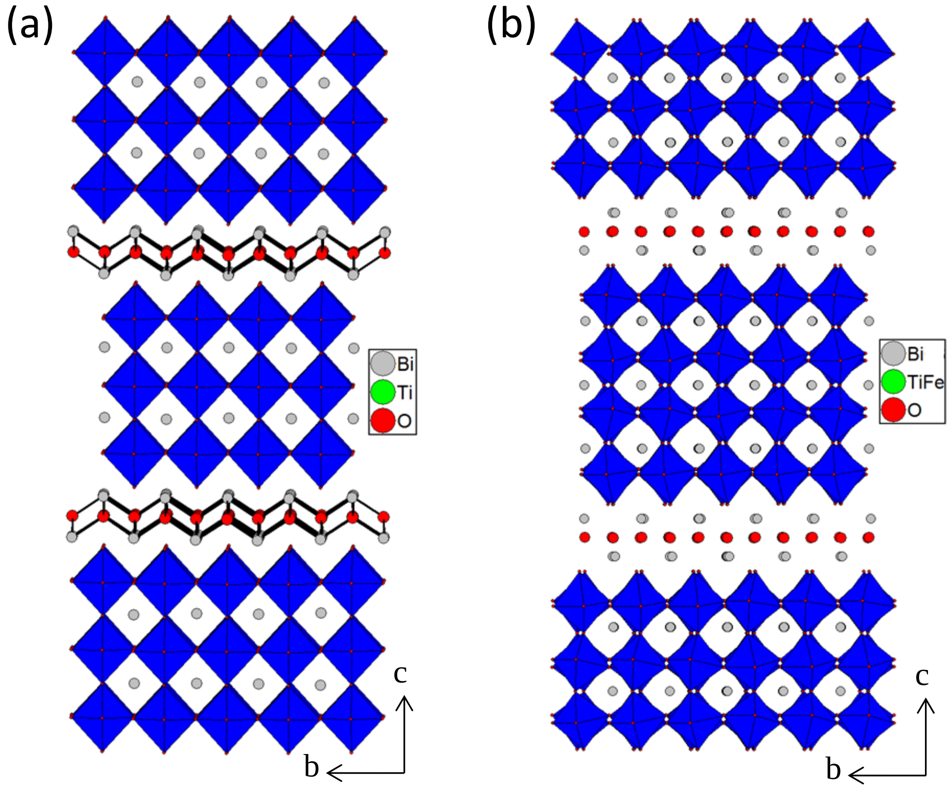

Figure 1. Crystal structure of (a) $Bi_4Ti_3O_{12}$ and (b) $Bi_5Ti_3FeO_{15}$.

exfoliation in water results in suspensions of few-layer materials. Our results on the exfoliation of $Bi_4Ti_3O_{12}$ agree well with those of Kim et al.[16]

Figure 2 shows typical PXRD patterns of few-layer samples of $Bi_5Ti_3FeO_{15}$ (n=4) and $Bi_7Ti_3Fe_3O_{21}$ (n=6) in comparison with those of bulk samples. All the samples had lamellar structures and there were no granules. The XRD patterns of the few-layer samples are generally broader and the intensity of the (*00l*) reflection is lower indicating that the destruction of the stacking along the (*00l*) direction has resulted in the few-layer structures. Clearly Li intercalation and deintercalation leads exfoliation of the layered structures. The reason that the (*00l*) reflection is affected because the layers are stacked in this direction with van der Waals forces between them. **Figure 3** shows AFM images with height profiles of two Aurivillius phases with n = 3 and 4, revealing the few-layer nanosheets to be 1.66 and 2.01 nm thick. These values correspond to a fraction of the *c*-parameter. Insets in Figure 3 show Tyndall scattering of the colloidal suspensions in ethanol confirming the presence of few-layers in the exfoliated samples. We show typical TEM images of few-layer $Bi_6Ti_3Fe_2O_{18}$ and $Bi_7Ti_3Fe_3O_{21}$ in **Figure 4** to illustrate crystalline features of these materials. The electron diffraction pattern in Figure 4(b) shows clearly the nanosheets

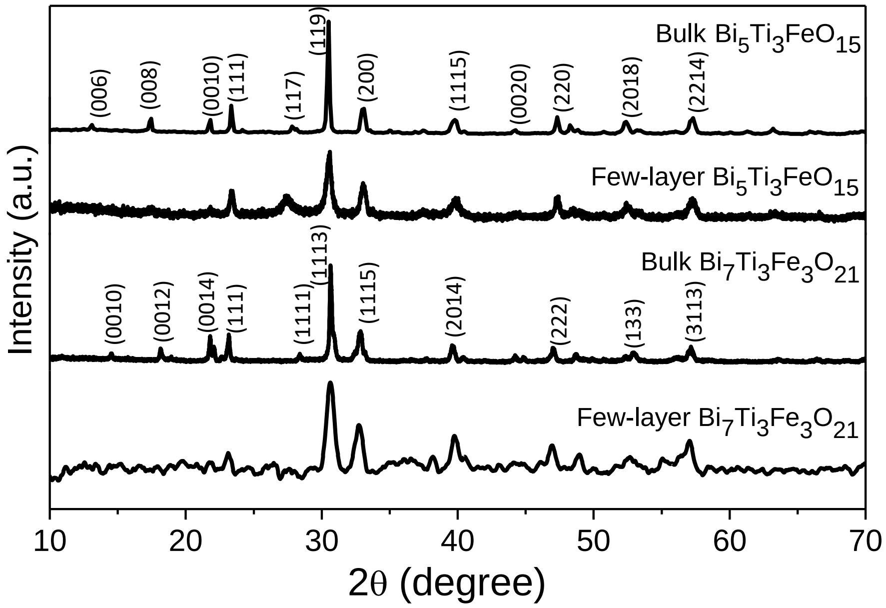

Figure 2. PXRD patterns of bulk and few-layer samples of $Bi_5Ti_3FeO_{15}$ and $Bi_7Ti_3Fe_3O_{21}$.

single crystalline. Interestingly, the few-layer species do not show any scrolling unlike single-layer species in certain instances.

Optical properties

UV-Vis spectra of the few-layer materials show blue-shifts of the absorption bands relative to the bulk samples due to quantum size effect (**Figure 5**). The absorption is mainly due to excitation from the valence band to conduction band, valence band mainly comprising of Bi 6s+Fe t_{2g}+ O 2p and conduction band comprising Ti 3d+Fe e_g orbitals. The low energy visible light photoexcitations correspond to the electronic excitation to Fe e_g orbitals from Bi 6s+Fe t_{2g}+ O 2p, the absorption from UV photons

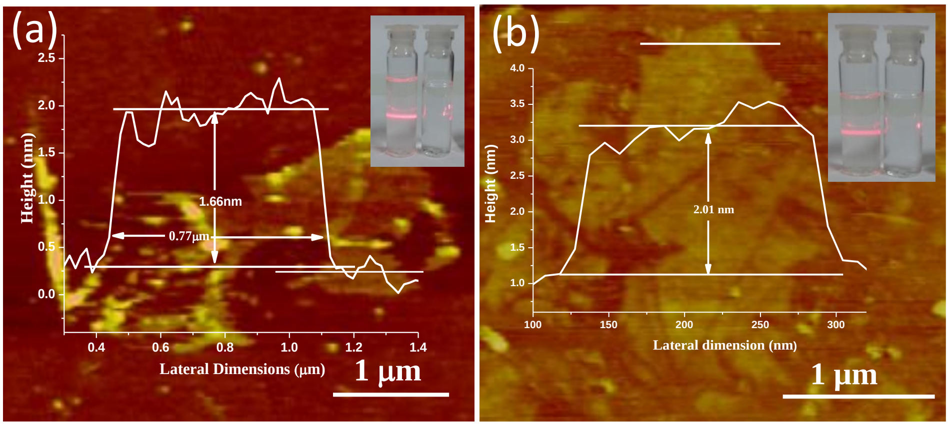

Figure 3. AFM images of few-layer samples of (a) $Bi_4Ti_3O_{12}$ and (b) $Bi_5Ti_3FeO_{15}$ prepared by Li intercalation. Inset shows Tyndall effect in the nanosheets dispersions. Bulk sample dispersed in ethanol do not show Tyndall cones.

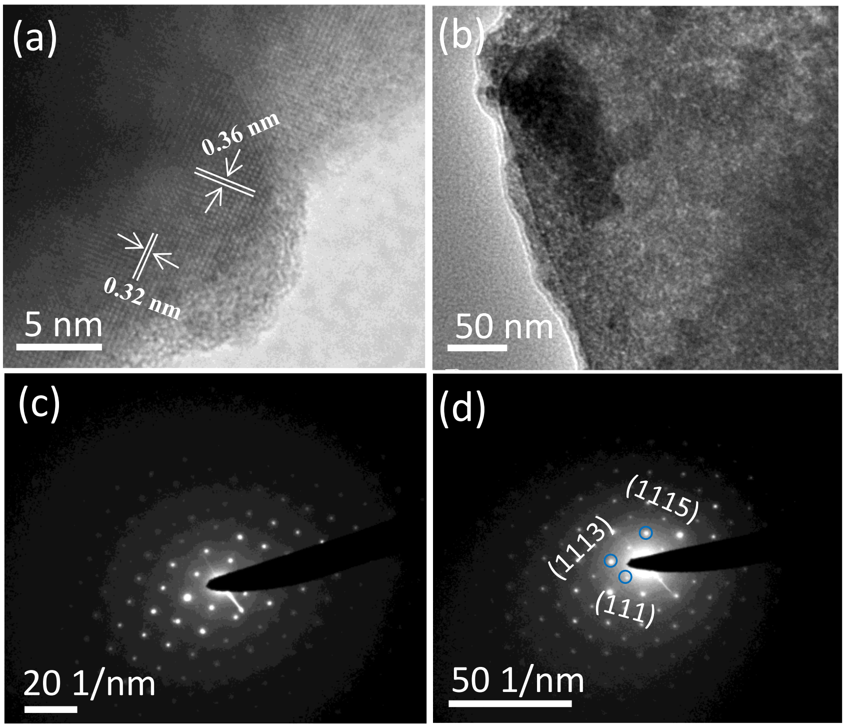

Figure 4. TEM images of few-layer samples of (a) $Bi_6Ti_3Fe_2O_{18}$ and (b) $Bi_7Ti_3Fe_3O_{21}$. The lattice spacing shown in between (*111*) and (*119*) planes.

arising from excitation to Ti 3d orbital because these orbits lie in higher energy states than the Fe e_g states. The absorption shoulder in the spectra at visible region may be due to the incorporation of some energy levels of the Fe 3d orbits.[14] In Figure 5 we show the spectra of $Bi_5Ti_3FeO_{15}$ and $Bi_7Ti_3Fe_3O_{21}$ with absorption maxima at 405 and 431 nm respectively in the bulk samples. The corresponding few-layer samples show maxima at 382 and 391 nm respectively. Raman spectra of few-layer and bulk samples were similar just like in the case of MoO_3.[4]

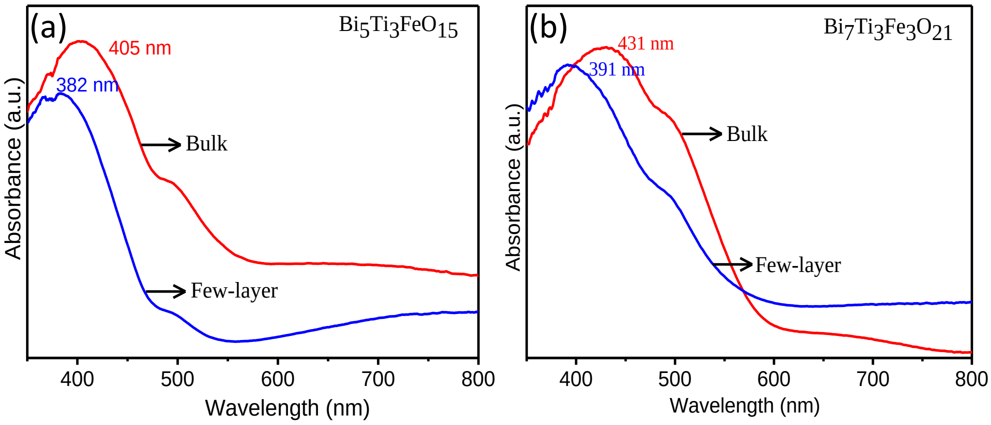

Figure 5. UV-Vis spectra of bulk and few-layer samples of $Bi_5Ti_3FeO_{15}$ and $Bi_7Ti_3Fe_3O_{21}$.

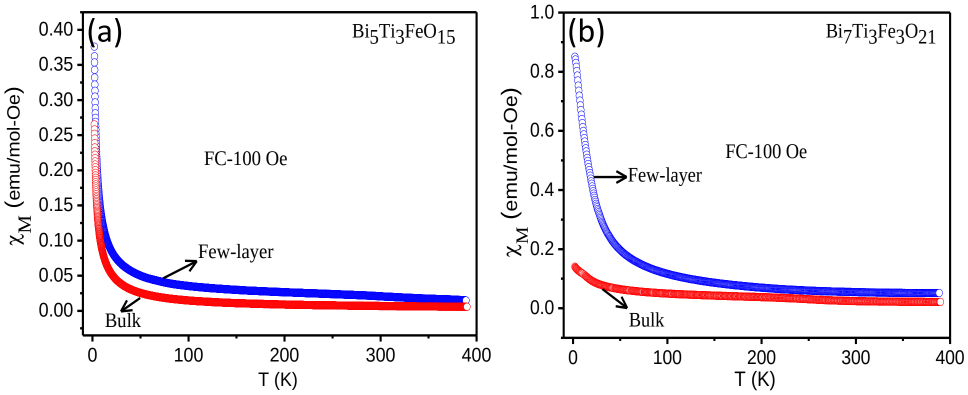

Figure 6. FC magnetization for bulk and few-layer samples of $Bi_5Ti_3FeO_{15}$ and $Bi_7Ti_3Fe_3O_{21}$.

Magnetic properties

Some of the Aurivillius phases studied by us contain iron and exhibit magnetic properties. Bulk samples of these materials are antiferromagnetic with Néel temperatures 80 K, 160 K, 190 K and 220 K for n = 4, 5, 6 and 7 respectively. We have compared the magnetic properties of bulk and few-layer samples and found that the few-layer samples have slightly higher magnetization values than the corresponding bulk material as shown in **Figure 6**. This is understandable since antiferromagnetic interaction in the bulk material is reduced in the few-layers samples; furthermore, the nanosamples would show surface magnetism.

5. Conclusions

Reaction with n-butyllithium provides a satisfactory method of obtaining few-layer species of the members of the Aurivillius family of oxides with the thickness corresponding to a fraction of the *c*-parameter. Since the bulk samples of these oxides are ferroelectrics, it may be possible to use the few-layer species as thin dielectric films in photovoltaics and other applications. Depositing the exfoliated nanosheets on various substrates and other layered materials can give rise to materials of interest.

6. References

[1] A. K. Geim, K. S. Novoselov, *Nat. Mater.* **2007**, *6*, 183-191.

[2] C. N. R. Rao, H. S. S. Ramakrishna Matte, U. Maitra, *Angew.Chem. Int. Ed.* **2013**, *52*, 13162-13185.

[3] J. N. Coleman, M. Lotya, A. O'Neill, S. D. Bergin, P. J. King, U. Khan, K. Young, A. Gaucher, S. De, R. J. Smith, I. V. Shvets, S. K. Arora, G. Stanton, H.-Y. Kim, K. Lee, G. T. Kim, G. S. Duesberg, T. Hallam, J. J. Boland, J. J. Wang, J. F. Donegan, J. C. Grunlan, G. Moriarty, A. Shmeliov, R. J. Nicholls, J. M. Perkins, E. M. Grieveson, K. Theuwissen, D. W. McComb, P. D. Nellist, V. Nicolosi, *Science* **2011**, *331*, 568.

[4] M. B. Sreedhara, H. S. S. R. Matte, A. Govindaraj, C. N. R. Rao, *Chem. Asian J.* **2013**, *8*, 2430-2435.

[5] Q. H. Wang, K. Kalantar-Zadeh, A. Kis, J. N. Coleman, M. S. Strano, *Nat Nano* **2012**, *7*, 699-712.

[6] V. Nicolosi, M. Chhowalla, M. G. Kanatzidis, M. S. Strano, J. N. Coleman, *Science* **2013**, *340*, 1226419.

[7] B.Aurivillius, *Ark.Kemi* **1949**, *1*, 463-471

[8] J. L. Hutchison, J. S. Anderson, C. N. R. Rao, *Proc. R. Soc. Lond. A.* **1977**, *355*, 301-312.

[9] C. N. R. Rao, B. Raveau, *Transition Metal Oxides:Structure, Properties, and Synthesis of Ceramic Oxides, Wiley-VCH, Weinheim* **1998**.

[10] A. Srinivas, D.-W. Kim, K. S. Hong, S. V. Suryanarayana, *Mater. Res. Bull.* **2004**, *39*, 55-61.

[11] X. W. Dong, K. F. Wang, J. G. Wan, J. S. Zhu, J.-M. Liu, *J. App. Phys.* **2008**, *103*, 094101.

[12] A. Srinivas, M. M. Kumar, S. V. Suryanarayana, T. Bhimasankaram, *Mater. Res. Bull.* **1999**, *34*, 989-996.

[13] N. A. Lomanova, V. V. Gusarov, *Inorg. Mater.* **2011**, *47*, 420.

[14] S. Sun, W. Wang, H. Xu, L. Zhou, M. Shang, L. Zhang, *J. Phys. Chem. C* **2008**, *112*, 17835-17843.

[15] T. Sasaki, M. Watanabe, *J. Am. Chem. Soc.* **1998**, *120*, 4682-4689.

[16] J.-Y. Kim, I. Chung, J.-H. Choy, G.-S. Park, *Chem. Mater.* **2001**, *13*, 2759.

[17] V. Chevallier, G. Nihoul, V. Madigou, *J. Solid State Chem.* **2008**, *181*, 439.

Chapter I.4

Effect of Nitrogen Substitution in V_2O_3 on the Metal-Insulator Transition

SUMMARY*

Impact of N-doping on the paramagnetic-antiferromagnetic transition associated with the metal-insulator (M-I) transition of V_2O_3 at 150 K has been studied in bulk samples as well as in nanosheets. The magnetic transition temperature of V_2O_3 is lowered to ~120 K in the N-doped samples. Electrical resistivity data also indicate a similar lowering of the M-I transition temperature. First-principles DFT calculations reveal that anionic (N) substitution and the accompanying oxygen vacancies reduce the energy of high-temperature metallic corundum phase relative to monoclinic one leading to the observed reduction in Nèel temperature. In the electronic structure of N-substituted V_2O_3, a sub-band of 2p states of trivalent anion (N) associated with its strong bond with the vanadium cation appears at the top of the band of O(2p) states, the 3d-states of V being slightly higher in energy. A weak magnetic moment occurs in the monoclinic phase of N-substituted V_2O_3 with O-vacancies, with a moment of −1 μ_B/N localized on vanadium atoms in the vicinity of oxygen vacancies.

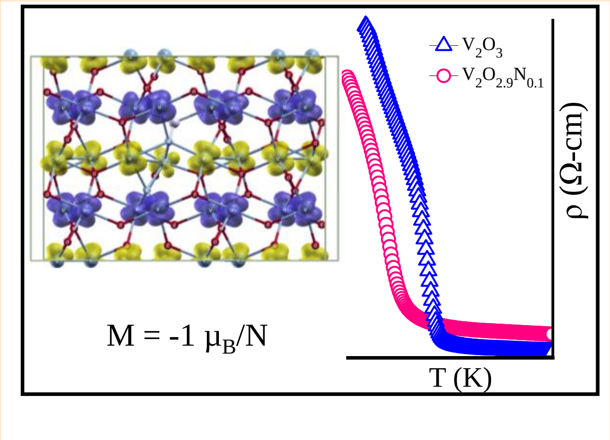

*A paper based on this work has appeared in ChemPhysChem (2015).

1. Introduction

Metal-insulator (M-I) transitions constitute a fascinating aspect of the physics and chemistry of materials. M-I transitions have been found in many metal oxides, sulfides and other materials and the transition in metal oxides has received considerable attention. [1, 2] Of the various metal oxides, the M-I transition in V_2O_3 is noteworthy because of the 10-million fold jump in resistivity that occurs sharply around 150 K. [1, 2] The transition is accompanied by a change in crystal structure (corundum-monoclinic) and magnetic properties. The insulating phase is antiferromagnetic while the metallic phase is paramagnetic. Pressure suppresses the transition rendering the material metallic down to the lower temperature.

Substitution of Ti and Cr have marked effect on the transition, with Ti exhibiting a positive pressure effect and Cr exhibiting negative pressure effect. [1, 2] We considered it important to examine the effect of aliovalent anion substitution on the M-I transition of V_2O_3, by doping the oxide with nitrogen, considering that such substitution affects the M-I transition of VO_2. [3] While substitution of N^{3-} in the place of O^{2-} would create anion vacancies, it would also affect the electronic structure of the oxide by means of the N 2p orbitals. We have prepared bulk V_2O_3 substituted with ~10 at% of nitrogen and nanosheets of V_2O_3 substituted with ~6 at% of nitrogen for the purpose. In order to understand the effect of nitrogen substitution on the M-I transition of V_2O_3, we have carried out extensive first-principles calculations.

2. Scope of the present investigations

Metal–insulator transitions (MIT) in transition metal oxides provided unique models for understanding correlation effects associated with the electron-electron interactions. Two of the most interesting and widely studied correlated materials are V_2O_3 and VO_2, which exhibit a metal-to-insulator phase transitions associated with magnetic phase transition. The dramatic changes in resistance accompanying with the MIT also allow for their potential applications in novel electronic devices. V_2O_3 exhibit phase transition from the metallic to insulating (and paramagnetic to antiferromagnetic) state at a transition temperature of 150 K. A lot of efforts have been devoted to tuning the phase transition temperature of V_2O_3 by strain, pressure and cation doping. A recent theoretical calculation predicted that the hole doping was superior to the electron doping for modulating the phase transition. Therefore, the hole doping be an efficient way to decrease the phase transition temperature.[3] We consider anion doping is an effective way to modulating the phase transition of V_2O_3. In this context nitrogen is widely considered to be the most promising p-type dopant due to its similar size to oxygen. In addition to doping, the dimensionality also has phenomenal effect on the magnitude of phase transition and in modulating MIT.[5] We have studied the effect of both anion doping and dimensionality on MIT of V_2O_3. We found significant reduction of T_C on substitution of the oxygen with nitrogen dopant. Accordingly, the current study for the N-doped V_2O_3 system may provide an appropriate platform for the deeper understanding for the relationship between the MIT modulation with hole carriers concentration and dimensionality.

3. Experimental Section

Materials

All the chemicals used for the synthesis are highly pure and purchased from commercial sources. Vanadium (V) oxide (Sigma-Aldrich, 99,6% metal basis), ammonium persulfate (4.5 g, s d fine, 98 %) Ammonia (Chemix Gases Ltd, India, 99.999), Hydrogen (Chemix Gases Ltd, India, 99.9995), High pure nitrogen (Chemix Gases Ltd, India, 99.9995), DI water (Merck Millipore system) are used without any further purification.

Synthesis

Preparation of V_2O_3 nanosheets:

Nitrogen substitution in V_2O_3 was achieved by ammonolysis of V_2O_5. In typical synthesis 100 mg of commercially available V_2O_5 powder was heated at 400 °C in ammonia atmosphere for 2 h and the flow rate of ammonia was kept to be 50 sccm. Pristine V_2O_3 was prepared by heating V_2O_5 at 400 °C for 2 h in hydrogen atmosphere. V_2O_3 nanosheets were prepared from bulk V_2O_5 via chemical route followed by reduction. In a typical synthesis, bulk V_2O_5 powder (100 mg) and ammonium persulfate (4.5 g) were dissolved in de-ionized water. The resulting clear solution was stirred at 55 °C for 2 d and freeze-dried in vacuo overnight using a lyophilizer. This leads to the formation of $(NH_4)_2V_6O_{16}$. The product so obtained was heated at 350 °C at the rate 5 ºC/min for 3 h in a H_2 atmosphere to obtain few-layer nanosheets of V_2O_3. Nitrogen doped V_2O_3 nanosheets were prepared in a similar way by heating $(NH_4)_2V_6O_{16}$ at 400 ºC at the rate 5 ºC/min in NH_3 for 2 h.

Characterization

Powder X-ray diffraction (PXRD) measurements of pristine and N-V_2O_3 samples were carried out with a Bruker D8 Discover diffractometer with Cu-Kα radiation. Cell parameters were obtained by le Bail fitting using *Full prof* programme. The nanosheets were imaged by transmission electron microscopy (TEM) with a JEOL JEM 3010 microscope, fitted with a Gatan CCD camera operating at an accelerating voltage of 300 kV. Atomic force microscope (AFM) imaging in taping mode was carried out with a Bruker Innova instrument. X-ray photoelectron (XP) spectra were recorded in an Omicron Nanotechnology spectrometer with an Mg Kα as X-ray source. Nitrogen content in the nitrogen substituted V_2O_3 was obtained from Thermo Scientific Flash 2000 Elemental Analyzer. Magnetic measurements were carried out with a SQUID VSM, Quantum Design, USA and electrical resistivity measurements were performed in Physical Property Measurement System (PPMS, Quantum Design, USA).

Computation details

Our calculations are based on first-principles density functional theory (DFT) as implemented in QUANTUM ESPRESSO package, [9] with interaction between ionic cores and valence electrons represented using ultrasoft pseudopotentials. [10] We treat spin dependent exchange correlation energy within a generalized gradient approximation of Perdew Burke-Ernzehof (PBE) parameterized form [11] and apply Hubbard U correction to treat on-site correlations of d-electrons of vanadium with U_{eff} = 3.5 eV, generally used for vanadium based systems. [12] We employ plane wave basis truncated with energy cutoffs of 30 Ry and of 180 Ry in representation of wave functions and charge density respectively. Within periodic boundary conditions, suitable supercells of monoclinic and corundum structures of V_2O_3 are used to model desired concentration of anion dopant. We use uniform mesh of 4 x 4 x 6 and 4 x 6 x 6 k-points in sampling integrations over Brillouin zone of corundum and monoclinic structures respectively, and smear the discontinuity in the occupation numbers of electronic states at Fermi level using Fermi-Dirac distribution with smearing width (k_BT) of 0.04 eV. We relax the structure to minimize energy until the Hellman-Feynman forces are less than 0.03 eV/Å in magnitude.

---

*Theoretical calculations presented in this chapter were carried out by the Dr. Summayya Kouser and Prof. Umesh V. Waghmare.

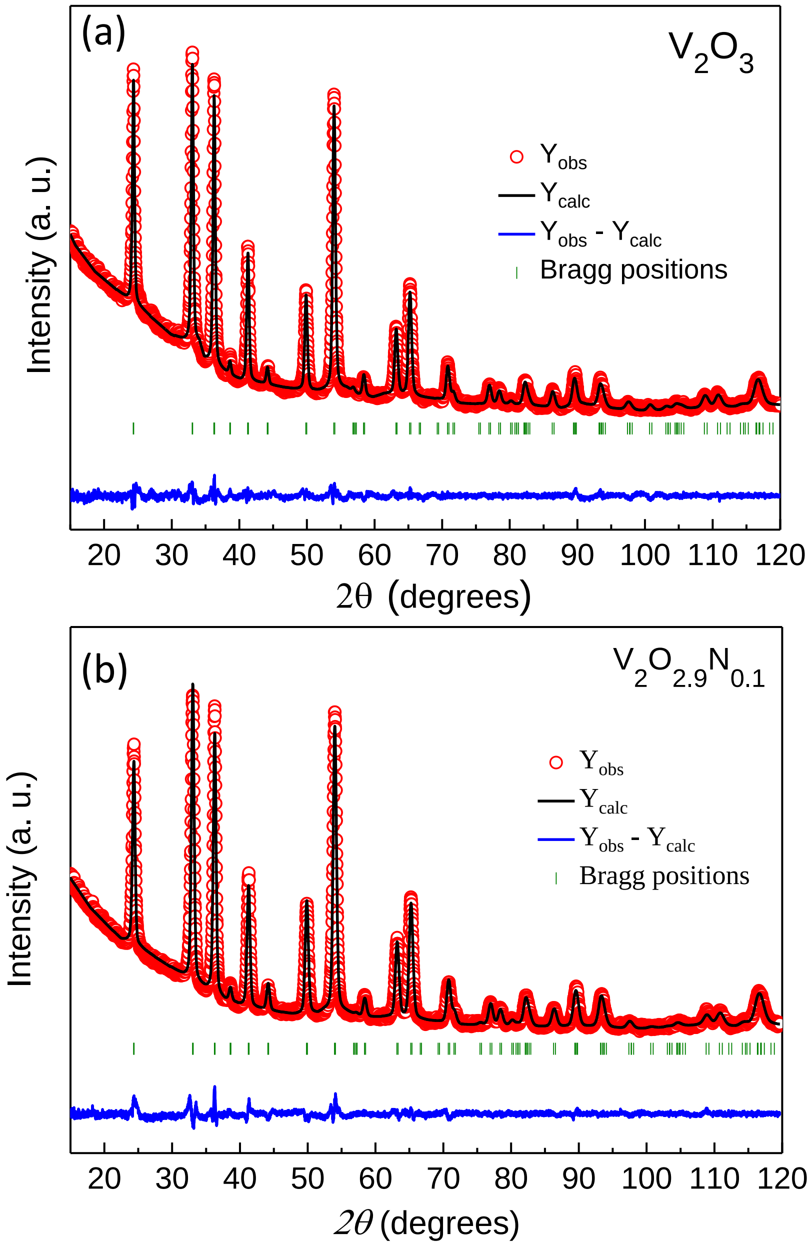

Figure 1. X-ray diffraction patterns of bulk samples of V_2O_3 and $V_2O_{2.9}N_{0.1}$. Rietveld fits are shown.

4. Results and Discussion

Effect of N-doping in bulk V_2O_3

Figure 1, we show the room temperature X-ray diffraction patterns of bulk V_2O_3 and $V_2O_{2.9}N_{0.1}$. Both the patterns correspond to the corundum structure. The lattice parameters of N-doped V_2O_3 are a = 4.9538(2) Å, c = 13.9979(8) Å compared a =

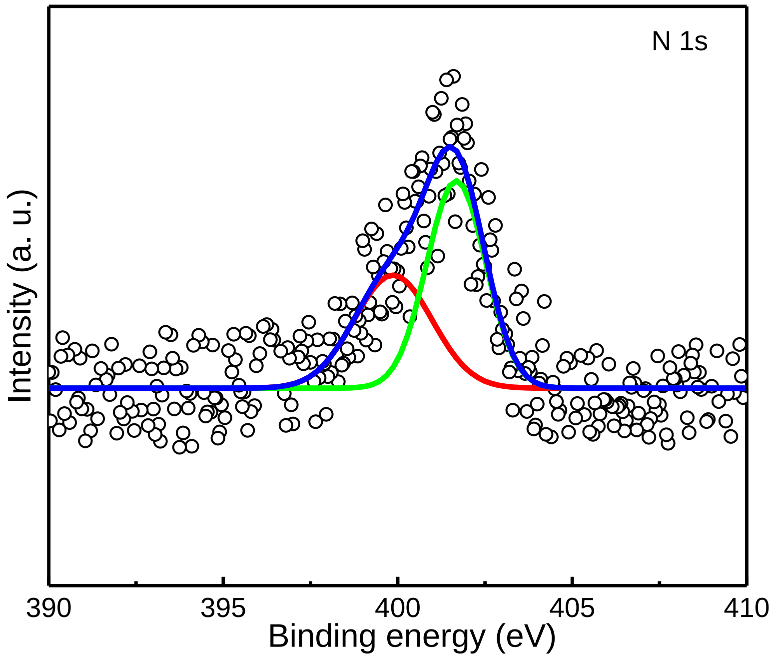

Figure 2. N 1s core-level XP spectrum of N-doped V_2O_3.

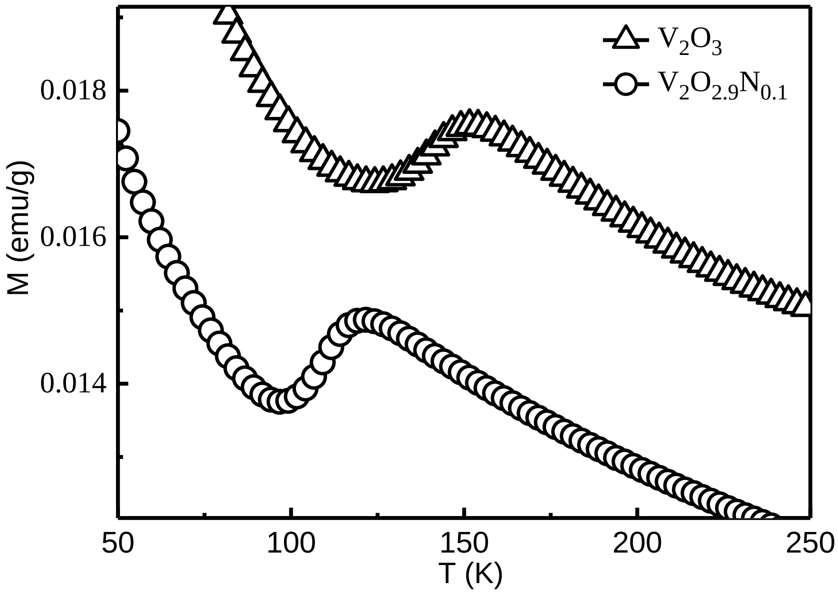

Figure 3. Temperature dependent FC (H=100 Oe) magnetization for bulk samples of V_2O_3 and $V_2O_{2.9}N_{0.1}$.

4.9537(2) Å, *c* = 13.9892(8) Å of pure V_2O_3. The c/a ratio in the N-doped sample is 2.826 compared to 2.824 in pure V_2O_3. An increase in the c/a ratio has indeed been observed near the M-I transition. In **Figure 2**, we show the N (1s) core-level spectrum of the bulk sample of N-doped V_2O_3. The spectrum can deconvoluted to yield signals due to substituted and adsorbed nitrogen species. Taking the proportion of the former, the composition of the doped sample was found to be $V_2O_{2.9}N_{0.1}$ which is also consistent with elemental analysis. In **Figure 3** shows the magnetization data of V_2O_3 and N-V_2O_3. We clearly see the decrease in the antiferromagnetic transition temperature to 120 K from ~150 K in pure V_2O_3. Electrical resistivity measurements on pellets show evidences for a similar change in the M-I transition although the sharp transition found in single crystals is not found (**Figure 4**).

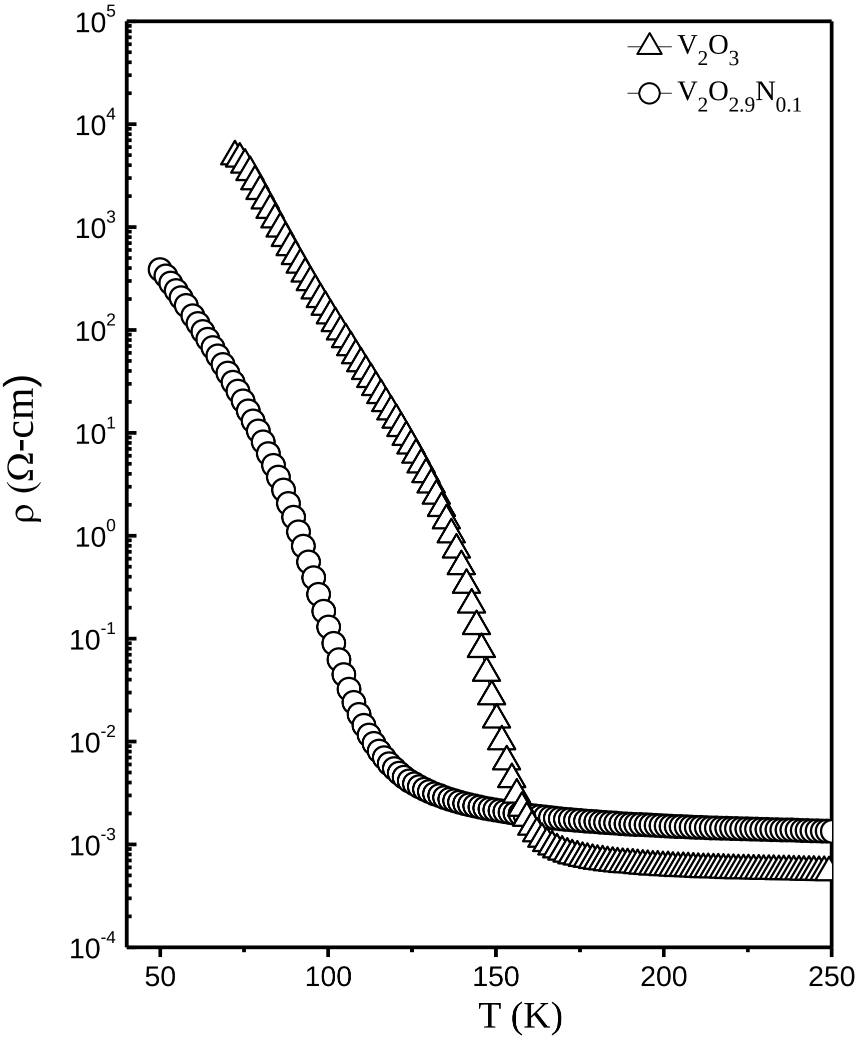

Figure 4. Temperature dependent electrical resistivity of bulk samples of V_2O_3 and $V_2O_{2.9}N_{0.1}$.

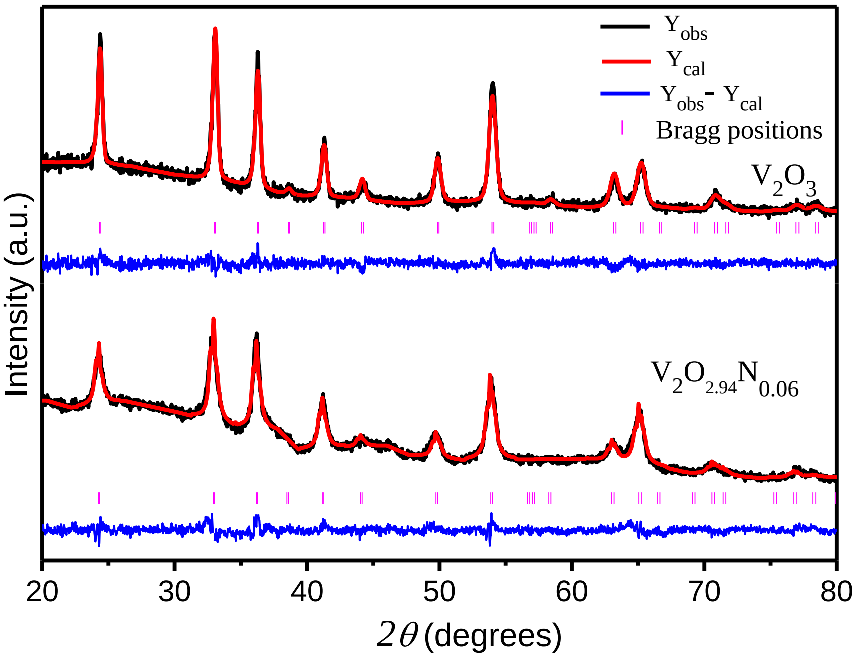

Figure 5. X-ray diffraction patterns of nanosheets samples of V_2O_3 and $V_2O_{2.94}N_{0.06}$. Rietveld fits are shown.

Effect of N-doping in nanosheets of V_2O_3

The nanosheets of V_2O_3 were characterized by X-ray diffraction, transmission electron microscopy and atomic force microscope (Figures 5 and 6). In **Figure 5** we show the XRD patterns of V_2O_3 and N-substituted V_2O_3 nanosheets which are fitted to corundum structure with $R\bar{3}c$ space group. The lattice parameters for the nanosheets of V_2O_3 and N-V_2O_3 are a = 4.9540(1) Å, c = 13.9883(5) Å and a = 4.9628(3) Å, c =

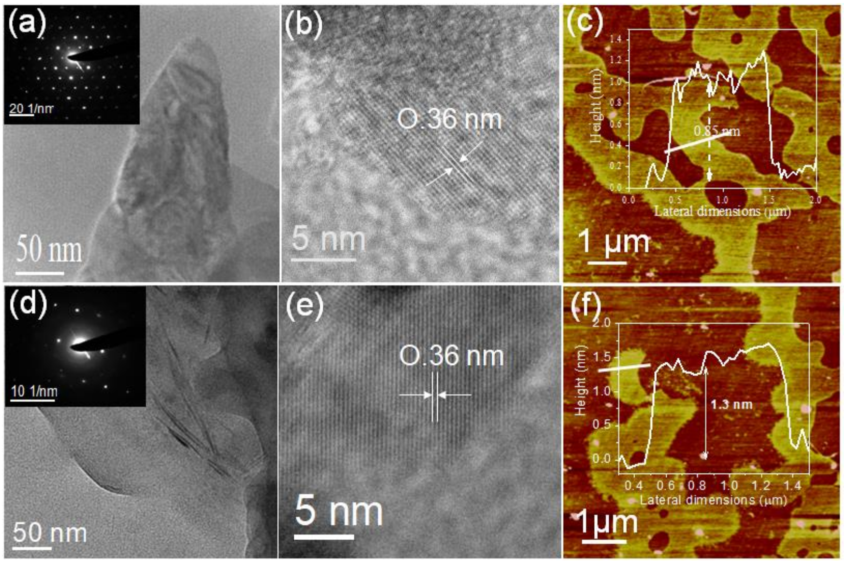

Figure 6. TEM and AFM images of nanosheets of V_2O_3 (a-c) and N-doped V_2O_3 (e-f). Insets of (a and d) show corresponding SAED pattern.

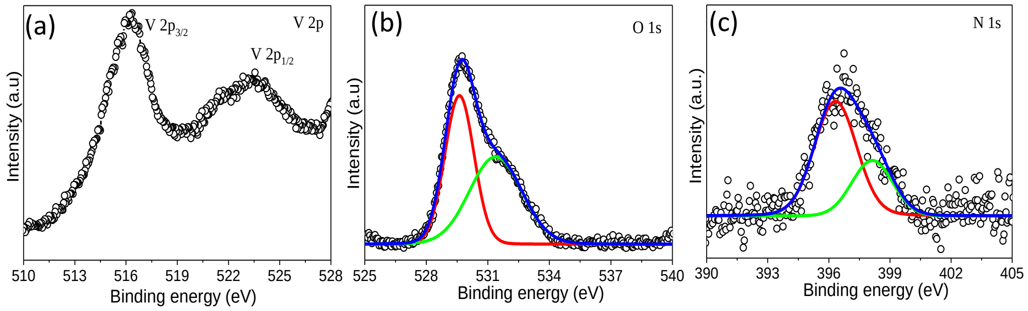

Figure 7. Core-level XP spectra of N 1s, O 1s and V 2p for N-doped V_2O_3 nanosheets.

14.0249(6) Å respectively. We observed broader FWHM peaks compared to the bulk, which confirms the nanostructure. The c/a ratio of the $V_2O_{2.94}N_{0.06}$ (2.826) nanosheets is higher than the V_2O_3 (2.823) nanosheets, similar to the bulk sample. The c/a ratio of N-doped sheets was slightly higher than the undoped nanosheets. TEM images show the single crystalline nature of the V_2O_3 and N-doped V_2O_3 nanosheets (**Figures 6** a-d). The AFM image shows the nanosheets to be ~1 nm thick (Figure 6 c and f).

In **Figure 7** we show core-level XP spectra of V 2p, O 1s and N 1s of N-V_2O_3. N 1s spectrum is deconvoluted to yield two peaks centered at 396.3 and 398.1 eV corresponding to substituted and adsorbed nitrogen respectively. The composition of nitrogen substituted sample was found to be $V_2O_{2.96}N_{0.06}$. The core-level spectrum of O 1s deconvoluted to yield two peaks centered at 529.6 and 531.4 eV corresponding to O bonding to V and surface hydrocarbons respectively. The peak of V 2p centered at 516.2 eV corresponds to V $2p_{3/2}$ which confirms the presence of only V^{3+}.

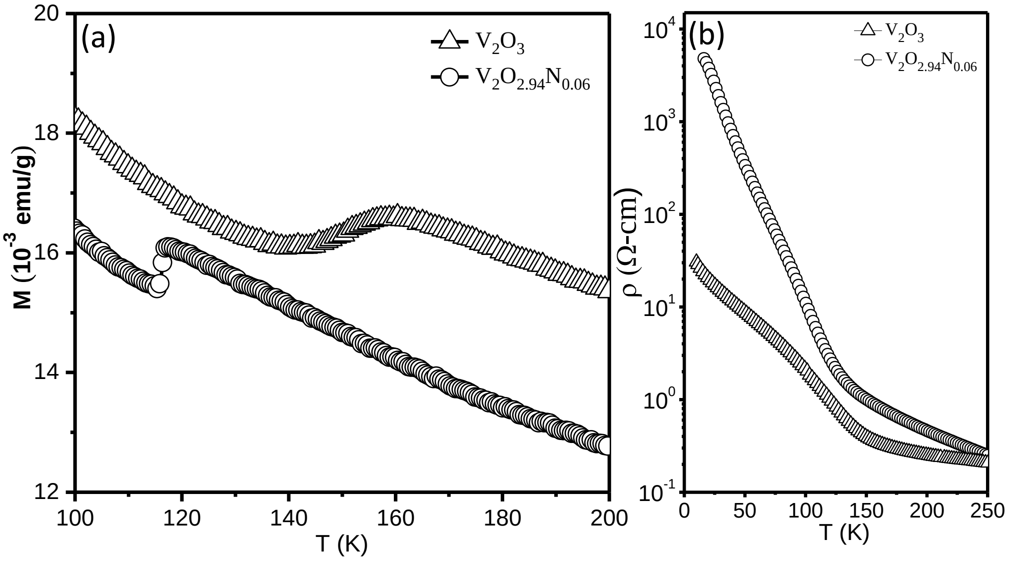

Figure 8. Temperature dependent (a) FC (H=100 Oe) magnetization and (b) electrical resistivity for nanosheets of V_2O_3 and N-doped V_2O_3.

Nanosheets and nanorods of V_2O_3 are reported to show the M-I transition at the same temperature as bulk V_2O_3.[4, 5] We found the M-I transition temperature of V_2O_3 nanosheets is to be close to that of the bulk sample. On N-doping, the magnetic transition temperature decreases to ~120 K (**Figure 8**a). Electrical resistivity measurements show that the M-I transition is shifted to ~120 K in the N-doped sample (Figure 8b).

First principle calculations

First-principles calculations have enabled us to understand how nitrogen-substitution affects the M-I transition of V_2O_3. From the calculations, we estimate the lattice constants of the monoclinic phase (**Figure 9**a) to be a = 7.39 Å, b = 5.17 Å and c = 5.58 Å, and those of corundum phase (Figure 9b) to be $a = b$ = 4.90 Å and c =

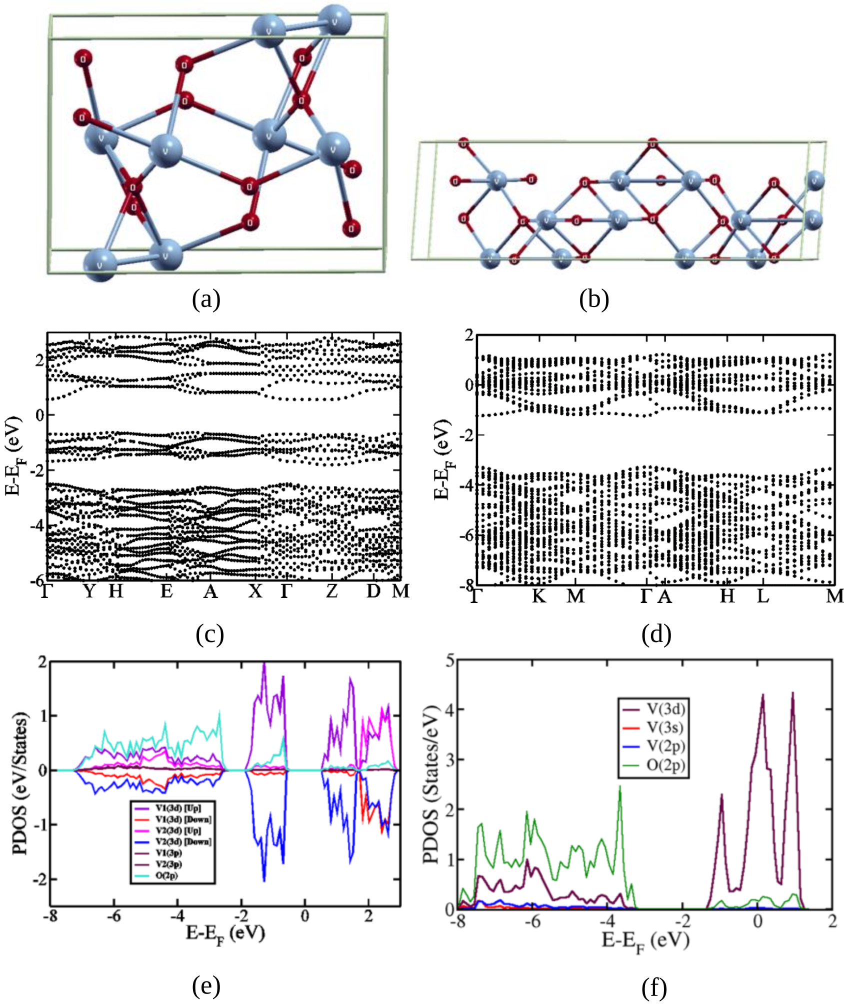
(a) (b)
(c) (d)
(e) (f)

Figure 9. Crystal structure (a), (b), electronic structure (c), (d) and projected density of electronic states (e), (f) of V_2O_3 in antiferromagnetic monoclinic and non-magnetic corundum phases respectively.

14.22 Å, which are within the typical DFT errors [6] with respect to their experimental values. The monoclinic phase of V_2O_3 is found to be relatively more stable than the corundum phase (i.e., $\Delta E = E^m - E^r = -1.57$ eV/f.u.; where E^m and E^r are the total energies of monoclinic and corundum phases respectively).

We have analysed the electronic structure of bulk m-V_2O_3 and r-V_2O_3 and find that m-V_2O_3 exhibits a direct band gap of 1.23 eV, which is probably underestimated, as is typical of DFT, and we expect it to be an insulating material (Figure 9c). On the other hand, r-V_2O_3 is metallic (Figure 9d). Analysis of the projected density of states (PDOS) of m-V_2O_3 reveals that energy bands immediately below the gap are mainly constituted of *d*-orbitals of V and partially of *p*-orbitals of O, while conduction bands (just above the gap) are also contributed by *d*-orbitals of V, suggesting that the electronic gap of m-V_2O_3 arises from correlations, crystal field splitting and antiferromagnetic superexchange (Figure 9e; V1, V2 represent V atoms with opposite spins). In r-V_2O_3, the *d*-orbitals of V lie at the Fermi level with a slight contribution from p-orbitals of O, consistent with its weaker stability according to Stoner's criterion (Figure 9f).

In order to understand the observed reduction in the Nèel temperature upon N-substitution in V_2O_3, we have studied three different compositions in both the monoclinic and corundum structures; (i) N substituted V_2O_3 with oxygen vacancy ($V_2O_{3-x}N_y$; 3y = 2x), (ii) N-substituted V_2O_3 ($V_2O_{3-x}N_y$; x = y), and (iii) O vacancy in V_2O_3 (V_2O_{3-x}; y = 0). The formation energy (E_f) of a substitution or vacancy defect is calculated using

$$E_f = E_{V_2O_{3-x}N_y} - E_{V_2O_3} + x.E_O + y.E_N$$

where E_α ($\alpha = V_2O_{3-x}N_y$, V_2O_3) is the total energy of the corresponding system and E_β (β = N, O) is the energy of the corresponding isolated atom. To relate our results with the experiment, we have considered a 2 x 2 x 1 periodic supercell of monoclinic phase containing 80 atoms and of corundum phase containing 120 atoms. Substitution of N in V_2O_3 would be accompanied by oxygen vacancies to maintain charge neutrality. To simulate $V_2O_{3-x}N_y$, we have substituted three O atoms with two N atoms and O-vacancy in the supercell of 80 and 120 atoms of monoclinic and corundum structures respectively. This can be done in many ways or configurations. For simplicity and based on our earlier work, [7] we have substituted them bonded to the same V atom amounting to 3.75 at% concentration in monoclinic phase and 2.50 at% in corundum

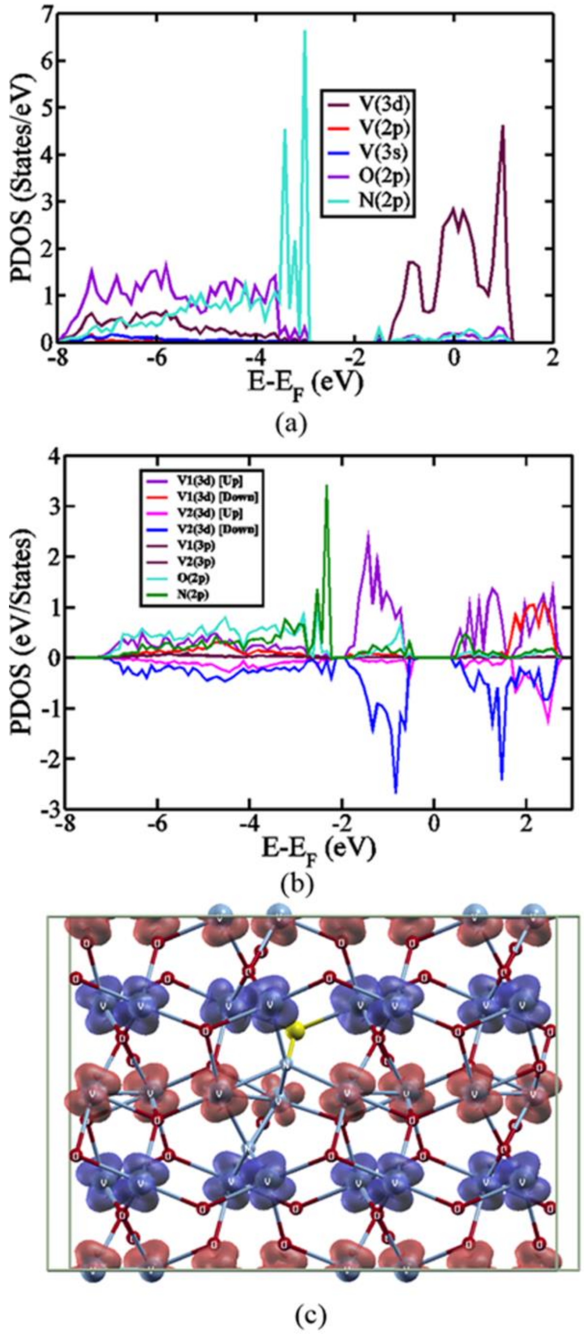

Figure 10. Projected density of electronic states of $V_2O_{3-x}N_y$ in monoclinic and (a) corundum (b) phases and visualization of spin density of m-$V_2O_{3-x}N_y$ (c) showing localized magnetic moment in the vicinity of O-vacancy (represented by pseudo yellow atom).

phase. We find that the formation energy of $V_2O_{3-x}N_y$ is quite high (~6.7 - 8 eV/2N/vacancy) and this is mainly due to the presence of oxygen vacancy (since E_f for V_2O_{3-x} is ~9.22 − 9.31) [**Table 1**]. Our results show that substitution of N in V_2O_3 with O-vacancy is relatively easier in the corundum phase (ΔE_f = -2.51 eV/2N, where $\Delta E_f = E_f^{V_2O_{3-x}N_y}$-$E_f^{V_2O_{3-x}}$) than in monoclinic phase (ΔE_f = -0.64 eV/2N). Hence, N substitution and the accompanying oxygen vacancies reduce the energy of the high-

Table 1. Comparison of formation energies of defects in monoclinic and corundum phases of V_2O_3.

Units of E_f	Formation Energy (E_f)		
	System	Monoclinic	Corundum
eV/2N/vacancy	$V_2O_{3-x}N_y$	8.67	6.72
eV/N	$V_2O_{3-x}N_x$	-0.07	-1.37
eV/vacancy	V_2O_{3-x}	9.31	9.22

temperature metallic phase relative to the insulating phase, leading to a reduction in the Nèel temperature as observed experimentally.

We shall now examine bond valence analysis and understand the structural origin of changes in the electronic structure upon inclusion of N-substitution or O-vacancies. From bond valence analysis, we find that V-O and V-V bond lengths of the V atom attached to the N impurity in m/r-$V_2O_{3-x}N_y$ are approximately 3.5-5% longer and 3.8-4.3% shorter respectively than those in the corresponding structures of pristine V_2O_3 (**Table 2**). The V-N bond length is shorter by ~1-5% (~1.90-1.98 Å) compared to V-N complexes reported in the literature. [8] A slight reduction (0.1 Å) in *a* and a slight increase in *c* (by 0.1 Å) of the corundum structure with N-substitution seen in our calculations are consistent within the DFT errors with the experimental observations, and are understandable from shortening of V-N bonds and elongation of V-O bonds. The overall structural change in V_2O_3 on substitution of N accompanying O-vacancy involves a drastic decrease in the effective coordination number (ECN) ~4.85 for V attached to N impurity and negligible change in the ECN of V(~5.82) in

Table 2. Comparison of Structural parameters of $V_2O_{3-x}N_y$ in monoclinic and corundum phases with its corresponding pristine V_2O_3 structures.

Structural Parameter (Å)	Monoclinic		Corundum	
	V_2O_3	$V_2O_{3-x}N_y$	V_2O_3	$V_2O_{3-x}N_y$
a	7.39	7.42	4.90	4.89
b	5.17	5.16	4.90	4.89
c	5..58	5.57	14.22	14.23
d_{V-V}	2.82	2.70	2.61	2.51
d_{V-O}	1.97	2.07	2.05	2.00, 2.14
d_{V-N}	-	1.91, 1.98	-	1.90, 1.95

the vicinity of site of substitution. Thus, the short V-N bonds constitute the structural origin of the significant changes in the electronic and magnetic properties presented below.

We now examine the effects of anion substitution on the electronic structure of V_2O_3. For r-$V_2O_{3-x}N_y$, the system remains metallic, the N(2*p*) levels lie below the Fermi level around ~-3 eV and we see a dip in electronic density of states at the Fermi level, contributing to its enhanced stability (**Figure 10**a). In m-$V_2O_{3-x}N_y$, though a sub-band of 2*p* states of trivalent anion (N) associated with its strong bond with the cation (V) appears at the top of 2*p* states of O, it still lies below the sub-band of 3*d* states of V, revealing that the band gap is between the split d-orbitals. However, we see a significant change in band gap ($E_g^{m-V_2O_{3-x}N_y}$ = 0.83 eV, $E_g^{m-V_2O_3}$ = 1.23 eV) as a result of strong hybridization of N(2*p*) orbitals with the V(3*d*) orbitals, evident from its relatively narrow sub-band of N(2*p*) states (Figure 10b). N-substitution accompanying oxygen vacancy in m-V_2O_3 leads to a localized magnetic moment of −1 μ_B/N on vanadium atoms that would be bonded to the vacant site (shown by a pseudo white atom) (Figure 10c). Though the absolute magnetic moment remains same, the analysis of Löwdin charges reveals that the population of the spin-down electrons on V atoms in the vicinity of oxygen vacancies is relatively higher than that of the spin-up electrons leading to an overall magnetic moment of -1 μ_B/N.

5. Conclusions

In conclusion, the metal-insulator transition of V_2O_3 at 150 K is markedly affected by nitrogen-substitution, the decrease in the transition temperature being ~30 degree even with a modest substitution of nitrogen. Results of our first-principles density functional theory-based calculations on nitrogen substituted V_2O_3 reveal that N substitution in V_2O_3 makes the high temperature metallic corundum phase lower in energy, leading to the observed reduction in Nèel temperature. This is also indicated in the electronic structure of r-$V_2O_{3-x}N_y$, where we see a dip in electronic density of states at the Fermi level and a wider sub-band of N(2*p*) states. In the monoclinic phase (m-$V_2O_{3-x}N_y$) too, N(2*p*) sub-band states of the less electronegative atom lies above the O(2*p*) states, but below the V(3*d*) states. Hybridization between N(2*p*) with the *d*-

states of V results in the reduction of the *d*-*d* gap and a local magnetic moment of -1 μ_B/N on V atoms bonded to the N sites and in the vicinity of O-vacancies.

6. References

[1] N. F. Mott, *Metal-Insulator Transitions, Taylor & Francis*, London, **1990**.

[2] P. P. Edwards, T. V. Ramakrishnan and C. N. R. Rao, *J. Phys. Chem*. **1995,** *99*, 5228-5239.

[3] W. Zhang, K. Wang, L. Fan, L. Liu, P. Guo, C. Zou, J. Wang, H. Qian, K. Ibrahim, W. Yan, F. Xu and Z. Wu, *J. Phys. Chem. C* **2014**. *118*, 12837-12844.

[4] A. C. Santulli, W. Xu, J. B. Parise, L. Wu, M. C. Aronson, F. Zhang, C.-Y. Nam, C. T. Black, A. L. Tiano and S. S. Wong, *Phys. Chem. Chem. Phys.* **2009**, *11*, 3718-3726.

[5] S.-W. G. Xu, X. Wang, X. Chen and L. Jiao, *RSC Adv*. **2015**, *5*, 17782-17785.

[6] P. D. Dernier and M. Marezio, *Phys. Rev. B* **1970**, *2*, 3771.

[7] J. Pan, U. V. Waghmare, N. Kumar, C. O. Ehi-Eromosele, and C. N. R. Rao, *ChemPhysChem* **2015**, *16*, 1502.

[8] A. Butler, Coord. *Chem. Rev*. **1999**, *187*, 17.

[9] P. Giannozzi, S. Baroni, N. Bonini, M. Calandra, R. Car, C. Cavazzoni, D. Ceresoli, G. L.Chiarotti, M. Cococcioni, I. Dabo, A. Dal Corso, S. de Gironcoli, S. Fabris, G. Fratesi, R. Gebauer, U. Gerstmann, C. Gougoussis, A. Kokalj, M. Lazzeri, L. Martin-Samos, N. Marzari, F. Mauri, R. Mazzarello, S. Paolini, A. Pasquarello, L. Paulatto, C. Sbraccia, S. Scandolo, G. Sclauzero, A. P. Seitsonen, A. Smogunov, P. Umari, and R. M. Wentzcovitch, *J. Phys. Condens. Matter* **2009**, *21*, 395502.

[10] D. Vanderbilt, *Phys. Rev. B* **1990**, *41*, 7892.

[11] J. P. Perdew, K. Burke, and M. Ernzerhof, *Phys. Rev. Lett.* **1996**, *77*, 3865.

[12] R. J. O. Mossanek and M. Abbate, *Phys. Rev. B* **2007**, *75*, 115110.

Part II

Nanosheets of Borocarbonitrides and Other Metal Nitrides

Chapter II.1

Nanosheets of 2D-Borocarbonitrides: Synthesis, Characterization and Selected Properties

SUMMARY*

We have prepared borocarbonitrides of various compositions with extended sheet morphology, by the reaction of few-layer graphene and characterized them in detail. Considering the important role played by surface functionalities, we have obtained quantitative estimates of the functionalities on graphene, BN and borocarbonitrides, by employing fluorescence labeling. Thus, the surface concentrations of carbonyl, carboxylic and hydroxyl groups on the graphene surface are 2.31×10^{20}, 28.17×10^{20} and 0.08×10^{20} per gram respectively. Borocarbonitrides contain amine and oxygen functionalities, with composition dependent concentrations. Supercapacitor performance and ORR activity of the borocarbonitrides are presented along with their surface areas. Borocarbonitride nanosheets reinforced polymer nanocomposites show enhanced mechanical and thermal properties.

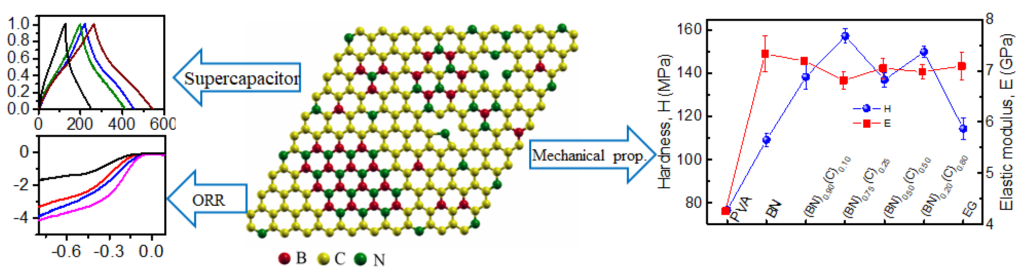

*Papers based on this work have appeared in Chemical Physics Letters (2016 & 2017).

1. Introduction

Graphene, the two-dimensional sheet of sp^2 carbons, has received great attention due to its novel properties with potential applications in nanoelectronics and energy storage.[1-3] Electronic devices based on graphene are of interest due to its high carrier mobility and ballistic transport properties.[4, 5] Field effect transistors (FETs) as well as photoresponse properties of suitably doped graphene have been reported.[6, 7] Chemical doping of graphene with nitrogen and other hetero atoms alters the electronic and electrochemical properties[8, 9] and theoretical calculations show that random doping of graphene with boron or nitrogen opens a small gap in the Dirac points.[10] Graphene sheets containing B and N over a wide compositional range results in borocarbonitrides, which are new materials with interesting electronic properties with applications in supercapacitors,[8, 11-13] oxygen reduction reaction (ORR) [14, 15] and other areas.[16]

There are several reports on B, N-doped graphene with different doping levels[8, 17] and B, N-doped graphene films have been generated using a thermal catalytic CVD method.[8, 18-23] Bulk borocarbonitrides, $B_xC_yN_z$, of different compositions have been prepared starting with mixtures of activated carbon, boric acid and urea.[24] Graphene with nitrogen (4.5 at.%) and boron (3 at.%) has been prepared using melamine diborate as the precursor.[25] Covalently cross-linked boron nitride and graphene with composition-dependent surface and electrical properties have been prepared recently.[26] Single and few-layer borocarbonitrides, $B_xC_yN_z$, containing hybridized bonds of B, C and N are reported to exhibit electronic and optical properties distinct from those of graphene and BN.[24, 27] In the light of this observation, we have sought to prepare borocarbonitrides by the reaction of graphene sheets with the precursor of nitrogen and boron and study their properties.

Graphene and related two-dimensional materials which possess a variety of oxygen containing functional groups on their surfaces. Similarly, the surface of boron nitride (BN) generally contains amine groups. Surfaces of borocarbonitrides ($B_xC_yN_z$, BCN for short) can contain surface functional groups common to both of graphene and BN, since the materials comprise domains of both these materials. In many recent studies, surface characterization of materials is generally limited to reporting the surface area and qualitative identification of the functional groups present on the surface, the latter being enabled by X-ray photoelectron spectroscopy (XPS). It is however desirable to have quantitative surface characterization of materials wherein the concentrations of the different surface species are specified. This is relevant since the presence of functional groups indeed affect the properties of the materials when used in various applications. A typical example would be the use of carbon materials in supercapacitors and energy devices. We have carried out the experiments to characterize surfaces of graphene, BN and BCN quantitatively by employing fluorescence spectroscopy.[28] In this method, the molecular label is covalently attached to the substrate as shown earlier.[28, 29] This is done by chemical labeling using fluorescent probes, wherein fluorescence labeling of surface species (FLOSS), helps to detect and quantify the surface functional groups as low as 10^9 groups/cm^2.[28] This technique has been used successfully to quantify surface functionalities in carbon nanotubes,[29, 30] carbon nanofibers,[31, 32] polymer surfaces[33, 34] and epoxy functionalised surfaces.[35, 36] The detection limit of FLOSS is much lower than that of XPS and other spectroscopic techniques.[36, 37]

A key attribute of nanomaterials is the substantial surface-to-volume ratio (STVR) they offer. The resultant alteration in the chemical and physical properties, as compared to the respective bulk properties, are not only scientifically interesting but can be exploited for engineering new materials and devices. One such class of materials are the polymer matrix composites (PMCs) reinforced with nanoparticles.[38] Because of their high STVR, even a small addition (typically less than 1 wt.%) of the nanofillers to the polymer matrix can result in a pronounced enhancement in latter's mechanical properties. In contrast, the traditional composites, wherein micro- or macro-scale reinforcement phases are used, would require as much as 60 vol.% reinforcements to attain a similar enhancement in performance.[39-41]

The substantial benefits of nanocomposites can only be accrued, however, only when the nanofillers are dispersed homogeneously and a strong interfacial interaction at the molecular level between filler and polymer surfaces occurs.[42, 43] For the latter, surface functionalization of the nanofillers, such that the functional groups and their reactivity are tailor-made for the specific polymer matrix under consideration, is absolutely essential.[44-45] While this can be achieved through judicious chemical means, dispersing the nanofillers uniformly in the matrix is a formidable challenge.

Here, the major advantage of the nanofillers, namely STVR, is also the main impediment as agglomeration of the nanoparticles, so as to minimize their surface area, is a common occurrence. Consequently, it is often difficult to disperse more than one vol.% of nanofillers in a polymer matrix.

It was successfully demonstrated that simultaneous addition of more than one type of nanofiller, especially those with differing dimensionality such as one-dimensional nanotubes to two-dimensional nanosheets (e.g., graphene), can lead to extraordinary synergy in enhancing the mechanical properties.[46] It was demonstrated that such synergy could also be exploited for preserving the excellent functional properties such as gas absorption characteristics of porous metal-organic frameworks (MOFs) while enhancing their mechanical properties by covalently linking them to graphene.[47] In the present work, we examine whether such synergistic benefits can also obtain in borocarbonitride, $(BN)_x(C)_{1-x}$, (BCN) nanosheet reinforced poly(vinyl alcohol), PVA, nanocomposites.

Nanosheets of BCN have attracted recent attention due to their novel properties, which can be tuned by varying the composition, i.e., boron nitride (BN)-to-carbon ratio.[48, 49] Moreover, they offer a diverse set of surface functionalities, domain structures, and a high degree of chemical heterogeneity, which make them considerably more interesting than either graphene or BN. Keeping this in view, some studies have explored the potential applications of BCN nanosheets in batteries, supercapacitors, gas adsorption, and catalysis.[50] Given the exceptional mechanical properties of either graphene and BN reinforced polymer nanocomposites,[51] and the possibility of synergy, we expect that BCN nanosheet polymer nanocomposites to exhibit excellent mechanical and thermal properties, particularly in view of the interesting chemical environments the BCN nanosheets offer. This possibility was investigated in this study through detailed characterization of thermal and mechanical properties.

2. Scope of the present investigations

Borocarbonitrides constitutes a new class of 2D materials with many fascinating properties. The composition of BCN can be tuned from gapless graphene to insulating boron nitride. The semiconducting properties of BCN make them more interesting than its analogues. Starting with graphene rather than other sources of carbon is expected to be advantageous in forming borocarbonitride nanosheets. We have successfully prepared varying compositions of $B_xC_yN_z$ by the reaction with graphene and characterized them by using various spectroscopic and microscopic techniques. The properties of these materials not only depends the chemical composition and surface area but also largely affected by surface functional groups. One such example is applications of nanotubes in electronics and nanocomposites, require knowledge functionalities on the surface. Precise identification and quantification of surfaces functional groups is very important to understand the properties. None of the conventionally used spectroscopy methods provide selectivity in identification together with sensitivity in quantification due to their detection limits. Fluorescence labeling of surface species to identify and quantify provides a solution using selective fluorescent probes. The high selectivity of covalent attachment combined with the sensitivity of the fluorescence measurements, allowed us reliably determine concentrations of the functionalities. We have investigated the surface functionalities of graphene, borocarbonitides of various compositions and boron nitride by FLOSS. In order to show possible relations between surface functionalities and specific properties with potential applications. We have measured supercapacitor characteristics as well as oxygen reduction reaction activity of borocarbonitrides of different compositions along with graphene.[52, 53]

Polymer nanocomposites reinforced with nanofiller with very low loading created new paradigm to traditional composite material with significant amount reinforcement phase. In the verge of searching suitable filler material to enhance the mechanical properties for the various applications carbon-based nanostructures such as carbon nanotubes and graphene emerged as potential filler materials. Homogeneous molecular level dispersion of nanofiller in the matrix can significantly stiffen the mechanical properties via strong interaction at the interface. The surface functional groups on the filler material play a crucial role in the interaction between polymer and nanofiller via chemical bonding or dipole interactions to stiffen the PMCs. Hence the functionalized graphene emerged as strong filler material for PMCs. The surface functionalities and the domain structure of BCN make it more interesting filler material than graphene and BN due to high chemical heterogeneity. Considering the recent results and exceptional mechanical properties based on graphene, carbon nanotubes polymer composites, we except that borocarbonitrides nanosheets dispersion in polymer matrix with lower filler content would result in the excellent mechanical, thermal and barrier properties in very economically viable nanocomposites.

3. Experimental Section

Materials

All the chemicals were purchased from commercial sources and were of high purity used directly without further purification. Natural graphite (Alfa Aesar, 99%), sulfuric acid (SD Fine 98%), H_2O_2 (Merck), boric acid (Merck), urea (SD Fine), KOH (SD Fine Chem Ltd, India, 85.5 %) and water (Millipore).

Synthesis

Preparation of graphene oxide, and exfoliated graphene:

Graphene oxide was prepared by the modified Hummers method[54, 55] using natural graphite flakes. In order to get few layered graphene oxide (GO), the suspension obtained was lyophilized. Reduced graphene oxide was obtained by treating GO with hydrazine hydrate at 70 °C. Exfoliated graphene (EG) was obtained by thermal exfoliation of GO at 1050 °C in N_2 atmosphere.[56] Reduced graphene oxide was obtained by treating GO with hydrazine hydrate at 70 °C.

Preparation borocarbonitride and boron nitride nanosheets:

Scheme 1 shows the pictorial illustration of the BCN synthesis. In a typical synthesis EG was reacted with varying proportions of urea and boric acid[24] to obtain $B_xC_yN_z$ samples of different compositions. The molar ratio of boric acid and urea and amount of EG are given in **Table 1**. In a typical synthesis, EG was dispersed in 20 ml double distilled water and the required amount of boric acid and urea was added to the dispersion. The mixture was sonicated for 30 min in an ultrasonication bath (Elmasonic, T1H5, 45 KHz) to get uniform dispersion. Water was evaporated under continuous stirring at 80 °C till the slurry get solidifies. As obtained slurry was transferred in to 15 ml alumina boat and heated in a tubular furnace at 900 °C for 5 h

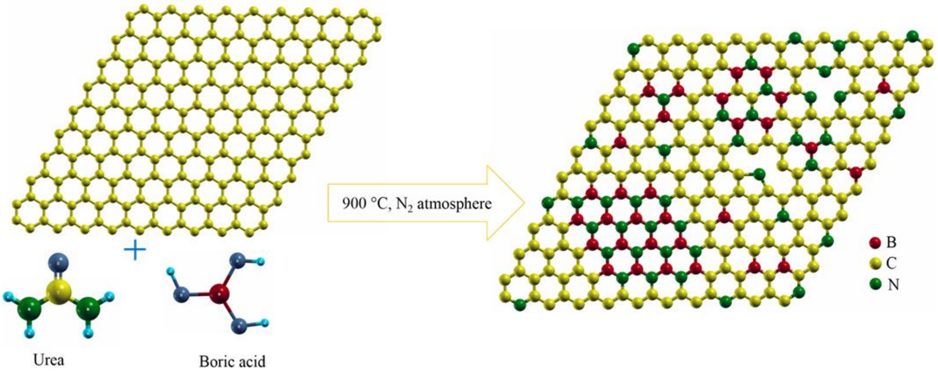

Scheme 1. Schematic representation of synthesis of BCN using graphene with boric acid and urea.

under high pure N_2 atmosphere. Heating and cooling rate maintained for 3 °C/min and N_2 flow is 15 ml/min. Four different compositions were obtained by varying amount of boric acid and urea and were characterized using various techniques. As obtained samples were used for further characterization and fluorescence labeling. BN was prepared in a similar way using boric acid and urea.[57]

Characterization

Powder X-ray diffraction patterns were collected using a Bruker D8 Discover diffractometer using Cu-Kα radiation with accelerating voltage 40 kV and current 30 mA. Gravimetric compositions of $B_xC_yN_z$ samples were determined by thermogravimetric analyses carried out in an oxygen atmosphere with a Metler Toledo TGA-850 TG analyzer. Raman spectra were recorded at different spots in the backscattering geometry using a 632 nm HeNe laser with a Jobin Yvon LabRam HR 800 spectrometer. Fourier transform infrared spectra (FTIR) were recorded in a Bruker FTIR spectrometer in KBr mode. Elemental mapping of B, N and C using energy dispersive X-ray spectroscopy (EDX) and morphology of nanosheets were obtained using scanning electron microscopy Nova NanoSEM 600 FESEM (FEI Company). Elemental compositions and bonding nature of the samples were determined by X-ray photoelectron spectroscopy (XPS) using a Omicron nanotechnology spectrometer, with a monochromatic Mg-K_α as X-ray source (E=1253.6 eV). Elemental analysis was carried out with a Thermo Scientific™ FLASH 2000 Series CHNS Analyser. Atomic force microscope (AFM) images were obtained on Si substrates in tapping mode using Bruker Innova instrument. Transmission electron microscopy (TEM) images were recorded with a FEI Tecnai G^2 S-Twin operated microscope at an accelerating voltage of 200 kV, fitted with a Gatan CCD camera. High-resolution TEM images and electron energy loss spectra (EELS) were recorded using Titan (cube) FEI aberration-corrected transmission electron microscope with an accelerating voltage 300 kV. ^{13}C and ^{11}B solid-state MAS NMR spectra were collected with a Bruker Avance III HD 400 MHz spectrometer. N_2 sorption isotherms at 77 K were recorded using a Quantachrome Quandasord-*SI* analyzer. Prior to measurements, the samples were heated at 120 °C under vacuum for 12 h. Optical spectra were recorded on Perkin–Elmer, Lambda 750 UV-Vis spectrometer from 800-200 nm wavelength range. Photoluminescence (PL) spectra were recorded with a Fluorolog-3 spectrophotometer fitted with Horiba Jobin Yvon Xe lamp light source. Differential scanning calorimetry (DSC) measurements were carried out in TA instrument in N_2 atmosphere with the heating and cooling rate of 3 °C/min.

Quantification of surface groups using fluorescent probes

We have used fluorescent labeling to systematically quantify the various surface groups present on graphene, boron nitride and borocarbonitrides. The fluorescent probes were chemically attached to the surface functional groups of the above mentioned materials as described in the literature.[29] In the case of graphene we have used the dansyl hydrazine for carbonyl group labeling and 1-(bromoacetyl) pyrene for carboxylic and hydroxyl groups by changing reaction conditions for the two. The amine group on the surface of BN was labeled with NHS-Cy5 which is specific to the group.

In BCN where both the domains of BN and graphene would be present, we expect all the functional groups named above to be present. We have therefore, used all the labeling agents for BCN. Calibration curves of the dyes were obtained by measuring the fluorescence intensities of dye solutions with known varying concentrations. The concentrations of the functional groups were determined by measuring the fluorescence intensity of the particular dye solution before contact with the sample and after the fluorescence labeling reaction with the labeled sample removed from the solution. The decrease in the fluorescence intensity is then related to concentration of the particular functional group using calibration curve. One of the major problems in fluorescent labeling is the possibility of physical adsorption of the dye molecules on the surface without covalently linking to the surface groups. In order to validate our results and to know physisorption we have carried out series of control experiments.

Fluorescence labeling of the carbonyl groups using dansyl hydrazine (DH):

To a 3 mg of sample under study, a 10 mL 0.68 mM solution of DH in methanol, 1.8 mL of 0.1M hydrochloric acid solution in methanol was added. The resulting solution was stirred in dark at room temperature for 62 h. After the completion of reaction, the resulting solutions were centrifuged and supernatant was transferred to a flask. The remaining sample was washed several times with fresh methanol to remove any physisorbed dye molecules. The washings were transferred to the same flask and diluted to known volume to record the PL. A control experiment was carried out without the sample under same conditions. Also, physisorption experiments were carried out without reagent.[29] The above reaction is specific to the carbonyl group and not for the carboxylic group. Direct reaction of carboxylic acids with amine derivatives like hydrazines is difficult as the hydrazines with their high pKa values deprotonate the carboxylic acid to form the carboxylate ion, which cannot undergo substitution reactions.

Fluorescence tagging of carboxyl group using 1-(bromoacetyl) pyrene:

Chemical tagging of carboxylic groups using 1-bromoacetyl pyrene has been carried out using standard procedure.[58] To a 2 mg of sample under study, a 2 mL 1.35 mM solution of 1-(bromoacetyl)pyrene in DMF, 0.54 mg of K_2CO_3 and 0.45 mg of KI were added. The resulting solution was stirred in dark at 50 °C for 12 h. After the completion of reaction, the resulting solutions were centrifuged and supernatant was transferred to a flask. The remaining sample was washed several times with fresh DMF to remove any physisorbed dye molecules. The washings were transferred to the same flask and diluted to known volume to record the PL. A control experiment was carried without the sample under same conditions. Also, physisorption experiments were carried out without reagent.

Fluorescence tagging of hydroxyl group using 1-bromoacetyl pyrene:

To a 2 mg of sample under study, a 2 mL 0.412 mM solution of 1-(bromoacetyl)pyrene in DMF, 0.2 mL of triethylamine (TEA) was added. The resulting solution was stirred in dark at room temperature for 10 h. After the completion of reaction, the resulting solutions were centrifuged and supernatant was transferred to a flask. The remaining sample was washed several times with fresh DMF to remove any physisorbed dye molecules. The washings were transferred to the same flask and diluted to known volume to record the PL. A control experiment was carried without the sample under same condition. Also, physisorption experiments were carried out without reagent.

Fluorescence labeling of the amine group on surfaces of BN and BCN using NHS-Cy5:

Fluorescence labeling of amine groups was carried out as described elsewhere.[59] To a 1 mg sample of the material under study, 3 mL of DMSO, a 5µL of 1.382 mM of NHS-Cy5 dye solution and 50 µL of triethylamine (TEA) were added. The resulting solution was stirred in dark at room temperature for 6 h. After the completion of reaction the resulting solutions were centrifuged and supernatant was transferred to a flask. The remaining sample was washed several times with fresh DMSO to remove any physisorbed dye molecules. The washings were transferred to the same flask and diluted to known volume to record the PL. A control experiment was carried without the sample under the same conditions. Physisorption experiments were carried out without any reagent.

Detailed steps for the calculations of surface functional groups:

The PL data for all the samples were plotted against the control. The decrease in fluorescence intensity for the samples were noted at the wavelength where the calibration curve had been derived. From the calibration plot, we determined the concentration of the reacted fluorescent probes. The concentration obtained was multiplied by the Avogadro number and divided by the amount of sample taken. This gives the number of groups on the surface of the material per gram. By dividing this number by the surface area of the sample (in cm^2/g) we get the number of groups per unit surface area of the material.

Preparation of BCN nanosheets reinforced PVA nanocomposites

Scheme 2 gives a representation of the steps involved in the preparation of polymer nanocomposites. First, 500 mg of PVA with a molecular weight of 14000 Da was dissolved in 40 mL of water at 70 °C. Then, the required amount of BCN, which was

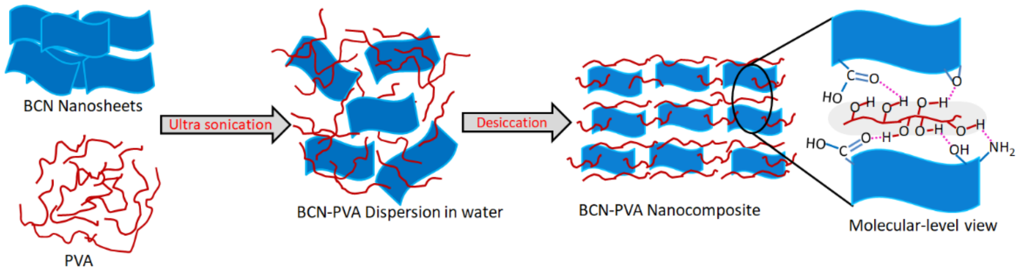

Scheme 2. Schematic illustration of BCN-PVA nanocomposite preparation and the possible molecular-level interaction between them.

dispersed in water-ethanol mixture of ~ 1.5 mL by sonicating for about 900 s, was added to the PVA solution. The resulting solution was further sonicated for 4 to 5 h, while maintaining a temperature of ~ 70 °C, such that the volume of the solution decreases through evaporation to less than 25% of the initial volume. The solution was then poured into a petridish, dried at 55 °C for 72 h, and then was desiccated further for at least 72 h prior to nanoindentation and other measurements. For comparison purposes, pure PVA and PVA reinforced with either EG or BN were also prepared by using identical processing steps. In all composites examined in this study, the amount of filler loading was fixed at 0.2 wt%.

Electrochemical measurements

Supercapacitors:

Supercapacitor measurements were performed on PGSTAT 262A (Techno Science Instruments) electrochemical workstation in 1 M H_2SO_4 aqueous electrolyte solutions under three-electrode assembly with a catalyst coated glassy carbon (GC) electrode as the working electrode with a large-area Pt foil and Ag/AgCl as counter and reference electrodes respectively. The working electrode was fabricated by dispersing 3 mg of sample in 1 mL ethanol-water mixture (1:1) from that 10 µL was drop cast on glassy carbon electrode followed by 10 µL of 0.05 wt.% Nafion solution was used as the binder. The electrodes were dried in air at 60 ^{o}C for 30 mins.

Cyclic voltammetry (CV) measurements were carried out at different scan rates from 5 to 100 mV/s. The specific capacitance (C_{sp}) was calculated using the following formula from CV,

$$C_{sp} = (i_{+} - i_{-})/(m \text{ x scan rate})$$

where i_{+} and i_{-} are the maximum values of current in the positive scan and negative scan respectively and *m* is the mass of the single electrode.

Specific capacitance was calculated from galvanostatic charge-discharge curves using the formula,

$C_{sp}= \quad (i)(\mathrm{dt})/(m \text{ x } dv)$

where *i* is the discharge current and dt/*dv* is the slope of the discharge curve.

Oxygen reduction reaction:

For the oxygen reduction reaction study standard three-electrode cell with a Pt plate as the counter electrode was employed. The catalyst was prepared by dispersing the catalyst (5 mg) in 1 mL mixture of ethanol and water in the presence of 0.05 wt.% Nafion. From this solution, 4 µL catalyst ink was drop coated on a glassy carbon electrode (GCE) (3 mm diameter). The commercial Pt-loaded carbon catalyst (Pt/C 40% on Vulcan XC, Sainergy Fuel cell India Ltd.) was used for comparison. 1 mg mL^{-1} Pt/C dispersion in isopropanol was prepared using ultrasonication. From this 10 µL was drop casted on GCE using microsyringe. Electrochemical measurements were performed in an O_2-saturated aqueous 0.1 M potassium hydroxide (KOH) solution (Ag/AgCl reference electrode). Rotating disc electrode (RDE) measurements were carried out with a system from Beckman instruments by coupling with a galvanostat/potentiostat (Techno Science instruments). The number of electrons transferred per oxygen molecule from the BCN modified electrode can be calculated by using the Koutechy-Levich equation

$$1/I = 1/i_k + 1/i_d$$

$$1/i = -1/(nFkC_o) - 1/(0.62\, nFD_o^{2/3}\gamma^{-1/6}C_o\omega^{1/2})$$

Here, *I* denotes the measured current densities at the respective potentials, while i_k and i_d represent kinetic and diffusion current densities respectively and *n* gives the overall number of electrons transferred per O_2 molecule. *F* is the Faraday constant (96485 C mol^{-1}), C_o the bulk concentration of O_2 (1.2×10^{-6} mol mL^{-1}), *k* the electron transfer rate constant, D_o the O_2 diffusion coefficient (1.73×10^{-5} cm^2 s^{-1}) in 0.1 M KOH, γ kinematic viscosity (0.0109 cm^2 s^{-1}) and ω the rotation speed of the electrode. The number of electrons transferred, *n*, is obtained by calculating the slope of i^{-1} *vs* ω^{-1} plot.

Nanoindentation

The nanoindentation technique was utilized to evaluate the mechanical properties. For this, the Triboindenter system (Hysitron, Inc., Minneapolis, MN, USA), equipped with a cono-spherical tip of radius (*R*) 1 μm was used. The choice of this particular tip geometry was made, instead of a sharp tip like Vickers or Berkovich that are generally used for nanoindentation, so as to reduce the displacement at any given load.[60] In all cases, the loading and unloading rates were maintained at 0.5 and 2 mN/s respectively, and the peak load was 500 μN. Faster loading and even speedier unloading rates were utilized to reduce viscoelastic recovery and to avoid the typical 'knee' during unloading. These parameters further help in obtaining a convergent solution for the power law fit.[61] A hold time of 250 s at the peak load was used to avoid the creep effects that typically result in the over estimation of Young's modulus, *E*. To avert any inaccuracy in the calculation of depth, *h*, the area function file had been calibrated using Polycarbonate instead of conventionally used fused quartz.[62] The load, *P*-displacement, *h* curves generated through the following procedure were further fitted using power law equation given by Oliver and Pharr to obtain the values of *E* (elastic modulus) and *H* (hardness).[63]

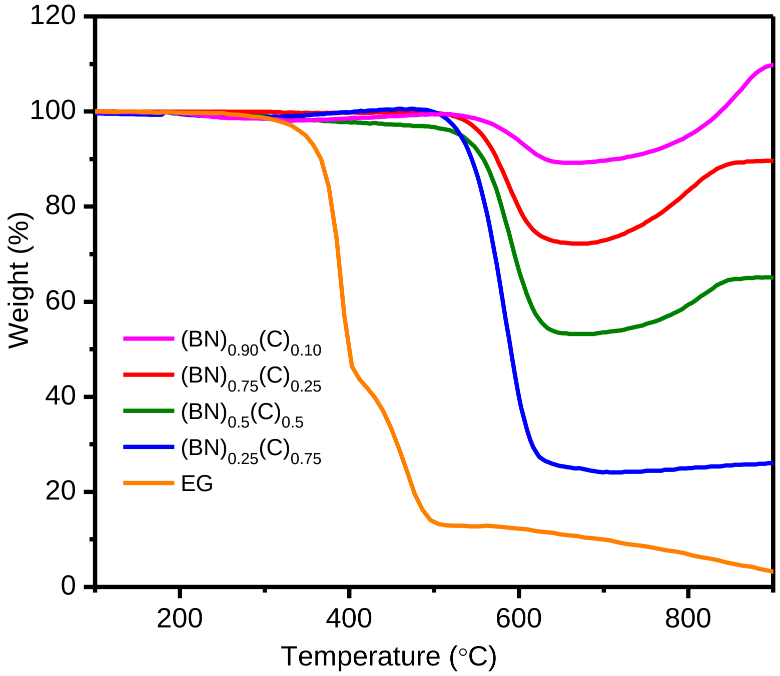

Figure 1. Thermogravimetric analysis of various compositions of BCN in comparison with EG.

4. Results and Discussion

Characteristics of borocarbonitride nanosheets

Borocarbonitrides (BCN) of four different compositions were prepared by heating urea and boric acid with few-layer graphene (EG) at 900 °C. The molar ratio of the precursor employed, gravimetric compositions and surface areas of the samples are presented in Table1. Of the four compositions, designated as BCN-1, BCN-2 BCN-3 and BCN-4, BCN-1 is most carbon-rich and BCN-4 has the least proportion of carbon. The composition has been revealed based on TGA, XPS and EELS data. Thermogravimetric curves of the borocarbonitrides in comparison with EG are shown in **Figure 1**. EG exhibits sharp weight loss of more than 90% in the temperature 350-500 °C and followed by gradual weight loss. BCN-1, BCN-2 BCN-3 and BCN-4 showing weight loss at 397, 440, 488 and 546 °C respectively corresponding to the combustion of the carbon component. The gravimetric compositions of the samples (Table 1) were calculated from the residual weight remaining above ~700 °C. The thermal stability of the BCN samples is seen to be higher in comparison with that of EG, BCN-4 with the largest contents of B and N showing highest thermal stability compared to other compositions.[64]

To examine bonding in the BCN samples and the nature of doping, XPS measurements were carried out by drop casting on Si substrates. **Figure 2**a-c show B 1s, C 1s and N 1s XP spectra of BCN-2. The B 1s feature of this composition can be deconvoluted into two peaks centered at 191.2 eV and 192.3 eV corresponding to B-C and B-N

Table 1. Compositions of borocarbonitrides along with molar ratios of the precursors used for synthesis. Atomic composition from XPS is compared with gravimetric compositions obtained from TGA.

Sample	Boric acid (g)	Urea (g)	EG (g)	Gravimetric Composition	Composition from XPS
BCN-1	0.005	0.5	0.060	$(BN)_{0.20}(C)_{0.80}$	$B_{0.06}C_{0.73}N_{0.21}$
BCN-2	0.010	0.5	0.060	$(BN)_{0.50}(C)_{0.50}$	$B_{0.13}C_{0.49}N_{0.38}$
BCN-3	0.040	1	0.060	$(BN)_{0.75}(C)_{0.25}$	$B_{0.26}C_{0.22}N_{0.52}$
BCN-4	0.080	2	0.060	$(BN)_{0.90}(C)_{0.10}$	$B_{0.38}C_{0.12}N_{0.50}$

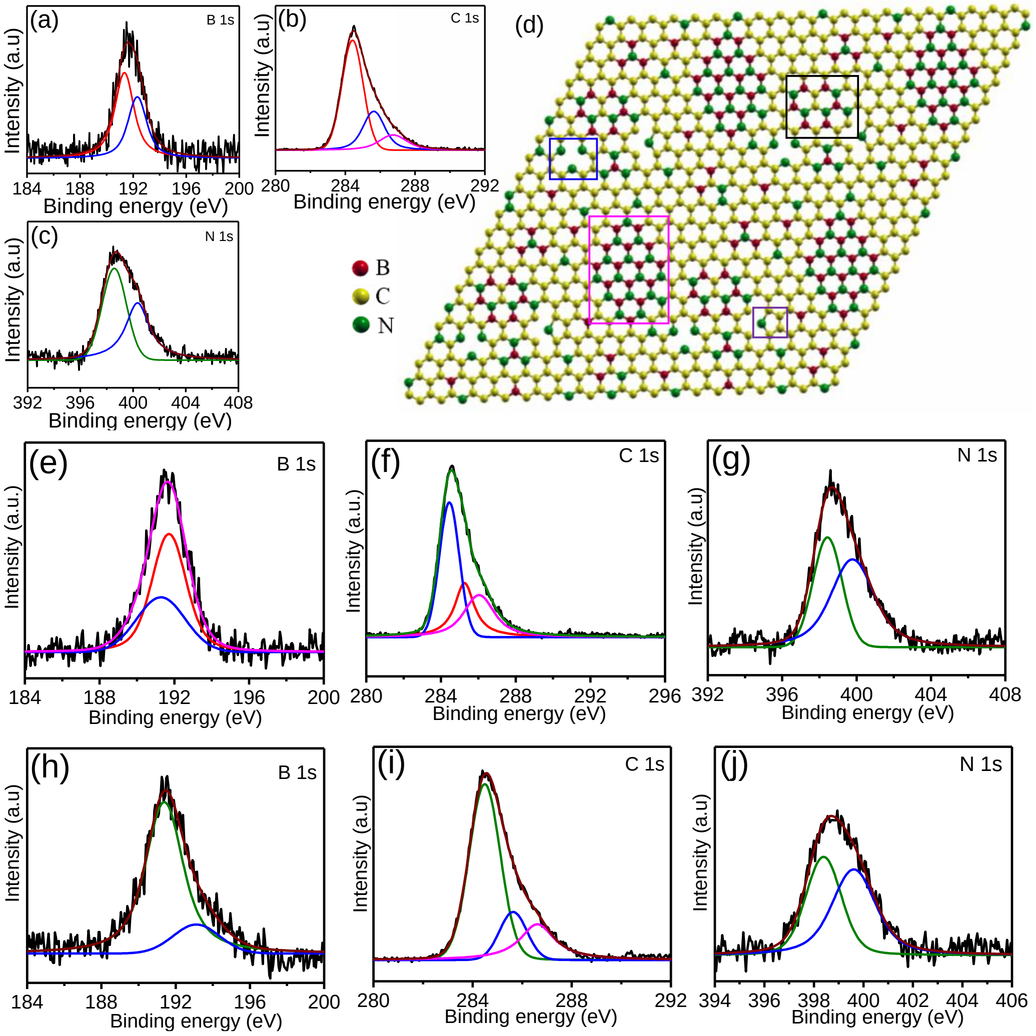

Figure 2. Core-level X-ray photoelectron spectrum (a) B 1s , (b) C 1s, (c) N 1s of BCN-2 and (d) schematic of $B_xC_yN_z$ atomic model depicting incorporation of B and N in graphene sheet, boxes shows different kind of nitrogen and domains. (e-g) Core-level XP spectrum B 1s, C 1s and N 1s of BCN-1 and BCN-3(h-j) respectively.

bonds.[24] High-resolution C 1s spectra can be fitted into four peaks at 283.7, 284.4, 285.4 and 286.5 eV due to B-C, sp^2 carbons (C=C), C-N and C-O bonds respectively. The N 1s spectra has been fitted into three major feature at 398.2 eV, 399.4 and 400.4 corresponding to N-B bonds, the pyridinic nitrogen and pyrollic nitrogen. Core-level spectra of BCN-1 and BCN-3 (Figure 2e-j) exhibit similar features, suggesting the presence of a random network of BCN along with the domains of graphene and BN. It is noteworthy the intensity of the signal at 399.4 eV is substantial even when the borocarbonitride has small proportion of boron suggesting the originate from being C-N bonds. The ratio of intensities of N 1s signals at 399.4 and 400.4 eV of the two types of nitrogen, indicates that pyridinic nitrogen dominates the BCN samples. The percentage of carbon and nitrogen in the samples were also obtained by a chemical

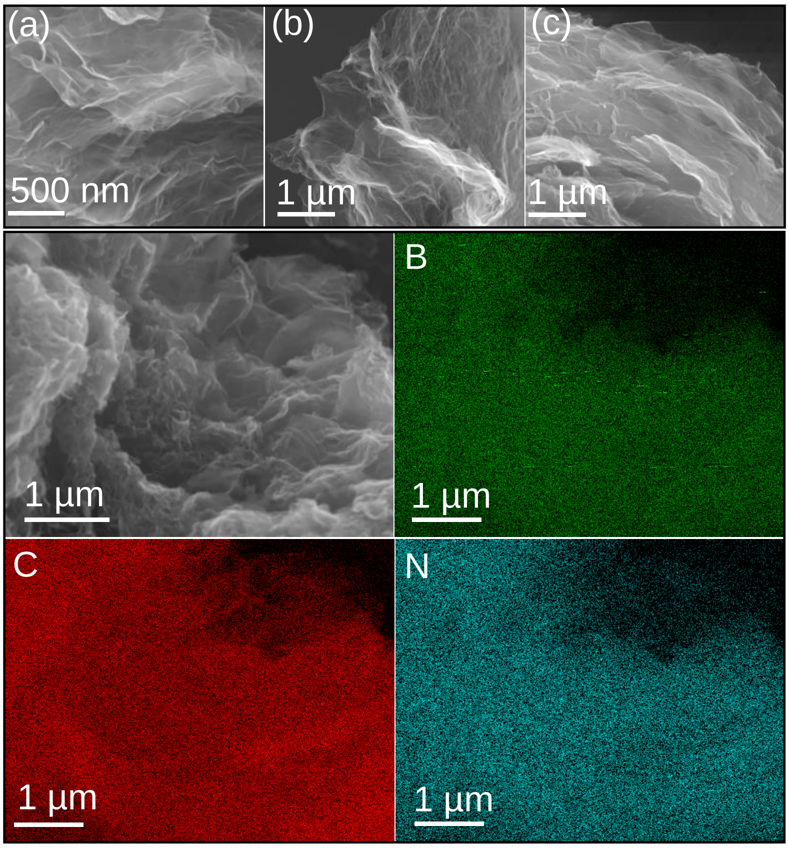

Figure 3. (a-c) FESEM images BCN-1, BCN-2 and BCN-3 and corresponding EDX elemental mapping of BCN-2. Boron (green), carbon (red) and nitrogen (cyan).

analyses using CHNS analyser. The results are in close agreement with those from XPS and thermogravimetric analyses. Elemental mapping using energy dispersive X-ray analysis (EDX) shows uniform distribution of B, C and N which confirms the homogeneity (**Figure 3**).

Electron energy loss spectra of BCN-1, BCN-2, BCN-3 and BCN-4 in **Figure 4** show the K-shell ionization edges of B, C and N respectively. The splitting of π* and σ* levels in B 1s, C 1s and N 1s spectra indicates sp^2 hybridization of these atoms as in BN and graphene. The EEL spectrum of boron has a peak at 191.5 eV due to the transition 1s electron to π* antibonding orbitals associated with planar sp^2 hybridization and a peak at 198.7 eV due to the transition of the 1s electron to the σ* antibonding orbital. The K-shell ionization edges of carbon at 282.7 eV and 293 eV correspond to 1s→ π* and 1s→ σ* transitions of graphene respectively.[65] Similarly, the nitrogen K-shell ionization spectrum shows peaks at 397.5 and 405.3 eV refers to1s→ π* and 1s→ σ* transition of BN.[66] The broad signals around 214 eV and 321 eV arise from extended energy-loss fine structure (EXELFS) due to backscattering from nearest neighbor of B and C respectively.[67] The atomic composition obtained

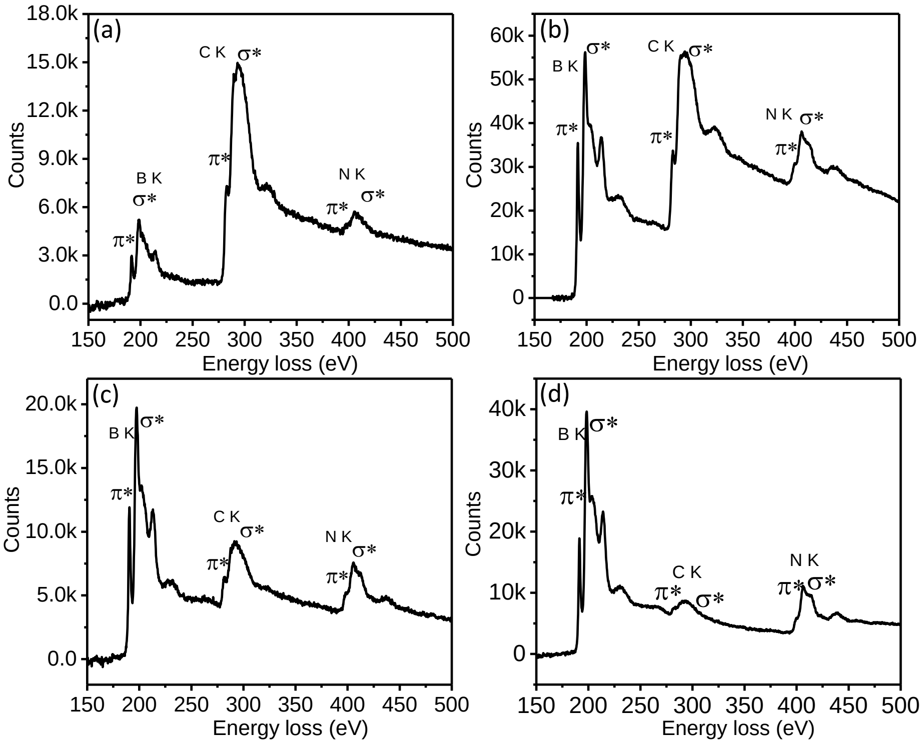

Figure 4. Electron energy loss spectrum (EELS) of (a) BCN-1 (b) BCN-2 and (c) BCN-3 and (d) BCN-4 respectively.

by EELS measurements are $B_{0.08}C_{0.75}N_{0.17}$, $B_{0.21}C_{0.49}N_{0.30}$, $B_{0.28}C_{0.25}N_{0.47}$ and $B_{0.41}C_{0.07}N_{0.52}$ respectively and were in good agreement with other results. Electron microscope images of EG and BCN are shown in **Figure 5**. The nanosheets are electron transparent and show wrinkled morphology like graphene ribbons. We have not observed any changes in the nanosheet morphology with varying composition. High-resolution transmission electron microscope (HRTEM) images of BCN clearely

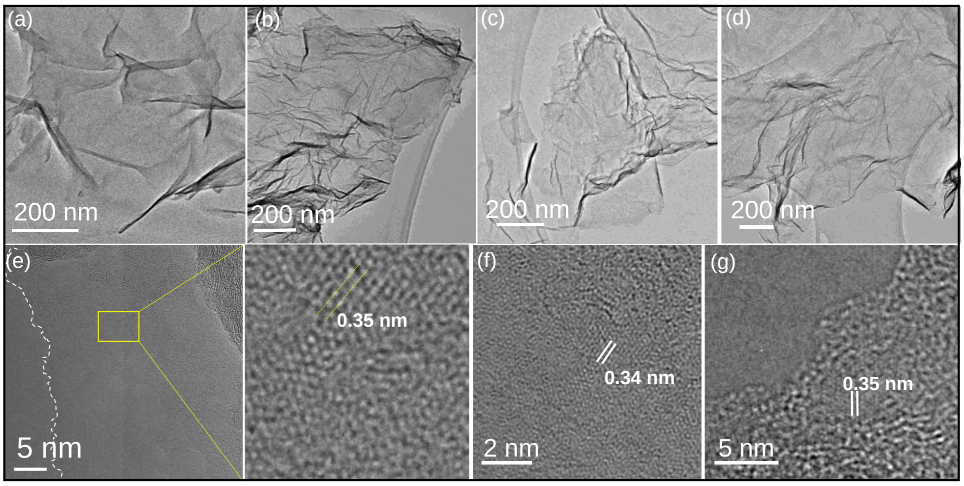

Figure 5. TEM images of (a) EG, (b) $(BN)_{0.20}(C)_{0.80}$, (c) $(BN)_{0.50}(C)_{0.50}$, (d) $(BN)_{0.75}(C)_{0.25}$ and (e-g) High resolution TEM images of $(BN)_{0.50}(C)_{0.50}$, $(BN)_{0.75}(C)_{0.25}$ respectively.

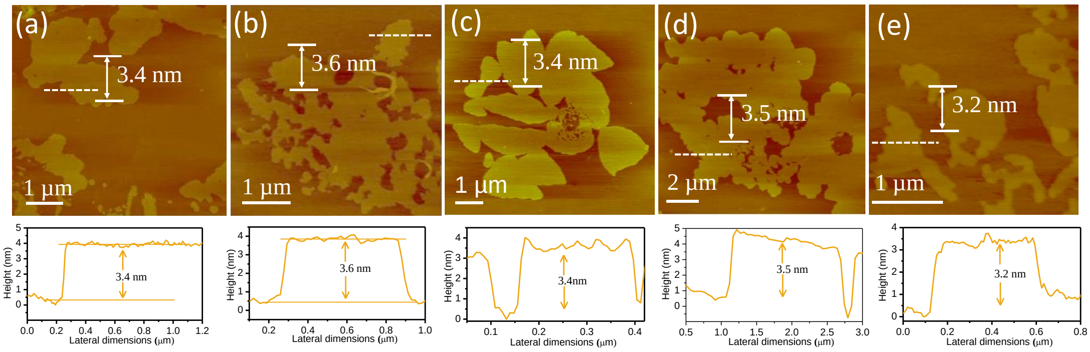

Figure 6. Tapping mode AFM images with corresponding height profile of (a) EG, (b) $(BN)_{0.20}(C)_{0.80}$, (c) $(BN)_{0.50}(C)_{0.50}$, (d) $(BN)_{0.75}(C)_{0.25}$ and (e) $(BN)_{0.90}(C)_{0.10}$.

show the presence of few layers in BCN with the interlayer separation of 0.35 nm (single layer) which is only slightly higher than graphene and BN (Figure 5 f & g). To evaluate the number of layers and surface topography of the samples, we have drop coated the nanosheets on Si(100) surface and carried out AFM measurements in the tapping mode. **Figure 6** shows AFM topography images of EG, $(BN)_{0.20}(C)_{0.80}$, $(BN)_{0.50}(C)_{0.50}$, $(BN)_{0.75}(C)_{0.25}$ and $(BN)_{0.90}(C)_{0.10}$ with the corresponding height profiles. The nanosheets display an average height of 2.4 to 2.6 nm irrespective of the composition revealing that the borocarbonitrides comprise 6-8 layers with lateral dimensions of a few µm. The AFM results also demonstrate that as-synthesised BCN samples contain only a few-layers with large lateral dimensions which enable fabrication of electronic devices.

The infrared spectrum of EG shows a characteristic strong band at 1570 cm^{-1} and a weak band around 1728 cm^{-1} due to C=C and carboxyl groups respectively (**Figure 7**a). The broad band around 1100-1250 cm^{-1} is due to C-O stretching and O-H bending vibrations. In addition to the bands due to graphene, the BCN samples exhibit characteristic bands at 1390 and 798 cm^{-1} due to B-N transverse optical mode and B- N-B bending mode vibrations.[68] The intensity of these bands increases with the BN content as expected. The oxygen functionalities present in EG facilitates the more doping of B and N into the graphene lattice,[64] and accordingly the C=O stretching and O-H band intensities decrease in the BCN compositions which indicats the removal of oxygen functionalities. Raman spectra of BCN show characteristic bands at 1362 and 1598 cm^{-1} respectively, the intensity of the first order band has contributions from defects and BN domains (Figure 7b). Nitrogen adsorption-desorption isotherm data of BCN samples recorded at 77 K are shown in Figure 7c.

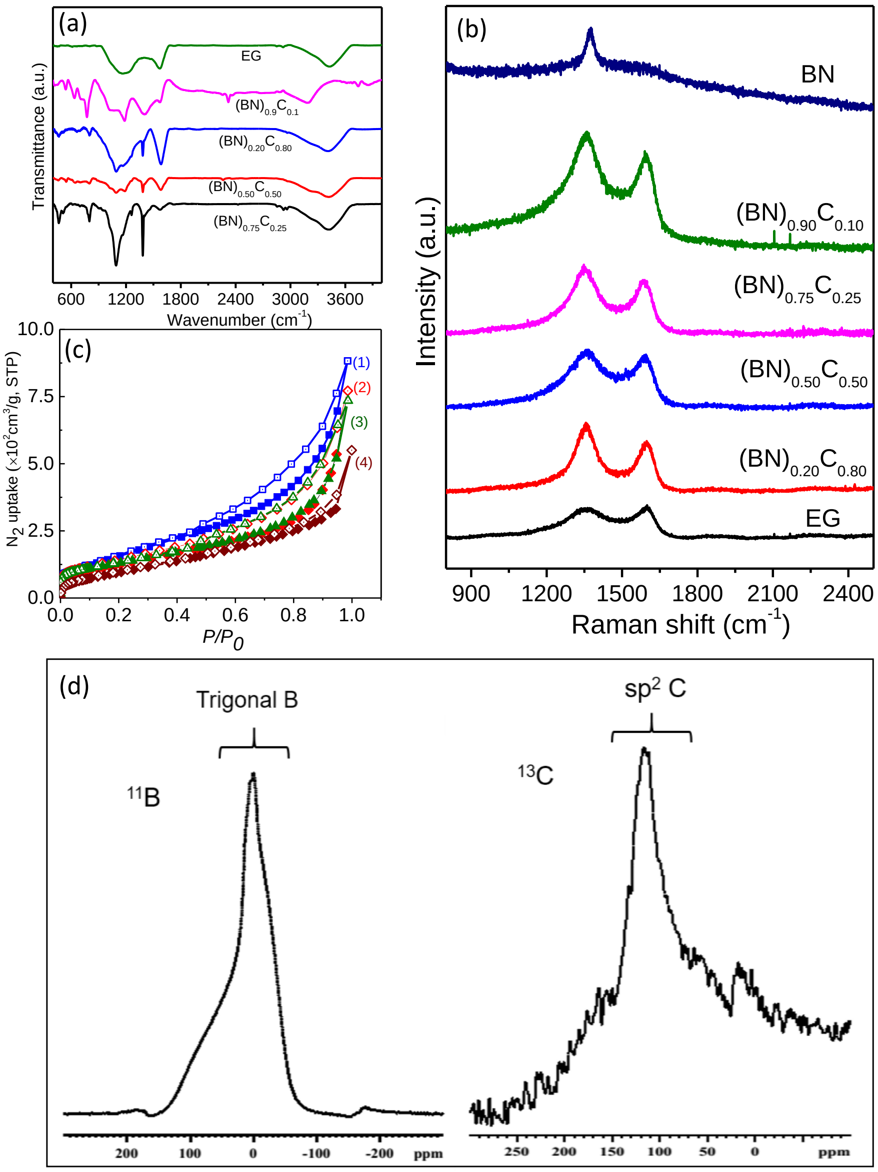

Figure 7. (a) Fourier transform infrared (FTIR) (b) Raman spectrum of EG and various compositions of BCN. (c) N_2 sorption profile of at 77 K (1-4 refers to $(BN)_{0.20}(C)_{0.80}$, $(BN)_{0.50}(C)_{0.50}$, $(BN)_{0.75}(C)_{0.25}$ and $(BN)_{0.90}(C)_{0.10}$ respectively. (d) ^{13}C and ^{11}B solid state NMR spectrum of $(BN)_{0.50}(C)_{0.50}$ composite at 20 kHz MAS and 14 kHz MAS respectively.

Brunauer−Emmet−Teller (BET) surface areas of $(BN)_{0.20}(C)_{0.80}$, $(BN)_{0.50}(C)_{0.50}$, $(BN)_{0.75}(C)_{0.25}$ and $(BN)_{0.90}(C)_{0.10}$ are 419, 437, 254 and 190 m^2g^{-1} respectively (**Table 2**). The isotherms are concave to the P/P_0 in the low-pressure region suggesting a combination of type-1 and type-2 behaviors with an H3 type hysteresis loop. This is characteristic of microporous material according to the International Union of Pure and Applied Chemistry (IUPAC) classification.[69] The obtained specific surface areas highlight the nanostructure of the composites and existence of micropores due to random arrangement of nanosheets. Figure 7d shows ^{13}C and ^{11}B solid-state nuclear magnetic resonance (NMR) spectra of $(BN)_{0.50}(C)_{0.50}$ recorded at 20 and 14 kHz respectively. The signal around 120 ppm in ^{13}C NMR corresponds to aromatic sp^2 carbon of graphene domain, the shoulder at 132 ppm is can be attributed to carbon in the vicinity of N atom.[70-72] The broad and weak signals around 60 and 20 ppm may be due to carbons in the vicinity of B and the sp^3 carbon respectively.[73] The ^{11}B spectrum has a prominent signal around 2-10 ppm corresponding to the trigonal boron in BN domains. Broadening of the boron signal (140 to -75 ppm) is found due to heterogeneity in the chemical environment.

Quantification of surface functionalities by FLOSS

We characterized graphene (EG) samples using various spectroscopic and microscopic techniques. Electron microscopic and atomic force microscopic images showed 2D planar sheet structures of these materials (Figures 5 & 6). Preliminary spectroscopic results revealed the presence of various functional groups like carbonyl, carboxylic and hydroxyl on the surfaces of the nanosheets (Figure 7). Quantification of these functional groups is of great significance due to their impact on the properties of materials.[74-76] The spectroscopic techniques such as FTIR, Raman and XPS[77] as well as titration methods[78, 79] suffer from poor detection limits, and hence cannot be used to quantify the exact amount of functional groups on graphene.[32] We employed FLOSS for the quantification of the functional groups due to its ability to detect below the detection limit any other available technique till date.[80] **Scheme 3** shows a pictorial representation of surface functionalities present on graphene and chemically labeling them using fluorescent probes. The carbonyl groups are chemically tagged with the DH probe and the carboxylic and hydroxyl groups with 1-(bromoacetyl)pyrene. In **Figure 8**a, we show the emission spectra of DH of various concentrations with excitation at 350 nm. The calibration curve is obtained from the emission spectra by monitoring the intensity at 513 nm and plotting the intensity as a function of concentration as shown in the inset of Figure 8a. In Figure 8b, we illustrate how the reaction of DH with the carbonyl groups on the surface of graphene results in the depletion of the fluorescent intensity of the dye due to the covalent attachment of DH molecules to carbonyl groups. The number of carbonyl groups present on the surface were estimated using calibration graph.

To confirm the quenching of fluorescence intensity due to covalent linking but

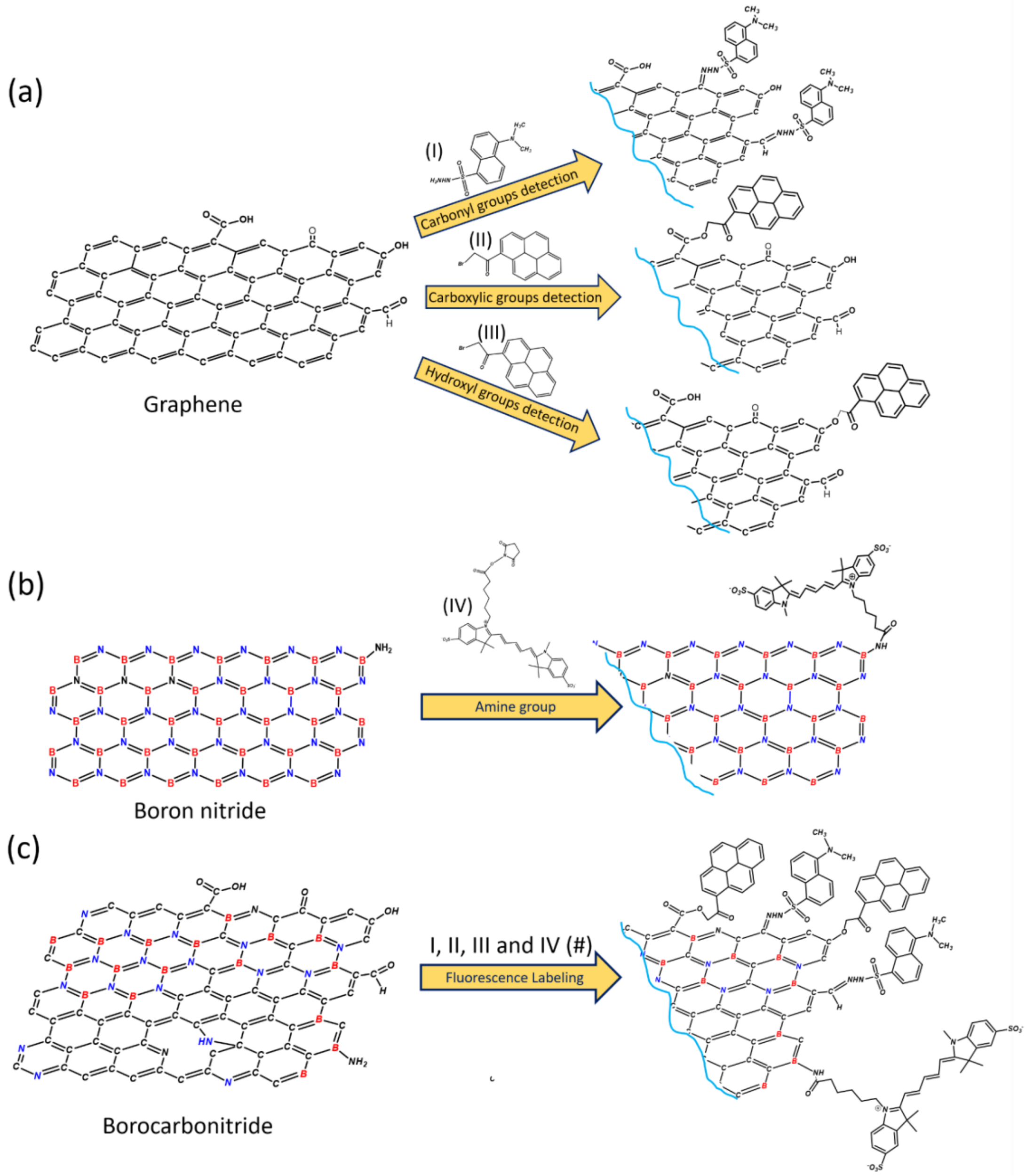

Scheme 3. Schematic representation of surface functional groups on (a) graphene (b) boron nitride and (c) borocarbonitride, and probing them using (I) dansyl hydrazine(carbonyl groups), (II) and (III) 1-(bromoacetyl)pyrene (for carboxylic and hydroxyl groups) and (IV) NHS-Cy5 (for amine groups) fluorescent probes. # indicates I, II, III and IV are different reactions. For the ease of representation we have shown all the fluorescent labels on a single BCN sheet. The reactions however are different and involve different experimental conditions performed independently.

not due to physisorption, we carried out control experiments without the reagent which showed that there was no observable change in PL intensity (see Figure 11a). Figure 8c shows the PL emission spectra of 1-(bromomoacetyl)pyrene collected over a known range of concentrations. The calibration curve derived by monitoring the intensity at 410 nm from Figure 8c is displayed in the inset. The reaction of 1-(bromomoacetyl)pyrene with the carboxylic and hydroxyl surface groups of the

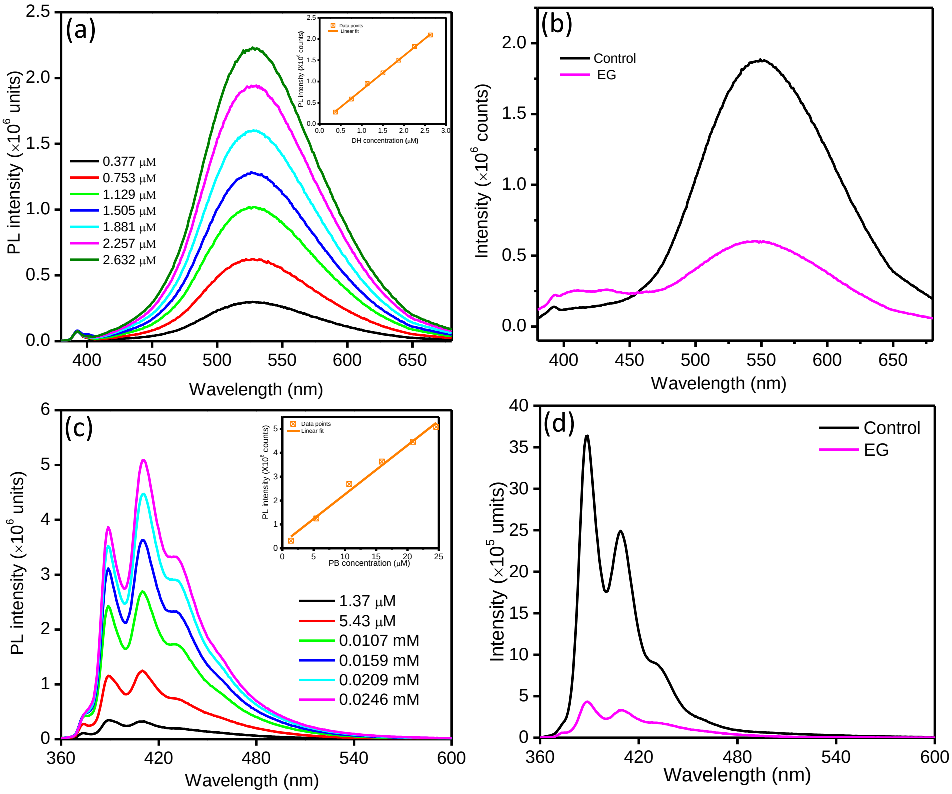

Figure 8. (a) Emission spectra of dansyl hydrazine (DH) of different concentrations (excitation wavelength 350 nm). Inset shows the calibration plot of fluorescent intensity as a function of concentration at 513 nm (b) Emission spectrum of DH reacted with carbonyls on graphene compared with the control measurement. (c) Emission spectra of 1-(bromoacetyl)pyrene of different concentrations (excitation wavelength 320 nm). Inset shows the calibration curve of fluorescent intensity as a function of concentration at 410 nm (d) Emission spectra of 1-(bromoacetyl)pyrene reacted with carboxylic groups of exfoliated graphene compared with the control experiment.

graphene are shown in Figure 8d and **Figure 9**a. The PL intensity of carboxylic group reaction shows satisfactory depletion due to the presence of a large number of these groups on the graphene surface. The hydroxyl group reaction shows reasonable decrease in the intensity compared to control reaction (Figure 9a). The estimates of carboxylic and hydroxyl groups based on these results are reasonable, although there could be a slight over estimation due to possible side reactions.

In contrast to the results on graphene, our studies on GO show the presence of large concentrations of all the oxygen functionalities on the surface. Thus carbonyl, carboxyl and hydroxyl concentrations are 6.70×10^{20}, 32.49×10^{20} and 19.20×10^{20} groups/g respectively. On reduction with hydrazine hydrate, the carbonyl groups are eliminated. The surface concentrations of carboxyl and hydroxyl groups in RGO are 12.15×10^{20} and 7.26×10^{20} groups/g respectively (Figure 9 c & b, Table 2).

Borocarbonitrides prepared by using graphene are expected to contain similar

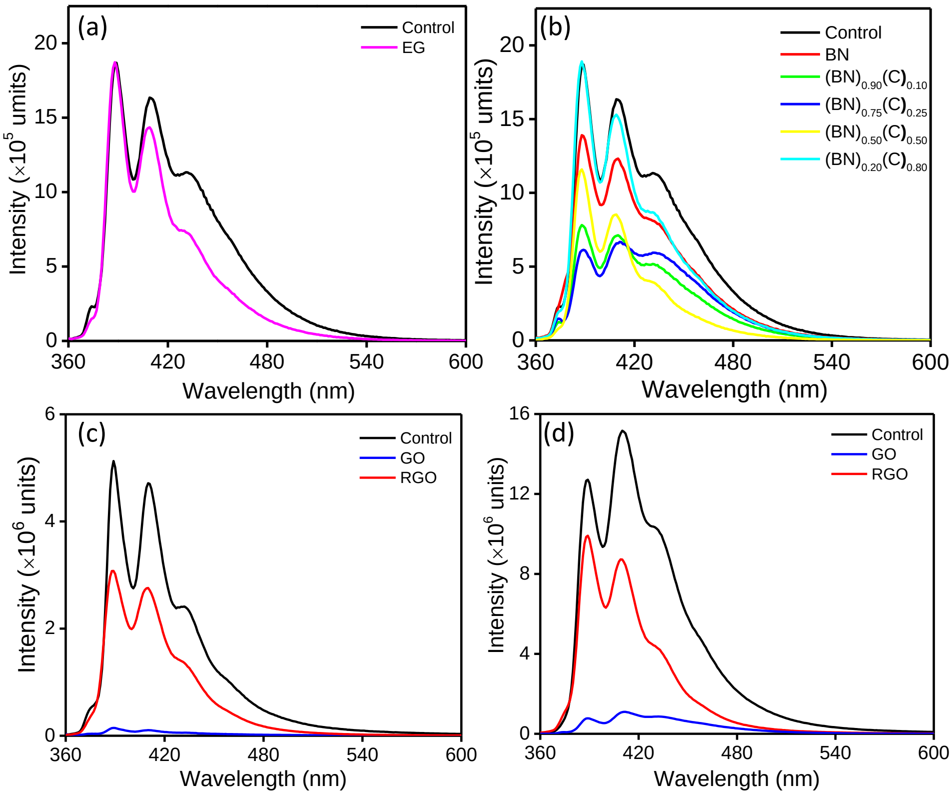

Figure 9. (a) Emission spectra of 1-(bromoacetyl)pyrene reacted with hydroxyl groups of exfoliated graphene compared with the control experiment (b) Emission spectra of PB reacted with hydroxyl groups of BCN along with the control experiment. (c) Emission spectra of 1-(bromoacetyl)pyrene reacted with carboxylic groups of GO and RGO compared with the control experiment (d) Emission spectra of PB reacted with hydroxyl groups of GO and RGO along with the control experiment.

oxygen functionalities like graphene, the amounts of which would vary with the composition. We have characterized the BCN surfaces in the same way as graphene. **Figure 10**a shows the DH reaction with different BCN compositions, compared with the control experiment. The decrease in the fluorescence intensity is attributed to covalent linking of DH molecules with carbonyls on the BCN surfaces. The density of carbonyl groups on BCN surfaces decreases with carbon content as expected (Table 2). The BCN composition with the highest carbon content shows the highest number of carbonyl groups (2.08×10^{20} groups/g) which is very much similar to graphene ($2.31x10^{20}$groups/g). The BCN surface with highest BN content, contains less number of carbonyl groups (0.96×10^{20} groups/g) compared to all other compositions. The systematic variation in number of carbonyl groups on BCN surface with compositions shows that BCN surface can be tuned to achieve the desired properties. Carboxylic groups on the BCN surface of various compositions were chemically tagged with1-(bromomoacetyl)pyrene and were estimated using calibration curve (inset of Figure 8c). The amount of carboxylic groups on the BCN surfaces varies with the

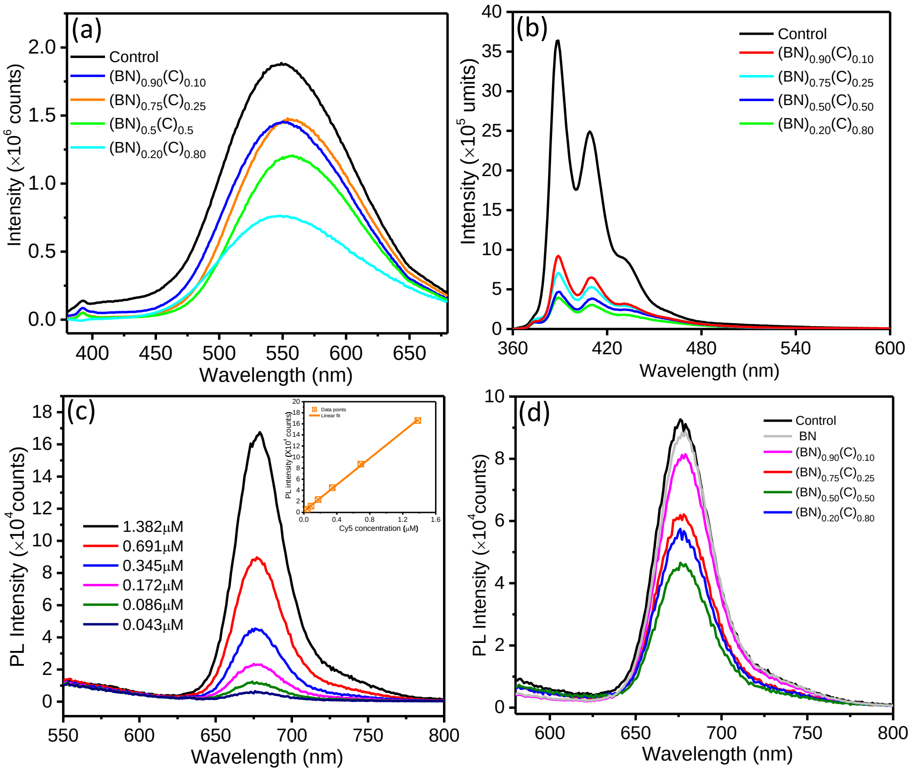

Figure 10. (a) Emission spectra of DH reacted with carbonyls of BCN compared with the control experiment (b) Emission spectra of 1-(bromoacetyl)pyrene reacted with carboxylic groups of BCN along with the control experiment.(c) Emission spectra of NHS-Cy5 of different concentrations (excitation wavelength 530 nm). Inset shows the calibration curve of fluorescent intensity as a function of concentration at 680 nm (d) Emission spectra of NHS-Cy5 reacted with amine groups of BN and BCN along with the control experiment.

compositions and decreases with the carbon content as observed in the case of carbonyl groups (Figure 10b). The calculated number of carboxylic groups might be slightly overestimated compared to carbonyl groups due to possible side reactions. We have not observed any trend in the number of surface hydroxyl groups with varying composition of BCN (Table 2 and Figure 9b).

In addition to oxygen containing functionalities, BCN would contain amine functionalities on the surface due to reaction of urea with graphene during synthesis. The number of these functionalities can vary with the composition due to variation in the number of graphene, BCN and BN domains with composition. On the other hand, BN which does not have any carbon content, is expected to contain only amine and hydroxyl groups. In order to probe the amine functionalities on BN and BCN surfaces, we have used the NHS-Cy5 as the fluorescent probe which is very specific to amine group. We have measured the fluorescence of various known concentrations of NHS-Cy5 with excitation at 530 nm as shown in Figure 10c. The calibration curve as a

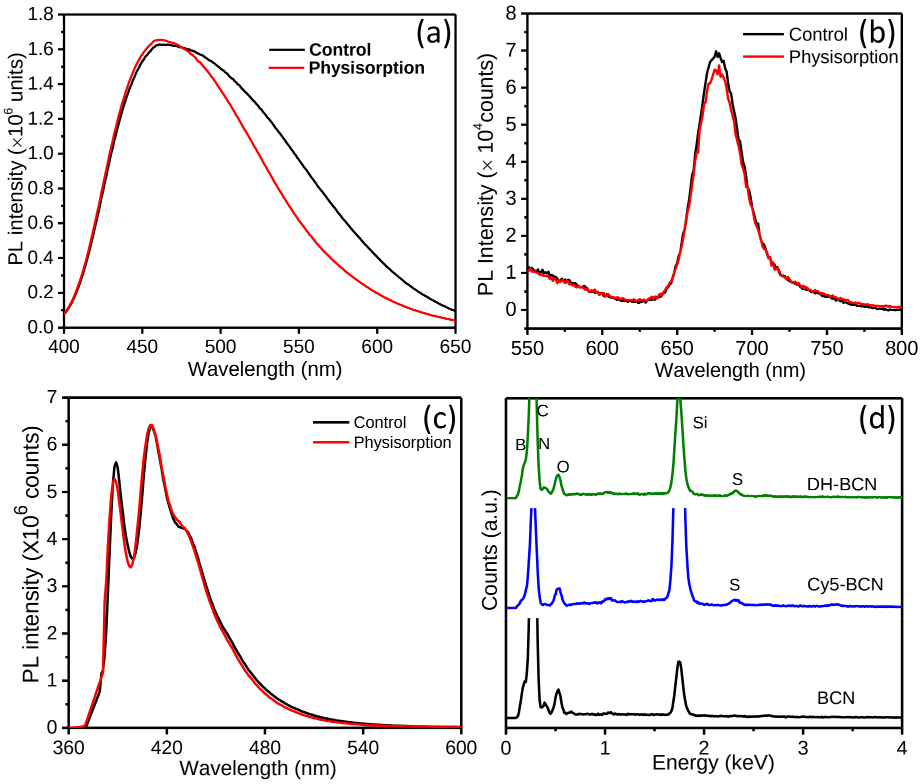

Figure 11. Physisorption of (a) DH, (b) NHS-Cy5 and (c) PB dye molecules on sample surface. (d) Energy dispersive X-ray spectra of chemically labeled BCN with DH, Cy5 along with pristine BCN.

function of concentration, derived from fluorescence results is shown in the inset and was used for quantification of amine groups. The FLOSS results of NHS-Cy5 reaction with the amine functional groups on BN and various compositions of BCN are shown in the Figure 10d. The content of amine groups increases with the carbon content in the sample but the composition with highest carbon content $(BN)_{0.20}C_{0.80}$ shows deviation from the observed trend and possesses a less number of amine groups compared to $(BN)_{0.50}C_{0.50}$. This can be attributed to the molar proportion of the aminating agent (urea) used to get $(BN)_{0.20}C_{0.80}$ composition is 10 times lesser than that of $(BN)_{0.50}C_{0.50}$. In contrast, as the BN content in BCN increases, the number of amine groups decreases drastically from 2.15×10^{20} to 0.42×10^{20}. This trend might be true because our FLOSS results of amine group on BN surface shows less than 5% of amine groups compared to $(BN)_{0.50}C_{0.50}$. From these results, we summarize that the number of amine functionalities on the surface of BCN will be higher than on BN alone. These results also suggest that functionalization of BN surface will be more difficult than other carbonaceous surfaces due to its chemical stability and insulating nature. To confirm that the fluorescence quenching is due to covalent linking, we

Table 2. Surface areas and FLOSS results of various surface functional groups on graphene, boron nitride and borocarbonitrides.

Samples	Surface area (m^2/g)	Carbonyl groups groups/g (groups/cm^2)	Carboxylic groups (groups/g) (groups/cm^2)	Hydroxyl groups (groups/g) (groups/cm^2)	Amine groups (groups/g) (groups/cm^2)
GO	28	6.70 X10^{20} (2.40 X10^{15})	≈32.49 X10^{20} (11603.57X10^{13})	≈19.20X10^{20} (685.71X10^{13})	-
RGO	76	-	≈12.15 X10^{20} (159.87X10^{13})	≈7.26X10^{20} (95.53X10^{13})	-
EG	948	2.31X10^{20} (2.44X10^{13})	≈ 28.17X10^{20} (29.72X10^{13})	≈ 0.08X10^{20} (0.08X10^{13})	-
$(BN)_{0.20}(C)_{0.80}$	454	2.08X10^{20} (4.58X10^{13})	≈28.65X10^{20} (63.11X10^{13})	≈ 0.01X10^{20} (0.02X10^{13})	1.75X10^{20} (3.85X10^{13})
$(BN)_{0.50}(C)_{0.50}$	437	1.77X10^{20} (4.05X10^{13})	≈27.36X10^{20} (62.61X10^{13})	≈ 8.79X10^{20} (20.11X10^{13})	2.15X10^{20} (4.92X10^{13})
$(BN)_{0.75}(C)_{0.25}$	254	1.32X10^{20} (5.20X10^{13})	≈25.45X10^{20} (100.20X10^{13})	≈ 1.34X10^{20} (44.64X10^{13})	1.40X10^{20} (5.51X10^{13})
$(BN)_{0.10}(C)_{0.90}$	190	0.96X10^{20} (5.05X10^{13})	≈23.68X10^{20} (124.63X10^{13})	≈ 10.39X10^{20} (54.68X10^{13})	0.42X10^{20} (2.21X10^{13})
BN	142	-	-	≈3.03X10^{20} (21.34X10^{13})	0.01X10^{20} (0.07X10^{13})

carried physisorption control experiments (**Figures 11**a-c). The sulfur signal in the EDAX spectrum of DH and NHS-Cy5 linked samples indicates the chemically bonded fluorescent probe to BCN surface (Figure 11d).

The EG sample shows the presence of carbonyl groups, but the concentration of carboxylic groups is higher than that of carbonyl and hydroxyl groups. The surface areas of borocarbonitrides increases with carbon content. The surface carbonyl groups per unit weight also increase with the carbon content and surface area (Table 2). The same is true of the concentration of carboxyl groups on the surface of BCN. These trends however get altered when we look at the concentrations per unit surface area as the specific surface areas varies largely with composition. We have not observed any appreciable trend in the case of surface hydroxyl groups. Physisorption of hydroxyl groups from the environment might be one of the contributing reasons.

Supercapacitor performance

We have studied supercapacitor performance and oxygen reduction reaction (ORR) studies on graphene and BCN samples to look for the possible effects of surface groups on the electrochemical behavior of these materials. The electrochemical performance was investigated by means of cyclic voltammetry (CV), galvanostatic charge-discharge curves in 1 M H_2SO_4 aqueous electrolyte. Cyclic voltammograms of samples measured at different scan rates (5-100 mV/s) at a voltage of 0-1 V. $(BN)_{0.75}(C)_{0.25}$ exhibits the largest curve area compared to EG and other BCN compositions and distinct pseudocapacitive peaks because of the high contents of nitrogen and boron (Table 1). **Figure 12**a shows cyclic voltammograms of EG and BCN compositions measured at 40 mV/s. The quasi-rectangular CV curves indicate excellent charge storage capability like an ideal supercapacitor. Figure 12b shows cyclic voltammograms of $(BN)_{0.75}(C)_{0.25}$ at different scan rates. It is noteworthy that

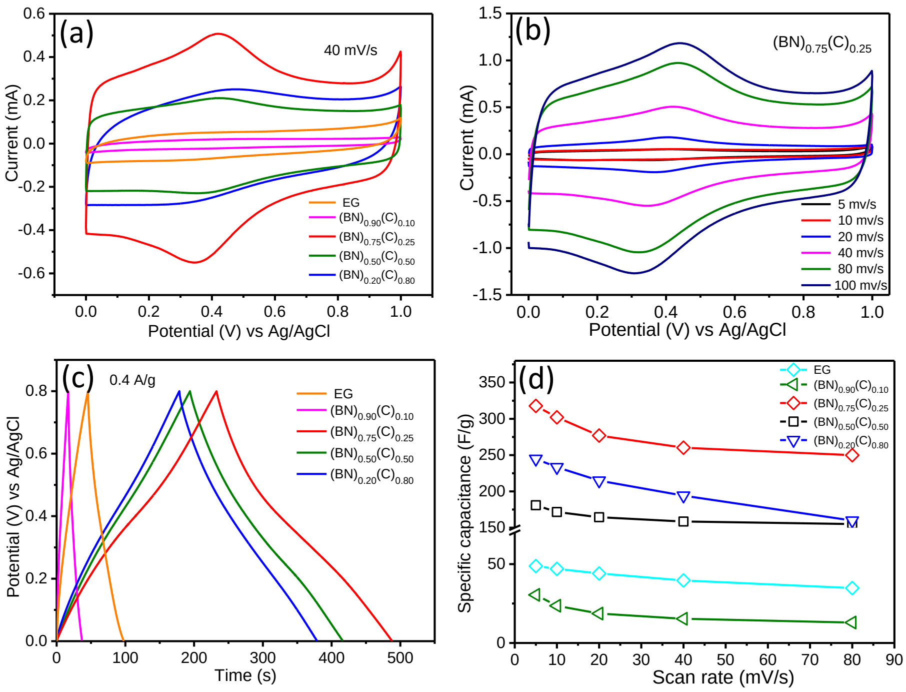

Figure 12. Supercapacitor performance of few-layered graphene and BCN supercapacitor electrodes in 1M H_2SO_4. (a) Cyclic voltammetry curves of BCN supercapacitor at a scan rate 40 mV/s. (b) Cyclic voltammogram of $(BN)_{0.75}(C)_{0.25}$ at different scan rates. (c) Galvanostatic charge-discharge curves at a current density of 0.4 A/g. (d) Specific capacitance of BCN samples as a function of scan rates.

$(BN)_{0.75}(C)_{0.25}$ shows excellent electrochemical stability over a wide range of scan rate with increase in current density. Figure 12c shows galvanostatic charge-discharge curves measured at a current density of 0.4 Ag^{-1} in a potential window of 0-0.8 V *vs* Ag/AgCl. The discharge time of $(BN)_{0.75}(C)_{0.25}$ is significantly longer than that of the other compositions and the curves look nearly symmetrical indicating remarkable charge storing ability of this composition. The discharge time of $(BN)_{0.75}(C)_{0.25}$ is significantly longer than EG and other BCN compositions indicating higher charge storing ability. Clearly B, N-doping gives rise to high specific capacitance compared to pristine graphene. Despite $(BN)_{0.75}(C)_{0.25}$ having a lower surface area than other BCN compositions, its capacitance is higher, which suggests that the pseudocapacitive effects of the nitrogen and boron atoms play an important role in the electrochemical performance. The capacitance of the samples increases with increasing contents of nitrogen and boron which allow good wettability and ease the access of the electrolyte ions to the BCN electrode surface. The calculated specific capacitance of $(BN)_{0.75}(C)_{0.25}$, $(BN)_{0.20}$ $C_{0.80}$ and $(BN)_{0.50}(C)_{0.50}$ are 276, 240 and 164 F/g respectively at 20 mV/s. The specific capacitance of the $(BN)_{0.75}(C)_{0.25}$ shows only a slight decrease to 96 % after 1000 cycles (**Figure 13**a). This indicates excellent cycle stability for capacitor applications. Figure 13b shows Nyquist plots in the frequency range 100 kHz–0.01 Hz measured at open-circuit potentials. The nearly vertical line in the low-frequency region for all electrode materials reflects excellent capacitive behaviour of these BCN samples. We observe a small charge transfer resistance (C_t) in BCN samples at high frequency ranges. The equivalent series resistance (ESR) of EG, BCN compositions found to be 37.0, 36.2, 35.8 and 35.6 ohm

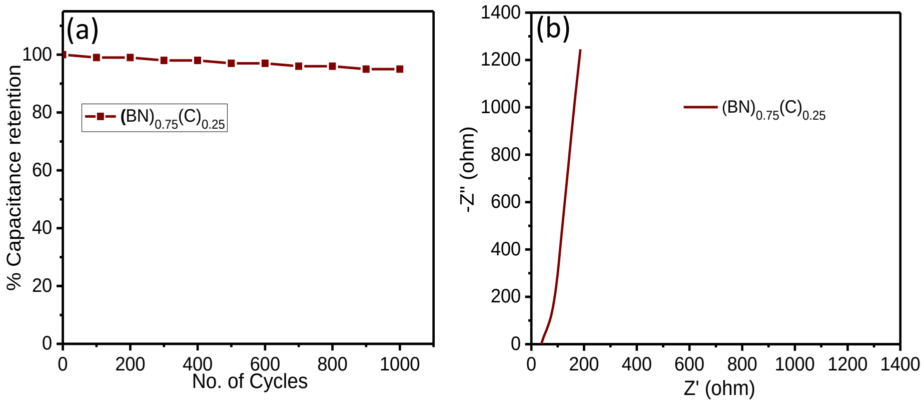

Figure 13. (a) Cyclic stability of $(BN)_{0.75}(C)_{0.25}$ at 1 A/g for 1000 cycles. (b) Nyquist plot of $(BN)_{0.75}(C)_{0.25}$.

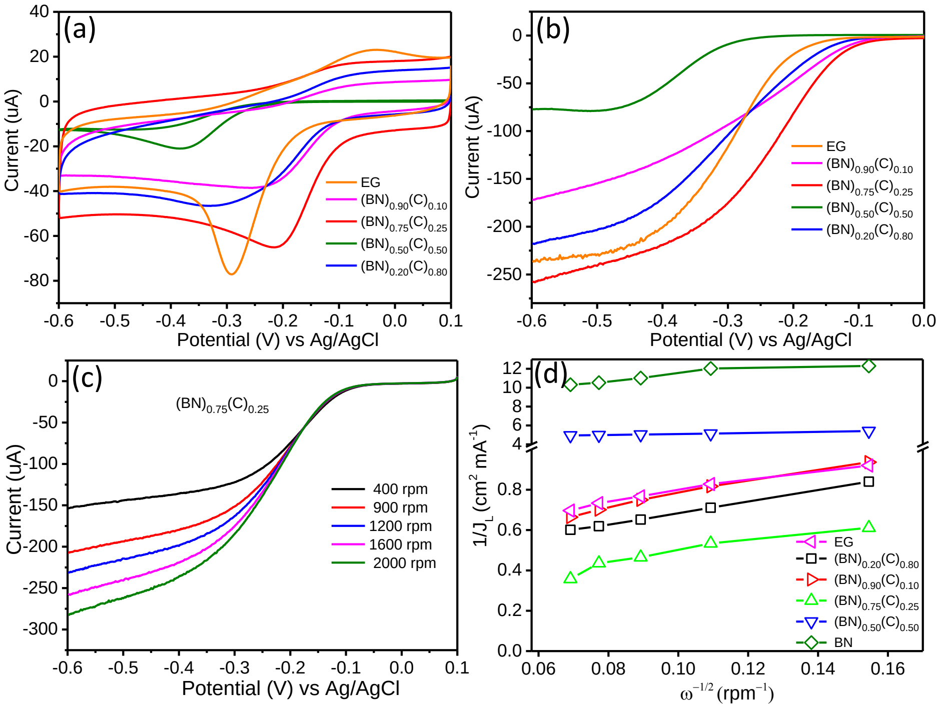

Figure 14. ORR catalytic performance of few-layered BCN samples in O_2 saturated 0.1M KOH electrolyte (a) cyclic voltammetry of BCN samples at 20 mV/s (b) LSV curves of BCN samples at a scan rate of 5 mV/s and rotation speed of 1600 rpm. (c) LSV curves of $(BN)_{0.75}(C)_{0.25}$ at different rotations (d) K–L plot of measured at potential -0.318V.

respectively. The good supercapacitor performance of $(BN)_{0.75}(C)_{0.25}$ can be attributed to the presence of pyridinic nitrogen atoms. The observed trend cannot be related to the surface concentration of any oxygen functionality. The concentration of the surface amine functionality varies as $(BN)_{0.50}(C)_{0.50}$ > $(BN)_{0.20}(C)_{0.80}$ > $(BN)_{0.75}(C)_{0.25}$ > $(BN)_{0.90}(C)_{0.10}$. $(BN)_{0.90}(C)_{0.10}$ shows the lowest capacitance and observed capacitance is relatively low due to the low electrical conductivity. Apart from pyridinic, pyrollic and graphitic nitrogens in the BCN lattice, surface amine functionalities could play a role in determining the charge storage ability.

Oxygen reduction reaction (ORR) performance

Electrocatalytic activity of EG and the BCN samples in the oxygen reduction reaction was evaluated by cyclic voltammetry (CV) at a slow scanning rate of 5 mV s^{-1} in O_2-saturated and N_2-saturated 0.1 M KOH electrolyte in a three-electrode system in the potential range from 0.2 to -1.0 V vs Ag/AgCl. The ORR electrocatalytic activity of EG and BCN samples in O_2-saturated 0.1 M KOH solution is shown in **Figure 14**a. BCN catalysts shows cathodic peaks in the range -0.09 to -0.24 V, indicating good O_2 reduction property. More importantly, the cathodic peak of $(BN)_{0.75}(C)_{0.25}$ is more positive than other compositions. To evaluate the electrocatalytic activity linear-sweep voltammetry (LSV) of BCN at a rotation speed of 1600 rpm was carried out on an RDE as shown in Figure 14b. The $(BN)_{0.75}(C)_{0.25}$ exhibits a higher current density compared to other compositions representing an enhanced catalytic activity for ORR. Furthermore, a set of LSV curves of $(BN)_{0.75}(C)_{0.25}$ recorded from 400 to 2000 rpm shows that the current density increases with the increase in rotation speed, since the diffusion distance shortens at higher rotation rates (Figure 14c). Koutecky−Levich plots (i^{-1} *vs* $\omega^{-1/2}$) were obtained from the polarization curves at a potential of -0.6 V for all the BCN catalysts (Figure 14d). The transferred electron number (n) per O_2 from the slopes of Koutecky−Levich plots is calculated to be ~3.7-3.9 for the BCN samples while in EG it is only 3.4. $(BN)_{0.75}(C)_{0.25}$ with more B, N dopants shows better wettability and ORR activity than other BCN and EG. The observed ORR onset potentials for various compositions are 0.09, 0.1, 0.14 and 0.24 for $(BN)_{0.75}(C)_{0.25}$, $(BN)_{0.90}(C)_{0.10}$, $(BN)_{0.20}(C)_{0.80}$ and $(BN)_{0.50}(C)_{0.50}$ respectively. Amine functionality also varies somewhat in this order except in the case of $(BN)_{0.90}(C)_{0.10}$.

Mechanical properties of BCN reinforced PVA composites

Schematic representation of EG, BCN, and BN with their respective functional groups are displayed in **Figure 15**. FLOSS results reveal the presence of multitude of active surface functional groups such as carboxylic acid, amine, aldehyde, epoxy, and hydroxyl groups, which make them highly polar. Images of the EG, BCN, and BN nanosheets obtained through TEM are displayed in Figures 15 d, e, and f, respectively. The lateral dimensions of these sheets are in microns, which is above the critical length required for an effective reinforcement.[82] Edge rolling of the individual nanosheets leads to wrinkled morphology, which was suggested to enhance the interfacial adhesion with the polymer.[83] Given the exceptional mechanical properties of either graphene and BN reinforced polymer nanocomposites,[51] and the possibility of synergy when we combine BN and graphene, BCN appears to offer a substantial potential as filler material than either EG or BN alone. The latter have single domains of types B–N or C–C respectively. BCN, in contrast, can have B-N, C-C domains along with B-C-N rings, which makes it more interesting from the reinforcement perspective as it offers a high degree of chemical heterogeneity as shown by XPS and electrochemical measurements.

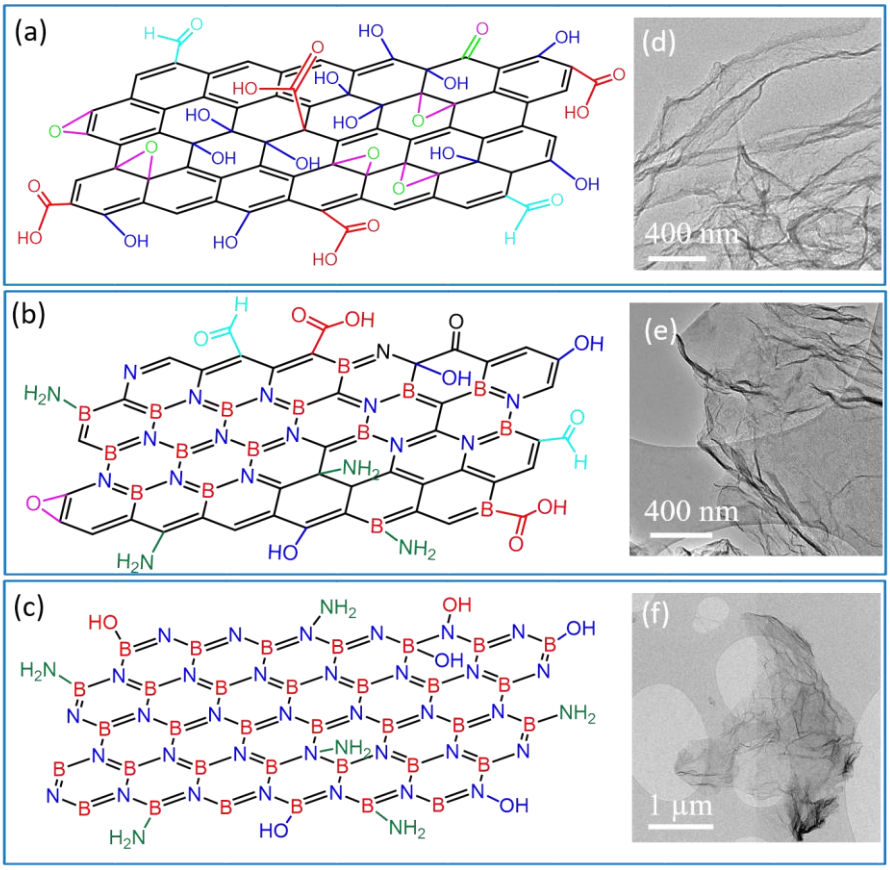

Figure 15. (a-c) Schematic representation of graphene, borocarbonitride and boron nitride with respective surface functional groups. (d-f) TEM images of respective nanosheets.

Characteristics of the BCN-PVA nanocomposites:

Scheme 2 shows the steps involved in the preparation of the BCN-PVA nanocomposites and their possible interaction at the molecular level. The polar functionalities present on the surface of the BCN can establish H-bonding with the hydroxyl groups present on PVA backbone, which is illustrated in Scheme 1. XRD analysis can provide valuable information on the crystallinity, orientation and size of ordered regions within the polymer matrix.[84] Representative XRD patterns obtained on pristine PVA, EG-PVA, BCN-PVA and BN-PVA nanocomposites are displayed in **Figure 16**a. In the base PVA, diffraction peaks at 11.5° and 19.5° correspond to diffractions from (110) and (101) planes respectively, give an indication of crystallinity in it. It is well known that the later, i.e., (101) diffraction peak of PVA, arises due to the intermolecular interference between PVA chains in the direction of the intermolecular hydrogen bonding.[84] Interestingly, all the BCN nanocomposites also show strong (101) diffraction peaks, which indicates to a higher crystallinity compared to pure PVA. This observation indicates that strong intermolecular H-

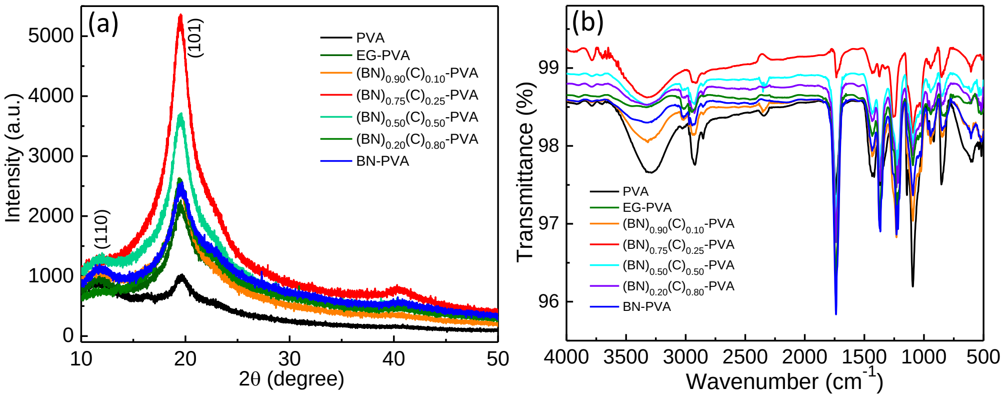

Figure 16. Characterization of EG, BCN and BN -PVA-nanocomposites. (a) X-ray diffraction patterns of nanocomposite along with pristine PVA (b) FTIR spectra EG, BCN and BN -PVA nanocomposites along with pristine PVA.

bonding occurs between PVA and BCN as well as the interaction of the filler material facilitates crystal growth preferably along (101) plane. The ratios of the intensity of the Bragg peaks associated with (101) to (110) planes of the nanocomposites are much higher than that observed in pristine PVA, which indicates higher degree of crystallinity in the former; for example, $I_{(101)}/I_{(110)}$ is 4.208 in the nanocomposite reinforced with 0.2 wt.% (BN)0.75(C)0.25, whereas it is only 1.061 in pristine PVA. The observation of a slight shift in the 2θ value of (101) plane also indicates to a strong interaction of the filler material with PVA.

FTIR is an efficient way to study the nature of hydrogen bonding and extent of it in the polymer composites. Figure 16b show FTIR spectra obtained on the

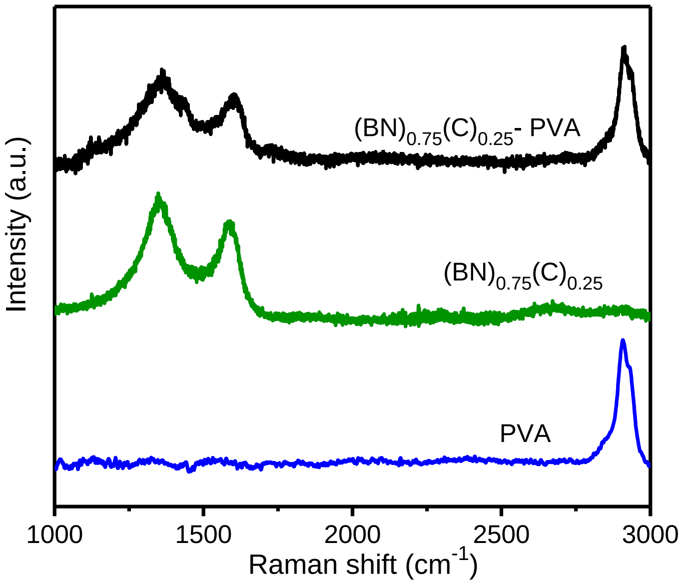

Figure 17. Raman spectrum of BCN-PVA nanocomposite in comparison with pristine PVA and BCN (BCN composition is BN)$_{0.75}$(C)$_{0.25}$).

nanocomposites along with pure PVA. The latter shows the characteristic band at 3282 cm^{-1}, which corresponds to the hydroxyl group absorption on the polymer backbone.[85] It shifts to a higher wave number upon the addition of filler to PVA, which again indicates stronger intermolecular interactions between BCN and PVA compared to hydrogen bonding within PVA.[86] A reduction in the intensity of –OH absorption in the composites further supports such strong interaction that takes place between the hydroxyl group of PVA and surface groups of BCN.[87] Raman spectra of nanocomposites (**Figure 17**) show the characteristic bands at 1350 and 1560 cm^{-1}, which correspond to BCN nanosheets, and at 2900 cm^{-1} that corresponds to PVA's optical phonon mode. No significant difference in the spectra collected at different places supports the conclusion about uniformity of nanosheet dispersion in the matrix. Cross-sectional FESEM images of BCN-PVA nanocomposites are displayed in **Figure 18**, which clearly show that the BCN nanosheets are embedded within the PVA matrix and uniformly distributed. To further confirm the uniformity of dispersion, the suspension was coated on Si and analysed; results show that good wetting of the nanosheets in the polymer matrix. SEM images (Figure 20c) also show the reinforced BCN nanosheets covered with PVA matrix and hence indicate a good adhesion to polymer.

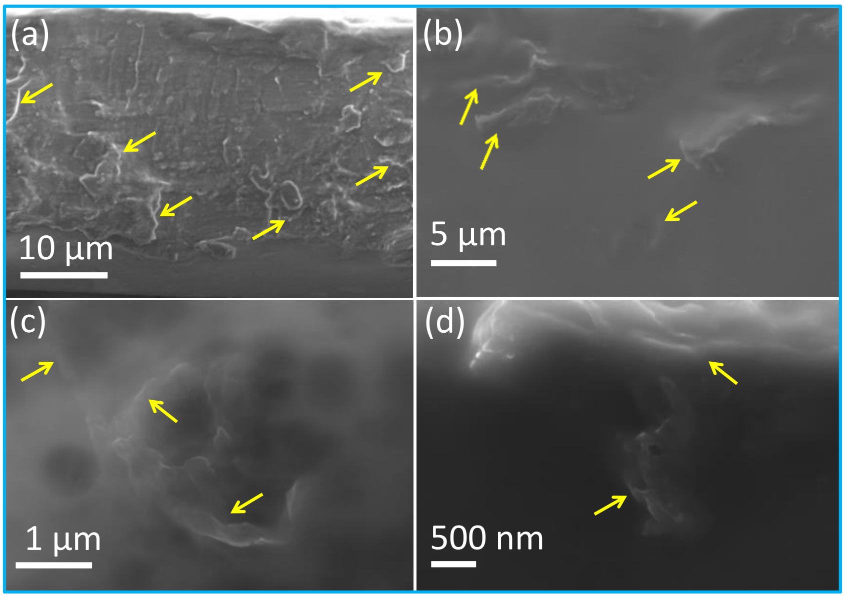

Figure 18. Characterization of BCN-PVA nanocomposites. (a-d) Cross-sectional FESEM images of BCN-PVA nanocomposite, the film is immersed in liquid nitrogen, fractured into pieces and fresh cut piece is taken for imaging.

Mechanical properties:

Representative load displacement (*P-h)* responses obtained from nanocomposites of BN, $(BN)_{0.90}(C)_{0.10}$, $(BN)_{0.75}(C)_{0.25}$, $(BN)_{0.50}(C)_{0.50}$, $(BN)_{0.20}(C)_{0.80}$ and EG to PVA matrix are displayed in **Figure 19**. Variations in the average values of *E* and *H*, extracted from these responses, with the composition are displayed in **Figure 20**. For the unreinforced PVA, *E* and *H* are 4.2±0.058 GPa and 76±1.2 MPa, respectively, which are within the ranges of respective values reported for PVA in literature.[88] Figure 20 shows that the addition of filler increases *E* to about 7 GPa, which is about 90% enhancement, irrespective of the filler type (be it EG, BN or BCN). The trends in *H* are different. The addition of either EG or BN to PVA enhances it to either 114 ± 5.1 or 109 ± 3.2 MPa respectively, which are themselves substantial at ~50% and ~43% respectively. The addition of BCN to PVA, by the same 0.2 wt.%, enhances *H* even further, with the $(BN)_{0.75}(C)_{0.25}$-PVA nanocomposite showing the highest *H* of 157 ± 3.4 MPa, i.e., more than double that of the base PVA. This result satisfies our initial expectation of synergistic benefit through the addition of BCN to PVA.

The substantial enhancement in the mechanical properties of the PVA upon the addition of nanofillers is possibly due to two factors: (i) an increase in the crystallinity within the polymer matrix and (ii) the reinforcement effect of the

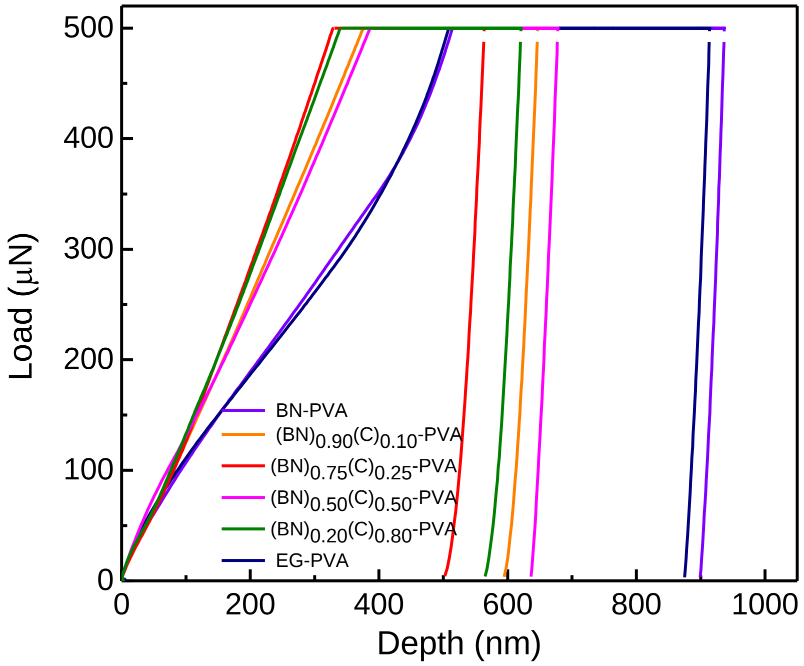

Figure 19. Load displacement (*P-h*) curves of EG, BCN and BN -PVA nanocomposites.

nanofillers give rise to substantially higher mechanical properties vis-a-vis PVA.[89] For the latter, an effective load transfer between the two constituent phases-the matrix and the nanofiller is essential, which strongly depends on the intermolecular H-bonding between PVA and BCN in the current context. Such a strong interaction restricts the mobility of the polymer chains, which, in turn, can alter the glass transition temperature (T_g) as well.[42, 87, 90] Since DSC is a suitable technique to determine both T_g and degree of crystallinity (χ) in a precise manner, DSC measurements were carried out for nanocomposites along with the pristine PVA. The results of these experiments are displayed in **Figure 21**, which show that the T_g of PVA (~78 °C) increases to 96 °C upon the addition of $(BN)_{0.75}(C)_{0.25}$. The observed increase in T_g, which is substantial, indicates strong molecular interaction of polymer chains with filler. This is further substantiated with the observations on the crystalline melting temperature (T_m). Both the pristine PVA and nanocomposites show T_m to be in the range of 180 to 200 °C; a slight increase in T_m of PVA on introduction of filler material suggests that it has a crucial effect on crystalline regions of PVA (Figure 21). The DSC scans obtained during cooling segment of the thermal cycle, also confirm the formation of newer nucleation centres on incorporation of fillers which in turn explain the inferred increase in crystallinity in them.

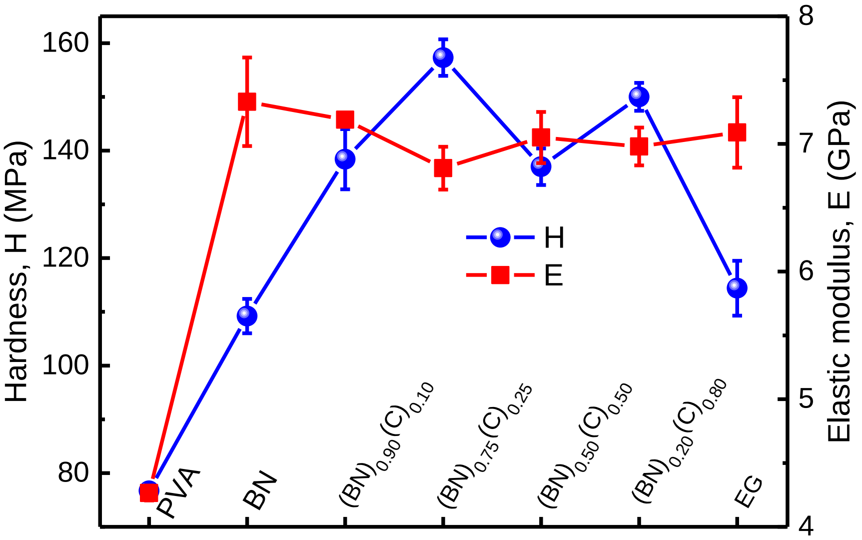

Figure 20. Mechanical properties of EG, BCN, and BN -PVA nanocomposites. Variation of hardness and elastic modulus of BCN-PVA nanocomposites across various BCN compositions along with BN and EG-PVA nanocomposites. Hardness and elastic modulus of pure PVA also shown for the comparison.

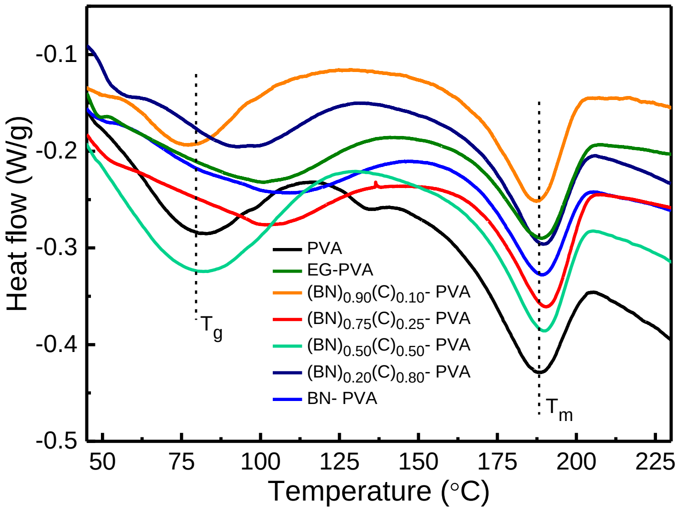

Figure 21. Degree of crystallinity and glass transition. DSC crystallite melting and glass transition curves of EG, BCN and BN –PVA nanocomposites along with pristine PVA.

Since PVA is a semi-crystalline polymer, the degree of crystallinity within it can alter its mechanical properties markedly. To examine this, we have plotted the variations manner. These observations suggest that the enhancement in *E* that was noted in all the nanocomposites is not due to increase in χ. Hence, it must be due to the stress transfer mechanism from the matrix to reinforcement phase[88, 91-92] which is aided by the strong interface between those two phases.[93] Since the *E* value of the reinforcement phase, be it EG or BN or BCN, is at least an order of magnitude higher than that of PVA, effective stress transfer leads to a substantially higher resistance to elastic deformation offered by the nanocomposites. This, in turn, results in the observed higher *E* of the nanocomposites. Furthermore, the results of XRD scans of the composites indicate that the filler material enhances the polymer chain alignment, i.e. BCN nanosheets sequentially arranged parallel to the PVA chains (Scheme 1). The

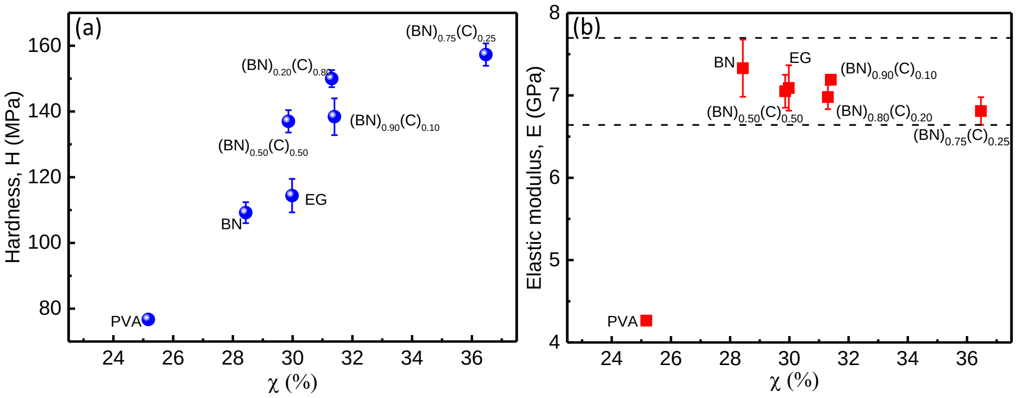

Figure 22. Mechanical properties vs degree of crystallinity. Variation of hardness (a) and elastic modulus (b) as a function of degree of crystallinity.

presence of the surface functional groups aids this process through strong intermolecular H-bonding. The alignment of the nanosheets and the presence of multitude of strong intermolecular interactions could be another reason for observed increase in *E*.

The enhancements observed in *H*, in contrast to that *E*, with the addition of BCN can be rationalized in turns of the observed positive correlation between *H* and χ. Since the hardness of any material is a measure of its resistance to plastic (or permanent) deformation, it is instructive to briefly examine the micromechanisms of plasticity in semi-crystalline polymers here. Typically, plasticity in these materials occurs, broadly, in four stages. They involve elongation of the chains that are in the amorphous regions, reorientation (or alignment) of the crystalline regions in the direction of the tensile stress, separation of crystalline units into chain-unfolded fibrillar structure, and finally tandem stretching of both the crystalline and amorphous regions. Since indentation made with a sharp tip involve large strains, the latter stages of deformation are especially relevant in the current context. Furthermore, the first two stages may not be that significant as such, given the high orientation that the BCN nanosheets induce within the polymers. Since the final stages are controlled by

Table 1. Summary of mechanical properties and degree of crystallinity of PVA matrix nanocomposites.

Nanocomposites	Degree of crystallinity (χ) (%)	Elastic modulus (*E*) (GPa)	Hardness (*H*) (MPa)
PVA	25.17	4.265±0.058	76.7±1.2
BN-PVA	28.43	7.33±0.347	109.2±3.2
$(BN)_{0.90}(C)_{0.10}$-PVA	31.40	7.19±0.038	138.4±5.6
$(BN)_{0.75}(C)_{0.25}$-PVA	36.47	6.81±0.168	157.3±3.4
$(BN)_{0.50}(C)_{0.50}$-PVA	29.86	7.05±0.200	137±3.4
$(BN)_{0.20}(C)_{0.80}$-PVA	31.31	6.98±0.148	150±2.6
EG-PVA	29.98	7.09±0.275	114.4±5.1

crystalline regions, we can infer that a polymer with a higher χ can offer considerably higher resistance to plastic deformation, which rationalizes the positive correlation found between H and χ in **Figure 22**. Since the addition BCN to PVA enhances the crystallinity in the latter, the substantially higher H in the nanocomposites can be attributed to the increased χ, which is facilitated by the presence of favorable surface functional groups in BCN.

5. Conclusions

The present study clearly demonstrates the success of FLOSS in determining the surface concentrations of functional groups on 2-D materials such as graphene and BN. The method is successful in the case of borocarbonitrides where both oxygen functionalities and amine groups respectively are quantitatively determined by FLOSS. The results on BCN are important in that they show the usefulness of the method in rather complex situations. The FLOSS results on carbonyl, carboxylic and amine groups are satisfactory. However, the hydroxyl group reaction does not give reliable result due to the lack of chemoselectivity. The concentrations of carbonyl and carboxylic groups increase with the carbon content and the surface areas. The FLOSS results on amine functionalities suggest this method to be a good way to characterize surface amine groups on other 2D layered materials as well. The specific capacitance of supercapacitors is small in the case of graphene although its surface area and surface functionalities are high. In the case of BCN, the samples show reasonable specific capacitance and ORR onset potential. We do not see any simple relation between specific capacitance and ORR onset potential with surface functionalities on these materials. The number of surface amine groups however, plays a crucial role on these properties. This present study has demonstrated potential applications of borocarbonitrides in catalysis and energy devices.

Polymer matrix nanocomposites with BCN dispersed in PVA were synthesized and characterized in detail. The high chemical heterogeneity of BCN and the method used for preparing it allows it to have several surface functional groups, which, in turn, makes it an interesting filler material for PMCs. These surface functionalities play a crucial role in the interfacial interaction between polymer and nanofiller. A 107% increment in hardness and 71% increment in elastic modulus were achieved by the addition of just 0.2 wt% of BCN to PVA. While the stiffness of the nanocomposites with varying chemical compositions of BCN are comparable with that of EG and BN nanocomposites, the hardness of the former are far superior to those reinforced with either BN or EG. The substantial improvement in the mechanical properties upon addition of nanofiller can be attributed to effective load transfer between the polymer matrix and the nanofiller, aided by H-bonding. Moreover, the surface roughness of these nanosheets not only improves the interfacial adhesion but also benefit as nucleation centers for the crystalline domains in the polymer. Thus an increase in the degree of crystallinity is observed. Furthermore, BCN reinforced PVA films have higher thermal stability as compared to pristine PVA. Hence, BCN nanosheets are superior reinforcement material for enhancing the mechanical and thermal properties of polymers as compared to well-studied graphene and BN. Also, BCN can be produced economically compared to carbon nanotubes and other kind of nanocarbons.

6. References

[1] A. K. Geim, *Science* **2009**, *324*, 1530-1534.

[2] C. N. R. Rao, A. K. Sood, K. S. Subrahmanyam, A. Govindaraj, *Angew. Chem. Int. Ed.*,**2009**, *48*, 7752-7777.

[3] C. N. R. Rao, U. Maitra, H. S. S. R. Matte, in *Graphene*, *Wiley-VCH* Verlag GmbH & Co. KGaA, **2012**, 1-47.

[4] A. S. Mayorov, R. V. Gorbachev, S. V. Morozov, L. Britnell, R. Jalil, L. A. Ponomarenko, P. Blake, K. S. Novoselov, K. Watanabe, T. Taniguchi, A. K. Geim, *Nano Lett.* **2011**, *11*, 2396-2399.

[5] K. S. Novoselov, A. K. Geim, S. V. Morozov, D. Jiang, Y. Zhang, S. V. Dubonos, I. V. Grigorieva, A. A. Firsov, *Science* **2004**, *306*, 666-669.

[6] D. J. Late, A. Ghosh, K. S. Subrahmanyam, L. S. Panchakarla, S. B. Krupanidhi, C. N. R. Rao, *Solid State Commun.* **2010**, *150*, 734-738.

[7] M. Z. Iqbal, S. Siddique, M. W. Iqbal, J. Eom, *J. Mater. Chem. C* **2013**, *1*, 3078-3083.

[8] C. N. R. Rao, K. Gopalakrishnan, A. Govindaraj, *Nano Today* **2014**, *9*, 324-343.

[9] M. Kota, N. S. Sharmila, U. V. Waghmare, C. N. R. Rao, *Mater. Res. Express* **2014**, *1*, 025603.

[10] X. Fan, Z. Shen, A. Q. Liu, J.-L. Kuo, *Nanoscale* **2012**, *4*, 2157-2165.

[11] K. Gopalakrishnan, K. Moses, A. Govindaraj, C. N. R. Rao, *Solid State Commun.* **2013**, *175–176*, 43-50.

[12] K. Gopalakrishnan, S. Sultan, A. Govindaraj, C. N. R. Rao, *Nano Energy* **2015**, *12*, 52-58.

[13] M. B. Sreedhara, H. S. S. R. Matte, A. Govindaraj, C. N. R. Rao, *Chem. Asian J.* **2013**, *8*, 2430-2435.

[14] K. Gopalakrishnan, C. N. R. Rao, *Mater. Res. Express* **2015**, *2*, 095503.

[15] K. Moses, V. Kiran, S. Sampath, C. N. R. Rao, *Chem.Asian J.* **2014**, *9*, 838-843.

[16] S.-M. Jung, E. K. Lee, M. Choi, D. Shin, I.-Y. Jeon, J.-M. Seo, H. Y. Jeong, N. Park, J. H. Oh, J.-B. Baek, *Angew. Chem. Int. Ed.* **2014**, *53*, 2398-2401.

[17] J. Zhu, C. He, Y. Li, S. Kang, P. K. Shen, *J. Mater. Chem. A* **2013**, *1*, 14700-14705.

[18] C. N. R. Rao, K. Gopalakrishnan, U. Maitra, *ACS Appl. Mater. Interfaces* **2015**, *7*, 7809-7832.

[19] T. Wu, H. Shen, L. Sun, B. Cheng, B. Liu, J. Shen, *New J. Chem.* **2012**, *36*, 1385-1391.

[20] G. Bepete, D. Voiry, M. Chhowalla, Z. Chiguvare, N. J. Coville, *Nanoscale* **2013**, *5*, 6552-6557.

[21] T.-W. Lin, C.-Y. Su, X.-Q. Zhang, W. Zhang, Y.-H. Lee, C.-W. Chu, H.-Y. Lin, M.-T. Chang, F.-R. Chen, L.-J. Li, *Small* **2012**, *8*, 1384-1391.

[22] Y. Zheng, Y. Jiao, L. Ge, M. Jaroniec, S. Z. Qiao, *Angew. Chem. Int. Ed.* **2013**, *52*, 3110-3116.

[23] X.-H. Li, M. Antonietti, *Angew. Chem. Int. Ed.* **2013**, *52*, 4572-4576.

[24] N. Kumar, K. Moses, K. Pramoda, S. N. Shirodkar, A. K. Mishra, U. V. Waghmare, A. Sundaresan, C. N. R. Rao, *J. Mater. Chem. A* **2013**, *1*, 5806-5821.

[25] Y. Xue, D. Yu, L. Dai, R. Wang, D. Li, A. Roy, F. Lu, H. Chen, Y. Liu, J. Qu, *Phys. Chem. Chem. Phys.* **2013**, *15*, 12220-12226.

[26] R. Kumar, K. Gopalakrishnan, I. Ahmad, C. N. R. Rao, *Adv. Funct. Mater.* **2015**, *25*, 5910-5917.

[27] L. Ci, L. Song, C. Jin, D. Jariwala, D. Wu, Y. Li, A. Srivastava, Z. F. Wang, K. Storr, L. Balicas, F. Liu, P. M. Ajayan, *Nat Mater* **2010**, *9*, 430-435.

[28] Y. Xing, N. Dementev, E. Borguet, *Curr. Opin. Solid State Mater. Sci.* **2007**, *11*, 86-91.

[29] N. Dementev, X. Feng, E. Borguet, *Langmuir* **2009**, *25*, 7573-7577.

[30] C. F. Chiu, N. Dementev, E. Borguet, *J. Phys. Chem. A* **2011**, *115*, 9579-9584.

[31] T. Pellenbarg, N. Dementev, R. Jean-Gilles, C. Bessel, E. Borguet, N. Dollahon, R. Giuliano, *Carbon* **2010**, *48*, 4256-4267.

[32] X. Feng, N. Dementev, W. Feng, R. Vidic, E. Borguet, *Carbon* **2006**, *44*, 1203-1209.

[33] S. R. Holmes-Farley, G. M. Whitesides, *Langmuir* **1986**, *2*, 266-281.

[34] A. Holländer, *Surf. Interface Anal.* **2004**, *36*, 1023-1026.

[35] C. Funk, P. M. Dietrich, T. Gross, H. Min, W. E. S. Unger, W. Weigel, *Surf. Interface Anal.* **2012**, *44*, 890-894.

[36] V. B. Ivanov, J. Behnisch, A. Holländer, F. Mehdorn, H. Zimmermann, *Surf. Interface Anal.* **1996**, *24*, 257-262.

[37] E. A. McArthur, T. Ye, J. P. Cross, S. Petoud, E. Borguet, *J. Am. Chem. Soc.* **2004**, *126*, 2260-2261.

[38] J. Njuguna, K. Pielichowski, S. Desai, *Polym. Adv. Technol.* **2008**, *19*, 947-959.

[39] T. Ramanathan, A. A. Abdala, S. Stankovich, D. A. Dikin, M. Herrera-Alonso, R. D. Piner, D. H. Adamson, H. C. Schniepp, X. Chen, R. S. Ruoff, S. T. Nguyen, I. A. Aksay, R. K. Prud'Homme, L. C. Brinson, *Nat. Nanotechnol.* **2008**, *3*, 327.

[40] T. Keller, *Prog. Struct. Mater. Eng.* **2001**, *3*, 132-140.

[41] P. Liu, Z. Jin, G. Katsukis, L. W. Drahushuk, S. Shimizu, C.-J. Shih, E. D. Wetzel, J. K. Taggart-Scarff, B. Qing, K. J. Van Vliet, R. Li, B. L. Wardle, M. S. Strano, *Science* **2016**, *353*, 364-367.

[42] J. Liang, Y. Huang, L. Zhang, Y. Wang, Y. Ma, T. Guo, Y. Chen, *Adv. Funct. Mater.* **2009**, *19*, 2297-2302.

[43] S. K. Sharma, J. Prakash, P. K. Pujari, *PCCP* **2015**, *17*, 29201-29209.

[44] S. Morimune, T. Nishino, T. Goto, *Polym. J.* **2012**, *44*, 1056.

[45] M. Cano, U. Khan, T. Sainsbury, A. O’Neill, Z. Wang, I. T. McGovern, W. K. Maser, A. M. Benito, J. N. Coleman, *Carbon* **2013**, *52*, 363-371.

[46] K. E. Prasad, B. Das, U. Maitra, U. Ramamurty, C. N. R. Rao, *PNAS* **2009**, *106*, 13186-13189.

[47] R. Kumar, D. Raut, U. Ramamurty, C. N. R. Rao, *Angew. Chem. Int. Ed.* **2016**, *128*, 7988-7992.

[48] M. P. Levendorf, C.-J. Kim, L. Brown, P. Y. Huang, R. W. Havener, D. A. Muller, J. Park, *Nature* **2012**, *488*, 627.

[49] N. Kumar, K. Moses, K. Pramoda, S. N. Shirodkar, A. K. Mishra, U. V. Waghmare, A. Sundaresan, C. N. R. Rao, *J. Mater. Chem. A* **2013**, *1*, 5806-5821.

[50] C. N. R. Rao, K. Gopalakrishnan, *ACS Appl. Mater. Interfaces* **2017**, *9*, 19478-19494.

[51] R. Jan, P. May, A. P. Bell, A. Habib, U. Khan, J. N. Coleman, *Nanoscale* **2014**, *6*, 4889-4895.

[52] C. N. R. Rao, K. Gopalakrishnan, *ACS Appl. Mater. Interfaces* **2017**, *9*, 19478–19494.

[53] M. B. Sreedhara, K. Gopalakrishnan, B. Bharath, R. Kumar, G. U. Kulkarni, C. N. R. Rao, *Chem. Phys. Lett.* **2016**, *657*, 124-130.

[54] K. S. Subrahmanyam, S. R. C. Vivekchand, A. Govindaraj, C. N. R. Rao, *J. Mater. Chem.* **2008**, *18*, 1517-1523.

[55] W. S. Hummers, R. E. Offeman, *J. Am. Chem. Soc.* **1958**, *80*, 1339-1339.

[56] K. S. Subrahmanyam, S. R. C. Vivekchand, A. Govindaraj, C. N. R. Rao, *J. Mater. Chem.* **2008**, *18*, 1517-1523.

[57] A. Nag, K. Raidongia, K. P. S. S. Hembram, R. Datta, U. V. Waghmare, C. N. R. Rao, *ACS Nano* **2010**, *4*, 1539-1544.

[58] A. Jana, S. Atta, S. K. Sarkar, N. D. P. Singh, *Tetrahedron* **2010**, *66*, 9798-9807.

[59] B. Gong, B.-K. Choi, J.-Y. Kim, D. Shetty, Y. H. Ko, N. Selvapalam, N. K. Lee, K. Kim, *J. Am. Chem. Soc.* **2015**, *137*, 8908-8911.

[60] C. Klapperich, K. Komvopoulos, L. Pruitt, *J. Tribol.* **2000**, *123*, 624-631.

[61] S. B. Kadambi, K. Pramoda, U. Ramamurty, C. N. R. Rao, *ACS Appl. Mater. Interfaces* **2015**, *7*, 17016-17022.

[62] B. J. Briscoe, L. Fiori, E. Pelillo, *JJ. Phys. D: Appl. Phys.* **1998**, *31*, 2395.

[63] W. C. Oliver, G. M. Pharr, *J. Mater. Res.* **2011**, *7*, 1564-1583.

[64] S. Sandoval, N. Kumar, A. Sundaresan, C. N. R. Rao, A. Fuertes, G. Tobias, *Chem. Eur. J.* **2014**, *20*, 11999-12003.

[65] R. D. Leapman, P. L. Fejes, J. Silcox, *Phys. Rev. B* **1983**, *28*, 2361-2373.

[66] R. Arenal, M. Kociak, N. J. Zaluzec, *Appl. Phys. Lett.* **2007**, *90*, 204105.

[67] M. Wibbelt, H. Kohl, P. Kohler-Redlich, *Phys. Rev. B* **1999**, *59*, 11739-11745.

[68] Y. Gu, M. Zheng, Y. Liu, Z. Xu, *J. Am. Ceram. Soc.* **2007**, *90*, 1589-1591.

[69] K. S. W. Sing, D. H. Everett , R. A. W. Haul , L. Moscou, R. A. Pierotti, J. Rouquerol , T. Siemieniewska, *Pure Appl. Chem.* **1984**, *57*, 603-619.

[70] C. Huang, C. Chen, M. Zhang, L. Lin, X. Ye, S. Lin, M. Antonietti, X. Wang, *Nat Commun* **2015**, *6*, 7698.

[71] S. Park, Y. Hu, J. O. Hwang, E.-S. Lee, L. B. Casabianca, W. Cai, J. R. Potts, H.-W. Ha, S. Chen, J. Oh, S. O. Kim, Y.-H. Kim, Y. Ishii, R. S. Ruoff, *Nat Commun* **2012**, *3*, 638.

[72] H. He, T. Riedl, A. Lerf, J. Klinowski, *J. Phys. Chem.* **1996**, *100*, 19954-19958.

[73] P. S. Marchetti, D. Kwon, W. R. Schmidt, L. V. Interrante, G. E. Maciel, *Chem. Mater.* **1991**, *3*, 482-486.

[74] S. Flink, F. C. J. M. van Veggel, D. N. Reinhoudt, *Adv. Mater.* **2000**, *12*, 1315-1328.

[75] S. W. Song, K. Hidajat, S. Kawi, *Langmuir* **2005**, *21*, 9568-9575.

[76] E. Gallegos-Suarez, M. Pérez-Cadenas, A. Guerrero-Ruiz, I. Rodriguez-Ramos, A. Arcoya, *Appl. Surf. Sci.* **2013**, *287*, 108-116.

[77] H. Gong, S.-T. Kim, J. D. Lee, S. Yim, *Appl. Surf. Sci.* **2013**, *266*, 219-224.

[78] H. P. Boehm, E. Diehl, W. Heck, R. Sappok, *Angew. Chem. Int. Ed.* **1964**, *3*, 669-677.

[79] H. Hu, P. Bhowmik, B. Zhao, M. A. Hamon, M. E. Itkis, R. C. Haddon, *Chem. Phys. Lett.* **2001**, *345*, 25-28.

[80] Y. Xing, E. Borguet, *Langmuir* **2007**, *23*, 684-688.

[81] K. F. Mak, J. Shan, T. F. Heinz, *Phys. Rev. Lett.* **2011**, *106*, 046401.

[82] G. Mittal, V. Dhand, K. Y. Rhee, S.-J. Park, W. R. Lee, *J. Ind. Eng. Chem.* **2015**, *21*, 11-25.

[83] C. Androulidakis, E. N. Koukaras, J. Rahova, K. Sampathkumar, J. Parthenios, K. Papagelis, O. Frank, C. Galiotis, *ACS Appl. Mater. Interfaces* **2017**, *9*, 26593-26601.

[84] P.-D. Hong, J.-H. Chen, H.-L. Wu, *J. Appl. Polym. Sci.* **1998**, *69*, 2477-2486.

[85] J. Chen, Y. Gao, W. Liu, X. Shi, L. Li, Z. Wang, Y. Zhang, X. Guo, G. Liu, W. Li, B. D. Beake, *Carbon* **2015**, *94*, 845-855.

[86] Y. Zhu, H. Wang, J. Zhu, L. Chang, L. Ye, *Appl. Surf. Sci.* **2015**, *349*, 27-34.

[87] M. Mohsin, A. Hossin, Y. Haik, *J. Appl. Polym. Sci.* **2011**, *122*, 3102-3109.

[88] M. Cadek, J. N. Coleman, V. Barron, K. Hedicke, W. J. Blau, *Appl. Phys. Lett.* **2002**, *81*, 5123-5125.

[89] L. S. Schadler, S. C. Giannaris, P. M. Ajayan, *Appl. Phys. Lett.* **1998**, *73*, 3842-3844.

[90] D. Barun, K. E. Prasad, U. Ramamurty, C. N. R. Rao, *Nanotechnology* **2009**, *20*, 125705.

[91] J. N. Coleman, M. Cadek, R. Blake, V. Nicolosi, K. P. Ryan, C. Belton, A. Fonseca, J. B. Nagy, Y. K. Gun'ko, W. J. Blau, *Adv. Funct. Mater.* **2004**, *14*, 791-798.

[92] L. Gong, I. A. Kinloch, R. J. Young, I. Riaz, R. Jalil, K. S. Novoselov, *Adv. Mater.* **2010**, *22*, 2694-2697.

[93] Z. Li, R. J. Young, I. A. Kinloch, *ACS Appl. Mater. Interfaces* **2013**, *5*, 456-463.

[94] Y.-J. Wan, L.-C. Tang, L.-X. Gong, D. Yan, Y.-B. Li, L.-B. Wu, J.-X. Jiang, G.-Q. Lai, *Carbon* **2014**, *69*, 467-480.

Chapter II.2

Synthesis and Characterization of Few-layer Nanosheets of GaN and Other Metal Nitrides

SUMMARY*

By making use of the fact that single- and few-layer nanosheets of GaS and GaSe are readily obtained by micromechanical cleavage because of their mica-like morphology, we have been able to prepare GaN nanosheets by the reaction of these chalcogenide nanosheets with ammonia at 600-650 ºC. The nitride nanosheets have been characterized by transmission electron microscopy, atomic force microscopy and other methods. Few-layer VN has been obtained by high-temperature ammonolysis of exfoliated V_2O_5 sheets. Ammonolysis of MoO_3 and MoS_2 nanosheets yields the nitride nanosheets.

---

*A paper based on this work has appeared in Zeitschrift für anorganische und allgemeine Chemie (2014).

1. Introduction

Motivated by recent research on graphene,[1] the two-dimensional one-atom-thick sheet of sp^2 carbon atoms, there has been considerable effort in investigating nanosheets (NSs) of other layered inorganic materials. The materials include transition metal dichalcogenides as well as metal oxides and metal-organic frameworks (MOFs).[2] Amongst the transition metal dichalcogenides, MoS_2 has gained considerable importance due to the novel electronic structure and properties of the nanosheets.[2a, 3] Two-dimensional nanosheets of layered metal oxides such as MoO_3 and V_2O_5 have been explored.[4] The study of layered nitrides is limited to BN which is structurally similar to graphene. The BN nanosheets have been prepared by various methods and their properties investigated,[5] but there has been no study of nanosheets of GaN and other nitrides to-date.

Low-dimensional nanostructures of metal nitrides are of interest due to their use in optical and electronic devices.[6] Among the group III nitrides, GaN has gained importance due to band gap tunability and use in optoelectronic devices.[7] GaN crystallizes in the hexagonal crystal structure with (002) preferred orientation. A monolayer of GaN having planar graphene-like structure has three-fold co-ordinated atoms.[8] Bi- and tri-layer GaN planar sheets obtained by the different types of stacking have been described.[8] Thin films of GaN have been grown on solid substrates by using MBE, MOCVD, ALD and other methods.[9] Preparation of metal nitride NSs by chemical methods is not reported, but there has been some effort to obtain different morphologies of nitride nanostructures by nitridation of oxides, phosphides, sulphides, metals and other materials.[10] In this context, the transformation of GaN nanowalls by nitridation of GaS nanowalls is noteworthy.[11] Chemical transformation of oxides or sulfides to nitride NSs is of value although such methods may lead to other morphologies.[12] Transition metal nitrides such as VN and MoN are known for mechanical, electrochemical and superconducting properties.[13] While transition metal nitrides with different morphologies have been synthesized,[14] to the best of our knowledge, there is no report of the preparation of the nitride NSs by the transformation of few-layer sulfides or oxides.

2. Scope of the present investigations

Discovery of graphene has opened up exploring physical and chemical properties of two-dimensional nanostructures such as nanosheets. In this context 2D inorganic materials such as transition metal dichalcogenides and oxides have been studied extensively. Recently monolayers of van der Waal oxides and sulphides have been explored and these studies evidence the exceptional properties at the atomically thin nanoscale regime and promising applications of nanosheets from optoelectronics to biology. The layered structure held with weak van der Waals force facilitates an easy approach toward obtaining single or few -layers via mechanical peeling. However, obtaining semiconductors planer nanosheets without intrinsic graphene-like structures is a key challenge. The metal nitride in particularly group-III nitrides and transition metal nitrides nanosheets are of interest due to their exceptional properties and nanosheets of these nitrides are not explored. Among, the gallium nitride (GaN) is a novel wide-gap semiconductor with tunable optoelectronic properties. Hence crystalline 2D single-layer GaN nanosheets hold great interest to study the fundamental properties and application. Similarly, the transition metal nitrides nanosheets also of interest to explore. We have prepared GaN nanosheets by the reaction of GaS and GaSe nanosheets with ammonia. Since GaS and GaSe have mica-like morphology one can readily obtain nanosheets (single to few layers) by micromechanical cleavage.[12] We believe that such simple synthesis of GaN nanosheets would have practical utility. We show that VN and MoN NSs can be prepared starting with few-layer V_2O_5 and MoO_3. Nanosheets of V_2O_5 and MoO_3 could be exfoliated by simple chemical means.

3. Experimental Section

Synthesis

Preparation of GaN NSs from few-layer GaS/GaSe:

Few-layer GaS/GaSe was prepared by micro-mechanical exfoliation[19] from bulk GaS/GaSe (>99.99 %) using scotch tape. The few-layer NSs were transferred on to a solid substrate (quartz or silicon). As transferred few-layer NSs of GaS/GaSe were heated under a continuous flow of ammonia gas (Chemix, 99.999 %) at 650 ºC for 5 h in a tube furnace to obtain NSs of GaN. The few-layer GaSe NSs transform into GaN NSs even at 600 ºC but in the case of GaS some amount sulfur remains at this temperature.

Preparation of few-layer V_2O_5 NSs and transformation into VN NSs:

Few-layer V_2O_5 nanosheets were prepared by method described elsewhere.[17] In a typical synthesis, bulk V_2O_5 (Sigma aldrich, 99.6 %) powder (100 mg) and ammonium persulfate (4.5 g, s d fine, 98 %) were dissolved in de-ionised water. The resulting clear solution was stirred at 55 ºC for two days and then freeze-dried in vacuum overnight using a lyophilizer. This leads to the formation of $(NH_4)_2V_6O_{16}$. The product so obtained was highly hygroscopic and was immediately heated to 400 ºC to obtain few-layer NSs of V_2O_5. Few-layer V_2O_5 nanosheets were heated in a tube furnace in a flow of ammonia at 500 ºC for 4h to produce VN NSs.

Preparation of MoN NSs from few-layer MoO_3:

Ultrathin NSs of few-layer MoO_3 was prepared by the oxidation of few-layer MoS_2.[2c] The few-layer oxide was converted into nitride NSs by heating in a tube furnace at 700 ºC for 6 h under a continuous flow of ammonia.

Characterization

Powder X-ray diffraction (PXRD) measurements were recorded using a Bruker D8 Discover diffractometer and Rigaku-99 diffractometer with Cu Kα radiation. GaN NSs were characterized by FESEM, Energy Dispersive X-ray Analysis (EDX) and other physical methods. The nanosheets were imaged using a Nova NanoSEM 600 FESEM system (FEI Company). Transmission electron microscope (TEM) images were recorded using JEOL JEM 3010 microscope, fitted with a Gatan CCD camera operating at an accelerating voltage of 300 kV. Atomic force microscope (AFM) imaging in contact mode was carried out in a Bruker Innova instrument. Electronic absorption spectra were recorded in a Perkin-Elmer Lambda 900 UV/Vis/NIR spectrometer in the diffuse reflectance mode. Photoluminescence measurements of GaN were recorded in Fluorolog-3 spectrophotometer using a Horiba Jobin Yvon Xe

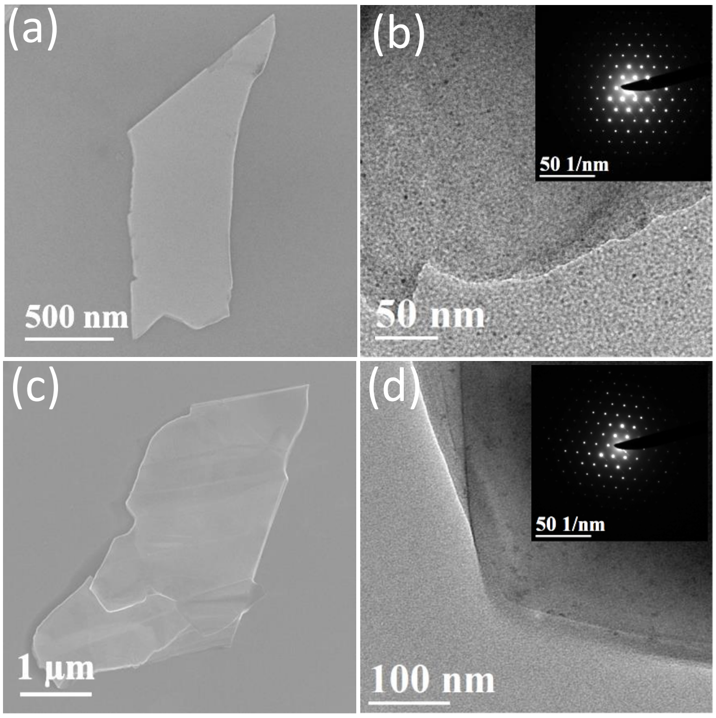

Figure 1. FESEM and TEM images of few-layer GaS (a, b) and GaSe (c,d) prepared by micro-mechanical exfoliation. Insets of the TEM images show electron diffraction patterns.

lamp as light source. Raman spectra were recorded in the backscattering geometry using a 632 nm HeNe laser with a Jobin Yvon LabRam HR spectrometer.

4. Results and Discussion

GaN nanosheets

Heating few-layer GaS or GaSe NSs in ammonia around 650 ºC results in the formation GaN NSs with the wurtzite structure. In **Figure 1**, we show the FESEM and TEM images of as-prepared few-layer GaS and GaSe NSs, which clearly indicate their mica-like morphology. These 2D flakes show characteristic optical contrast and can be readily identified under an optical microscope.[12] Electron diffraction (ED) patterns shown in the insets of Figure 1b and d indicate the samples to be highly crystalline with hexagonal symmetry. **Figure 2** shows FESEM and TEM images of GaN NSs obtained by heating few-layer GaS and GaSe in NH_3 at 650 ºC and 600 ºC respectively. These images reveal that the initial NS morphology of the chalcogenide is retained after nitridation. The EDX spectrum shows peaks corresponding to Ga and N with no sulphur or selenium left behind (**Figure 3**a). The ED patterns shown as insets of Figure

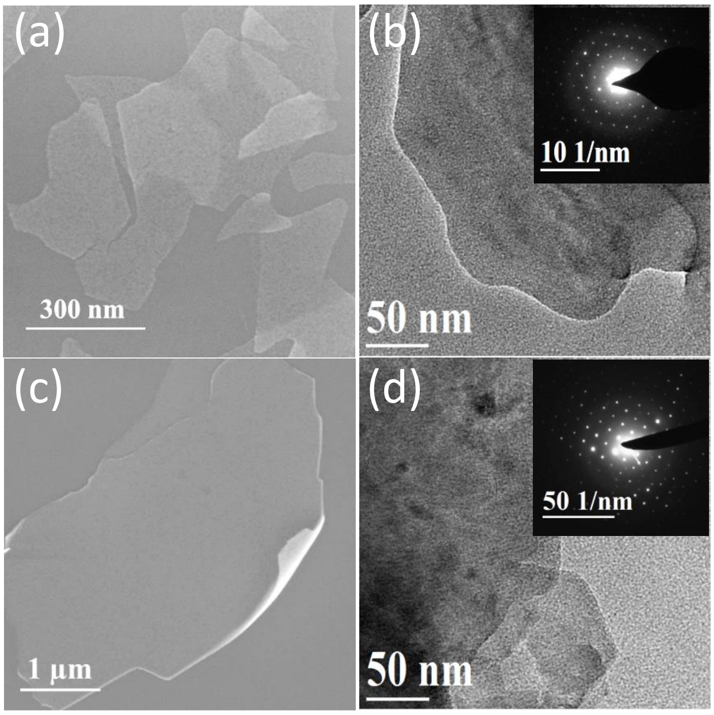

Figure 2. FESEM and TEM images of GaN nanosheets prepared from few-layer GaS (a, b) and GaSe (c, d). Insets of TEM images show ED patterns.

2b and d indicate that GaN has the expected wurtzite structure. Heating beyond 700 ºC during ammonolysis results in breaking up of the nitride NSs. XRD patterns show characteristic patterns of GaN (Figure 3b). EDAX of powders showed no traces of GaS or GaSe after ammonolysis.

AFM images with the height profiles of few-layer GaS and GaSe are shown in **Figure 4**a and c respectively. The images show thin flake-like morphology with a thickness of 2.3 and 3.0 nm which corresponding to 2-3 layers. Figure 4b and d show AFM images and the height profiles of GaN NSs obtained from few-layer GaS and

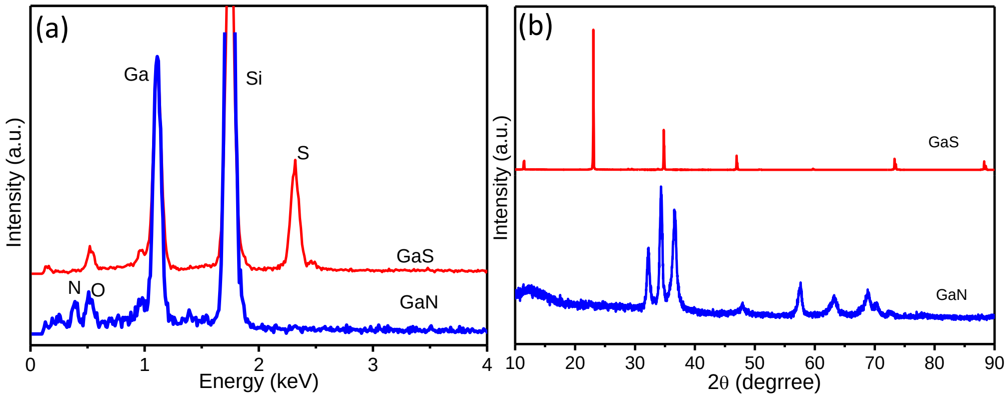

Figure 3. (a) Energy dispersive X-ray analysis of GaN and GaS. (b) PXRD patterns of GaS and GaN nanosheets. The patterns of GaN from GaSe was similar.

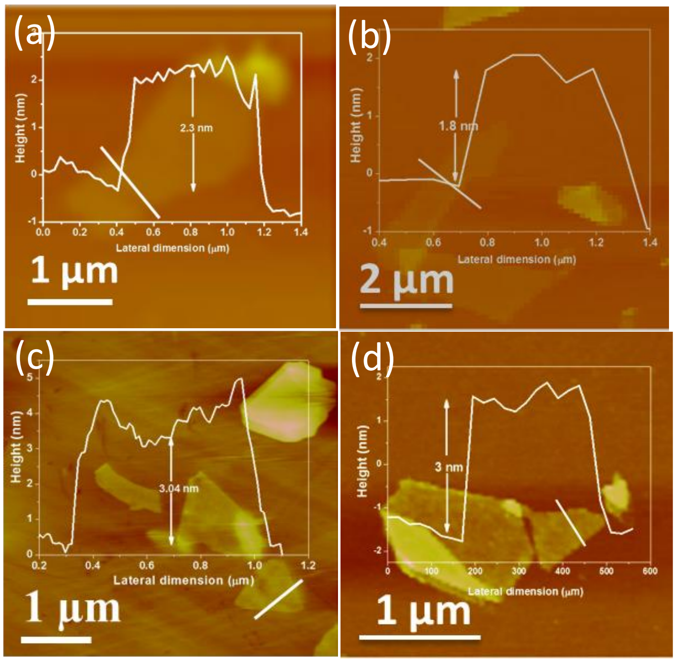

Figure 4. AFM image with a corresponding height profile of (b) GaN nanosheets prepared from few-layer GaS (a). (d) GaN nanosheets prepared from few-layer GaSe (c).

GaSe. The NS morphology is retained in the nitrides and the thickness of GaN nanosheets is 1.8 nm and 3.0 nm respectively corresponding to 6-10 layers. Single layer GaN can be obtained by ammonolysis of single-layer GaS or GaSe deposited on a solid substrate.

Transformation of few-layer GaS and GaSe to GaN is further confirmed by photoluminescence and Raman spectroscopy. In **Figure** 5A and B, we show room temperature photoluminescence spectra of GaN NSs obtained from few-layer GaS and GaSe. The deconvoluted PL spectrum of GaN NSs obtained from few-layer GaS exhibits a prominent band centered at 3.43 eV due to the band edge emission and a broad band centered at 2.93 eV due to blue emission.[15] The photoluminescence spectrum of GaN NSs obtained from few-layer GaSe shows similar features. Raman spectra of GaN NSs show the bands exhibited by bulk GaN with minor shifts. Thus E_2^2 mode redshifts in the NSs compared to the bulk due to compressive strain.[16]

VN and MoN nanosheets

We have synthesized VN NSs from few-layer V_2O_5. In V_2O_5, the layers are stacked along the *c* direction and are held together by van der Waals forces. Few-layer V_2O_5 is prepared by the reaction of ammonium persulfate with bulk V_2O_5.[17] Few-layer V_2O_5 crystallizes in orthorhombic crystal structure (space group: *Pmmn, a* =

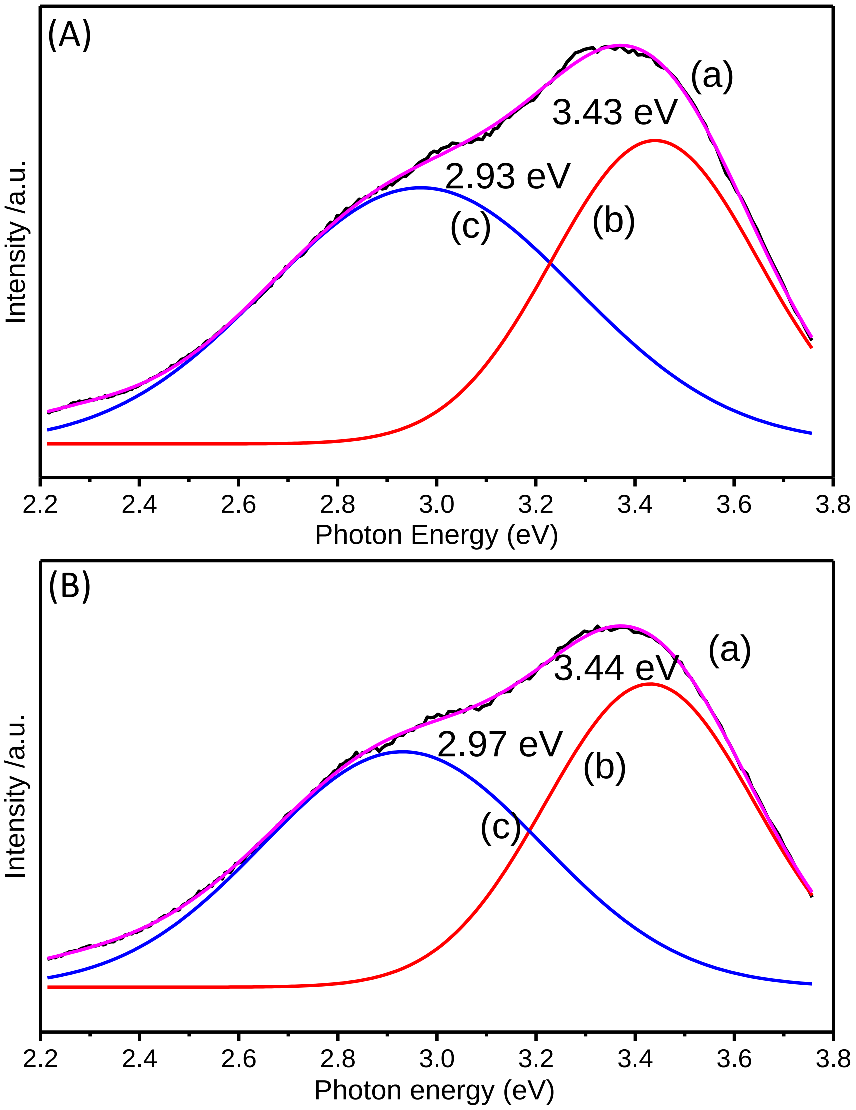

Figure 5. Room temperature photoluminescence spectra of GaN nanosheets prepared from few-layer GaS (A) and GaSe (B).; (a) Sum of the fitted curve with experimental data, (b) band edge emission, (c) defect-related emission.

11.5160Å, *b* = 3.5656Å and *c* = 4.3727Å, JCPDS No: 41-1426). In the PXRD patterns of the few-layer sample, the relative intensity of *(001)* plane is decreased as compared to bulk V_2O_5 (**Figure 6**A). In Figure 6B, we show the UV-visible absorption spectrum of few-layer V_2O_5 along with that of the bulk material. The absorption maxima of few-layer and bulk material are around 475 nm 434 nm respectively, the blue-shift in the absorption maximum in the few-layer sample being expected in nanostructures.[18] On reaction with NH_3, the V_2O_5 nanosheets gave nanosheets of VN as indicated by the XRD pattern (**Figure 7**a). VN NSs crystallize in the fcc structure (space group: *Fm*-3*m*, *a* = 4.137Å, JCPDS No: 78-1315). In **Figure 8**a and b we show the TEM images of few-layer V_2O_5 and VN NSs. The thin layers confirm the retention of nanosheet

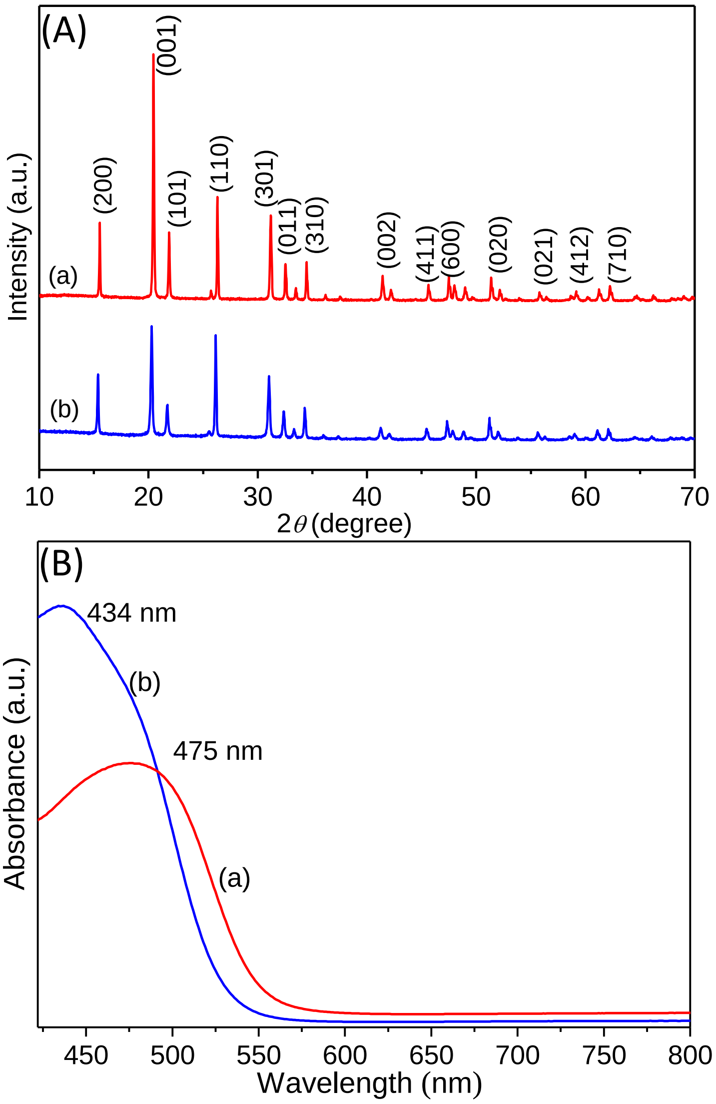

Figure 6. (A) PXRD patterns of (a) bulk and (a) few-layer nanosheets of V_2O_5. (B) UV-Vis absorption spectra of (a) bulk V_2O_5 and (b) few-layer nanosheets of V_2O_5.

morphology. The ED pattern shown in the inset of Figure 8a is due to the orthorhombic few-layer V_2O_5. AFM images and height profiles of VN nanosheets reveal that the morphology of the few-layer oxide (**Figure 9**a) is essentially retained after nitridation (Figure 9b). The thickness of the VN layer was 2.7 nm while the starting V_2O_5 nanosheet was 2.5 nm thick. The breadth of the XRD reflections of VN in **Figure** 7 arises from the presence of small particles on the nanosheets.

We prepared MoO_3 nanosheets by the literature procedure.[2c] On heating these nanosheets in NH_3 at 700 °C, we obtained nitride nanosheets. We show the XRD pattern in Figure 7a. MoN NSs crystallize in the hexagonal crystal structure (space group: $P6_3mc$, a = 5.745Å and c = 5.622Å, JCPDS No: 89-5024). In addition to hexagonal MoN, we also see reflections at $2\theta = 43^\circ$ and 62.5° corresponding to

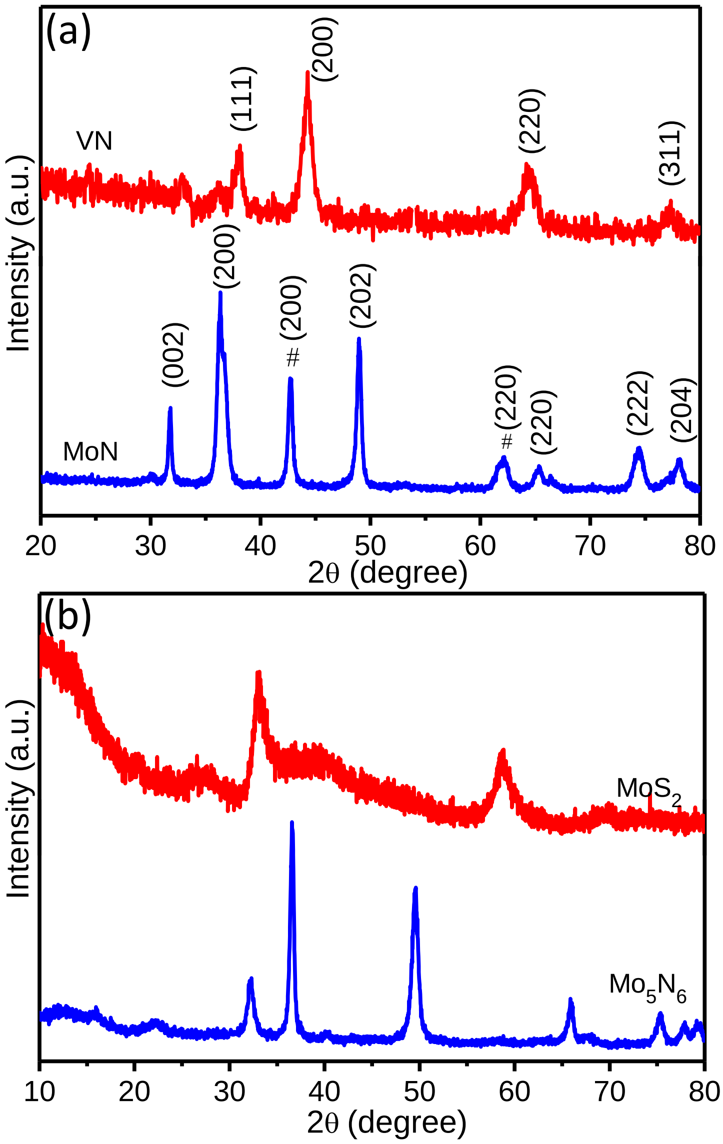

Figure 7. (a) PXRD patterns of VN and MoN nanosheets. (#) corresponds to Mo_2N. (b) PXRD patterns of (a) few-layer MoS_2 (b) Mo_5N_6 nanosheets.

tetragonal Mo_2N. The broadness of peaks in the PXRD pattern arises due to the presence of two nanostructures. In Figure 8c and d we show TEM images of few-layerNSs of MoO_3 and molybdenum nitride, inset of Figure 8a & c shows ED pattern orthorhombic MoO_3 NSs. MoO_3 NSs transform to nanosheets containing a mixture of hexagonal MoN and tetragonal Mo_2N phases. We have obtained AFM images and height profiles of molybdenum nitride nanosheets (Figure 9d) with a thickness of 1.86 ED pattern of MoO_3 NSs. MoO_3 NSs transform to nanosheets containing a mixture of nm whereas the MoO_3 nanosheet was 1.65 nm thick (single layer MoO_3 1.4 nm). TEM and AFM studies reveal that the NS morphology is retained after nitridation at 700 ºC. It should be possible to optimize conditions to obtain nanosheets of only one of the

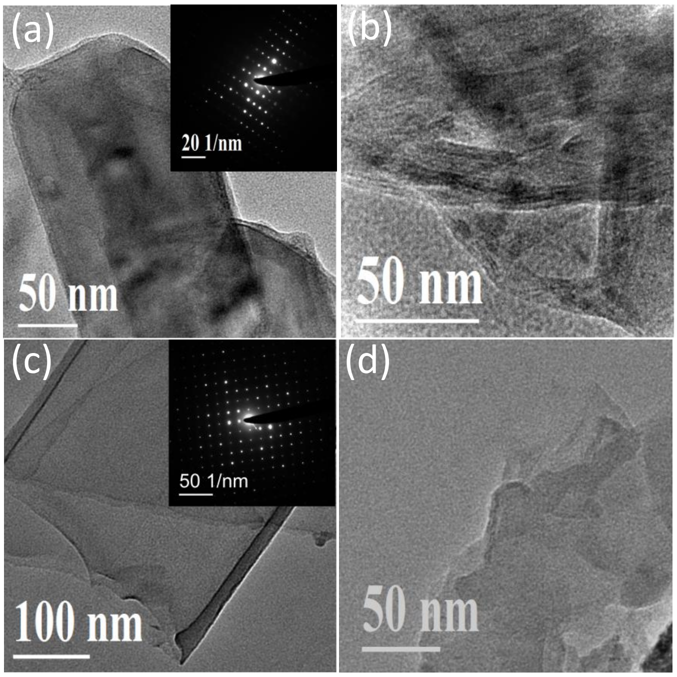

Figure 8. TEM images of VN (b) nanosheets prepared from few-layer V_2O_5 (a) and MoN (d) nanosheets prepared from few-layer MoO_3 (c). Insets (a) and (c) shows corresponding ED patterns.

Mo nitrides. We have carried out ammonolysis of few-layer MoS_2 at 700 ºC and obtained nanosheets of the composition Mo_5N_6 (Figure 7b).

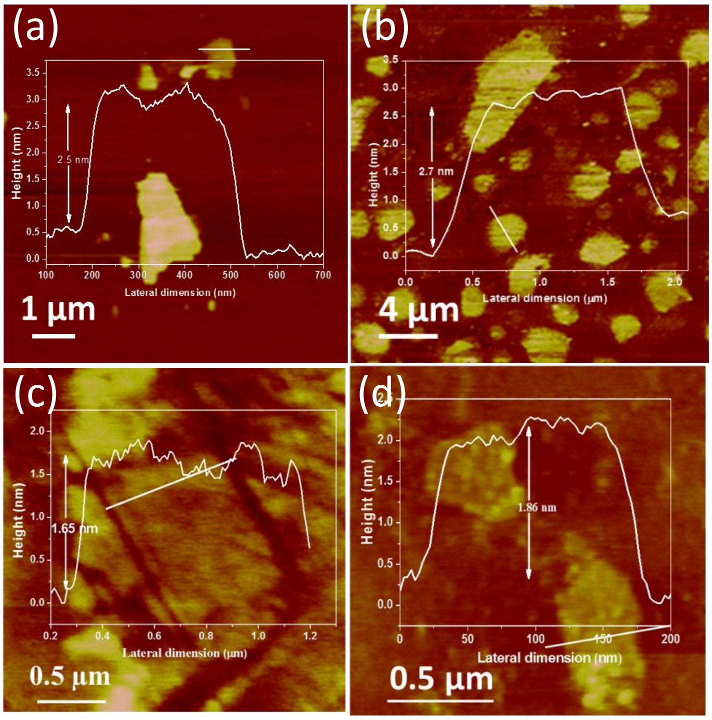

Figure 9. AFM images with a corresponding height profile of VN (b) nanosheets prepared from few-layer V_2O_5 (a) and MoN (d) nanosheets prepared from few-layer MoO_3 (c).

5. Conclusions

The present study demonstrates how metal nitride nanosheets can be prepared by the chemical transformation of oxide and chalcogenide nanosheets. It is noteworthy that nanosheets of GaN are readily prepared by the ammonolysis of GaS and GaSe nanosheets. Preliminary studies have demonstrated success in preparing VN and MoN nanosheets from the oxide nanosheets. The simple methodology described here can be exploited to prepare good nanosheets of these and other metal nitrides. Ammonolysis of MoS_2 NSs also yields nitride NSs.

6. References

[1] a) A. K. Geim, *Science* **2009**, *324*, 1530-1534; b) A. K. Geim, K. S. Novoselov, *Nat Mater* **2007**, *6*, 183-191; c) K. S. Novoselov, V. I. Falko, L. Colombo, P. R. Gellert, M. G. Schwab, K. Kim, *Nature* **2012**, *490*, 192-200.

[2] a) C. N. R. Rao, U. Maitra, U. V. Waghmare, *Chem. Phys. Lett.* **2014**, *609*, 172-183; b) C. N. R. Rao, H. S. S. Ramakrishna Matte, U. Maitra, *Angew. Chem. Int. Ed.* **2013**, *52*, 13162-13185; c) M. B. Sreedhara, H. S. S. R. Matte, A. Govindaraj, C. N. R. Rao, *Chem. Asian J.* **2013**, *8*, 2430-2435; d) M. B. Sreedhara, B. E. Prasad, M. Moirangthem, R. Murugavel, C. N. R. Rao, *J. Solid State Chem.* **2015**, *224*, 21-27.

[3] a) Q. H. Wang, K. Kalantar-Zadeh, A. Kis, J. N. Coleman, M. S. Strano, *Nat. Nanotechnol.* **2012**, *7*, 699-712; b) D. J. Late, B. Liu, H. S. S. R. Matte, V. P. Dravid, C. N. R. Rao, *ACS Nano* **2012**, *6*, 5635-5641.

[4] a) M. M. Y. A. Alsaif, K. Latham, M. R. Field, D. D. Yao, N. V. Medehkar, G. A. Beane, R. B. Kaner, S. P. Russo, J. Z. Ou, K. Kalantar-zadeh, *Adv. Mater.* **2014**, *26*, 3931-3937; b) G. Zhao, J. Li, L. Jiang, H. Dong, X. Wang, W. Hu, *Chem. Sci.* **2012**, *3*, 433-437; c) Y. Li, J. Yao, E. Uchaker, J. Yang, Y. Huang, M. Zhang, G. Cao, *Adv. Energy Mater.* **2013**, *3*, 1171-1175.

[5] a) A. Nag, K. Raidongia, K. P. S. S. Hembram, R. Datta, U. V. Waghmare, C. N. R. Rao, *ACS Nano* **2010**, *4*, 1539-1544; b) L. Song, L. Ci, H. Lu, P. B. Sorokin, C. Jin, J. Ni, A. G. Kvashnin, D. G. Kvashnin, J. Lou, B. I. Yakobson, P. M. Ajayan, *Nano Lett.* **2010**, *10*, 3209-3215; c) C. Zhi, Y. Bando, C. Tang, H. Kuwahara, D. Golberg, *Adv. Mater.* **2009**, *21*, 2889-2893.

[6] a) H. Le, Y. Qu, K. Jun, L. Yan, L. Jingbo, *Journal of Physics: Condensed Matter* **2014**, *26*, 295304; b) P. Patsalas, S. Logothetidis, *J. Appl. Phys.* **2001**, *90*, 4725-4734.

[7] a) A. H. Mueller, M. A. Petruska, M. Achermann, D. J. Werder, E. A. Akhadov, D. D. Koleske, M. A. Hoffbauer, V. I. Klimov, *Nano Lett.* **2005**, *5*, 1039-1044; b) F. CAPASSO, *Science* **1987**, *235*, 172-176; c) Y. Dong, B. Tian, T. J. Kempa, C. M. Lieber, *Nano Lett.* **2009**, *9*, 2183-2187; d) H. Li, J. Dai, J. Li, S. Zhang, J. Zhou, L. Zhang, W. Chu, D. Chen, H. Zhao, J. Yang, Z. Wu, *J. Phys. Chem. C* **2010**, *114*, 11390-11394.

[8] D. Xu, H. He, R. Pandey, S. P. Karna, *J. Phys. Condens. Matter* **2013**, *25*, 345302.

[9] a) W. Shan, T. J. Schmidt, X. H. Yang, S. J. Hwang, J. J. Song, B. Goldenberg, *Appl. Phys. Lett.* **1995**, *66*, 985-987; b) C. Y. Fong, S. S. Ng, F. K. Yam, H. Abu Hassan, Z. Hassan, *J Sol-Gel Sci Technol* **2014**, *71*, 329-332; c) D. Kapolnek, X. H. Wu, B. Heying, S. Keller, B. P. Keller, U. K. Mishra, S. P. DenBaars, J. S. Speck, *Appl. Phys. Lett.* **1995**, *67*, 1541-1543; d) N. H. Karam, T. Parodos, P. Colter, D. McNulty, W. Rowland, J. Schetzina, N. El-Masry, S. M. Bedair, *Appl. Phys. Lett.* **1995**, *67*, 94-96; e) S. A. Nikishin, N. N. Faleev, V. G. Antipov, S. Francoeur, L. Grave de Peralta, G. A. Seryogin, H. Temkin, T. I. Prokofyeva, M. Holtz, S. N. G. Chu, *Appl. Phys. Lett.* **1999**, *75*, 2073-2075.

[10] a) K. Sardar, C. N. R. Rao, *Adv. Mater.* **2004**, *16*, 425-429; b) F. Tessier, R. Marchand, Y. Laurent, *J. Eur. Ceram. Soc.* **1997**, *17*, 1825-1829.

[11] U. K. Gautam, S. R. C. Vivekchand, A. Govindaraj, C. N. R. Rao, *Chem. Commun.* **2005**, 3995-3997.

[12] D. J. Late, B. Liu, H. S. S. R. Matte, C. N. R. Rao, V. P. Dravid, *Adv. Funct. Mater.* **2012**, *22*, 1894-1905.

[13] a) C. L. Bull, P. F. McMillan, E. Soignard, K. Leinenweber, *J. Solid State Chem.* **2004**, *177*, 1488-1492; b) A. Gomathi, A. Sundaresan, C. N. R. Rao, *J. Solid State Chem.* **2007**, *180*, 291-295; c) T. C. Liu, W. G. Pell, B. E. Conway, S. L. Roberson, *J. Electrochem. Soc.* **1998**, *145*, 1882-1888.

[14] a) A. Y. Ganin, L. Kienle, G. V. Vajenine, *J. Solid State Chem.* **2006**, *179*, 2339-2348; b) A. M. Glushenkov, D. Hulicova-Jurcakova, D. Llewellyn, G. Q. Lu, Y. Chen, *Chem. Mater.* **2009**, *22*, 914-921.

[15] a) Woo-Sik Jung, Choon Sup Ra, B.-K. Min, *Bull. Korean Chem. Soc.* **2005**, *26*; b) M. A. Reshchikov, H. Morkoç, *J. Appl. Phys.* **2005**, *97*, 061301.

[16] J. Wang, F. Demangeot, R. Péchou, A. Ponchet, A. Cros, B. Daudin, *Physical Review B* **2012**, *85*, 155432.

[17] Z.-l. Wang, D. Xu, L.-m. Wang, X.-b. Zhang, *ChemPlusChem* **2012**, *77*, 124-128.

[18] J. L. D. Xue, *Nanoscale Res Lett* **2010**, *5*, 1619-1626.

[19] D. J. Late, B. Liu, J. Luo, A. Yan, H. S. S. R. Matte, M. Grayson, C. N. R. Rao, V. P. Dravid, *Adv. Mater.* **2012**, *24*, 3549-3554.

Part III

Atomic layer deposition (ALD) of ultrathin films of metal oxides and Sulfides

Chapter III.1

A brief overview of Atomic Layer Deposition

SUMMARY

Atomic layer deposition (ALD) is a chemical vapor phase technique capable of producing thin films of a variety of materials with control over atomic scale thickness. Considering sequential self-limiting reaction, ALD offers exceptional conformality on high aspect ratio structures with highly controllable manner. These advantages enable ALD technique to overcome key challenges associated with the size and dimension decrease of nanomaterials and devices. Today, ALD is one of the leading techniques employed for deposition of nanometer thick films at an industrial level. Moreover, advancements in the instrumentation ensured that ALD growth processes is scalable to large area substrates making this technique very promising. With scaling down of semiconductor and microelectronic devices, ALD scores over other conventional methods for the fabrication process. This chapter presents the history, evolution, need and the basic concept underlying of atomic layer deposition. The challenges regarding the single phase material deposition and crystallinity related aspects are also discussed.

1. ALD history and evolution

The concept of the atomic layer deposition process was first discovered by Prof. V.B. Aleskovskii in the Soviet Union in 1950s.[1, 2] ALD has been demonstrated twice under different names: molecular layering (ML) in the Soviet Union and atomic layer epitaxy (ALE) in Finland. The principle of ALD was first published under the name of molecular layering in 1952, however no significant evolution in research was found till 1970s. The first patent for ALD was filed by Prof. Tuomo Suntola and co-workers from Finland.[3-5] The motivation for the development of ALD was the need for a deposition method for thin-film electroluminescent (TFEL) flat-panel displays.[6] For such an application, high-quality dielectric and luminescent films are required on large-area substrates. Thus, ALD was developed in the 1980s for the fabrication of luminescent ZnS and Al_2O_3 insulator films for electroluminescent flat panel displays. The applicability of ALD to epitaxial compound semiconductors was demonstrated and great efforts were made in the preparation of III–V compounds in the late 1980s. The major driving force for the success of ALD has been the microelectronics industry for the down-scaling of device dimensions. The renaissance of ALD began in the mid-1990s, with the interest being mainly focused on silicon-based microelectronics. Semiconductor industry became interested in ALD because it is a deposition method with control over the film thickness and conformal films on nonplanar substrates. Shrinking device dimensions and increasing aspect ratios in integrated circuits (IC) require the introduction of new materials and thin-film deposition techniques.[7] In 2007, Intel introduced its first microprocessor with 45 nm thick HfO_2 based gate dielectric fabricated by ALD. Considering the advantages such as lower processing temperatures and pin-hole free films, lower deposition rates become less important which further increase the attraction on the ALD method in IC industries. ALD is considered as one deposition method with the greatest potential for producing very thin conformal films with control of thickness and composition of the films possible at the atomic level.[8] The advancement in the instrumentation and key features over other deposition techniques, ALD has been employed to fabricate and manipulates the device properties for several applications such as catalysis,[9, 10] electronic and optoelectronic materials and energy devices.[11]

2. Principle and characteristics of ALD

ALD is a chemical vapor deposition technique that relies on surface saturating irreversible chemisorption of the gaseous precursor on solid surface. The distinct feature of ALD which is a special modification of CVD is that, film growth takes place in a cyclic manner.[8] ALD process is based on the self-limited adsorption of precursor molecules only by surface reaction and it differs from the conventional CVD process in the way that it is carried out. One ALD cycle typically consists of four essential steps, which are schematically illustrated in **Figure 1**. In step 1 the precursor is exposed to the substrate surface which chemisorb on the surface irreversibly, leave by-product and terminates the surface with new reactive groups, step 2 involves the evacuation or purging of the excess precursors and by-products from the chamber using inert gas. In step 3 exposure of the reactant species, typically oxidants or reagents, which chemically reacts with surface groups of precursor and step 4 involves the evacuation or purging of the reactants and by-product molecules from the chamber. The growth cycles are repeated as many times as required for the desired film thickness. Depending on the process and the chemistry of reactants being used, one

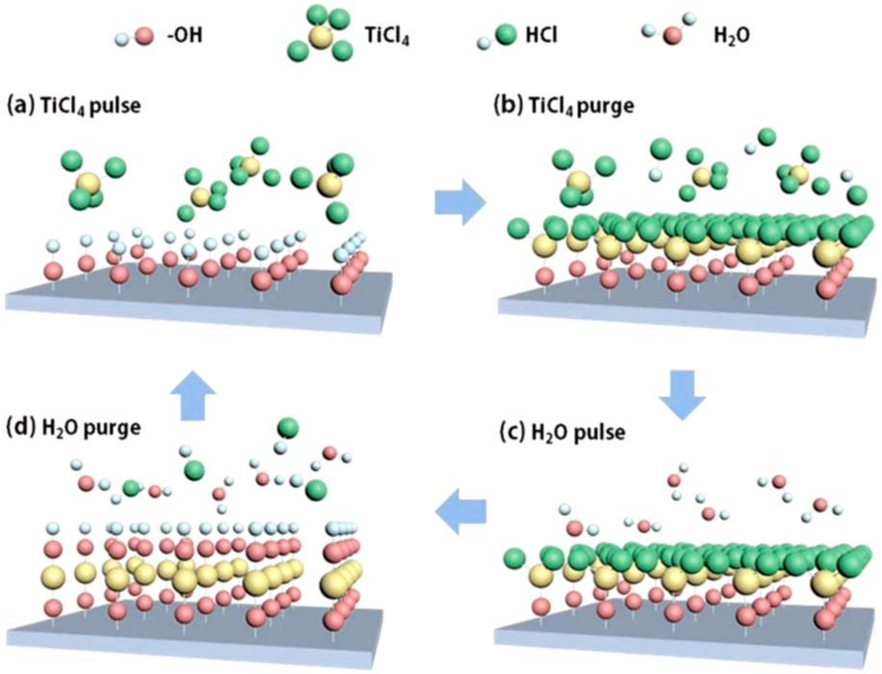

Figure 1. Schematic illustration of the one ALD cycle of TiO_2 using $TiCl_4$ and H_2O as Ti and oxygen precursor respectively. Reproduced with permission from ref.[11]

cycle can take time from milli seconds to a few seconds, and may deposit sub monolayer to monolayer per cycle. The cycle duration depends particularly on the aggressiveness of the reaction and saturation. The effect of time on the chemisorption coverage and amount deposited in each cycle is illustrated in **Figure 2**a-c. The material deposited is linearly dependent on number of cycles (Figure 2d). In ALD, contrast to CVD, reactions with negative value of ΔG are desired. Although there are many similarities between ALD and CVD, a clear and distinctive feature of ALD lies in the self-limitation for precursor adsorption and alternate sequential exposure of precursors and reactants. Under such conditions the growth is uniform and the thickness of the film increases steadily in each growth cycle (Figure 2e). Commonly, in the growth of

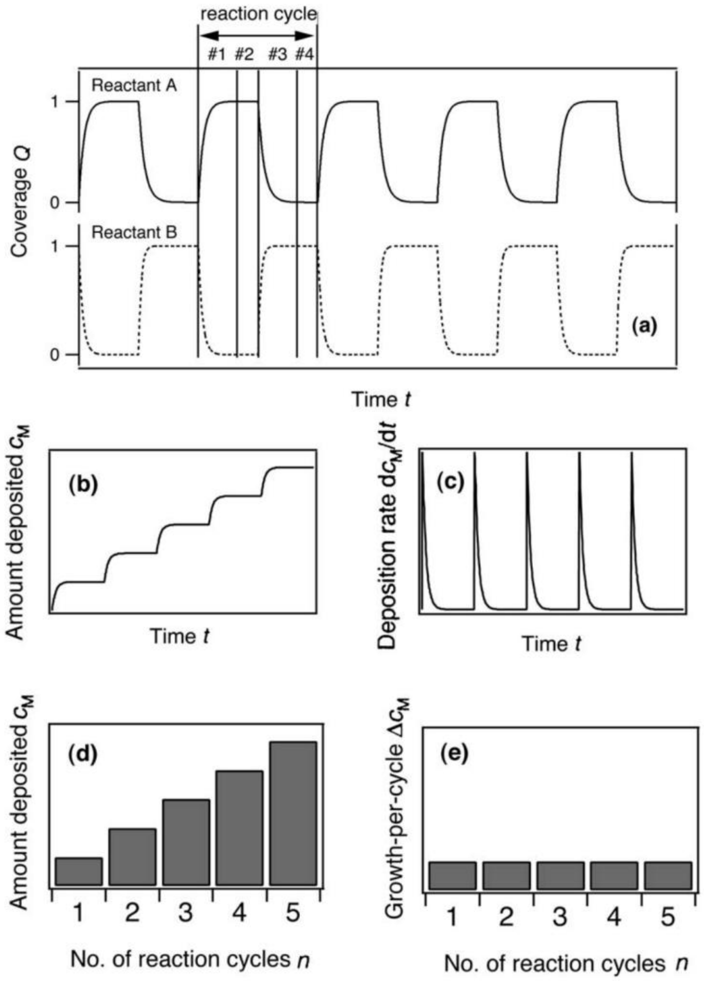

Figure 2. Schematic representation of five ALD cycles (a) chemisorption coverage Q of reactant A (solid line) and reactant B (dotted line) as a function of time t. (b) The amount of sample adsorbed as a function of time t. (c) The growth rate as a function of time t (time derivative of the curve in panel b) (d) amount of material deposited as a function of the number of reaction cycles n, and (e) the GPC as a function of the number of reaction cycles n. Reproduced with permission from ref.[8]

binary compounds such as metal oxides, a reaction cycle mainly consists of two simple steps. In first step the metal precursor is allowed to react with the surface, and in the other step it reacts with the oxygen precursor. Between the steps a purge is applied to remove the excess of precursor and the reaction by-products.

The essential characteristics of ALD process are uniform and conformal deposition on large area and high aspect ratio substrates. The self-terminating growth mechanism facilitates the conformal growth with accurate thickness on large areas. The thickness of the films can be controlled in a straightforward manner by controlling the number of reaction cycles, therefore enabling the controlled growth at monolayer level. As a consequence, ALD film growth is not flux-dependent as is the case with CVD and physical vapor deposition (PVD). Irreversible self-saturation nature of ALD, automatically lead to the stoichiometric films with same amount of material adsorb anywhere irrespective of the shape of the substrate,[12] amount of reactant and exposure time.[8] Precursor partial pressures also does not affect the amount of material adsorbed during growth. Another key feature of ALD is that the growth rate is weakly dependent on the temperature within the ALD temperature window.

3. ALD precursors

ALD involves the delivery of precursor in vapor phase, precursors or reactants used should be volatile and have enough vapor pressure at the operating temperature. ALD precursors can be gases, volatile liquids, or solids. The vapor pressure must be sufficient enough for effective mass transportation and efficient chemical reaction, all solid and some liquid precursors need to be heated, in order to attain optimum vapor pressure. The self-limiting growth demands for the evaporation rates to remain constant are more relaxed than in CVD, thus making it easier to use solid precursors. The solid or liquid reactant should be vaporizable at a temperature lower than ALD reaction temperature for effective transport and to avoid condensation. Thermal stability of the precursor over a long deposition time is very necessary, if the precursors required to heat to obtain sufficient volatility. The challenging task of pulsing evaporated precursors at high temperatures is solved by inert-gas valving. Decomposition would destroy the self-limiting growth mechanism and the related advantages. With the above general requirements precursor must adsorb chemically on the surface sites and should have good reactivity towards other reactant. The reaction by-products should be inert and should not interfere with the film growth. In some applications, such as protective coatings, slightly thermally unstable precursors can be acceptable if their decomposition is slow (compared to the pulsing sequence times), and makes only a negligible contribution to the overall growth. The type of adsorption, molecular or dissociative, and reaction mechanisms has been extensively studied *in-situ* with quartz-crystal microbalance and mass spectrometric measurements. Different mechanisms have been found for different precursors. Typical metal precursors used are halides, especially chlorides, alkyl compounds, and alkoxides. Recently, organometallic compounds such as cyclopentadienyl complexes, β-diketonates, imides, alkyl and silyl amides have gained more attention.[13] Every precursor has its own benefits and limitations regarding stability, reactivity, by-products and impurities left in the films. The most commonly used nonmetal precursors are water, hydrogen peroxide, ozone, hydrogen sulfide, ammonia, hydrazine, for metal oxides, sulfides and nitrides respectively.[8, 14]

4. ALD temperature window

One important parameter that must be carefully investigated in ALD is growth temperature. A real ALD process occurs only when the deposition temperature is placed within a precise range, which has been identified as the “ALD window”. **Figure 3** shows nearly ideal non-ideal behavior regions of ALD growth.[15, 16] ALD window corresponds to the range in which the growth rate of the process is fairly stable within the experimental error. The growth rate should be constant even with the higher precursor pulse times. However, it is worth mentioning that many ALD processes are fully determined by the density of surface species and this density is temperature-dependent, the resultant growth per cycle (GPC) is also temperature dependent. The growth rate outside the ALD window is affected due to undesired chemical and physical phenomena. The lower growth rates below the window is due to insufficient thermal energy supplied to the molecules and higher due to condensation of the precursor molecules. Within the ALD window, the slight in variation of growth rates may affected by the thermally promoted gas phase reactions (Figure 3). The large increase in the growth rate after the ALD window is due to the CVD kind of reaction,

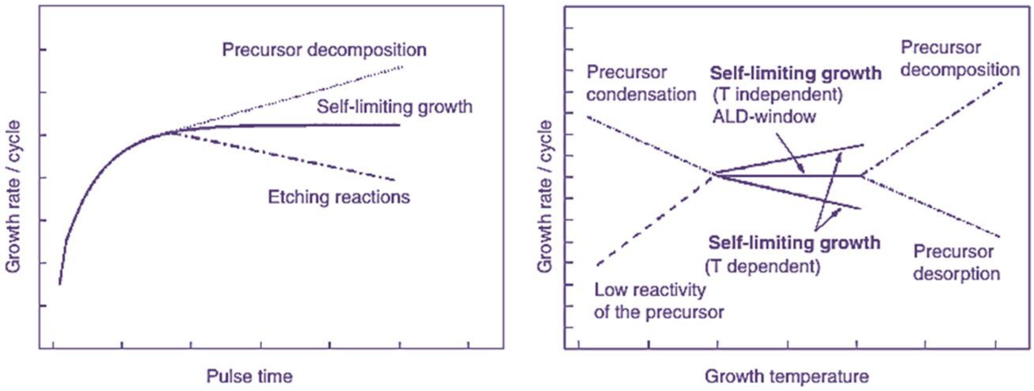

Figure 3. Schematic representation of possible behavior for the ALD growth rate versus precursor pulse time and temperature showing the ALD window.[15]

whereas the decrease in the growth rate can be attributed to desorption of precursor molecules from the surface or back etching from the by-products.[15, 17] Moreover, surface species needed for ALD could also desorb from the surface at higher temperatures and be unavailable for additional surface reactions. In order to achieve good ALD growth one should optimize for the ALD window, which depends on nature of the precursor and its characteristics. The different precursors of the same metal may have different ALD temperature window due to their different chemistries. Once the precursor’s dose and the ALD window have been established, growth rate should be constant, and film thickness must have linear relationship with number of ALD cycles. If the growth rate is stable and the film deposition occurs uniformly on the substrate surface, it is possible to realize extremely conformal ultrathin films with steady thickness.[8, 15] ALD growth may not be possible with many precursors which are used in CVD, because they might not show self-limiting reaction. Some precursor may involve surface reaction that may never reach completion.[18] These reactions will display self-limiting growth but large amounts of impurities remain in the films.

5. Surface chemistry of ALD

Since ALD growth involves self-terminating gas-solid reactions, the surface chemistry of the reaction fully describes the atomistic growth mechanism. The gas-solid reaction involves adsorption of a gaseous reactant molecule upon the surface. ALD reactions are irreversible chemical adsorption with self-terminating in nature. The creation of a strong bond can seen between the metal precursor and substrate. The basic chemical mechanism involves two vapour phase reactive chemical species, typically a metal-organic precursor and a co-reactant such as an oxygen source or a reducing agent. The precursor and co-reactant species are pulsed sequentially into a reaction chamber containing a receptive growth surface, resulting in two time separated half reaction steps.[8] Time-separated exposure is ensured by purging the reactor with inert gas between the exposure steps. A typical ALD cycle and their surface chemical reaction is presented schematically in Figure 1. In the first step the precursor chemically reacts and form bonds to the surface without fully decomposing. The precursor also changes the dominant surface termination, leaving the surface ready to react with the co-reactant. At the saturation level, remaining vapour of the precursor is insensitive to surface and are pushed out of the deposition zone. In second ALD half reaction, the co-reactant supplied, reacts on the surface. The vapour products are purged out, and the ALD cycle starts over again. Once the precursor has reacted with sites prepared during the previous co-reactant exposure, the surface reaction stops that is, the surface sites prepared by the precursor reaction are reactive to the co-reactant, but not the precursor itself. One must ensure that enough precursor is delivered to achieve full saturation, otherwise, growth will be non-ideal and non-uniform. In common thermal ALD processes, these half-reactions are driven by a favourable change in free energy (i.e., $\Delta G < 0$), and any activation barrier is easily traversed.[16] In plasma or other energetically enhanced ALD processes, different reactants are used that change the overall reaction thermodynamics.[19] The plasma or other external energy source is supplied during at least one of the half-reaction steps to allow the entire reaction to proceed.

6. Types of ALD

ALD closely resembles the CVD process on the basis of binary reaction thus it is also known as modified version of CVD. In CVD, two reactants are pulsed at a time during the course of deposition, the reaction takes place at the space and surface, results in the film growth. On the other hand ALD process proceeds through sequential pulsing of precursors on to the chamber where ligand exchange reaction takes place only on the surface not in the space. A monolayer growth was achieved through two half cycle reactions with a precise control over thickness. In each half cycle the by-product and excess of reactant were purged by inert gas. With the advancement of technique and instrumentation there are mainly three types of ALD, namely thermal, plasma enhanced and catalytic ALD. Thermal ALD is most commonly employed technique to deposit various materials such as metal oxides, sulphides and nitrides. The surface termination reaction occurs spontaneously in thermal ALD through simple ligand exchange reaction process. One of the well-studied thermal ALD processess is deposition of Al_2O_3 using tri-methyl aluminium and water. Recently plasma assisted ALD (PEALD) received greater potential due to its ability to deposit metals and metal nitrides, which are very difficult to achieve through simple thermal process.[20, 21] PEALD is an energy-enhanced method for the synthesis of ultra-thin films with sub nanometer level in which a plasma is employed during one step of the cyclic process. Plasma assisted is also referred to as plasma enhanced ALD and in some cases radical enhanced ALD. During the deposition, the surface is exposed to the species such as ions, radicals generated by a plasma at least once in a cycle. Typical O_2, N_2 and H_2 or mixture of them can be used to generate plasma, such plasma can replace the ligand exchange process of H_2O and NH_3. The reactive species such as radicals and ions present in the plasma help to quickly terminate the surface reaction. The plasma also reduces nucleation delays in some materials and lowers the activation energy needed for some precursors. PEALD allows deposition at significantly lower temperatures with better film properties and offers several merits for the deposition of ultra-thin films over thermal ALD. In catalytic ALD, a catalyst is used along with the precursor during the deposition. Catalyst employed with the precursor accelerates the reaction by reducing activation energy and also decreases the process temperature.

7. Crystallinity of ALD grown films

ALD grown films can be amorphous, polycrystalline, crystalline or even contain mixture of amorphous and crystalline phases.[16] The crystallinity of the films depend on the many growth parameters such as temperature, thickness, precursor, impurity, plasma conditions, and substrate.[16] The crystallinity and phase of the material play crucial role in deciding the film characteristics and properties.[16] Same materials can exist in either amorphous or crystalline state with different phases. Both amorphous and crystalline phase are important for various applications. For example, if dielectric properties are considered then amorphous films exhibit lower leakage current with better barrier properties than crystalline films. On the other hand, crystalline films show highest κ-values compared to amorphous and polycrystalline one. The crystallinity also depends on the processing temperature, thickness of the material. It is well-known that increase in temperature increases the crystallinity, other changes may also occur such as decomposition of precursor and side reaction from by-products. Thus choice of process temperature also dictates the choice of available precursor. The crystallinity of the film can also be achieved by post annealing treatment. For example TiO_2 can be deposited as amorphous films at the temperature below 160 °C and as crystalline films above 160 °C using $TiCl_4$ and H_2O. Certain precursor yields crystalline films and some gives amorphous under similar temperature profiles however, it is difficult to separate the effect of reactant from effect of temperature. V_2O_5 film deposited using vanadium-tri-iso-propoxide and H_2O plasma yield amorphous film at 150 °C whereas, with O_2 plasma gives crystalline phase. The increased local temperature by additional energy in the form of plasma, radicals and ions can further influence crystallization in the case of PEALD. The surface of substrate has large influence on the crystallinity of a film since it determines the initiation of growth which in turn affects subsequent growth. The lattice mismatch of underlying substrate with film also has a pronounced effect on the crystallinity and crystallographic orientation. Epitaxial growth requires some degree of lattice- or domain-matching between the deposited film and the substrate. Some single crystalline films such as TiO_2, In_2O_3 have been obtained based on domain epitaxial models on c-Al_2O_3 and Y-stabilized ZrO_2 (YSZ) respectively.[22, 23] Thickness also affects the crystallinity of films, thinner films may appear amorphous and start crystallizing after given thickness. The growth parameters discussed above are often interlinked to one another in deciding the crystallinity.

8. ALD capabilities and applications in microelectronics

The ability for sub-nanometre thickness control of high quality pin-hole free films and perfect conformality on the high aspect ratio substrates, which are becoming ever more significant with shrinking of device dimensions. ALD is a useful process for the fabrication of microelectronics due to its ability to produce accurate thicknesses and uniform surfaces in addition to high quality film production of various different materials. In microelectronics, ALD is employed as a potential technique to deposit high-*k* gate oxides, dielectrics, ferroelectrics, and metals and nitrides for electrodes.[16] In high-*k* gate oxides, where the control of ultra-thin films are essential, ALD is only likely to come into wider use below 100 nm technology. In metallization, conformal films are required; currently it is expected that ALD will be used in mainstream production at the 65 nm node. In dynamic random access memories (DRAMs), the conformality requirements are even higher and ALD is a method of choice when feature sizes become lesser than 100 nm. Several products that use ALD include magnetic recording heads, MOSFET gate stacks, DRAM capacitors, non-volatile ferroelectric memories, and many others. The ALD on biological templates, atmospheric pressure ALD, area selective ALD for spatial patterning, are emerging areas which shows that the field of ALD is growing rapidly and expanding into many applications outside of semiconductor processing. The main virtues of ALD are its precise thickness control and its extreme conformality on high aspect ratio structures. These virtues have been recognized by the above mentioned emerging application areas. ALD has been already successfully employed in fabrication of electrochemical devices,[4, 24] battery electrodes,[25] catalytic surfaces, and many more applications yet to come.

9. ALD at JNCASR

The ALD system installed in our laboratory is a Beneq TFS-200 from Beneq (Finland) shown in **Figure 4**. The TFS 200 represents State-of-the-art design and technical solution that enables deposition of superior quality coatings on a broad array of substrate materials and sizes. It has three different modes for deposition of materials viz., thermal, remote plasma and fluidized bed reactor (FBR) together with ozone generator to use ozone as co-reactant in place of any oxygen source. The instrument is connected with six gas lines, including two instrument nitrogen, ammonia, hydrogen sulphide, and two plasma gases (oxygen and nitrogen). The TFS 200 can coat wafers, planar objects and porous bulk materials, as well as particles (using FBR) and complex 3D objects with high aspect ratio features. Currently we have a capability of using two liquid source precursors and one hot source (can be operated at 300 °C) at a time. The deposition can be monitored in-situ using Quartz crystal microbalance (QCM) and

Figure 4. Photograph of Beneq TFS-200 ALD system installed at JNCASR, Bengalore (India).

residual gas analyser (RGA).

10. Summary

With the ever increasing demand for controllable and conformal films, atomic layer deposition is one of the most effective methods possible with its sequential self-limiting reactions to meet the expectation of device community. ALD processes have been developed for a wide variety of materials, ranging from metals to metal oxides to complex ternary materials. However, the growth of pristine single phase materials having preferred orientation with the underlying substrate has significant practical utility, however, most of ALD deposited materials are limited to polycrystalline or amorphous. The subsequent chapters deal with the atomic layer deposition of single phase crystalline epitaxial films of anatase *p*-TiO_2, V_2O_5 and MoS_2.

11. References

[1] E. Ahvenniemi, A. R. Akbashev, S. Ali, M. Bechelany, M. Berdova, S. Boyadjiev, D. C. Cameron, R. Chen, M. Chubarov, V. Cremers, A. Devi, V. Drozd, L. Elnikova, G. Gottardi, K. Grigoras, D. M. Hausmann, C. S. Hwang, S.-H. Jen, T. Kallio, J. Kanervo, I. Khmelnitskiy, D. H. Kim, L. Klibanov, Y. Koshtyal, A. O. I. Krause, J. Kuhs, I. Kärkkänen, M.-L. Kääriäinen, T. Kääriäinen, L. Lamagna, A. A. Łapicki, M. Leskelä, H. Lipsanen, J. Lyytinen, A. Malkov, A. Malygin, A. Mennad, C. Militzer, J. Molarius, M. Norek, Ç. Özgit-Akgün, M. Panov, H. Pedersen, F. Piallat, G. Popov, R. L. Puurunen, G. Rampelberg, R. H. A. Ras, E. Rauwel, F. Roozeboom, T. Sajavaara, H. Salami, H. Savin, N. Schneider, T. E. Seidel, J. Sundqvist, D. B. Suyatin, T. Törndahl, J. R. v. Ommen, C. Wiemer, O. M. E. Ylivaara, O. Yurkevich, *J. Vac. Sci. Technol., A* **2017**, *35*, 010801.

[2] V. B. Aleskovskii, *J. Appl. Chem. USSR.* **1974**, *47* 2207.

[3] G. N. Parsons, J. W. Elam, S. M. George, S. Haukka, H. Jeon, W. M. M. Kessels, M. Leskelä, P. Poodt, M. Ritala, S. M. Rossnagel, *J. Vac. Sci. Technol., A* **2013**, *31*, 050818.

[4] H. Kim, H.-B.-R. Lee, W. J. Maeng, *Thin Solid Films* **2009**, *517*, 2563-2580.

[5] J. A. T. Suntola, *U.S. Patent* **1977**, *4, 058*, 430.

[6] R. L. Puurunen, *Chem. Vap. Deposition* **2014**, *20*, 332-344.

[7] M. Leskelä, M. Ritala, *Angew. Chem. Int. Ed.* **2003**, *42*, 5548-5554.

[8] R. L. Puurunen, *J. Appl. Phys.* **2005**, *97*, 121301.

[9] J. Su, Z. Li, Y. Yu, X. Wang, *Adv. Mater. Interfaces* **2017**, *4*, 1600835.

[10] T. Wang, Z. Luo, C. Li, J. Gong, *Chem. Soc. Rev.* **2014**, *43*, 7469-7484.

[11] L. Wen, M. Zhou, C. Wang, Y. Mi, Y. Lei, *Adv. Energy Mater.* **2016**, *6*, 1600468.

[12] C. Detavernier, J. Dendooven, S. Pulinthanathu Sree, K. F. Ludwig, J. A. Martens, *Chem. Soc. Rev.* **2011**, *40*, 5242-5253.

[13] M. Leskelä, M. Ritala, *Thin Solid Films* **2002**, *409*, 138-146.

[14] P. Seoung Gon, K. Do-Heyoung, *Jpn. J. Appl. Phys.* **2004**, *43*, 303.

[15] M. Ritala, J. Niinisto, in *Chemical Vapour Deposition: Precursors, Processes and Applications*, The Royal Society of Chemistry, **2009**, pp. 158-206.

[16] V. Miikkulainen, M. Leskelä, M. Ritala, R. L. Puurunen, *J. Appl. Phys.* **2013**, *113*, 021301.

[17] J.-W. Lim, H.-S. Park, S.-W. Kang, *J. Electrochem. Soc.* **2001**, *148*, C403-C408.

[18] S. M. George, *Chem. Rev.* **2010**, *110*, 111-131.

[19] G. N. Parsons, S. M. George, M. Knez, *MRS Bull.* **2011**, *36*, 865-871.

[20] H. B. Profijt, S. E. Potts, M. C. M. v. d. Sanden, W. M. M. Kessels, *J. Vac. Sci. Technol., A* **2011**, *29*, 050801.

[21] K. Hyungjun, O. Il-Kwon, *Jpn. J. Appl. Phys.* **2014**, *53*, 03DA01.

[22] J. D. Emery, C. M. Schlepütz, P. Guo, R. P. H. Chang, A. B. F. Martinson, *Cryst. Growth Des.* **2016**, *16*, 640-645.

[23] T. J. Kraus, A. B. Nepomnyashchii, B. A. Parkinson, *ACS Appl. Mater. Interfaces* **2014**, *6*, 9946-9949.

[24] R. W. Johnson, A. Hultqvist, S. F. Bent, *Mater. Today* **2014**, *17*, 236-246.

[25] L. Ma, R. B. Nuwayhid, T. Wu, Y. Lei, K. Amine, J. Lu, *Adv. Mater. Interfaces* **2016**, *3*, 1600564.

Chapter III.2

Atomic Layer Deposition of *p*-type Epitaxial Thin Films of Undoped and N-doped Anatase TiO_2

SUMMARY*

Employing atomic layer deposition, we have grown *p*-type epitaxial undoped and N-doped anatase TiO_2(001) thin films on *c*-axis Al_2O_3 substrate. From X-ray diffraction and transmission electron microscopy studies, crystallographic relationships between the film and the substrate are found to be <001>TiO_2//<0001>Al_2O_3 and <-110>TiO_2//<01-10>Al_2O_3. N-doping in TiO_2 thin films enhances the hole concentration and mobility. The optical band gap of anatase TiO_2 (3.23 eV) decreases to 3.07 eV upon N-doping. The epitaxial films exhibit room-temperature ferromagnetism and photoresponse. A TiO_2-based homojunction diode was fabricated with rectification from the *p*-*n* junction formed between N-doped *p*-TiO_2 and *n*-TiO_2.

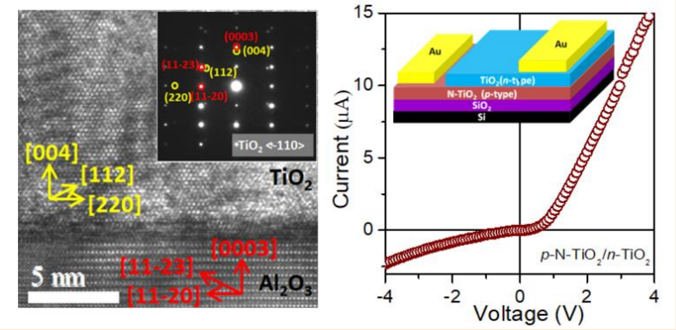

*A paper based on this work has appeared in ACS Applied Materials & Interfaces (2016).

1. Introduction

Titanium dioxide (TiO_2) is a prototypical semiconductor widely used in energy and environmental applications. TiO_2 in the anatase form is more promising than rutile in several applications.[1-2] TiO_2 thin films are used as a high-*k* dielectric layer in semiconductor devices and also as transparent layer in display panels. In view of finding new functional applications of TiO_2, there has been considerable work on epitaxial thin films.[3-7] The square symmetry lattice constant of the (001) plane of anatase (0.3785nm) is close to the lattice constants of $LaAlO_3$ and $SrTiO_3$ substrates, with lattice mismatch of only 0.2% and 2.7% respectively. Epitaxial anatase TiO_2 thin films on these substrates have been deposited using physical vapor deposition techniques such as sputtering, pulsed laser deposition and molecular beam epitaxy.[2-9] Properties of epitaxial thin films are easily tuned by strain engineering. TiO_2 (anatase) thin films on Al_2O_3 substrate with a large lattice mismatch (≈20%) promise to possess interesting properties and it appears important to grow epitaxial films of anatase on Al_2O_3 substrates. While there is some work on epitaxial rutile TiO_2 thin films on Al_2O_3 substrates, to the best of our knowledge epitaxial TiO_2 (anatase) thin films on Al_2O_3 substrates have not been gown by any deposition method. Atomic layer deposition (ALD) is a versatile method for depositing high-quality films with control of film thickness and composition. ALD is employed mainly for the growth of high-*k*-dielectric films and nanostructures of polycrystalline materials and there are only a few reports on the epitaxial growth of thin films of TiO_2 and other oxides.[10-16]

While the absence of *p*-type conductivity limits the efficient use of TiO_2 on devices, there have been a few attempts to attain *p*-type conductivity in TiO_2 by manipulating structure-property relation and chemical doping.[5, 17-19] Stabilizing *p*-type conductivity in the un-doped TiO_2 thin film is still a major challenge. In a recent paper, Andrei *et al.* have reported the *p*-type conductivity un-doped TiO_2 thin films deposited by ALD.[20] However the as-grown films show the mixed phase with polycrystallinity. Since the properties of TiO_2 largely depends on its phase and crystallinity, the growth of *p*-type TiO_2 in the form of thin film with single phase and crystallinity has huge impact on its properties for practical applications.

2. Scope of the present investigations

TiO_2 is a well-known n-type semiconductor with widespread use in photocatalytic and semiconductor devices. The properties of TiO_2 is mainly dependent on its crystal phases, TiO_2 exists in three different polymorphs- anatase, rutile and brookite. Anatase phase of TiO_2 found to be more catalytically active than other two phases. The p-type conductivity can boost up the applicability TiO_2 in diodes and electronics but the alteration of electronic conductivity type in TiO_2 from n-type to p-type still remains a fundamental challenge. The lack of effective methods to achieve the single anatase phase with the p-type conductivity limits potential applicability of TiO_2 optoelectronics. In the present study, we have successfully grown single phase *p*-type epitaxial anatase TiO_2 thin films on Al_2O_3 (0001) substrates by ALD at 300 °C without post-annealing. Nitrogen-doping enhances the hole concentration and mobility of epitaxial TiO_2 thin film. Room temperature ferromagnetism persists in both undoped and N-doped TiO_2 thin films. We have also fabricated a TiO_2 based homojunction diode on a Si/SiO_2 substrate.

3. Experimental Section

Thin film growth

Deposition of epitaxial anatase TiO_2 thin films:

Undoped and N-doped epitaxial anatase TiO_2 thin films were grown by atomic layer deposition on single crystalline Al_2O_3 (0001) substrates using a commercial flow-type ALD reactor (Beneq, TFS-200). High purity chemical precursors, $TiCl_4$ (Alfa Aesar 99.99%), double distilled water (Merck Millipore) and NH_3 (Chemix, 99.999%) were employed as Ti, O and N sources respectively. Prior to deposition, the substrates were cleaned by rinsing in an ultrasonic bath of acetone, isopropanol and mixture of 5:1:1 H_2O:H_2O_2:NH_4OH. The reactor and chamber was pumped down and stabilized at a pressure of 1 and 10 mbar respectively. Ultra-pure N_2 (99.9999%) gas, used as process and carrier gas, was allowed into the reactor at a flow of 600 sccm. The pulse and purge times of $TiCl_4$ were 400 ms and 2 s, while the pulse and purge times of H_2O were 200 ms and 2 s respectively. N doping in TiO_2 films was achieved by allowing one pulse of NH_3 and $TiCl_4$ in the interval of 10 pulses of $TiCl_4$ and H_2O. The pulse and purge times of NH_3 were 200 ms and 2 s. The pressure in the reactor varied between 1-3 mbar during pulsing of $TiCl_4$, H_2O and NH_3 respectively. The reactor temperature was maintained at 300 °C and the deposition carried out for 1500 cycles at a growth rate of 0.03 nm per cycle.

Characterization

X-ray diffraction (XRD) patterns of the films were recorded with a Panalytical X-ray diffractometer (Empyrean) with θ-2θ scan using a Cu-K_α radiation (λ=1.5404 Å). The sample for transmission electron microscopy (TEM) was prepared by the "lift-off" method using focused ion beam (FIB) milling in FEI Quanta 3D dual beam SEM/FIB system. Cross-sectional and high-resolution TEM images were obtained using FEI aberration-corrected TEM (TITAN 80-300) operated at 300 kV. Raman spectra were recorded using a 632 nm HeNe laser with a Jobin Yvon LabRam HR spectrometer. X-ray photoelectron spectra (XPS) were recorded using a Omicron nanotechnology spectrometer with Mg-K_α source (E=1253.6 eV). The surface roughness and topography of the films were determined using atomic force microscopy (AFM, Bruker Innova). Optical transmission spectra were recorded in Perkin–Elmer UV-Vis spectrometer from 200-800 nm range.

Room temperature carrier concentration and mobility were determined using Ecopia HMS-3000 Hall effect measurement system. Room temperature magnetic measurements (M-H curve) were carried out with a superconducting quantum interference device (SQUID MPMS, Quantum Design). Photoresponse measurements were performed with a Keithley instrument under dark and ultraviolet (365 nm) LED light illumination for a sweeping voltage ±1 V. The device was fabricated using optical lithography (Intelligent Micro patterning Ltd., 365 nm) by making 6 µm gold electrodes gap.

TiO_2 homojunction device fabrication

A p-n homojunction was fabricated on SiO_2/Si substrate using TiO_2 thin films with p- and n-type carriers. On ALD p-type undoped and N-doped TiO_2 films, we deposited 90 nm n-type TiO_2 layer with an electron concentration 6.4×10^{18}/ cm^3 and mobility of 2 cm^2/V.s by KrF excimer pulsed laser deposition (PLD). PLD was carried out at oxygen partial pressure of 0.05 mTorr with laser energy 150mJ and pulse frequency 5 Hz respectively. The substrate temperature during deposition was maintained at 500 °C. The distance between the target and substrates was kept constant at 50 mm. The *p-n* homojunction was achieved by masking half-portion of *p*-type TiO_2 layers and depositing *n*-type TiO_2 layer in the unmasked portion. On the surface of *n*-and *p*-type layers gold top electrodes were deposited by sputtering and electrical contacts are given with the help of them. The diode I-V characteristics were measured using Keithley 4200 semiconductor characterization system.

4. Results and Discussion

Characteristics epitaxial anatase TiO_2

On deposition of TiO_2 and N-doped TiO_2 (N-TiO_2) films, we observe a change in color of the Al_2O_3 substrate to pale blue and pale yellow. XRD patterns of the TiO_2 and N-TiO_2 thin films in θ-2θ scan are shown **Figure 1**a. The (004) and (008) reflections of anatase are seen along with the (0006) and (00012) reflections of the Al_2O_3, suggesting the epitaxial nature of the TiO_2 thin films on the *c*-axis Al_2O_3 substrate. No other reflections from rutile or brookite phases of TiO_2 are observed in the XRD patterns. The epitaxial reflections (004) and (008) show shifts relative to the unstrained sample of anatase. The large lattice mismatch (+20%) results in relaxation of the TiO_2 lattice on Al_2O_3 due to dislocations (as seen by TEM). The shifts could arises from the

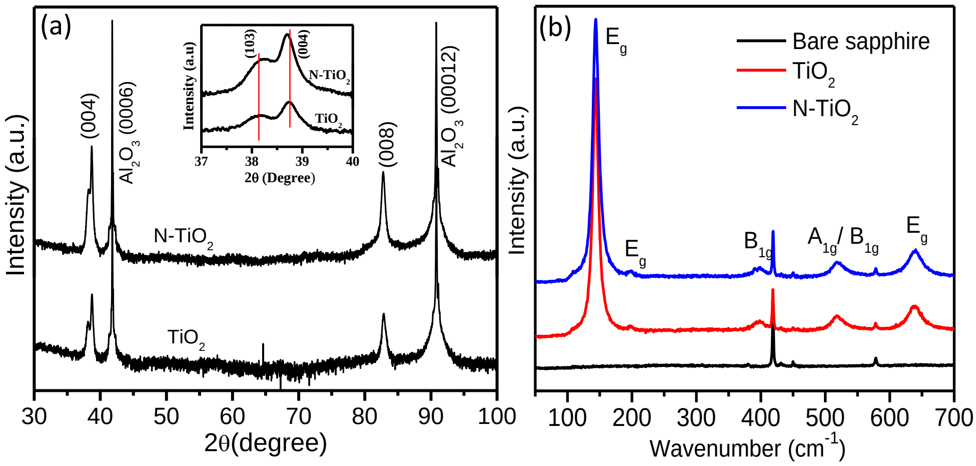

Figure 1. (a) XRD pattern of epitaxial anatase TiO_2 and N-TiO_2 thin films on Al_2O_3 substrate. Inset shows XRD pattern around (004) plane of TiO_2 and N-TiO_2 thin films. (b) Raman spectra of epitaxial anatase TiO_2 and N-TiO_2 thin films on Al_2O_3 substrate.

presence of metal atom vacancies in the thin anatase films. There is a shoulder in the (004) reflection (see inset) at $2\theta=38.15°$ due to the (103) reflection of anatase. The (103) plane is the crystallographic shear plane arising from a Magneli phase commonly observed in epitaxial anatase thin films.[8, 9] The (004) reflection gets shifted to lower 2θ upon N doping, suggesting substitutional nitrogen.

Figure 1b shows the Raman spectra of TiO_2 and N-TiO_2 thin films along with that of bare Al_2O_3 substrate. Raman spectra show five characteristic bands due to anatase TiO_2 in the 100-700 cm^{-1} range. The Raman bands due to E_g, E_g, B_{1g}, A_{1g}/B_{1g} and E_g phonon modes occur at 143, 197, 396, 520 and 640 cm^{-1} respectively.[21] All the Raman modes are shifted relative to unstrained anatase. The intensity of the band due to the E_g mode at 143 cm^{-1} is ten-fold higher than that of the other bands indicating the existence of long-range order in TiO_2 and N-TiO_2 thin films. No Raman bands due to rutile or brookite phases are detected.

The epitaxial relation between the anatase film and the Al_2O_3 substrate was confirmed with a TEM study. Cross-sectional bright field TEM image of the TiO_2 film on the Al_2O_3 substrate is shown in **Figure 2**a gives the thickness of the TiO_2 film to

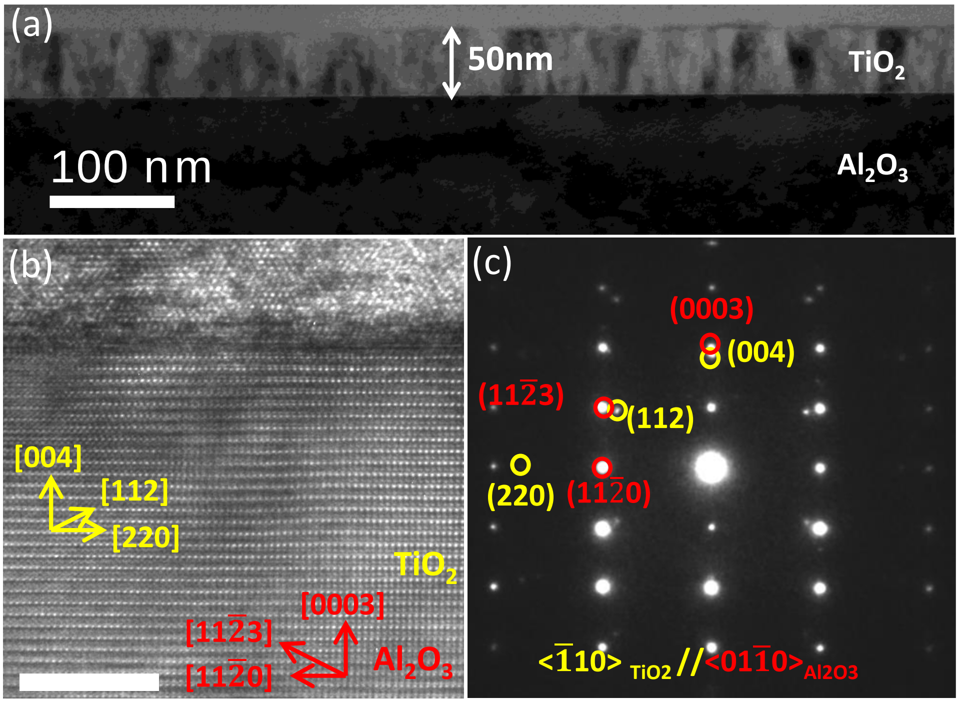

Figure 2. (a) Cross-sectional low magnification TEM image of TiO_2/Al_2O_3 interface. (b) High-resolution TEM image with corresponding (c) ED pattern of epitaxial anatase TiO_2 thin film on Al_2O_3 substrate. Sports circled with yellow and red color in the ED pattern are the epitaxial reflections belongs to anatase TiO_2 thin film and Al_2O_3 substrate respectively.

be 50 nm. The N-TiO_2 film also has a similar thickness. The clear interface between the film and substrate is seen in the image. Figure 2b shows a high-resolution TEM image of TiO_2/Al_2O_3 cross-sectional area taken with the electron beam parallel to the [10-10] direction of the substrate. The high-resolution TEM image shows the abrupt interface between the anatase film and the Al_2O_3 substrate. The electron diffraction (ED) pattern in Figure 2c reveals the epitaxial nature of the anatase film on the Al_2O_3 substrate. Three sets of parallel crystallographic relations, <004>TiO_2//<003>Al_2O_3, <112>TiO_2//<11-23>Al_2O_3 and <220>TiO_2//<11-20>Al_2O_3, can be identified in the ED pattern. The inverse fast Fourier transformation (IFFT) was reconstructed from the FFT image of Figure 2b with the <112> and <11-23> reflections of the anatase film and the Al_2O_3 substrate (**Figure 3** a & b). In the inverse FFT image, every seven <112> planes of anatase film matches with eight <11-23> planes of the Al_2O_3 substrate, suggesting the formation of misfit dislocations at the interface by strain relaxation. This infers the domain matching epitaxial growth of anatase on Al_2O_3 substrate.[22]

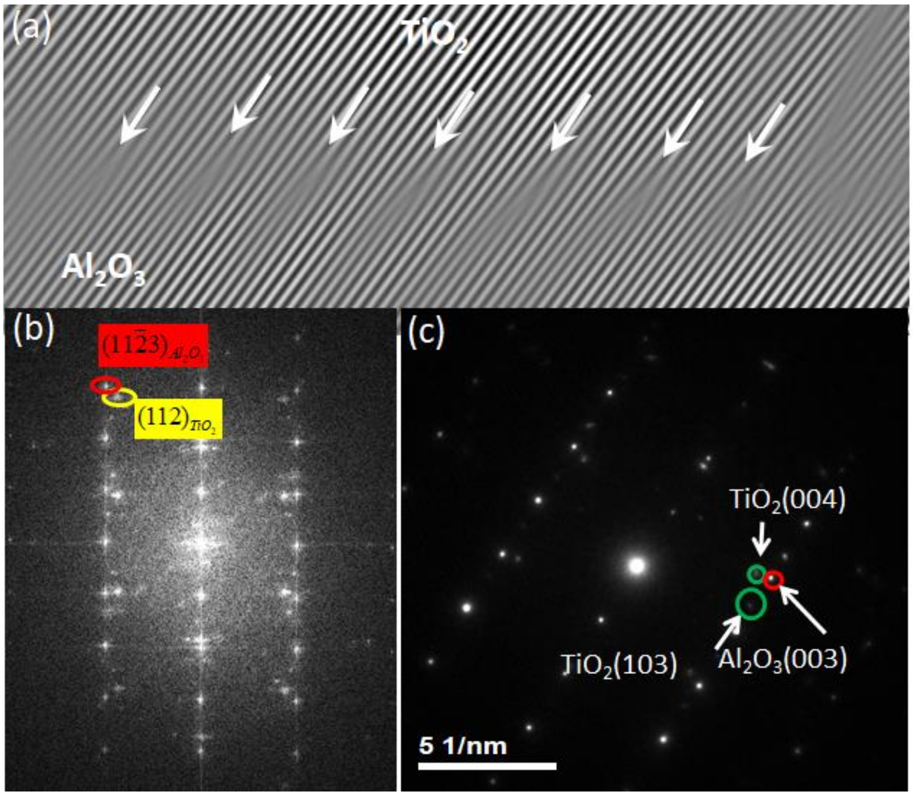

Figure 3. (a) Inverse FFT image reconstructed from the <112> and <11-23> reflections of the anatase film and the Al_2O_3 substrate. (b) FFT image acquired at the interface between epitaxial anatase TiO_2 film and the Al_2O_3 substrate. (c) Electron diffraction patterns acquired at the interface between epitaxial anatase TiO_2 film and the Al_2O_3 substrate.

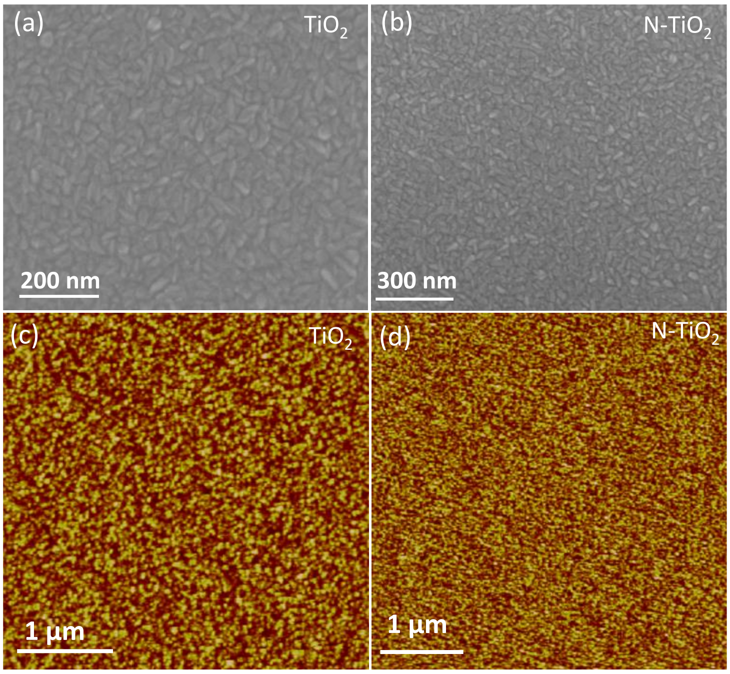

Figure 4. FESEM and AFM images of anatase epitaxial (a, c) TiO_2 and (b, d) N-TiO_2 thin films on Al_2O_3 substrate.

From the TEM and XRD analysis, the epitaxial relationships between the TiO_2 film and the Al_2O_3 substrate are obtained as <001>TiO_2//<0001> Al_2O_3 and <-110>TiO_2//<01-10>Al_2O_3. The present study establishes the formation of single phase epitaxial anatase TiO_2 and N-TiO_2 thin films on the Al_2O_3 (0001) substrate and the epitaxial relation between them. The ED pattern in Figure 3c shows the (103) crystallographic shear plane arising from a Magneli phase. FESEM and Atomic force microscopy (AFM) image of TiO_2 and N-TiO_2 films shows smooth surfaces with granular morphology. The RMS roughness of the TiO_2 film is 5 nm and that of for N-TiO_2 film is 8 nm (**Figure 4**).

X-ray photoelectron spectroscopy was used to determine chemical composition of the films. The Ti 2*p*, O 1*s* and N 1*s* core-level spectra were corrected with C 1s core-level spectrum (**Figure 5**). In the Ti 2p core-level signal, the Ti $2p_{3/2}$ and Ti $2p_{1/2}$ binding energies in the TiO_2 thin film are 458.4 and 464.2 eV respectively with an energy difference of 5.8 eV characteristics of Ti in 4+ state. The N-TiO_2 thin film exhibits a shift in both these states towards lower binding energies and appears at 458.0 and 463.7 eV respectively. The shifts in Ti $2p_{3/2}$ and Ti $2p_{1/2}$ states show that the N atoms substitute the O atoms in the TiO_2 lattice. It is known that the N doping strongly affects the properties of TiO_2 thin films.[23-24] The high-resolution O 1s peak of the TiO_2 film is deconvoluted into two peaks centered at 529.6 and 531.4 eV

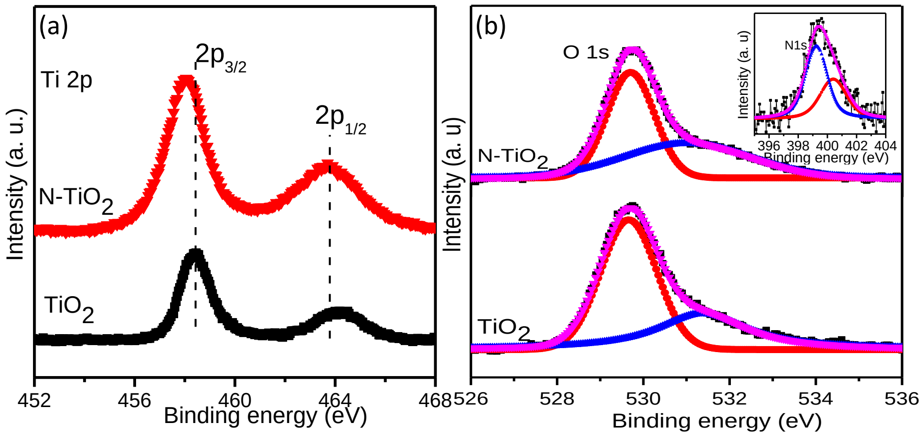

Figure 5. High resolution XP spectra of (a) Ti 2*p* and (b) O 1*s* signal of TiO_2 and N-TiO_2 thin films. Inset of (b) shows high resolution XP spectra of N 1*s* signal of N-TiO_2 film.

respectively. The peak at 529.6 eV is due to Ti-O bonding in TiO_2 and the peak at 531.4 eV is due to O bonding with surface impurities. Similarly, the O1s peak of the N-TiO_2 film could be deconvoluted into two peaks, in which the peak due to Ti-O bonding appears at 529.7 eV and peak due to surface species appears at 531.2 eV respectively. The N 1s signal in the N doped TiO_2 film can be deconvoluted into two components centered at 399.2 eV due to substitutional N and at 400.5 eV due to surface nitrogen (inset of Figure 5b). From XPS analysis, the substitutional N percentage in the N-TiO_2 film is estimated to be 4.0 at. %.

Room temperature Hall measurements were carried out to determine conductivity-type, carrier concentration and mobility of anatase epitaxial TiO_2 and N-TiO_2 thin films. We observe a positive Hall coefficient of 8928 cm^3/C for TiO_2 and 5208 cm^3/C for N-TiO_2, confirming *p*-type conductivity of the films. The Hall mobility was calculated from the equation

$$\mu = \frac{1}{ne\rho}$$

where *n* is carrier concentration, *e* is electron charge and ρ is resistivity of TiO_2 and N-TiO_2 films. From Hall measurements, the hole concentration, mobility and resistivity of the TiO_2 film are 7×10^{14} $/cm^3$, 1.2 cm^2/V-s and 7.22×10^3 Ω-cm respectively. Similarly, for the N-TiO_2 film, the hole concentration, mobility and resistivity are 1.2×10^{15} $/cm^3$, 4.6 cm^2/V-s and 1.16×10^3 Ω-cm respectively. TiO_2 inherently exhibits *n*-type conductivity due to the presence of oxygen vacancies and titanium interstitials, they are shallow donors. On the other hand, titanium vacancies are shallow acceptors responsible for *p*-type conductivity.[25] We believe that the *p*-

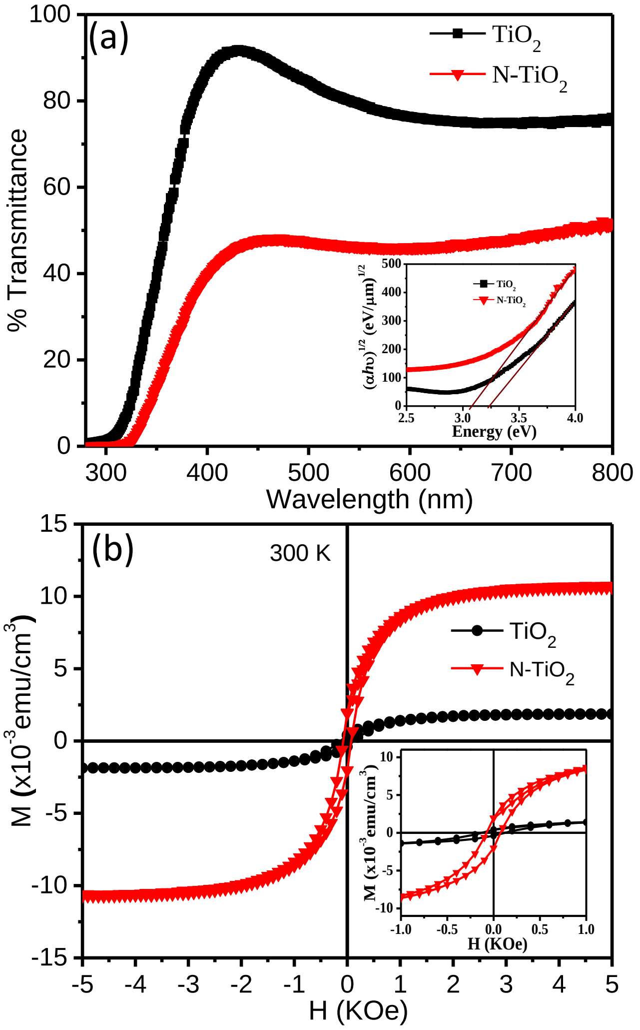

Figure 6. (a) Optical transmittance spectra of epitaxial anatase TiO_2 and N-TiO_2 thin films on Al_2O_3 substrate. Inset shows $(\alpha h\nu)^{1/2}$ versus hν plot. (b) Magnetization versus magnetic field (M-H) curves of epitaxial anatase TiO_2 and N-TiO_2 thin films measured at room temperature. Inset shows enlarged part of the M-H curves of the films.

type conductivity behavior in ALD grown TiO_2 and N-TiO_2 thin films arises from titanium vacancies.

Optical and magnetic properties

Figure 6a shows the optical transmittance spectra of the TiO_2 and N-TiO_2 thin films in the range 200-800 nm. The films exhibit a transmittance band in the visible region and an absorption band edge in the ultraviolet region. The band edge of epitaxial anatase TiO_2 thin film (317 nm) shows red shift upon N doping (323 nm). The TiO_2 film shows high transmittance of about 80%, while N-TiO_2 shows about 50% transmittance in the visible region. The optical bandgap of the films estimated from the Tauc plots are shown inset of Figure 6a. From $(\alpha h\nu)^{1/2}$ versus $h\nu$ plots, the bandgap of TiO_2 is determined as 3.23 eV, which is close to the value of bulk anatase TiO_2. The bandgap decreases to 3.07 eV in the N-TiO_2 film.

Oxygen vacancies and other defects in the film induce room temperature ferromagnetism (RTFM) in un-doped *n*-type epitaxial anatase TiO_2 thin films.[26-27] It has been suggested that Ti vacancies induce magnetism in *p*-type TiO_2.[28] This prediction was experimentally realized recently by observing RTFM in un-doped anatase TiO_2 nanoparticles.[17] In Figure 6b, we show magnetization versus magnetic field (M-H) curves of TiO_2 and N-TiO_2 thin films measured at 300 K in the field range -10 to +10 kOe. TiO_2 and N-TiO_2 films with the same dimensions were used for magnetic measurements. After subtracting the substrate contribution, the volume of the films was estimated as 0.003612 cm^3. Figure 6b show a distinct hysteresis loop with saturation magnetization in both the films due to room-temperature ferromagnetism. TiO_2 shows weaker ferromagnetic features than N-TiO_2 as expected. The saturation magnetization of the TiO_2 film is 1.8×10^{-3} emu/cm^3 and 0.01 emu/cm^3 for the N-TiO_2 film. The enlarged M-H curve (see inset of Figure 6b) in the field range -1 to +1 kOe reveals that TiO_2 film exhibits a remanent magnetization of 0.0005 emu/cm^3 and a coercive field of 130 Oe. The N-TiO_2 film exhibits a remanent magnetization of 0.002 emu/cm^3 and a coercive field of 75 Oe respectively.

Epitaxial anatase TiO_2 and N-TiO_2 thin films show photoresponse under illumination of ultraviolet (UV) radiation. From the I-V characteristic (**Figure 7**), it is observed that the TiO_2 thin film registers 0.1 µA dark current and 0.24 µA photocurrent at forward applied bias of 1V. Similarly, the N-TiO_2 thin film registers

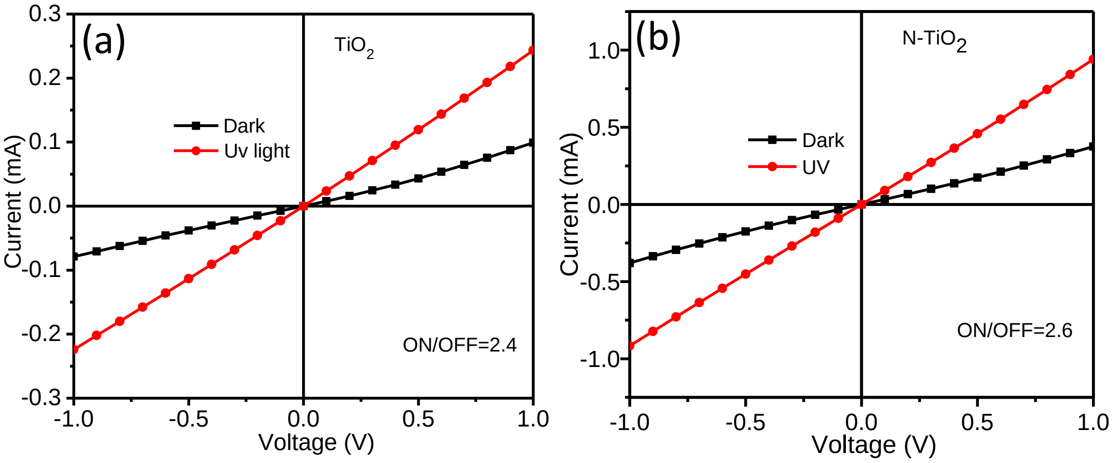

Figure 7. I-V characteristics of epitaxial anatase (a) TiO_2 and (b) N-TiO_2 thin films under dark and UV photoillumination conditions.

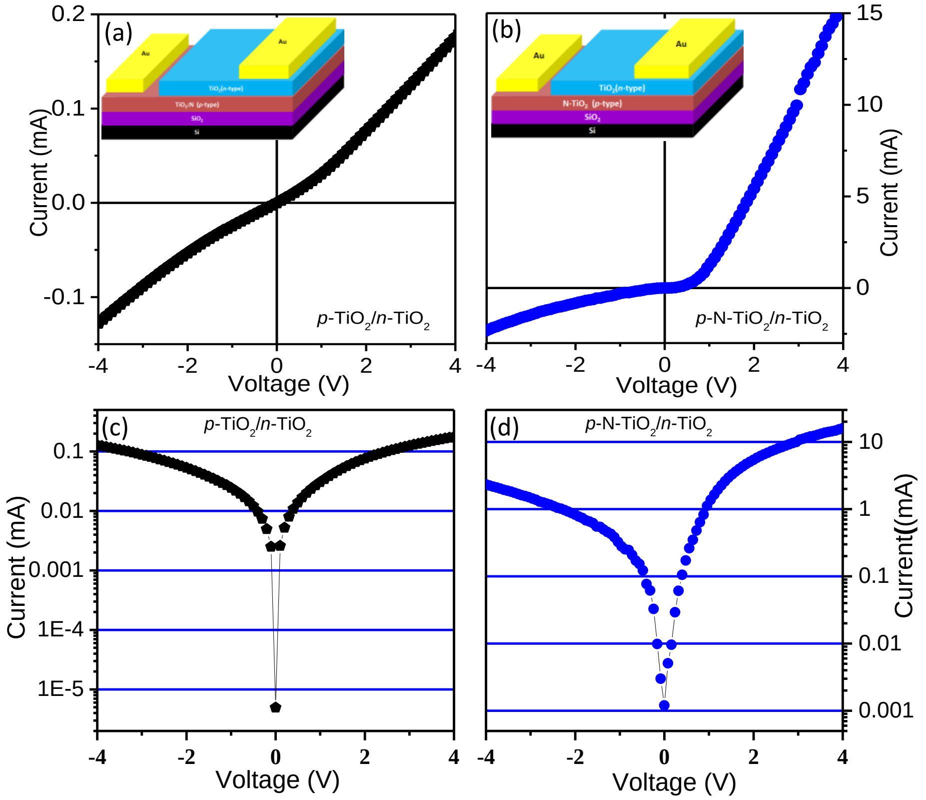

Figure 8. I-V characteristics of *p-n* homojunction of (a) *p*-TiO_2/*n*-TiO_2 and (b) *p*-N-TiO_2/ *n*-TiO_2 devices. The device architecture in both cases is shown as insets. I-V characteristic in log scale of *p-n* homojunctions made with (c) *p*-TiO_2/*n*-TiO_2 and (d) *p*-N-TiO_2/*n*-TiO_2 devices.

0.36 μA dark current and 0.96 μA photocurrent at forward applied bias of 1 V. The on/off ratio of the TiO_2 film is 2.4 and increases to 2.6 for N-TiO_2 thin film.

TiO_2 based p-n homojunction diodes

Reports on TiO_2 based homojunction diode are few.[20, 29] Taking advantage of the *p*-type conductivity in ALD grown TiO_2 and N-TiO_2 thin films, we have fabricated a TiO_2 based homojunction diode on SiO_2/Si substrate. The diode I-V characteristics were examined for two *p-n* homojunctions made with *p*-TiO_2/*n*-TiO_2 and *p*-N-TiO_2/*n*-TiO_2 devices. The I-V characteristics for the two *p-n* junctions devices are shown in **Figure** 8a & b. The corresponding schematic of the device architecture devices are shown as insets in Figure 8a & b. The *p*-TiO_2/*n*-TiO_2 device shows weak rectification behavior. In contrast, the *p*-N-TiO_2 /*n*-TiO_2 device shows 10 times better rectification (Figure 8 c & d) of the *p–n* junction with a turn-on voltage at about 1 V under forward-biased voltage and a moderate leakage current under reverse-biased voltage. To examine the validity of the *p–n* junction of *n*-TiO_2/*p*-N-TiO_2 device, we have measured I-V characteristics between the *p*-type N-TiO_2 layer and a gold electrode, and a *n*-type TiO_2 layer and gold electrode. In both the cases, we observe linear I-V characteristics ensure that the rectification behavior *n*-TiO_2/*p*-N-TiO_2 device is arises from the *p*-*n* junction.

5. Conclusions

In conclusion, epitaxial thin films of anatase TiO_2 (001) have been successfully deposited on Al_2O_3 (001) substrates by atomic layer deposition at 300 °C. N-doping of TiO_2 affects structural, optical, electrical and magnetic properties of the epitaxial films. Titanium vacancies seems to be the primary source of *p*-type conductivity and room temperature ferromagnetism in undoped and N-doped TiO_2 thin films. The observation of diode rectification from the TiO_2 based *p*-*n* homojunction has opened the way for using TiO_2 thin films for device applications.

6. References

[1] L. Liu, H. Zhao, J. M. Andino, Y. Li, *ACS Catal.* **2012**, *2*, 1817-1828.

[2] T. Luttrell, S. Halpegamage, J. Tao, A. Kramer, E. Sutter, M. Batzill, *Sci. Rep.* **2014**, *4*, 4043.

[3] Y. Matsumoto, M. Murakami, T. Shono, T. Hasegawa, T. Fukumura, M. Kawasaki, P. Ahmet, T. Chikyow, S.-y. Koshihara, H. Koinuma, *Science* **2001**, *291*, 854-856.

[4] N. H. Hong, J. Sakai, W. Prellier, A. Hassini, A. Ruyter, F. Gervais, *Phys. Rev. B* **2004**, *70*, 195204.

[5] X. Li, S. Wu, P. Hu, X. Xing, Y. Liu, Y. Yu, M. Yang, J. Lu, S. Li, W. Liu, *J. Appl. Phys.* **2009**, *106*, 043913.

[6] Y. Hirose, N. Yamada, S. Nakao, T. Hitosugi, T. Shimada, T. Hasegawa, *Phys. Rev. B* **2009**, *79*, 165108.

[7] Y. Furubayashi, T. Hitosugi, Y. Yamamoto, K. Inaba, G. Kinoda, Y. Hirose, T. Shimada, T. Hasegawa, *Appl. Phys. Lett.* **2005**, *86*, 252101.

[8] R. Ciancio, E. Carlino, G. Rossi, C. Aruta, U. Scotti di Uccio, A. Vittadini, A. Selloni, *Phys. Rev. B* **2012**, *86*, 104110.

[9] T. Luttrell, S. Halpegamage, E. Sutter, M. Batzill, *Thin Solid Films* **2014**, *564*, 146-155.

[10] D.-H. Kim, W.-S. Kim, S. Kim, S.-H. Hong, *ACS Appl. Mater. Interfaces* **2014**, *6*, 11817-11822.

[11] T. J. Kraus, A. B. Nepomnyashchii, B. A. Parkinson, *ACS Appl. Mater. Interfaces* **2014**, *6*, 9946-9949.

[12] A. R. Akbashev, G. Chen, J. E. Spanier, *Nano Lett.* **2014**, *14*, 44-49.

[13] M. Coll, J. Gazquez, A. Palau, M. Varela, X. Obradors, T. Puig, *Chem. Mater.* **2012**, *24*, 3732-3737.

[14] M. D. McDaniel, T. Q. Ngo, S. Hu, A. Posadas, A. A. Demkov, J. G. Ekerdt, *Appl. Phys. Rev.* **2015**, *2*, 041301.

[15] M. Coll, J. M. Montero Moreno, J. Gazquez, K. Nielsch, X. Obradors, T. Puig, *Adv. Funct. Mater.* **2014**, *24*, 5368-5374.

[16] A. R. Akbashev, A. V. Plokhikh, D. Barbash, S. E. Lofland, J. E. Spanier, *APL Mater.* **2015**, *3*, 106102.

[17] S. Wang, L. Pan, J.-J. Song, W. Mi, J.-J. Zou, L. Wang, X. Zhang, *JACS* **2015**, *137*, 2975-2983.

[18] Z. Li, D. Ding, C. Ning, *Nanoscale Res. Lett.* **2013**, *8*, 25.

[19] Y. P. Yu, W. Liu, S. X. Wu, S. W. Li, *J. Phys. Chem. C* **2012**, *116*, 19625-19629.

[20] A. T. Iancu, M. Logar, J. Park, F. B. Prinz, *ACS Appl. Mater. Interfaces* **2015**, *7*, 5134-5140.

[21] I. A. Alhomoudi, G. Newaz, *Thin Solid Films* **2009**, *517*, 4372-4378.

[22] J. Narayan, B. C. Larson, *J. Appl. Phys.* **2003**, *93*, 278-285.

[23] S. H. Mohamed, O. Kappertz, J. M. Ngaruiya, T. Niemeier, R. Drese, R. Detemple, M. M. Wakkad, M. Wuttig, *Phys. Status Solidi A* **2004**, *201*, 90-102.

[24] S. H. Mohamed, O. Kappertz, T. Niemeier, R. Drese, M. M. Wakkad, M. Wuttig, *Thin Solid Films* **2004**, *468*, 48-56.

[25] B. J. Morgan, G. W. Watson, *Phys. Rev. B* **2009**, *80*, 233102.

[26] A. Sundaresan, C. N. R. Rao, *Nano Today* **2009**, *4*, 96-106.

[27] N. H. Hong, J. Sakai, N. Poirot, V. Brizé, *Phys. Rev. B* **2006**, *73*, 132404.

[28] H. Peng, J. Li, S.-S. Li, J.-B. Xia, *Phys. Rev. B* **2009**, *79*, 092411.

[29] A. Hazra, P. Bhattacharyya, *IEEE Trans. Electron Devices* **2015**, *62*, 1984-1990.

Chapter III.3

Atomic Layer Deposition of Ultrathin Epitaxial Films of V_2O_5

SUMMARY*

Ultrathin epitaxial films (10 to 90 nm thick) of V_2O_5 have been grown on c-Al_2O_3 by atomic layer deposition using vanadyl acetylacetonate as the vanadium precursor along with oxygen plasma. Various process parameters have been optimised for the purpose, and excellent crystalline films could be obtained below 200 °C, without the need for post-heat treatment. With a moderate temperature window, the process yields a growth rate of 0.45 Å /cycle. The films have been characterized by electron microscopy, atomic force microscopy, Raman spectroscopy and other means. The films exhibit a (001) preferred orientation with respect to c-Al_2O_3 and undergo compressive strain at the initial few monolayer growth to adjust epitaxially with the substrate. Heterojunction diodes based on TiO_2(*p*)-(*n*)V_2O_5 as well as a humidity sensor have been fabricated using the V_2O_5 films.

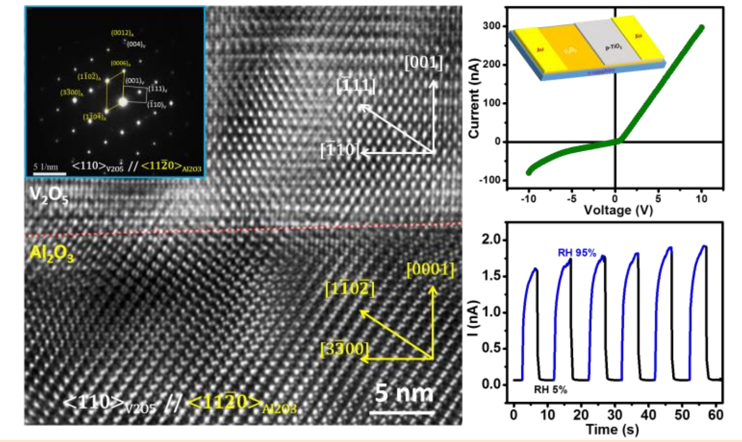

---

*A paper based on this work has appeared in ACS Applied Materials & Interfaces (2017).

1. Introduction

Vanadium oxides show many interesting optical and electrical properties including sharp metal to insulator transitions.[1-3] Among the different vanadium oxides, vanadium pentoxide (V_2O_5) is a widely investigated material.[4-7] V_2O_5, crystallizing in the orthorhombic structure (P*mmn* space group, a = 11.5190, b = 3.5640 and c = 4.3730 Å), comprises a 2D layered structure with zig-zag double chains of VO_6 octahedra forming sheets parallel to the b axis. The $(V_2O_4)_n$ double chain polyhedra share edges along (001) and share corners in the (100) direction.[1] There is growing interest to deposit stoichiometric V_2O_5 thin films for use in lithium and sodium ion batteries.[8-9] V_2O_5 thin films have been deposited on various substrates by several techniques which include physical vapor deposition,[10] pulsed laser deposition,[11] sputtering, e-beam evaporation,[12] electrospinning, and spray pyrolysis. The V_2O_5 films obtained by these methods at a relatively low substrate temperature (below 300 °C) are generally amorphous.[13] Deposition of V_2O_5 thin films and their properties are described extensively in reviews.[13-14] Single crystalline epitaxial films are preferable for energy-related device applications.[15] The lack of proper growth parameters to deposit epitaxial V_2O_5 films uniformly on a large area limits its use in device applications.

Atomic layer deposition (ALD) is a versatile method for the deposition atomically thin films.[16] It has gained wide attention of the device community since it enables precise control of thickness at the atomic level with pinhole-free films.[17-18] There have been efforts to deposit VO_x films using ALD by employing $VO(O^iPr)_3$,[19-22] $VOCl_3$,[23] $VO(thd)_2$,[24-25] and $VO(acac)_2$ [26] as precursors, but these have yielded the amorphous or polycrystalline films with mixed phases.[27-29] The ALD films described hitherto require post-annealing,[30] which degrades the quality and properties of the films due to the crack formation.[15, 31] It seems therefore important to grow single crystalline epitaxial films with a specific phase, as an active interfacial layer for device applications without post-annealing treatment.[15] The main purpose of the present study was to deposit the single crystalline epitaxial films of V_2O_5 by ALD and to investigate some of the important properties.

2. Scope of the present investigations

Oxides of vanadium exist in several stable oxidation forms such as V_2O_3, VO_2 and V_2O_5 and exhibit metal to insulator transition accompanied by crystal structure change. V_2O_5 is well-studied van der Waals layered multifunctional material attracted due to its excellent electrochemical properties in batteries and supercapacitors. The applications of V_2O_5 are less extended towards electronics and sensing due to difficulty in flat films of V_2O_5 over a large area. ALD is a versatile technique to grow uniform flat films with precise control of thickness at atomic level compare any other deposition techniques. The epitaxial films are preferred for device applications, there is no reports on epitaxial crystalline films since ALD involves low deposition temperature. Considering that epitaxial films of oxides such as TiO_2 have successfully grown by ALD,[32-33] we have carried out investigations on the deposition of epitaxial V_2O_5 films by this technique. We have been able to successfully grow single-phase crystalline epitaxial V_2O_5 films on c-Al_2O_3 by employing $VO(acac)_2$ and oxygen plasma using ALD. We have studied the growth kinetics by varying the growth parameters and arrived at optimised conditions to obtain crystalline epitaxial films below 200 °C, without any post-temperature treatment. We have also fabricated a V_2O_5 film based humidity sensor and a TiO_2-V_2O_5 based p-n heterojunction diode.

3. Experimental Section

Thin film growth

Deposition of epitaxial V_2O_5 thin films:

Epitaxial orthorhombic V_2O_5 thin films were grown by plasma-enhanced atomic layer deposition (PEALD) on single crystalline *c*-Al_2O_3 (0001) substrates using a flow type ALD reactor (Beneq, TFS 200 Finland Oy). Prior to the deposition, the substrates were cleaned thoroughly using H_2SO_4 and H_2O_2 in the ratio 4:1 at 120 °C followed by ultrasonication in acetone and isopropanol and dried under nitrogen. Highly pure vanadyl acetylacetonate ($VO(acac)_2$, 99.9%) and oxygen (Chemix, 99.9995) were employed as V and O_2 plasma sources respectively. Ultra-pure N_2 (Chemix, 99.9995) was used as a carrier and purging gas at the rate of 600 sccm throughout the deposition.

The chamber and reactor were pumped down to 10 and 1 mbar respectively before the starting recipe. The reaction chamber was slowly heated to 200 °C and to stabilized at the temperature for 30 min. $VO(acac)_2$ was kept in the hot source HS-300 bubbler (Beneq, Oy) and heated slowly to 140 °C to vaporize it. The precursor line was maintained at a slightly higher temperature than that the hot source to avoid condensation. Oxygen plasma was generated using Advanced Energy Cesar RF power generator equipped with ALD, the plasma power set to be 100 W. The films were deposited by sequential pulsing of $VO(acac)_2$ and oxygen plasma. The optimized pulse and purge times for $VO(acac)_2$ were 4 s and 2 s respectively, whereas the pulse and purge times for oxygen plasma were both 2 s. A variation in the reactor pressure between 1-3 mbar was observed during pulsing and purging, the chamber pressure being almost intact. The complete ALD cycle sequence was pulse $VO(acac)_2$/purge//pulse O_2 plasma/purge for 4 s/2 s//2 s/2 s. Deposition was carried out for 250, 500, 1000 and 2000 cycles at 200 °C and the films cooled down to room temperature. The as-obtained films were used for further characterization without post temperature treatment. To ascertain the ALD temperature window and the self-terminating nature of ALD process, depositions were carried out at different reactor temperatures and pulse times of $VO(acac)_2$. The growth rate per cycle was calculated by dividing the thickness of the film by a number of cycles, it was found to be 0.45 Å/cycle.

TEM sample preparation:

TEM samples were prepared by a lift-off method using focused ion beam (FIB) technique. A dual beam FIB/SEM system (quantum 3D, Icon analytical) operating at an accelerating voltage 0.5-30 kV equipped with a gallium source was employed for the purpose. The sample was prepared using various beam currents ranging from 30 pA to 5 nA and acceleration voltage of 5 to 30 kV respectively. FIB process involves four steps (1) deposit the protective material on the film in selected area (2) cut-off the selected region using FIB (3) lift-off and transferred to TEM grid (4) final thinning and cleaning the surface. During the first step, 15 µm area of the film was selected and protected with platinum coating in order to avoid the damages to the film. The two trenches were milled using high current Ga ion beam on either side, the trenches are stepped down by tilting the sample at 55° and cut from both the sides. At this stage lamella is left attached to its bulk from other two corners. Thin down the lamella using low current focused Ga ion until it is transparent to electrons. Reduce the beam current and polish the lamella for its nominal thickness. Cut the top two corners of the lamella and lift-off using Omni-probe and transfer it on to TEM grid. Fix the lamella by Pt deposition and polish it for final thinning. Once it transparent to electron clean the surface and analyze it in TEM.

Characterization

The crystallinity of the as-deposited films was confirmed by the X-ray diffraction (XRD) patterns recorded with a Panalytical diffractometer (Empyrean) using monochromatic Cu Kα radiation (λ = 1.5404Å). Raman spectra were recorded in backscattering geometry using a 632 nm HeNe laser with a Jobin Yvon LabRam HR spectrometer. X-ray photoelectron (XP) spectra were recorded using an Omicron nanotechnology spectrometer with Mg Kα X-ray source (E = 1253.6 eV). Field emission scanning electron microscope (FESEM) Nova NanoSEM 600 FESEM equipped with an Energy Dispersive X-ray (EDX) analysis system (FEI Company) was employed to ascertain the film thickness (in cross-section mode) and surface morphology. The surface roughness and topography of the films were determined using atomic force microscopy in tapping mode (AFM, Bruker Innova). The sample for transmission electron microscopy (TEM) was prepared by the "lift-off" method using focused ion beam (FIB) milling in FEI Quanta 3D dual beam SEM/FIB system. Cross-sectional high-resolution TEM (HRTEM) and electron energy loss spectroscopy (EELS) were obtained using FEI TITAN 80−300 operated at 300 kV. Optical transmission spectra were recorded in a PerkinElmer UV−Vis spectrometer from 200 to 800 nm range. Room-temperature carrier concentration and mobility were determined using Ecopia HMS-3000 Hall effect measurement system. Photoresponse measurements were performed with a Keithley instrument under dark and ultraviolet (365 nm) LED light illumination. The device was fabricated using optical lithography (Intelligent Micropatterning Ltd., 365 nm) by making 6 µm Au gap electrodes.

TiO_2-V_2O_5 (p-n) Heterojunction

A heterojunction p-n diode was fabricated on the *c*-Al_2O_3 substrate using TiO_2 films with p- carriers and V_2O_5 with n-type carriers. By employing thermal ALD, a 45 nm

TiO_2(p-type) thin film with a hole concentration 7 × 10^{14} /cm^3 and mobility of 1.2 cm^2/V·s was deposited. In brief, the film was deposited at 300 °C with the growth rate of 0.3 Å/cycle using $TiCl_4$ and water as Ti and O precursor. The ALD cycle sequence is pulse-$TiCl_4$/Purge-N_2//pulse-H_2O/purge-N_2 for 400 ms/2 s//200 ms/2 s respectively. The p−n heterojunction was achieved by masking half-portion of deposited 45 nm n-type V_2O_5 layers and depositing 45 nm p-type TiO_2 film in the unmasked region. Similarly a layer of n-type TiO_2 an electron concentration 6.4×10^{18} /cm^3 and mobility of 2 cm^2 /V.s was deposited on V_2O_5 by KrF excimer pulsed laser deposition (PLD).[32] On the surface of n-and p-type layers, gold electrodes were deposited by sputtering for electrical contacts. The I−V characteristics were measured using a Keithley 4200 semiconductor characterization system.

Humidity sensing and photoresponse

For the humidity sensing and photoresponse measurements, the Au electrodes were patterned using conventional optical lithography (IMP SF 100) followed by thermal evaporation. The device was subjected to humidity measurement under various relative humidity conditions (obtained by bubbling fresh nitrogen into deionized water) and the response was recorded using Keithley 4200. Similarly, photoresponse measurements were done under UV light, on and off state.

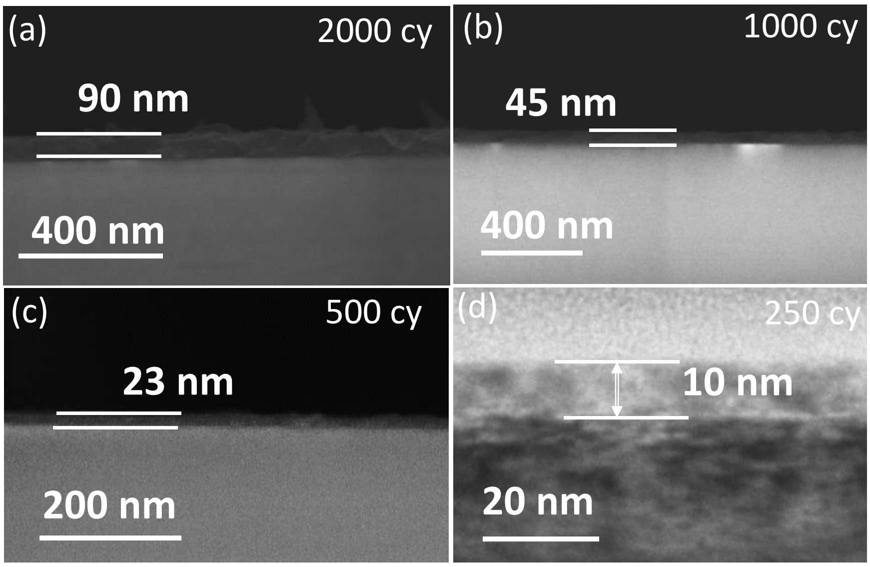

Figure 1. Cross-sectional SEM images of thin films of (a) 2000 (b) 1000 (c) 500 and (d) 250 (TEM image) cycles. Films were freshly cut for cross-sectional analysis in SEM. TEM sample was prepared by FIB technique.

4. Results and Discussion

Characteristics of epitaxial V_2O_5 films

Epitaxial orthorhombic V_2O_5 thin films of thickness (10-90 nm) were deposited on transparent c-axis Al_2O_3 substrates by employing $VO(acac)_2$ and oxygen plasma as V and O precursors respectively. The thickness of the films was measured using cross-sectional SEM and TEM (**Figure 1**). The films were light yellow in color (inset of **Figure 2**a). To achieve large-scale uniformity and a self-terminating reaction, the process was optimized for both the temperature window and the precursor pulse rate. The growth rate per cycle (GPC) shown in Figure 2(a) indicates steady state between 190 and 210 °C, suggesting that the ALD process operates in a moderate temperature window. Non-uniformity in the films as well as a decrease in GPC were observed below 185 °C and above 210 °C. The GPC decreases and non-uniformity increases

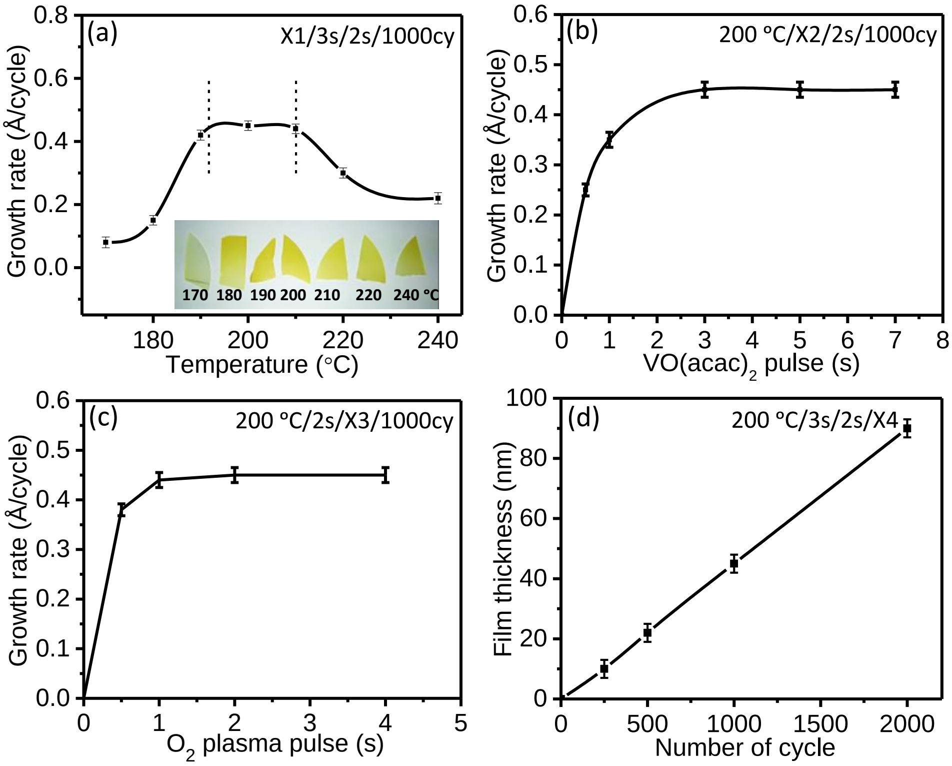

Figure 2. Cross-sectional FESEM based result of the ALD process. (a) Growth rate as a function of substrate temperature (inset shows the images of the V_2O_5 films at different growth temperatures). (b) Saturation behavior of $VO(acac)_2$ with pulse time (c) growth rate as a function of O_2 plasma pulse time and (d) film thickness as functions of cycle number. Error bars indicate the standard deviation of thickness within the detection limit of SEM. (The sequence temperature/$VO(acac)_2$ pulse/O_2 plasma pulse/cycle number is abbreviated as X1/X2/X3/X4).

above 210 °C may be due to desorption of reactive surface groups from the substrate. Below 180 °C, there may be insufficient activation energy to complete the surface saturation reaction.[16]

An important characteristic of ALD growth is the saturation behavior of the surface reaction with precursor pulse in each ALD cycle. To evaluate the self-saturation growth rate, we monitored the deposition by varying the $VO(acac)_2$ pulse dose time at 200 °C (Figure 2b). Reaction with $VO(acac)_2$ saturates quickly, the GPC of the deposition remaining constant for pulses > 2-3 s, indicating a self-limiting reaction with surface groups, and eliminating the possibility of CVD type of growth. From Figure 2b it is clear that the 3 s pulse of $VO(acac)_2$ is sufficient to saturate the surface and plasma pulse of 2 s required to oxidize the organic part of the precursor (Figure 2c). We allowed a purging time of 4 s and 2 s for $VO(acac)_2$ and oxygen plasma respectively to avoid any undesired reactions. In an ideal ALD process, the growth rate remains constant independent of the number of cycles. Figure 2d show the thickness and GPC functions of the cycle number. The thickness of the film increases linearly with the cycle number indicating typical ALD growth. The GPC is constant over the number of cycles due to layer by layer deposition. We observed a constant growth rate of 0.45 Å/cycle in this temperature window which is higher than the ozone (0.27 Å /cy) and water (0.3 Å /cy) based ALD process with vanadyl triisopropoxide.[21, 22] Ideally ALD growth rate should be close to one monolayer V_2O_5 (2.19 Å in 001

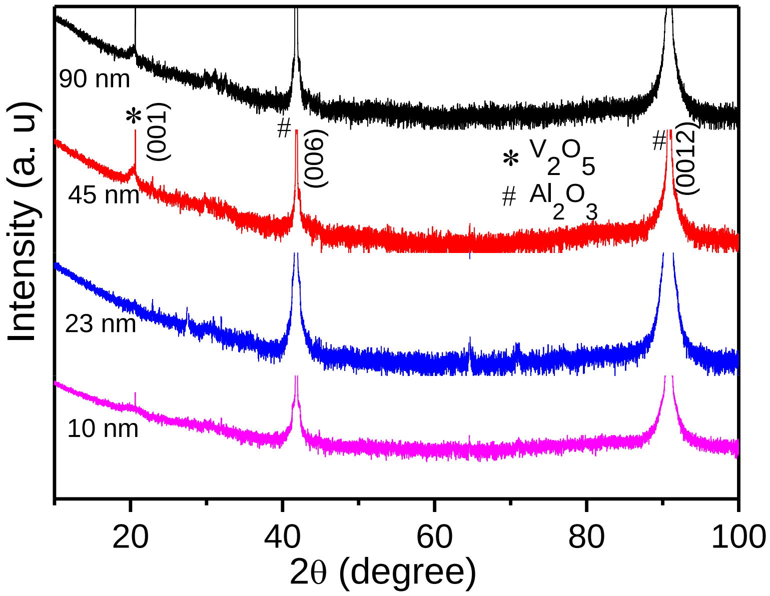

Figure 3. PXRD patterns of as deposited V_2O_5 thin films using $VO(acac)_2$ and O_2 plasma by ALD.

direction) per cycle, but the observed growth rate is lower since the reaction involves large $VO(acac)_2$ molecules. By considering the previous report on O_2 plasma-based ALD process by Musschott et al., the underlying monolayer mechanism would be combustion type of mechanism as indicated by the growth rate. CO_2 and H_2O are the possible by-products in the O_2 plasma-based process.

The crystallinity of the as-deposited films was confirmed by the XRD, Raman, and TEM studies. XRD patterns of the V_2O_5 films (**Figure 3**), show a (001) reflection along with the (0006) reflection of c-Al_2O_3, suggesting that the orthorhombic structure grows along the crystallographic *c* direction. The preferential growth indicates the epitaxial nature of the V_2O_5 thin films on *c*-Al_2O_3. The intensity of the (001) reflections increases with the film thickness which suggests further degree of crystallinity.[24] Raman spectroscopy is a useful technique to study the structure and phase of the thin films,[32, 34] and we show Raman spectra of V_2O_5 thin films as a function of film thickness (10-90 nm) in **Figure 4**a. The spectra show seven characteristic bands between 100 to 1000 cm^{-1} of orthorhombic V_2O_5 confirming the crystallinity of the films.[34] The bands due to the B_{3g}, B_{2g}, A_g, A_g, A_g, B_{2g} and A_g phonon modes at 148, 286, 308, 407, 531, 706 and 998 cm^{-1} respectively are shifted by 4 to 5 cm^{-1} towards higher energies compared to the bulk powder due to strain in the films. The prominent B_{3g} bending mode at 148 cm^{-1} is strongly associated with the ordered layer structure[35] and with the preferred orientation with (0006) of Al_2O_3.[36] The blue shift in the A_g symmetric stretching vibration mode of thin films (998-1000 cm^{-1}) compared to bulk (994.5 cm^{-1}) indicates compressive strain in the films. As the

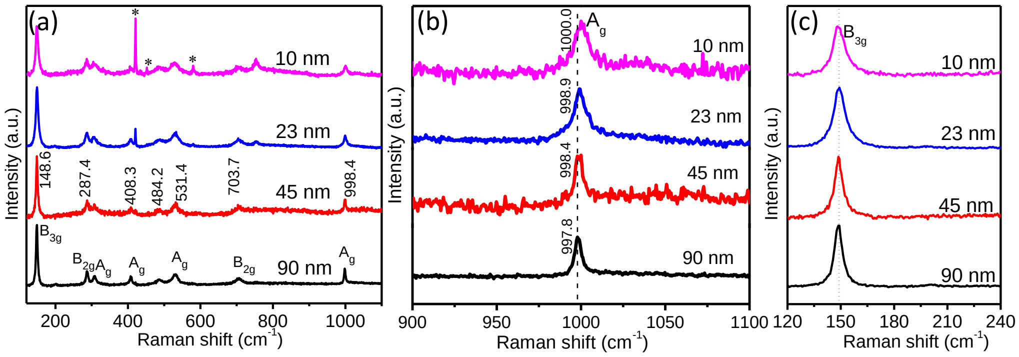

Figure 4. (a) Raman spectra of epitaxial V_2O_5 thin films of different thickness (10-90nm) grown on Al_2O_3 substrates (b) Raman shift of the A_g stretching vibration mode due to strain and (c) expanded region of the B_{3g} bending mode (* indicates the peaks corresponding to the substrate).

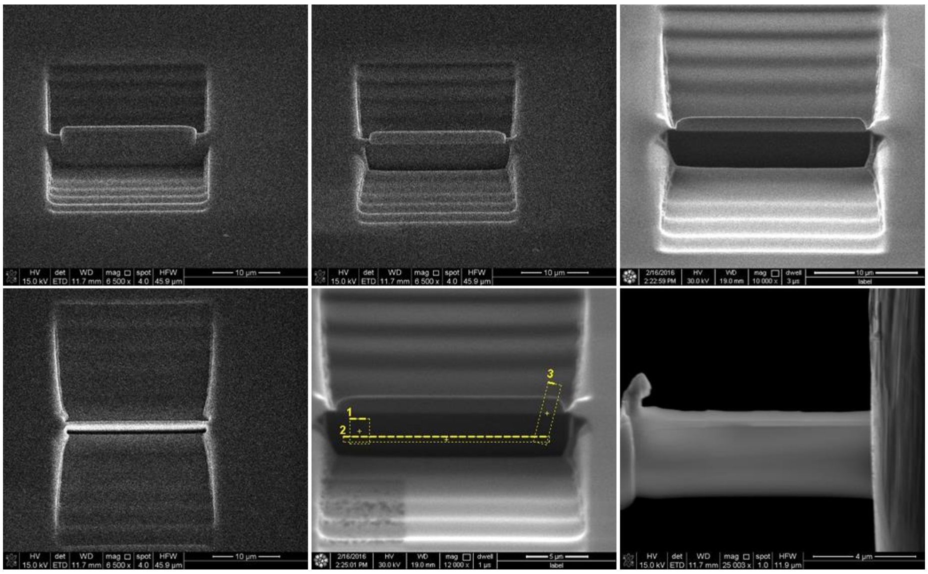

Figure 5. FIB processing SEM images of epitaxial thin films of V_2O_5 on c-Al_2O_3.

film thickness increases from 10 nm (1000 cm^{-1}) to 90 (997.8 cm^{-1}) nm, the strain decreases due to lattice relaxation (Figure 4b). The absence of any shift in the peak position of the bending modes indicates similar structural ordering in all the films (Figure 4c).[34]

The crystallographic epitaxial relations of orthorhombic V_2O_5 films with c-Al_2O_3 were analysed by cross-section HRTEM studies. The TEM samples were prepared by the lift-off method using FIB technique (**Figure 5**). A cross-sectional bright-field TEM image of the V_2O_5 film on Al_2O_3 shown in **Figure 6**a gives the thickness of the V_2O_5 film to be 10 nm. Figure 6b shows the EEL spectrum collected on the substrate (red line) and at the interface of the film and substrate (blue line). The spectrum at the interface shows the two distinguished peaks at 518 eV and 525.5 eV corresponds to V L_3 and L_2 edge emission due to V 2p to 3d transition.[37-38] Figure 6c displays the selected area electron diffraction (SAED) patterns collected at the interface along the [11-20] zone axis of the sapphire. The ED pattern shows well-ordered single crystalline spots as well as epitaxial nature of the orthorhombic V_2O_5 film on Al_2O_3 substrate. Three sets of parallel crystallographic relations, <001>V_2O_5//<0003>Al_2O_3, <-111>V_2O_5//<1-10-1>Al_2O_3 and <-110>V_2O_5//<3-300> Al_2O_3 can be identified from the ED pattern. The high-resolution TEM image at the V_2O_5/Al_2O_3 interface with the electron beam parallel to [11-20] direction of the substrate in Figure 6d shows a clear and an atomically smooth interface between the orthorhombic V_2O_5 and c-Al_2O_3, suggesting the growth of a high-quality crystalline

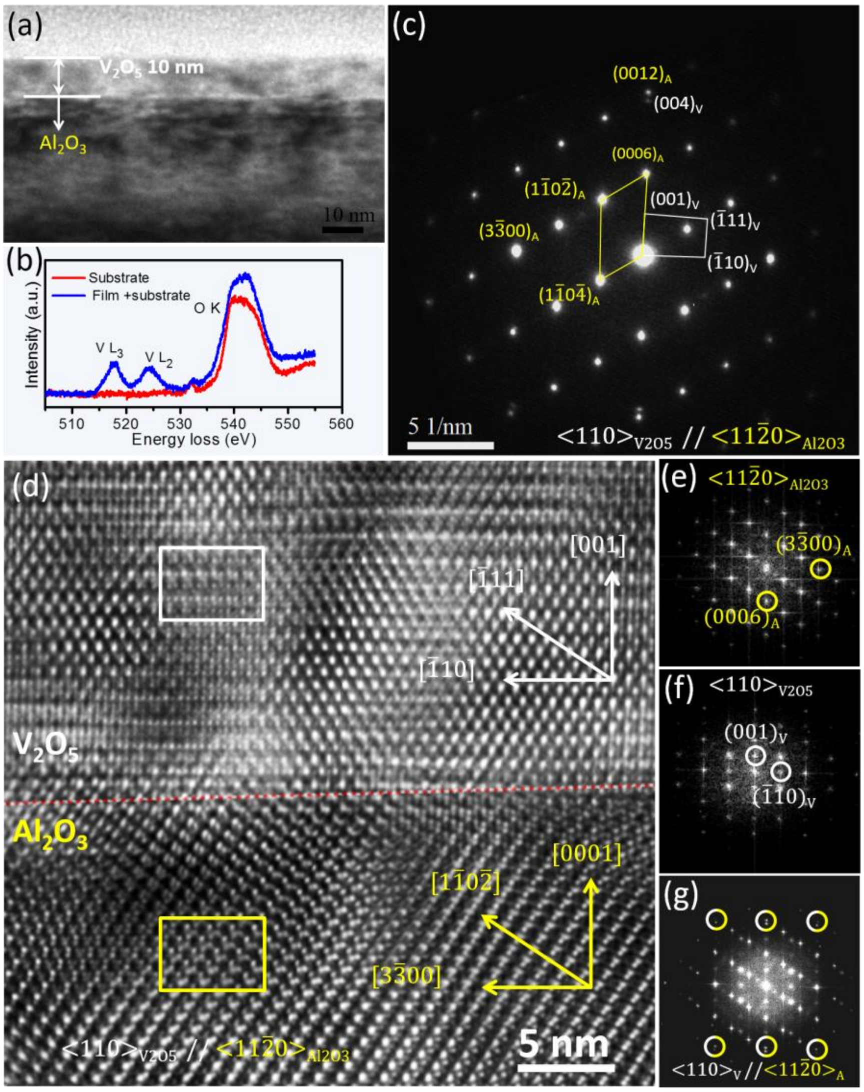

Figure 6. (a) Cross-sectional low magnification TEM image of FIB processed V_2O_5/Al_2O_3 interface. (b) Electron energy loss (EEL) spectra of the V_2O_5 film in comparison with the substrate. (c) Selected area electron diffraction pattern of V_2O_5/Al_2O_3 interface. (d) High-resolution TEM image of the epitaxial V_2O_5 film on the Al_2O_3 substrate. Local Fourier transformation (FT) images of (e) the Al_2O_3 substrate (f) the epitaxial V_2O_5 film and (g) the film and substrate interface respectively (the spots marked shows epitaxial growth). The spots and crystallographic directions marked in yellow color correspond to Al_2O_3 substrate and in white color for V_2O_5.

film on c-Al_2O_3. These results suggest c-Al_2O_3 is an ideal substrate to grow smooth epitaxial orthorhombic V_2O_5 films at low temperatures. The calculated d spacings of <001>, <-110> and <-111> are 4.51, 2.77 and 2.4Å respectively. The unit cell parameters obtained using these crystallographic planes are *a*=4.54 Å *b*=3.56 Å and *c*=4.51 Å. The large decrease in the '*a*' parameter compared to the bulk value (*a*=11.51 Å) suggest compressive strain along the (-110) direction in order to adopt epitaxially with substrate. Also, compared to the bulk value of the <-110> spacing of V_2O_5 (d=3.40 Å), the observed value 2.77 Å suggests reduction of the unit cell '*a*' parameter to accommodate with sapphire (3-300) plane (d=1.37 Å). This can be understood if we examine the in-plane periodicity of sapphire <3-300> and V_2O_5 <-110> lattice spacing. The spacing in <-110> plane of V_2O_5 (2.77 Å) exactly matches with twice the lattice spacing of <3-300> of c-sapphire (2.74 Å). Hence V_2O_5 compresses along <-110> from 3.4 to 2.7 Å in order to accommodate with c-sapphire and this periodicity is in accordance with the epitaxy. This compression of the lattice parameter accounts for the observed Raman shift. Fast Fourier transformation (FFT) patterns in Figure 6 e and f are due to c-Al_2O_3 and orthorhombic V_2O_5, constructed parallel to <11-20 > and <110> direction. The crystallographic Bragg planes <0006>, <3-300> of Al_2O_3 and <100>, <-110> of V_2O_5 were identified using d spacing values. The FFT pattern at the interface (Figure 6g) shows spots corresponds to V_2O_5 and Al_2O_3 which are epitaxially related, and in agreement with the SAED pattern obtained at the interface (Figure 6c). The present study establishes the formation of single-phase crystalline epitaxial orthorhombic V_2O_5 on c-Al_2O_3 as well as interfacial integrity.

The surface morphology of V_2O_5 films was investigated as a function of film thickness (number of cycles) using SEM and AFM. **Figure 7**a-d show SEM images indicating the film surface to be smooth with small grains, the grain size increases with thickness. A similar trend is also observed in AFM images (Figures 7e-h). The 10 nm film (250 cycles) is atomically very smooth with small grains, the RMS roughness of the film increases with cycle number. The values being 0.85, 3.3, 5.2

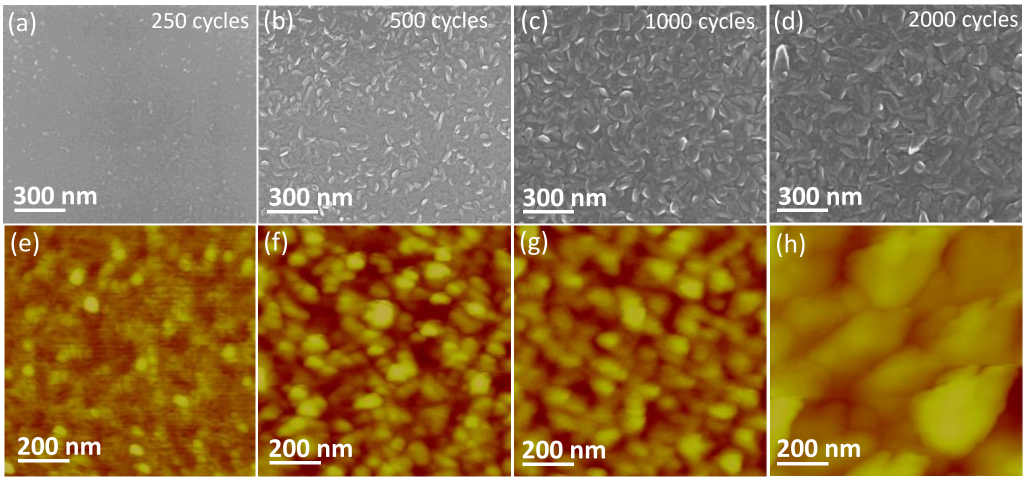

Figure 7. FESEM (a-d) and AFM (e-h) images of as-deposited 10, 23, 45 and 90 nm epitaxial V_2O_5 thin films on Al_2O_3 substrate.

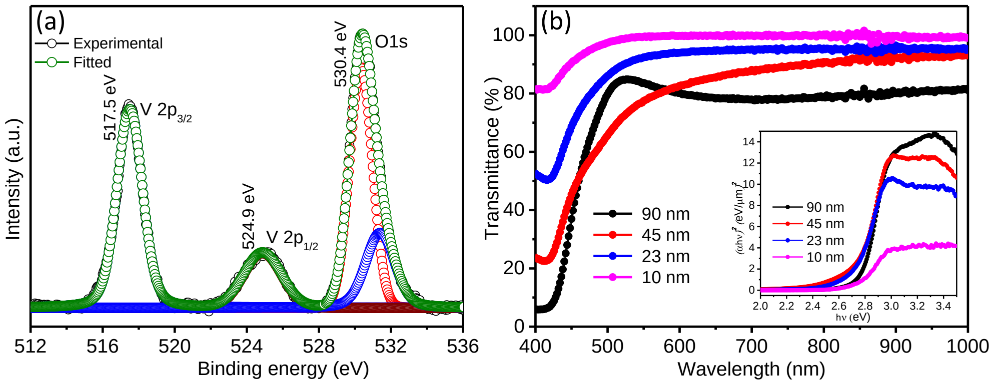

Figure 8. (a) Core-level V 2p and O 1s XP spectra of V_2O_5 thin films grown on c-Al_2O_3 (b) optical transmittance spectra of epitaxial V_2O_5 thin film (10-90nm) on Al_2O_3 substrate (inset of shows $(\alpha h\nu)^2$ versus hν plots to obtain band gap).

and 12.8 nm for 250, 500, 1000 and 2000 cycles respectively.

X-ray photoelectron spectroscopy was employed to determine the chemical composition and oxidation state of 'V' in the films. Core-level spectra show the V $2p_{3/2}$ and $2p_{1/2}$ (**Figure 8**a) binding energies of the film to be at 517.5 and 524.9 eV respectively confirming the stoichiometric V_2O_5.[39] The energy difference between V $2p_{3/2}$ and $2p_{1/2}$ is exactly 7.4 eV which is characteristic of the V^{5+} oxidation state.[40] There is no evidence for lower oxidation states of vanadium. The UV-Visible spectrum of the V_2O_5 films shows the absorption band edge in the visible region around 500 nm corresponding to the band gap of V_2O_5, consistent with the literature reports (Figure 8b). The 10 nm film shows the highest optical transmittance in the whole spectral region with negligible scattering. The band gap as the function of absorption coefficient is shown in the inset of Figure 8b. The minor shift in the band gap values as a function of film thickness is may be due to the strain.

Room-temperature Hall measurements were carried out to determine the type of conductivity, carrier concentration and mobility of epitaxial V_2O_5 thin film. We

Table 1. Room-temperature Hall measurement data of epitaxial V_2O_5 thin films.

V_2O_5 film thickness	Hall-coefficient (cm^3/C)	Carrier concentration ($/cm^3$)	Mobility ($cm^2/V \cdot s$)
10 nm	-1.13×10^5	-5.50×10^{13}	20.4
23 nm	-1.50×10^5	-4.14×10^{13}	215.1
45 nm	-6.37×10^4	-9.78×10^{13}	473.3
90 nm	-7.906×10^4	-7.89×10^{13}	902.5

observe the negative Hall coefficient of the films confirms the n-type conductivity. The average hall coefficient for 10 nm film is 1.134×10^5 cm^3/C. From Hall measurements, the carrier concentration, mobility and the resistivity of the 10 nm film found to be 5.506×10^{13} $/cm^3$, 20.4 $cm^2/V.s$, and 5.554×10^3 Ω·cm respectively. A similar trend of Hall coefficient, concentration, mobility and resistivity are found with 23, 45, and 90 nm films (**Table 1**).

TiO_2/V_2O_5 based p-n heterojunction diode

Ultrathin p-n heterojunction diodes are of interest due to the wide range tunability of charge transport and their use in complex optoelectronic circuits.[41] By taking advantage of p-type conductivity of TiO_2 from our earlier report,[32] we have fabricated an epitaxial heterojunction p-n diode on the Al_2O_3 substrate. In order to validate the result from Hall measurements, the diode I-V characteristics were recorded for the two junction device made with p-TiO_2/n-V_2O_5 and n- TiO_2/n-V_2O_5 (**Figure 9**a and b). The p-type TiO_2 layer was deposited using ALD and the n-type TiO_2 layer by PLD. The p-TiO_2/n-V_2O_5 shows the good rectification behavior of the p-n junction (Figure 9a) with the turn-on voltage at about 0.6 V under the forward-biased voltage and a moderate leakage current in reverse-biased voltage. The device with n-TiO_2 shows a

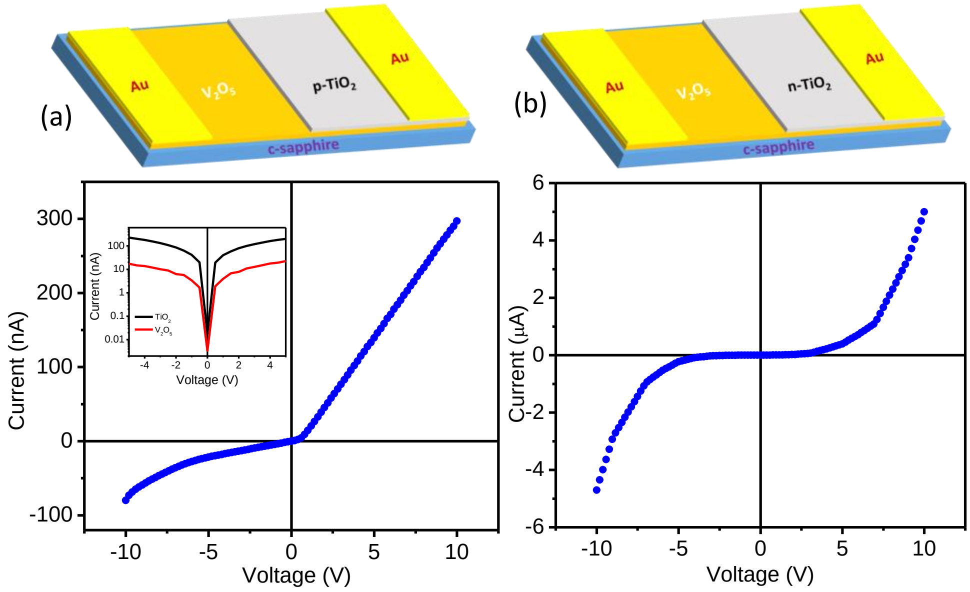

Figure 9. I−V characteristics of p−n heterojunction of (a) p-TiO_2/n-V_2O_5 device (inset shows the I-V measured on individual films) (b) n-TiO_2/n-V_2O_5 device. The corresponding graphical image of the device architecture is shown.

typical semiconductor behavior (Figure 9b). To examine the validity of the p−n junction of the p-TiO_2/n-V_2O_5 device, we have measured I−V characteristics between the p-type TiO_2 layer and a gold electrode and between an n-type V_2O_5 and gold electrode (inset of Figure 9a). In both the cases, we observed linear I−V characteristics.

V_2O_5 based humidity sensor

V_2O_5 is known to be a good sensor for toxic, flammable gasses and humidity.[42-43] We have fabricated an epitaxial V_2O_5 two-probe device by lithography to investigate the humidity sensing properties. We have recorded the sensing property of the device at room temperature under various relative humidity (RH) conditions obtained by bubbling dry nitrogen into water. The RH cycles of 5% and 95% were employed to record response and recovery time and the results are shown in **Figure 10**a. The device shows excellent response and recovery time of 2.35 and 0.5s respectively. The current-time (I-T) measurements were recorded for several cycles to check the reproducibility of the device for response and recovery time (Figure 10b). The V_2O_5

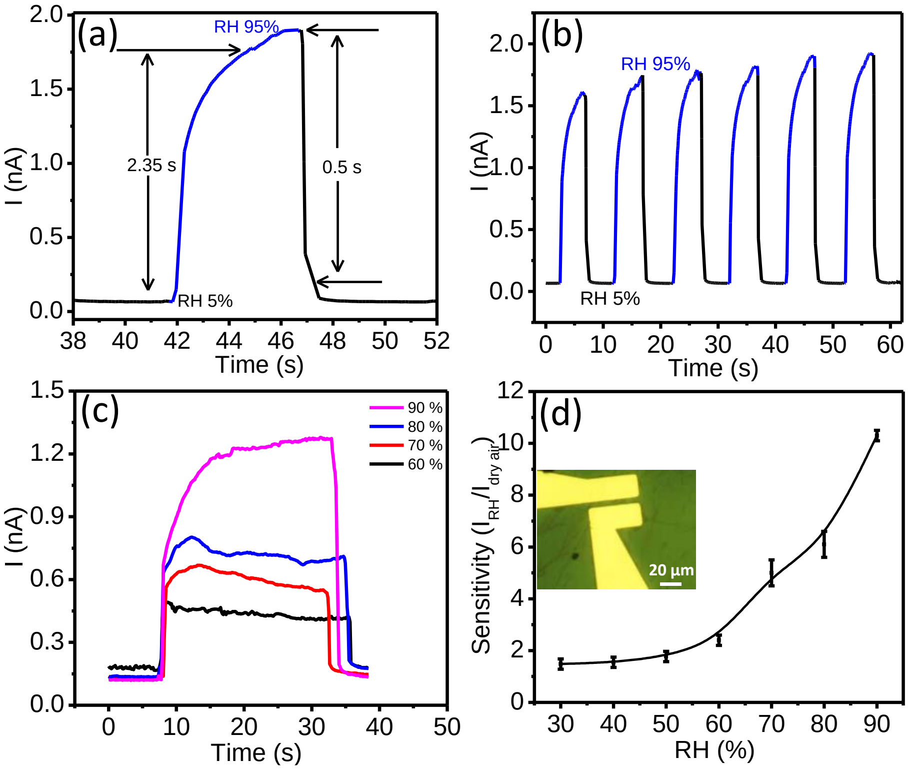

Figure 10. Response of the 10 nm epitaxial V_2O_5 film humidity sensor at room temperature. (a) Response-recovery curve to a pulse of 95% relative humidity (b) current-time (I-T) response of the device for several cycles (c) response-recovery under various relative humidity and (d) sensitivity vs different relative humidity (inset shows the optical image of the device).

based nanosheets device also exhibits the similar kind of sensing properties but shows very poor response and recovery time due to trap states.[43] The excellent response and recovery time of the device attributed to ALD grown epitaxial V_2O_5 flat films possess very less traps and pinhole states. Figure 10c shows that the (I-T) current decreases for lower RH but the response and recovery time are still intact. The sensitivity of the device is better at higher RH but it decreases drastically at RH less than 50% (Figure 10d). The current increase with RH pulse arises from the adsorbed water molecules donate the electrons to n-V_2O_5 and push the Fermi level closer to conduction band edge hence it increases current. We have compared our results with the various oxide based humidity sensors reported (see **Table 2**).[44-49] The epitaxial V_2O_5 device shows superior response time.

Table 2. Comparison of response and recovery time for various oxide based humidity sensors.

Material	Response Time (s)	Recovery Time (s)	Reference
SnO_2 nanowires	120-170	20-60	44
ZnO nanowire	3	20-30	45
TiO_2 (LiCl doped)	3	7	46
V_2O_5 nanotubes	8-12	20-25	47
VO_2@ZnO	7	35	48
V_2O_5 nanosheets	240	300	43
MoO_3 nanorods	118	5	49
V_2O_5 thin film	*2-3*	*0.5-1*	*Present work*

5. Conclusions

It is gratifying that we have been able to obtain ultrathin crystalline epitaxial films of V_2O_5 by using oxygen plasma with $VO(acac)_2$. The films show blue shift in the Raman spectra due to strain caused by epitaxial growth. It is also satisfying that making use of the n-type behaviour of V_2O_5, we are able to fabricate a heterojunction diode with p-type TiO_2. It is noteworthy that the humidity sensor based on the V_2O_5 film has superior sensitivity relative to literature reports on other oxide-based sensors.

6. References

[1] J. B. Goodenough, *Prog. Solid State Chem.* **1971**, *5*, 145-399.

[2] C. N. R. Rao, *Anu. Rev. Phys. Chem.* **1989**, *40*, 291–326.

[3] C. N. R. Rao, B. Raveau, *Transition Metal Oxides: Structure, Properties, and Synthesis of Ceramic Oxides, Wiley*, **1998**.

[4] J. Livage, *Chem. Mater.* **1991**, *3*, 578-593.

[5] A.-M. Cao, J.-S. Hu, H.-P. Liang, L.-J. Wan, *Angew. Chem. Int. Ed.* **2005**, *44*, 4391-4395.

[6] M. R. J. Scherer, L. Li, P. M. S. Cunha, O. A. Scherman, U. Steiner, *Adv. Mater.* **2012**, *24*, 1217-1221.

[7] S. Nishio, M. Kakihana, *Chem. Mater.* **2002**, *14*, 3730-3733.

[8] C. Navone, R. Baddour-Hadjean, J. P. Pereira-Ramos, R. Salot, *J. Electrochem. Soc.* **2009**, *156*, A763-A767.

[9] C. Navone, S. Tintignac, J. P. Pereira-Ramos, R. Baddour-Hadjean, R. Salot, *Solid State Ionics* **2011**, *192*, 343-346.

[10] S. Guimond, J. M. Sturm, D. Göbke, Y. Romanyshyn, M. Naschitzki, H. Kuhlenbeck, H.-J. Freund, *J. Phys. Chem. C* **2008**, *112*, 11835-11846.

[11] S. Lee, T. L. Meyer, S. Park, T. Egami, H. N. Lee, *Appl. Phys. Lett.* **2014**, *105*, 223515.

[12] A. Kumar, P. Singh, N. Kulkarni, D. Kaur, *Thin Solid Films* **2008**, *516*, 912-918.

[13] S. Beke, *Thin Solid Films* **2011**, *519*, 1761-1771.

[14] N. Bahlawane, D. Lenoble, *Chem. Vap. Deposition* **2014**, *20*, 299-311.

[15] L. Wen, M. Zhou, C. Wang, Y. Mi, Y. Lei, *Adv. Energy Mater.* **2016**, *6*, 1600468.

[16] R. L. Puurunen, *J. Appl. Phys.* **2005**, *97*, 121301.

[17] S. M. George, *Chem. Rev.* **2010**, *110*, 111-131.

[18] R. W. Johnson, A. Hultqvist, S. F. Bent, *Mater. Today* **2014**, *17*, 236-246.

[19] H. Groult, E. Balnois, A. Mantoux, K. Le Van, D. Lincot, *Appl. Surf. Sci.* **2006**, *252*, 5917-5925.

[20] J. Keranen, C. Guimon, A. Auroux, E. I. Iiskola, L. Niinisto, *Phys. Chem. Chem. Phys.* **2003**, *5*, 5333-5342.

[21] J. Musschoot, D. Deduytsche, H. Poelman, J. Haemers, R. L. Van Meirhaeghe, S. Van den Berghe, C. Detavernier, *J. Electrochem. Soc.* **2009**, *156*, 122-126.

[22] X. Chen, E. Pomerantseva, P. Banerjee, K. Gregorczyk, R. Ghodssi, G. Rubloff, *Chem. Mater.* **2012**, *24*, 1255-1261.

[23] S. A. Trifonov, V. A. Lapikov, A. A. Malygin, *Russ. J. Appl. Chem.* **2002**, *75*, 969-973.

[24] E. Østreng, O. Nilsen, H. Fjellvåg, *J. Phys. Chem. C* **2012**, *116*, 19444-19450.

[25] E. Ostreng, K. B. Gandrud, Y. Hu, O. Nilsen, H. Fjellvag, *J. Mater. Chem. A* **2014**, *2*, 15044-15051.

[26] J. Keränen, A. Auroux, S. Ek, L. Niinistö, *Appl. Catal., A* **2002**, *228*, 213-225.

[27] X. Chen, E. Pomerantseva, K. Gregorczyk, R. Ghodssi, G. Rubloff, *RSC Adv.* **2013**, *3*, 4294-4302.

[28] J. C. Badot, A. Mantoux, N. Baffier, O. Dubrunfaut, D. Lincot, *J. Mater. Chem.* **2004**, *14*, 3411-3415.

[29] T. Blanquart, J. Niinisto, M. Gavagnin, V. Longo, M. Heikkila, E. Puukilainen, V. R. Pallem, C. Dussarrat, M. Ritala, M. Leskela, *RSC Adv.* **2013**, *3*, 1179-1185.

[30] V. Miikkulainen, M. Leskelä, M. Ritala, R. L. Puurunen, *J. Appl. Phys.* **2013**, *113*, 021301.

[31] E. Olsson, A. Gupta, M. D. Thouless, A. Segmüller, D. R. Clarke, *Appl. Phys. Lett.* **1991**, *58*, 1682-1684.

[32] K. Vasu, M. B. Sreedhara, J. Ghatak, C. N. R. Rao, *ACS Appl. Mater. Interfaces* **2016**, *8*, 7897-7901.

[33] J. D. Emery, C. M. Schlepütz, P. Guo, R. P. H. Chang, A. B. F. Martinson, *Cryst. Growth Des.* **2016**, *16*, 640-645.

[34] S.-H. Lee, H. M. Cheong, M. J. Seong, P. Liu, C. E. Tracy, A. Mascarenhas, J. R. Pitts, S. K. Deb, *Solid State Ionics* **2003**, *165*, 111-116.

[35] I. E. Wachs, J.-M. Jehng, F. D. Hardcastle, *Solid State Ionics* **1989**, *32*, 904-910.

[36] C. V. Ramana, R. J. Smith, O. M. Hussain, M. Massot, C. M. Julien, *Surf. Interface Anal.* **2005**, *37*, 406-411.

[37] D. S. Su, H. W. Zandbergen, P. C. Tiemeijer, G. Kothleitner, M. Hävecker, C. Hébert, A. Knop-Gericke, B. H. Freitag, F. Hofer, R. Schlögl, *Micron* **2003**, *34*, 235-238.

[38] D. Su, *Anal. Bioanal.Chem.* **2002**, *374*, 732-735.

[39] E. Hryha, E. Rutqvist, L. Nyborg, *Surf. Interface Anal.* **2012**, *44*, 1022-1025.

[40] R. J. Colton, A. M. Guzman, J. W. Rabalais, *J. Appl. Phys.* **1978**, *49*, 409-416.

[41] D. Jariwala, V. K. Sangwan, C.-C. Wu, P. L. Prabhumirashi, M. L. Geier, T. J. Marks, L. J. Lauhon, M. C. Hersam, *PNAS* **2013**, *110*, 18076-18080.

[42] A. R. Raju, C. N. R. Rao, *J. Chem. Soc., Chem. Commun.* **1991**, 1260-1261.

[43] M. S. Pawar, P. K. Bankar, M. A. More, D. J. Late, *RSC Adv.* **2015**, *5*, 88796-88804.

[44] Q. Kuang, C. Lao, Z. L. Wang, Z. Xie, L. Zheng, *J. Am. Chem. Soc.* **2007**, *129*, 6070-6071.

[45] Y. Zhang, K. Yu, D. Jiang, Z. Zhu, H. Geng, L. Luo, *Appl. Surf. Sci.* **2005**, *242*, 212-217.

[46] Z. Li, H. Zhang, W. Zheng, W. Wang, H. Huang, C. Wang, A. G. MacDiarmid, Y. Wei, *J. Am. Chem. Soc.* **2008**, *130*, 5036-5037.

[47] H. Yin, K. Yu, H. Peng, Z. Zhang, R. Huang, J. Travas-Sejdic, Z. Zhu, *J. Mater. Chem.* **2012**, *22*, 5013-5019.

[48] W. Li, Y. Ma, S. Ji, G. Sun, P. Jin, *Ceram. Int.* **2016**, *42*, 9234-9240.

[49] L. Khandare, S. S. Terdale, D. J. Late, *Adv. Device Mater.* **2016**, *2*, 15-22.

Chapter III.4

Atomic Layer Deposition of Epitaxial MoS_2 Nanowall Networks and Their Performance in Thin film Na-ion Batteries

SUMMARY*

We have grown ultrathin crystalline epitaxial thin films of MoS_2 on c-sapphire employing atomic layer deposition, without the need for post-annealing. The films have been characterized by various microscopic and spectroscopic techniques. The crystallographic epitaxial relationships between the films and the substrate are <01-10> Al_2O_3 || <11-20> MoS_2 and <0001>Al_2O_3 || <0001> MoS_2. Interestingly, the films show a high density of nanowalls and exhibit high surface to volume ratio. The high surface area of the nanowall network results in excellent electrochemical characteristics as demonstrated by the performance of the Na-ion battery with MoS_2 as the active electrode. The battery exhibits high capacity, remarkable stability, cyclability and high rate capability over a wide range of operating currents, even in the absence of conducting and binder additives. The MoS_2 Li-ion battery also exhibits similar features.

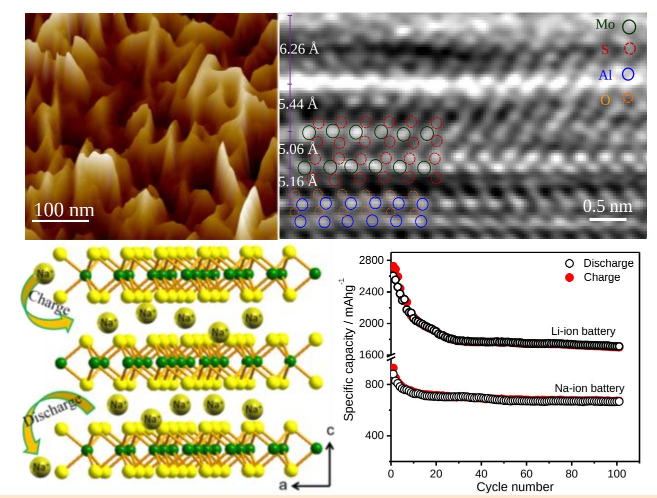

*A paper based on this work has appeared in Journal of Materials Chemistry A (2018).

1. Introduction

Discovery of graphene has triggered the direction of semiconductor research towards 2D materials.[1, 2] Despite the challenges of obtaining the large area nanofilms, potential applications of these materials make them attractive.[3, 4] In particular, layered transition metal dichalcogenides (TMDCs) have received much attention due to their useful electronic properties.[5] Thus, van der Waals structures involving TMDCs exhibit unique properties.[6] Among the 2D layered TMDCs, molybdenum sulfide (MoS_2) has emerged as the most interesting material in terms of electronic and structural properties.[7, 8] Semiconducting 2H MoS_2 has a band gap which can be exploited for electronic and optoelectronic applications.[9, 10] Single-layer MoS_2, being a direct band gap semiconductor, exhibits intense photoluminescence,[11, 12] and its properties depend on the thickness and crystallinity of the layers.[13] Since the crystallinity and absence of grain boundaries are crucial for application of MoS_2 films,[14] it is important to grow epitaxial crystalline films of pristine atomic layers. For this purpose, we have employed atomic layer deposition (ALD).[15] Since films deposited by ALD are often polycrystalline or amorphous,[16] there is a need for effort to obtain crystalline epitaxial films at relatively low temperatures. There are a few examples of epitaxial oxide films grown by ALD.[17-19] Crystalline epitaxial films of TMDCs have not been explored by ALD.[20] Recent attempts at ALD of MoS_2[21-23] have yielded polycrystalline or amorphous films, requiring post-processing treatments to attain suitable levels of crystallinity.[24-26] MoS_2 is known to be a promising anode material in alkali metal ion rechargeable batteries with reasonable capacity.[27-31] Metal chalcogenides in powder form have a tendency to undergo changes during electrochemical redox process.[32-35]

2. Scope of the present investigations

TMDCs in complementary to gapless graphene received the great attention due to their semiconducting properties. Intriguing layered van der Wall structure few layers of TMDCs exhibit unique properties compared to their bulk. In this connection MoS_2 emerged as promising material and attained tremendous interest due to electronic and structural properties. Semiconducting 2H MoS_2 is widely studied material and has advantages in having suitable band gap for electronic and optoelectronic applications. The properties of MoS_2 largely dependent on the thickness, crystallinity and nanostructuring. Recently, MoS_2 shown to be a promising anode material in Li-ion rechargeable batteries with reasonable capacity. Demand for high and portable energy sources, Na-ion batteries are alternative state-of-art-battery by the replacing its Li-ion counterpart. Although, Sodium constitutes a cheaper and easily obtainable anode compared to Lithium, the large size and sluggish ion movement across the electrolyte plagues its widespread applicability in Na-ion batteries (NaBs). While, on one hand, there is a massive hunt for suitable solid electrolyte for Na conduction, the other option is to design advanced electrode systems to enhance the electrode-electrolyte interface to alleviate the interfacial resistance. In that direction, it becomes a real challenge to develop high quality anode and cathode architectures that, apart from enabling easy ion access and tackling massive volume expansion that is associated with Na-ions intercalation, should maintain good connectivity. This is expected to decrease the interfacial resistance, ensuring excellent battery cyclability. The recent time has witnessed the development of advanced fabrication techniques such as CVD, PLD and ALD which not only ensure a very extremely high purity sample preparation, but also promotes a good connectivity to the substrate. ALD scores of the other techniques on several grounds such as low temperature deposition, atomic grade stoichiometric and excellent uniformity and hence can be applied for electrode fabrication in metal ion cells. MoS_2 nanowall networks grown by ALD on the current collector would be expected to offset such structural incongruities and exhibit excellent battery cycling.

In this work, we have grown MoS_2 nanowall network to offset such structural incongruities. We have been able to grow the single crystalline epitaxial films of MoS_2 nanowall networks successfully on c-sapphire by thermal ALD without post-annealing treatment using $MoCl_5$ and H_2S precursor. The epitaxial nanowall networks grown have been characterized by various microscopic and spectroscopic techniques. Nanowalls constitute MoS_2 nanosheets show inclined vertical growth with high surface to volume ratio. The mechanism of nanowall growth has been unrevelled by AFM topographic measurements. We have found good cyclability of the nanowalls grown directly on current collector under a wide varying current densities for Na as well as Li batteries. It is noteworthy that the electrodes do not contain carbon and binder additives. We believe that the use of ALD grown layered TMDCs can influence the future work on rechargeable Na/Li batteries.

3. Experimental Section

Thin film growth

Deposition of crystalline epitaxial MoS_2 thin films:

Crystalline epitaxial hexagonal 2H MoS_2 thin films were grown by atomic layer deposition on single crystalline *c*-sapphire (0001) substrates using a flow type ALD reactor (Beneq, TFS 200 Finland Oy). Prior to the deposition, the substrates were cleaned thoroughly using H_2SO_4 and H_2O_2 in the ratio 4:1 at 120 °C followed by ultrasonication in acetone and isopropanol and dried under nitrogen. High purity molybdenum pentachloride ($MoCl_5$, 99.9%) and hydrogen sulfide (Bhuruka gases, 97.5%) were employed as Mo and S sources respectively. Ultra-high pure N_2 (Chemix, 99.9995) was used as a carrier and purging gas at the flow rate of 600 sccm throughout the deposition. The chamber and reactor were pumped down to 10 and 1 mbar respectively before the starting recipe for the deposition. The reaction chamber was heated to 300 °C and held 30 min for temperature stabilization. $MoCl_5$ was kept in the hot source HS-300 bubbler (Beneq, Oy) and heated slowly to 105 °C to vaporize it. The hot source head and precursor lines from the hot source to the reactor were maintained at a slightly higher temperature than hot source to avoid condensation of $MoCl_5$. The films were deposited by sequential pulsing of $MoCl_5$ and H_2S. The hot source was boosted with high purity nitrogen for 1s before pulsing $MoCl_5$ to the reactor, to make sure enough vapor pressure of the precursor. The optimized pulse and purge times for $MoCl_5$ were 2 s and 3 s respectively, whereas the pulse and purge times for H_2S were 1 s and 3 s. A variation in the reactor pressure between 1-3 mbar was observed during pulsing and purging, but the chamber pressure is almost intact. The complete ALD sequence for MoS_2 growth was pulse $MoCl_5$/purge//pulse H_2S/purge for 2 s/3 s//1 s/3 s. The deposition was carried out for 10, 100, 500, 1000, 1500 and 2000 cycles at 300 °C and the films cooled down to room temperature under vacuum. The as-obtained films were used for further characterization without post-annealing. To ascertain the ALD temperature window and the self-terminating nature of ALD process, depositions were carried out at different reactor temperatures and pulse times and purge times.

TEM Sample preparation:

TEM cross-sectional specimens are prepared first by mechanical polishing and then Ar ion milling to perforation to generate large electron thin transparent area. All the high-resolution transmission electron microscopy (HRTEM) imaging was carried out in a double aberration corrected TITAN 80-300 kV microscope under Cs ~ 40 µm and a positive defocus ~ 8 nm, which gives a direct interpretation of images.

Characterization of MoS_2 thin films

X-ray diffraction (XRD) patterns of the as-deposited films were recorded with a Panalytical diffractometer (Empyrean) with θ-2θ scan using monochromatic Cu $K\alpha_1$ radiation (λ = 1.5404Å) to confirm the crystallinity. Raman optical modes of MoS_2 were recorded using a 514 nm Ar laser with a Jobin Yvon LabRam HR spectrometer in backscattering geometry. X-ray photoelectron (XP) spectra were recorded using an Omicron nanotechnology spectrometer with Mg Kα X-ray source (E = 1253.6 eV). Optical transmission spectra were recorded on a PerkinElmer UV−Vis spectrometer from 200 to 800 nm range. Optical microscope images were captured using Leica DM2700 M microscope fitted with LED illumination. Field emission scanning electron microscope (FESEM) Nova NanoSEM 600 FESEM equipped with an Energy Dispersive X-ray (EDX) analysis system (FEI Company) was employed to ascertain the film thickness (in cross-section mode) and surface morphology. The surface roughness and topography of the films were determined using atomic force microscopy (AFM) in contact mode (Bruker Innova) using high-resolution SNL-10 Bruker AFM probe with the tip radius of 2 nm. The sample for transmission electron microscopy (TEM) was prepared by the by mechanical polishing and Ar ion milling. Cross-sectional high-resolution TEM (HRTEM) was performed using double aberration corrected FEI TITAN 80−300 operated at 300 kV. Room-temperature carrier concentration and mobility were determined using Ecopia HMS-3000 Hall effect measurement system.

Electrode fabrication and electrochemical measurements

Electrochemical stability and lithium and sodium battery performance studies are tested in coin-cells (CR-2032). For the sodium ion cell, Na-foil (Aldrich, thickness = 0.75 mm) is used as a counter and a reference electrode, Whatman glass fiber as a separator and 1M $NaPF_6$ in EC:DEC (1:1 v/v) as the electrolyte. For the lithium-ion cell, Li-foil (Aldrich, thickness = 0.75 mm) is used as a counter and reference electrode, Whatman glass fiber as separator and 1M $LiPF_6$ in EC:DMC (1:1 v/v) as electrolyte. For electrochemical measurements, the ALD grown MoS_2 layers on the stainless steel current collector of the coin cell are used directly as the working electrode. In this case, the working electrode is devoid of acetylene black or polyvinylidene fluoride (PVDF) which is conventionally used as electron conductor and binder respectively during electrode casting. The mass loading per electrode on the current collector is about 120 µg obtained after running 2000 ALD cycles. All cell assembly is done at 25 °C in an Argon filled glove box (MBraun) (H_2O <1, O_2< 1 ppm). The cyclic voltammogram is obtained in CH Instrument (CH 403), while the galvanostatic charge/discharge cycling are obtained on Neware Battery Cycler using TC53 software at different C-rates (1C = 167 mA g^{-1}) in two sets of the voltage ranges of 0.2 – 3.0 V and 1.0 – 3.0 V (versus Li^+/Li and Na^+/Na).

4. Results and Discussion

Epitaxial MoS_2 nanowall network

Epitaxial MoS_2 nanowalls of varying thickness were deposited on the transparent c-plane sapphire and other substrates using thermal ALD by employing $MoCl_5$ and H_2S as the precursors. The ALD reactor temperature window, precursor pulse rates, and other process parameters were optimised to achieve large area uniformity as well as self-limiting surface saturation reaction. The best quality crystalline films on c-sapphire were obtained at reactor temperature of 300 °C with hot source at 105 °C. Optical microscope images show the presence of MoS_2 films with large area uniformity (**Figure 1**). Uniformity here refers to that of surface morphology and roughness of the film rather than film thickness. It is difficult to measure the thickness of the film precisely due to nanostructuring. The surface roughness and morphology

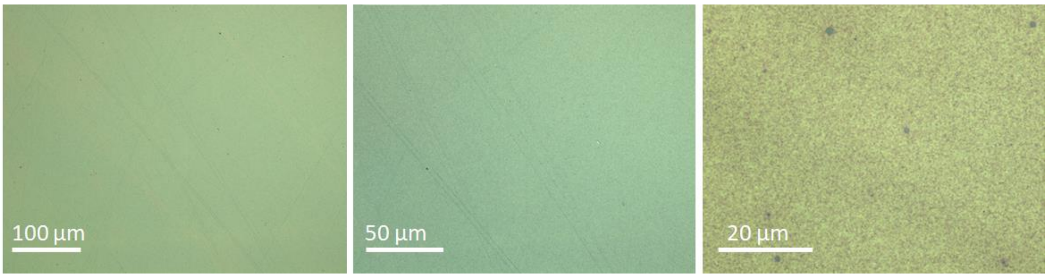

Figure 1. Optical microscope images of MoS_2 thin film of 2000 ALD cycles grown on c-sapphire.

are different for different ALD cycles. On repeating the growth, we find the same trend which implies that growth is uniform. The pulsing and purging times of the precursors were optimised to achieve self-limiting growth and good quality films. To avoid intermixing of the precursors and etching reactions from by-products, the purging time was kept sufficiently long. Prolonged precursor injection time causes non-uniformity in the films due to back etching. We carried out several depositions by varying the temperature from 150 °C to 300 °C. Films deposited at 150 °C appeared to be uniform and smooth, but further characterization revealed chlorine contamination (**Figure 2**a-c). It suggests incomplete reaction due to insufficient thermal activation energy to self-terminate the reaction.[15] Deposition at 200 °C showed a clear improvement in the film with a reduced amount of chlorine (Figure 2d-f). On the further evolution of the ALD temperature window, we did not encounter chlorine contamination above 250

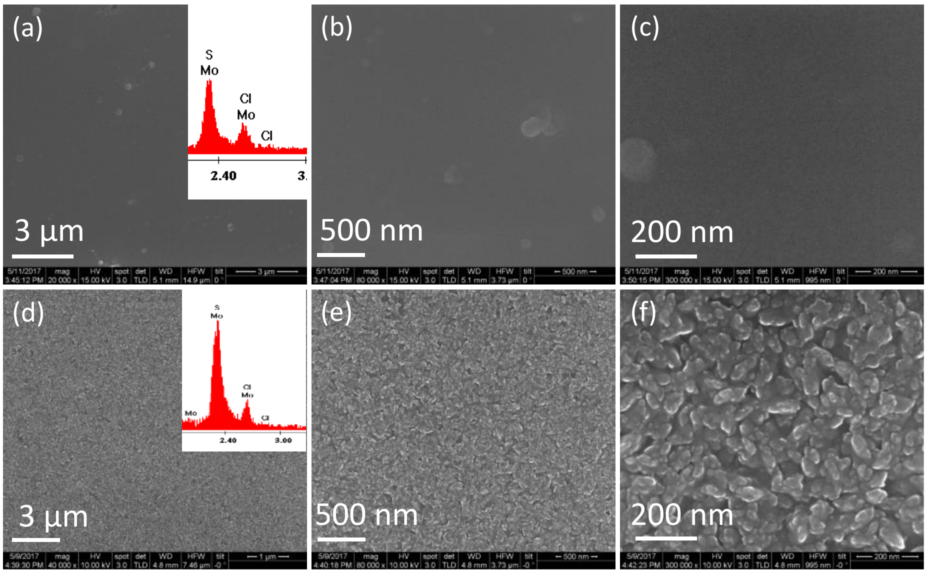

Figure 2. FESEM images of as-deposited MoS_2 thin films at 150 °C (a-c) and 200 °C (d-f) on the c-sapphire substrate. Inset of the Figure (a) and (d) shows corresponding EDAX spectrum. The EDX spectrum reveals the Cl contamination in the films.

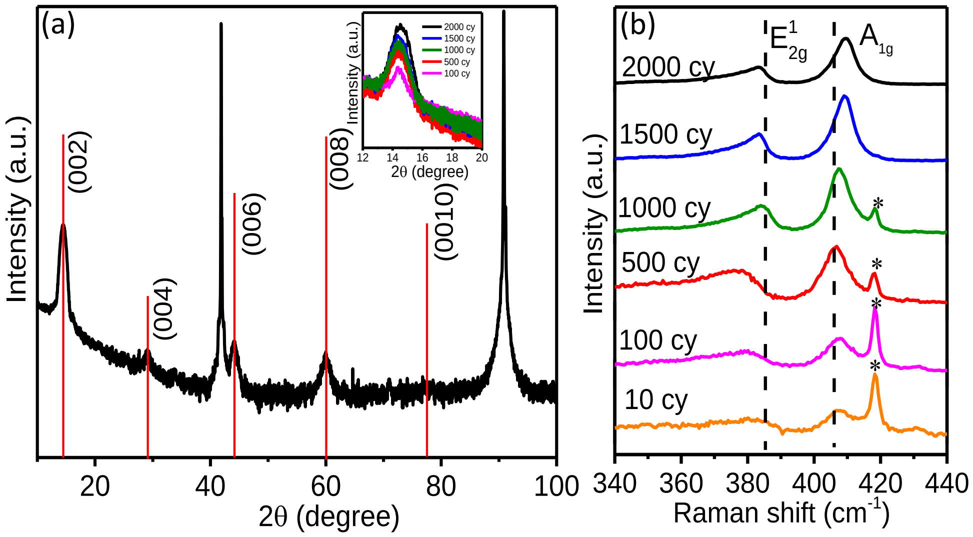

Figure 3. (a) Long duration θ-2θ scan XRD pattern of epitaxial MoS_2 thin films on c-sapphire substrate. The red reference line indicates the XRD patterns of single crystal MoS_2 along (001) direction. The inset shows XRD pattern around (002) plane of MoS_2 thin films of varying thickness. (b) Raman spectra of epitaxial MoS_2 thin films of different thickness grown on c-sapphire substrate (* indicates the peaks corresponding to the substrate).

°C, but the samples were amorphous. Self-saturation surface reaction was observed in this temperature window from 250 to 300 °C by varying the precursor input time. The ALD temperature window is based on many growth trials and their ex-situ characterization results. In the defined temperature window we got uniform films with no Cl contamination at higher purging times. Persistent growth with the same morphology, crystallinity and surface roughness occurs at 300 °C, even with higher dosages of $MoCl_5$ and H_2S, and eliminates the possibility of CVD type of reaction. We fixed the deposition temperature as 300 °C, pulsing and purging times 2s and 4s respectively, and carried out all further depositions.

The crystallinity of the as-deposited films was confirmed by XRD studies. The films were highly crystalline unlike other ALD grown films reported[15] and did not require post-annealing. **Figure 3**a shows a long duration θ-2θ scan of MoS_2 grown at 300 °C for 2000 cycles revealing the reflections corresponding to MoS_2 and c-sapphire. The reflections are indexed as (002), (004), (006), (008) and (0010) of single crystalline hexagonal 2H MoS_2. The red reference lines indicate the reflections of MoS_2 single crystals oriented along the c-direction. The presence of only the (00l) family of reflections in the X-ray diffraction pattern suggests that the film is epitaxial. However, HRTEM images show roughness of the films due to regions of the films turning upwards. The reflections corresponding to the vertical growth regions are not observed in the X-ray diffraction pattern due to the restricted geometry. This is also indicative that the film is not polycrystalline with random distributions of grains are required to obtain peaks in the X-ray pattern. The epitaxial relation from XRD studies is <0001> MoS_2//<0001> Al_2O_3. The inset of Figure 3a shows the (002) reflection of MoS_2 thin film of varying thickness. The intensity of the (002) reflection increases with film thickness as expected due to long-range ordering in that direction. The thickness of the film grown for 100 cycles is of the order of few nanometers, the reflections remains intense and visible indicating high crystallinity. Films grown on other substrates such as Si(100), SiO_2/Si and quartz at 300 °C were amorphous. The crystalline nature on c-sapphire is likely due to the same crystal structure with less lattice mismatch of the film with the underlying substrate.

The electronic structure and optical band gap of MoS_2 are dependent on the number of layers or the film thickness.[36] We investigated the optical properties of MoS_2 thin films by Raman scattering excited by 514 nm laser under ambient conditions (Figure 3b). The Raman spectra show strong signals due to the in-plane E^1_{2g} and the out-of-plane A_{1g} optical phonon modes. The phonon mode frequencies vary with thickness,[36, 37] wherein the A_{1g} mode softens and the in-plane E^1_{2g} mode stiffens with decreasing film thickness.[37, 38] Interestingly, MoS_2 films grown over 10-100 cycles show distinguishable E^1_{2g} and A_{1g} bands indicating local ordering of atomic arrangements even at a few nanometer scale. The broader FWHM of the bands in the 10 cycle grown MoS_2 is due to the nano regime lateral dimension and phonon

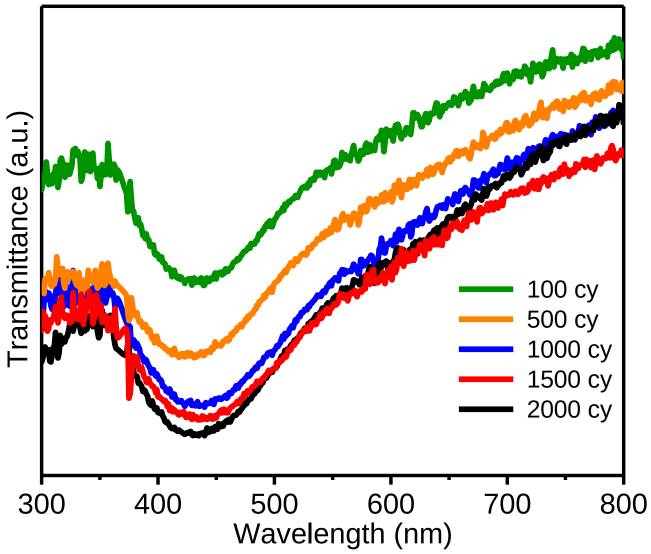

Figure 4. Optical transmittance spectra of MoS_2 nanowall network on c-sapphire of varying thickness.

confinement.[8] Optical transmittance spectra of as-deposited films show the absorption corresponding to the band gap of MoS_2 which is in consistence with literature reports (**Figure 4**).[39]

X-ray photoelectron (XP) spectroscopy was adapted to understand the chemical bonding nature of the deposited films. As deposited film shows characteristic signal due to Mo 3d and S 2p corresponding to MoS_2 bonding (**Figure 5**). Figure 5a shows the survey scan XP spectra of epitaxial MoS_2 thin film on sapphire. We also observed C and O peak in the as-deposited films which are may be due to surface contamination. In order to know proper bulk composition, we sputtered the film with high pure argon for 10 s to remove few nanometer from the surface. C and O signals

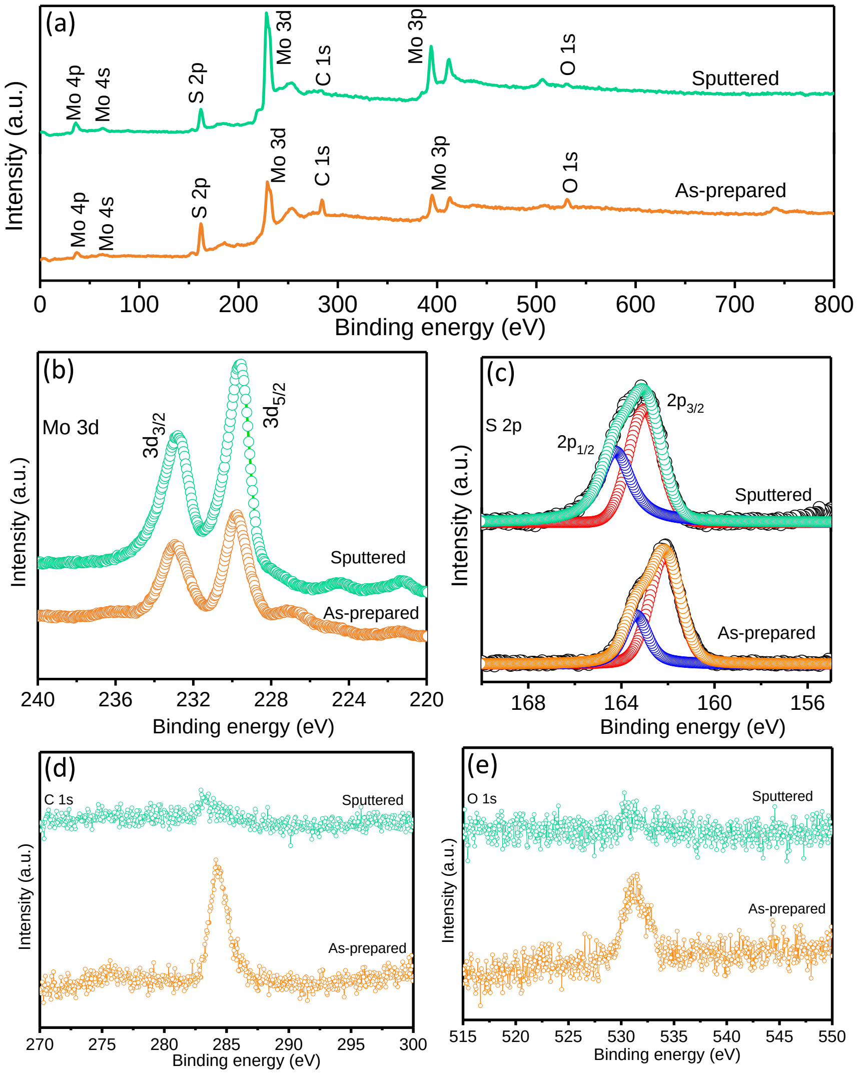

Figure 5. (a) Survey scan XP spectrum of MoS_2 thin film grown on c-sapphire and corresponding core-level spectrum of Mo 3d (b) and S 2p. (c) Core-level XP spectrum of (d) C 1s and (e) O 1s in as-prepared and sputtered thin films of MoS_2.

are disappeared in the sputtered sample, which represents the pure MoS_2 without any contamination. The core-level XP spectra of Mo 3d shows the characteristic peak of $3d_{5/2}$ and $3d_{3/2}$ at 229.5 and 232.8 eV respectively, which are attributed to Mo^{4+} bonding with S (Figure 5b). There no peak observed for Mo-O bonding (Mo^{6+}, 236.2 eV) in the collected spectrum of Mo 3d, indicates high-quality MoS_2. The core-level XP spectrum of S 2p levels is shown in Figure 5c. The asymmetry and broad peak in S 2p spectra is not only due to the chemical environment but also overlapping of S $2p_{3/2}$ and S $2p_{1/2}$ signal. Therefore, S 2p spectrum deconvoluted into two peaks and were appear at 162.9 and 163.4 eV corresponding S $2p_{3/2}$ and S $2p_{1/2}$ of MoS_2 bonding respectively. The core-level spectra of sputtered sample show more prominent and distinguishable signals compared to as-deposited films. We have also collected the C 1s and O 1s core-level spectra before and after sputtering (Figure 5 d and e), reveals there is no contamination of C and O in the films.

Surface morphology and thickness of the MoS_2 epitaxial films were examined by FESEM. **Figure 6**a-c show the plane-view images of epitaxial MoS_2 thin film of 2000 cycles on c-sapphire. Large area images show a uniform network kind of structure in which MoS_2 grows vertically. High-resolution images reveal that each individual nanosheet of MoS_2 grows vertically and combines with the edges of other nanosheets, making nanowall network throughout. The cross-sectional image of the 2000 cycle film shows vertical growth with an average film thickness of 70 nm (Figure 6d). To see clear 3D growth of the nanowall network, we have collected FESEM images at tilted angles of 45° and 60° (Figure 6e and f respectively). The tilted images from the top-view clearly show assembly of vertically aligned nanosheets forming nanowall networks. The growth of nanowalls is uniform and regular, the thickness of the each nanowall remaining same throughout the network. The false coloured FESEM image presented in Figure 6f shows the presence of pores or voids in between the nanowalls. Individual nanowalls can be seen clearly in Figure 6h with an average wall thickness of 25-30 nm. In order to evaluate the growth mechanism, we have examined samples after various ALD cycles from 10 to 2000 cycles. MoS_2 grown for 1500, 1000, and 500 cycles show similar nanowall networks in comparison with 2000 cycles with smaller wall and film thickness (**Figure 7**a-i). The 100 and 10 cycle grown ALD films are flat and there is no vertical growth seen due to few nanometer thickness (Figure 7 l-m).

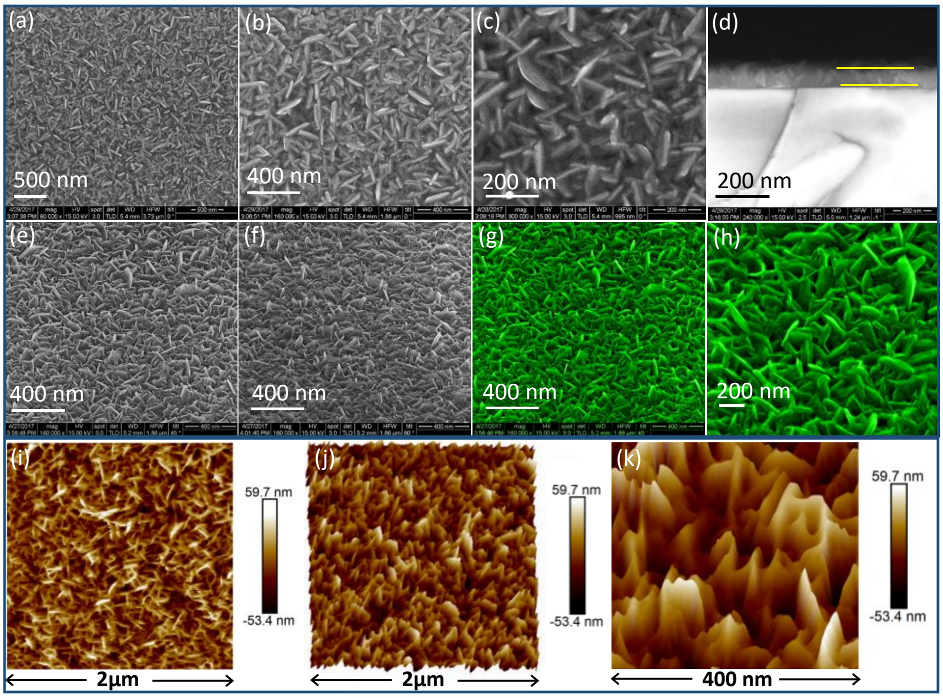

Figure 6. (a-c) Plane-view FESEM images showing surface morphology of as-deposited 2000 ALD cycles grown epitaxial MoS_2 thin films on c-sapphire substrate (d) corresponding cross-sectional view for thickness measurements. (e-h) Top-view FESEM images showing 3D surface morphology of as-deposited 2000 ALD cycles grown epitaxial MoS_2 thin films tilted at 45° and 60°. (g) False coloured image to for the better view of nanowalls (h) Zoomed view of a (g) to see connection between individual nanowall to form a network. (i-k) AFM images of as-deposited epitaxial MoS_2 thin films on c-sapphire substrate of 2000 cycles. The images (j) & (k) shows 3D projection to see clear nanowalls formation and (k) revels the zoomed view of portion of (j) nanowalls to distinguish individual wall.

The atomic force microscope (AFM) topographic image in Figure 6i shows a 2D view of the surface of a 2000 cycles sample on c-sapphire. The uniformity and large area growth of the nanowalls network is seen clearly. The thickness of the individual nanowall is around 30 nm which constitutes approximately 45 MoS_2 layers in each nanowall. The vertical growth of MoS_2 nanowalls is seen in the 3D image (Figure 6j). Each nanowall is interconnected with the adjacent layers to form the network. The high-resolution zoom-in image (Figure 6k) shows individual nanowalls, with nanowalls of an average height of 60 to 70 nm. The nanowalls are separated by valleys, the depth and area of valleys vary with nanowall dimensions. AFM images of 1500, 1000 and 500 cycles show similar topography (**Figure 8**), the dimensions of the nanowalls decreasing with the number of cycles. The RMS roughness of the sample decreases with the cycle number and the roughness values are 15.6, 8.2, 5.6, 3.07 nm for 2000, 1500, 1000, 500 ALD cycles respectively. To understand the growth mechanism of nanowall network, the early growth cycles were characterized by AFM

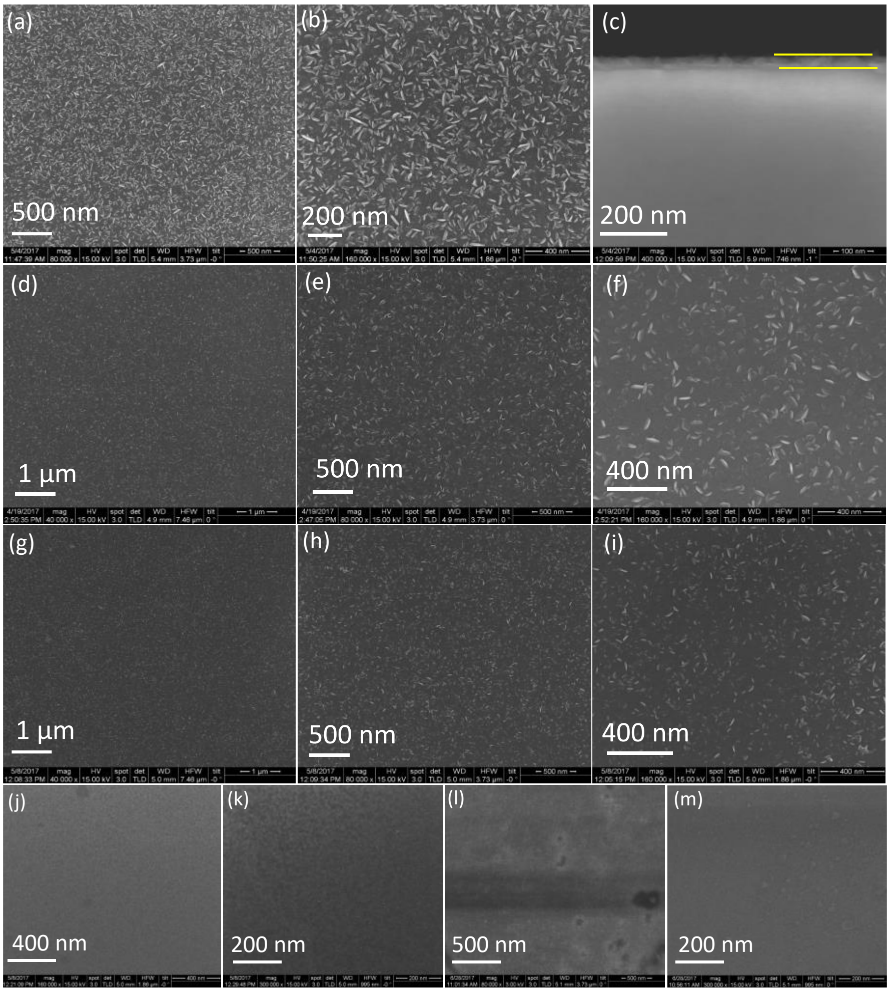

Figure 7. FESEM images showing surface morphology of as-deposited (a-c) 1500, (d-f) 1000, (g-i) 500, (j, k) 100 and (l, m) 10cycles epitaxial MoS_2 films.

topography. The 10 cycle ALD grown film shows well connected regular shape line patterns of MoS_2 (Figure 8m-o), which serve as nucleation centers for the vertical growth of the nanowall network. MoS_2 grown on other substrates exhibit similar morphologies.

Low magnification cross-sectional bright field TEM image of 1500 cycles ALD grown MoS_2 film on *c*-plane sapphire substrate is shown in **Figure 9**a. The film is smooth up to a thickness of few nanometers and then becomes rough with the further growth. The vertical inclined growth of nanowalls is seen in the cross-sectional image. The average thickness of the film is 50 nm. A HRTEM image of MoS_2 and sapphire interface and the FFT pattern from individual layers are given in Figure 9b & c. The epitaxial relationship for the horizontal layers is <01-10> Al_2O_3 || <11-20> MoS_2 and <0001>Al_2O_3 || <0001> MoS_2. Similar HRTEM images along <01-10> of MoS_2

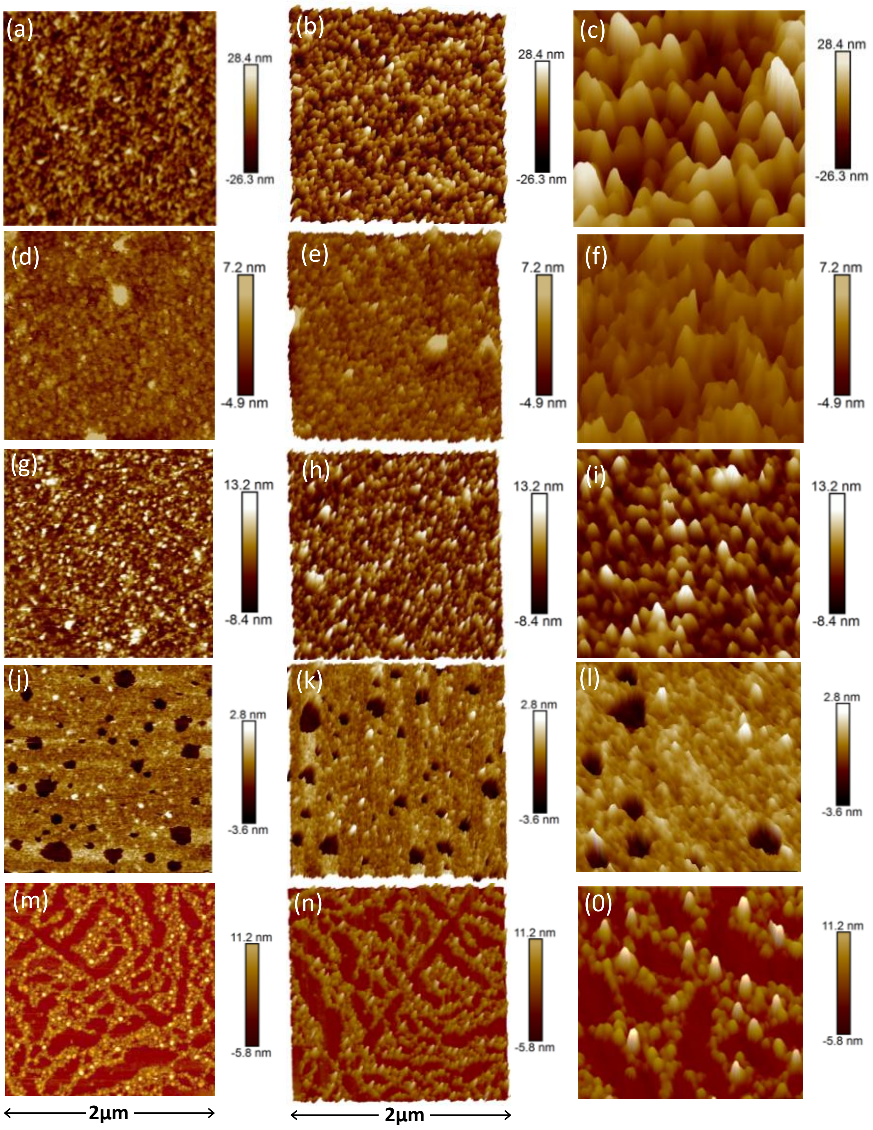

Figure 8. AFM images of as-deposited (a-c) 1500, (d-f) 1000, (g-i) 500, (j-l) 100 and (m-o) 10 cycles epitaxial MoS_2 thin films on c-sapphire substrate. The images (b, e, h, k & n) shows 3D projection and (c, f, i, l & o) shows zoom in view image to distinguish individual wall.

are given in **Figure 10**a. Details of the atomic registry between MoS_2 and sapphire are shown in Figure 9d. We see the arrangement of bottom S atoms of the first MoS_2 layer on top of the O atoms of sapphire substrate. The S-S distance on top of sapphire substrate in the bottom most layer is 2.68 Å (a = 3.09 Å). The equal S-S distance is observed in the ALD grown MoS_2 film compared to PLD grown film where two different S-S interatomic distance is observed.[40] The Mo-Mo distance 2.68 Å (a = 3.09 Å), 2.72 Å (a = 3.14 Å) with compressive strain of 2.06%, 0.64% in the 1st, 2nd layer respectively and the strain further decreases away from the interface.

In some regions of the ALD films, we notice the inclined and vertical growth features (Figure 9 e-g). However, electron diffraction and FFT study at different spots

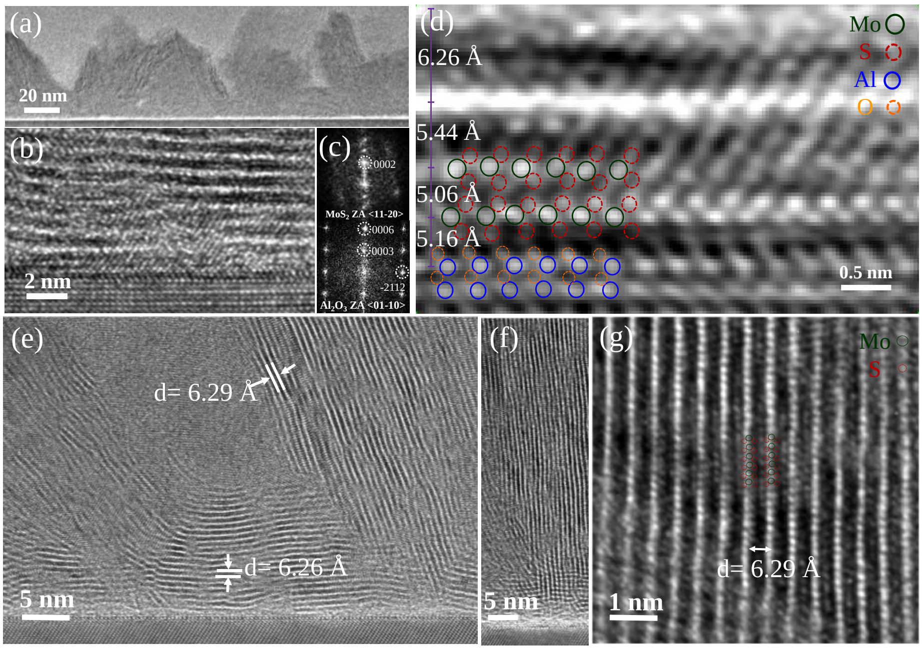

Figure 9. (a) Low magnification cross-sectional TEM-BF image of MoS_2 epitaxial film on c-plane sapphire. The film is smooth up to 30 nm, then becomes rough with further growth. Average thickness of the film is 50 nm. (b) HTREM image of MoS_2 film on sapphire along <01-10> direction of Al_2O_3. The epitaxial relationship between MoS_2 and sapphire for the horizontal layers is <01-10> Al_2O_3 || <11-20>MoS_2 and <0001> Al_2O_3||<0001>MoS_2. (c) FFT patterns corresponds to MoS_2 and c-sapphire respectively. (d) Details of the atomic registry between MoS_2 and sapphire interface is shown. Patches of (e) inclined, (f and g) vertically grown MoS_2 by ALD. Inter planer spacing along c-direction is indicated in both the images.

do not show any streaking or splitting in the out-of-plane diffraction spots indicate that the tilt and twist between the crystallites are small. Even though the restricted growth on sapphire makes the film epitaxial with initial interface layers horizontal, eventually the film tends towards its more preferred vertical orientation forming nanowall structure under present growth condition. It is quite possible that these vertical orientations may not be captured in X-ray pattern due to restricted geometry. Hence the film grown on c-sapphire shows preferred orientation with interface epitaxy whereas MoS_2 grown on other substrates appear to be amorphous. Planar faults are observed in the ALD grown MoS_2 epitaxial thin film (Figure 10d). The faults are because of discontinuous Mo atoms in a plane and S atomic planes are found to be shared between the Mo atomic planes above and below. These defects might influence the physical properties of few layers MoS_2 films. Films grown at a lower deposition temperature of 150 °C (**Figure 11**a) are amorphous. Films deposited for 10 and 25 cycles at 300 °C also appear to be amorphous with regions of nanocrystalline MoS_2 (Figure 11 b and d). This may be due to the shorter duration of overall deposition

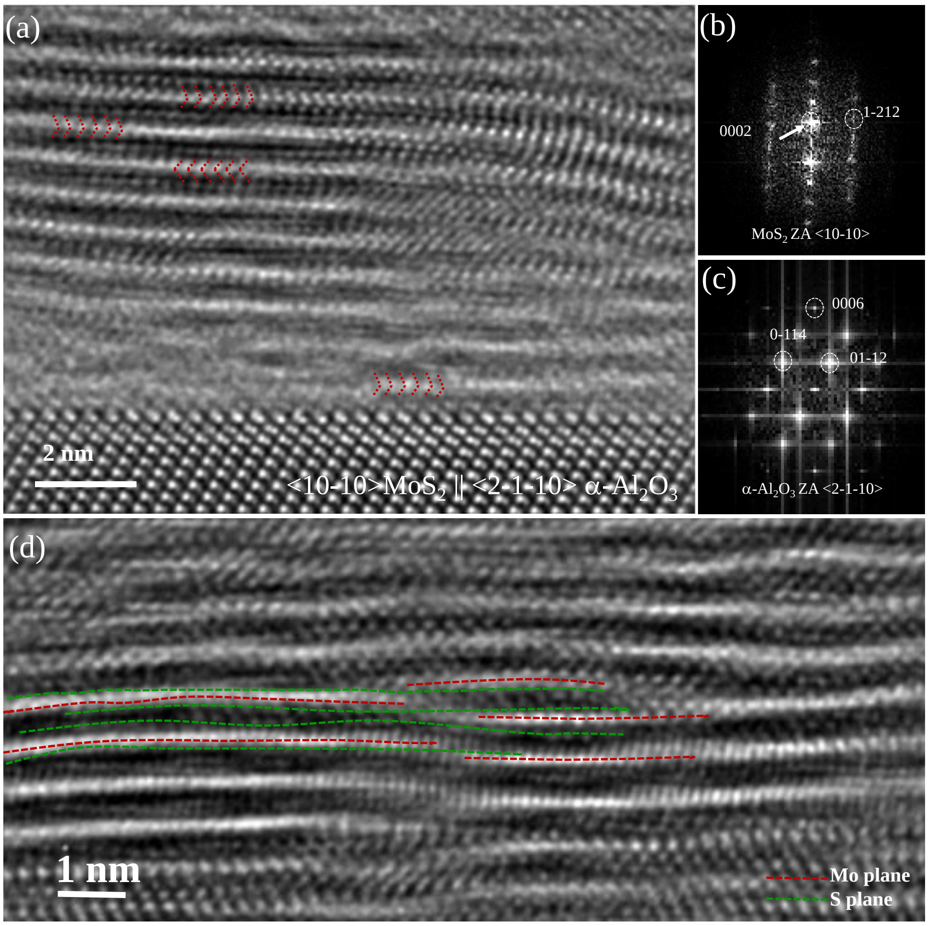

Figure 10. (a) HRTEM image of MoS_2 on c-sapphire along <11-20> of Al_2O_3. The epitaxial relationship between MoS_2 and sapphire is <10-10>MoS_2 || <2-1-10> Al_2O_3. (b, c) FFT patterns corresponds to MoS_2 and c-sapphire respectively. (d) Planer defects in MoS_2 van der walls epitaxial stacks. The origin of such fault due to discontinuous Mo layers, whereas the S atomic planes are continuous.

time which is important for crystallization, compared to 1500 cycles. The amorphous regions undergo crystallization under electron beam exposure (Figure 11 c and e).

In addition to sapphire substrate, we have grown MoS_2 on other substrates such as Si(100), SiO/Si, quartz and stainless steel. Interestingly, irrespective of the substrate, MoS_2 retains the nanowall network morphology and composition. The underlying substrates are of importance since different applications demand different substrates. The FESEM images in **Figure 12** show the growth of MoS_2 nanowall network on the stainless steel substrate which we have used in the battery application.

MoS_2 based thin film sodium and lithium ion batteries

The MoS_2 nanowall network architecture possess high surface to volume ratio and this unique architecture is expected to result in good Na/Li intercalation. With this purpose,

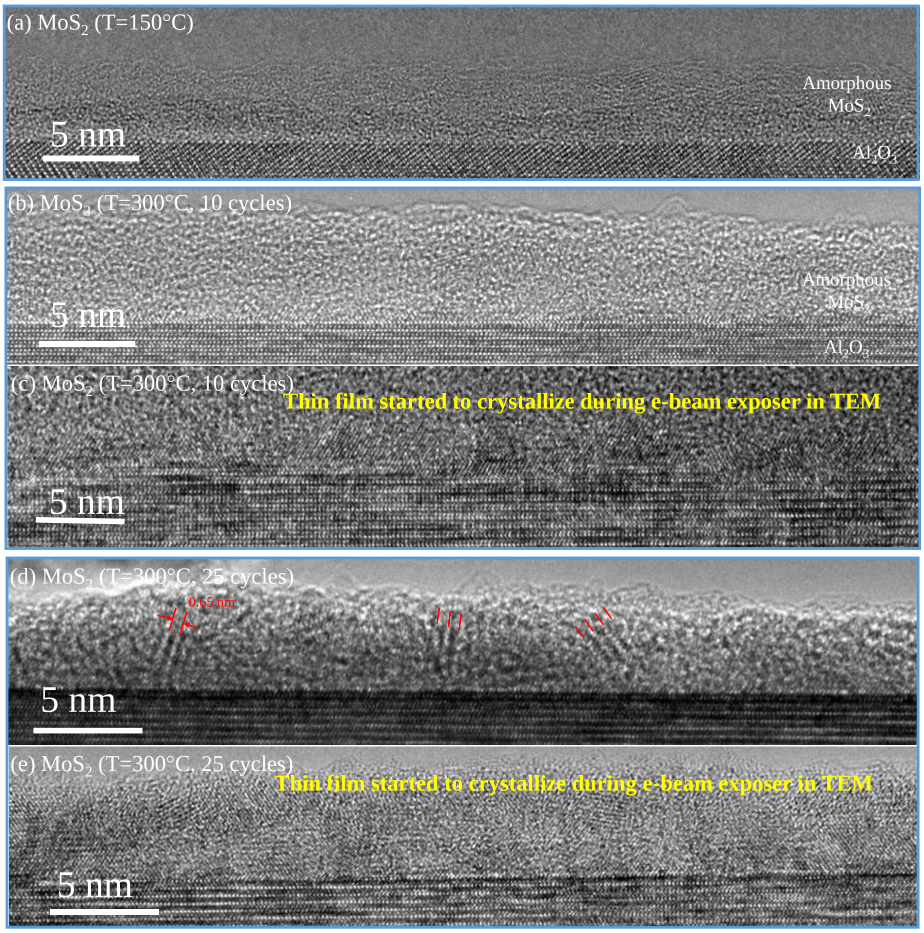

Figure 11. Cross-section TEM images of MoS_2 on *c*-plane sapphire substrate grown by ALD at (a) 150 °C, (b and c) 300 °C for 10 cycles and (d and e) 300 °C for 25 cycles.

MoS_2 nanowall network working electrode was directly deposited on the stainless steel current collector by ALD. As-deposited MoS_2 was characterized by FESEM, EDAX and Raman spectroscopy (Figure 12). Raman spectrum shows the 2H phase of MoS_2 has been formed and EDAX mapping reveals the uniform distribution of Mo and S throughout the film. The ALD grown MoS_2 nanowall network can be thought of as few layers of MoS_2 which are chemically attached to the substrate.

The reduction process of MoS_2 in Li/Na-ion battery is well established[41] and occurs in two steps:

Intercalation of Li/Na-ions:

$MoS_2 + Li/Na^+ + e^- \rightarrow (Li/Na)_xMoS_2$ $E_0= 1 – 3.0$ V.......... (i)

Conversion of $(Li/Na)_xMoS_2$ to Li_2S/Na_2S towards the deep discharge states:

$(Li/Na)_xMoS_2 \rightarrow Mo + (Li/Na)_2S$ $E_0= 0.2\text{-}1$ V……….(ii)

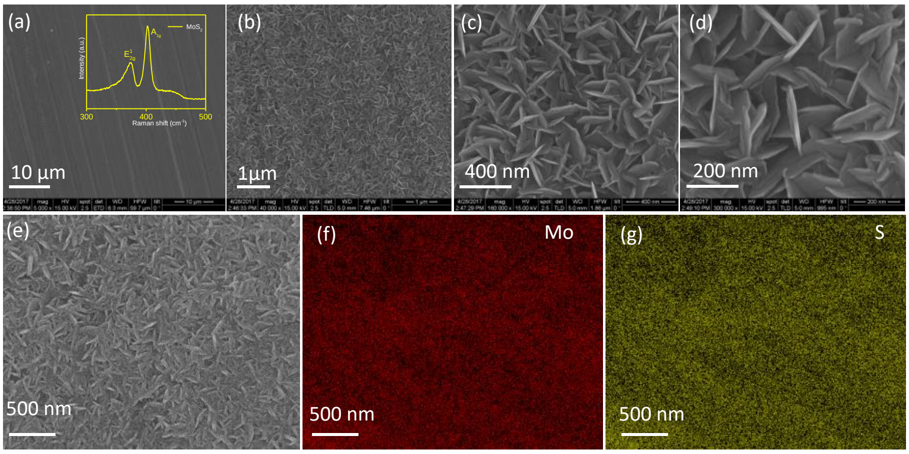

Figure 12. (a-e) FESEM image of MoS$_2$ thin film deposited on stainless steel substrate for electrochemical measurements. Inset of (a) shows corresponding Raman spectra. (f and g) EDAX elemental mapping of MoS$_2$ thin film deposited on stainless steel substrate, Mo (red) and S (green).

The former step induces reversibility by maintaining structural integrity of the material while the latter step provides higher capacity at the cost of degradation of material due to subsequent decomposition. Features of the electrochemical Na-ion storage are shown in **Figure 13**. The galvanostatic charge-discharge curve exhibits prominent plateaus in the voltage range 0.5 – 2.3 V (onset of Na-intercalation) and at 0.35 V (MoS$_2$ → Na$_2$S and Mo) during discharge. The charging process shows a sloping profile between 1.0 – 2.5 V (Figure 13a). In the range 0.2 – 3.0 V, a specific capacity of 1065 mAhg^{-1} is obtained. This decreased to 890 and 760 mAh g^{-1} in the 2nd and 5th cycles respectively. A nominal decrease in the specific capacity is observed beyond this however, the capacity stabilizes to 667 mAhg^{-1} at the end of 100 cycles. At 0.5 Ag^{-1} with an almost 100% coulombic efficiency (Figure 13c), a specific capacity of 667 mAhg^{-1} is quite remarkable. To the best of our knowledge, this is the highest reported capacity so far in the case of thin film or miniature scale batteries. The gradual decrease in capacity caused due to steady electrochemical decomposition of MoS$_2$, can be offset by restricting the cycling to higher potentials. This only enables the Na-ion intercalation process.

Galvanostatic charge-discharge cycling of the MoS$_2$ nanowall network in the voltage regime 1.0 – 3.0 V (Figure 13c) exhibited a specific capacity of 400 mAhg^{-1}. Though it is lower than the value of obtained in the wider voltage range, it exhibits extremely stable cyclability (Coulumbic efficiency$\approx$ 100%). We can therefore, conclude that the ALD grown MoS$_2$ nanowall network stores more than 1 Na-ion per MoS$_2$ (1 Na-ion $\approx$ 167 mAhg^{-1}). The cell with ALD grown MoS$_2$ nanowall network

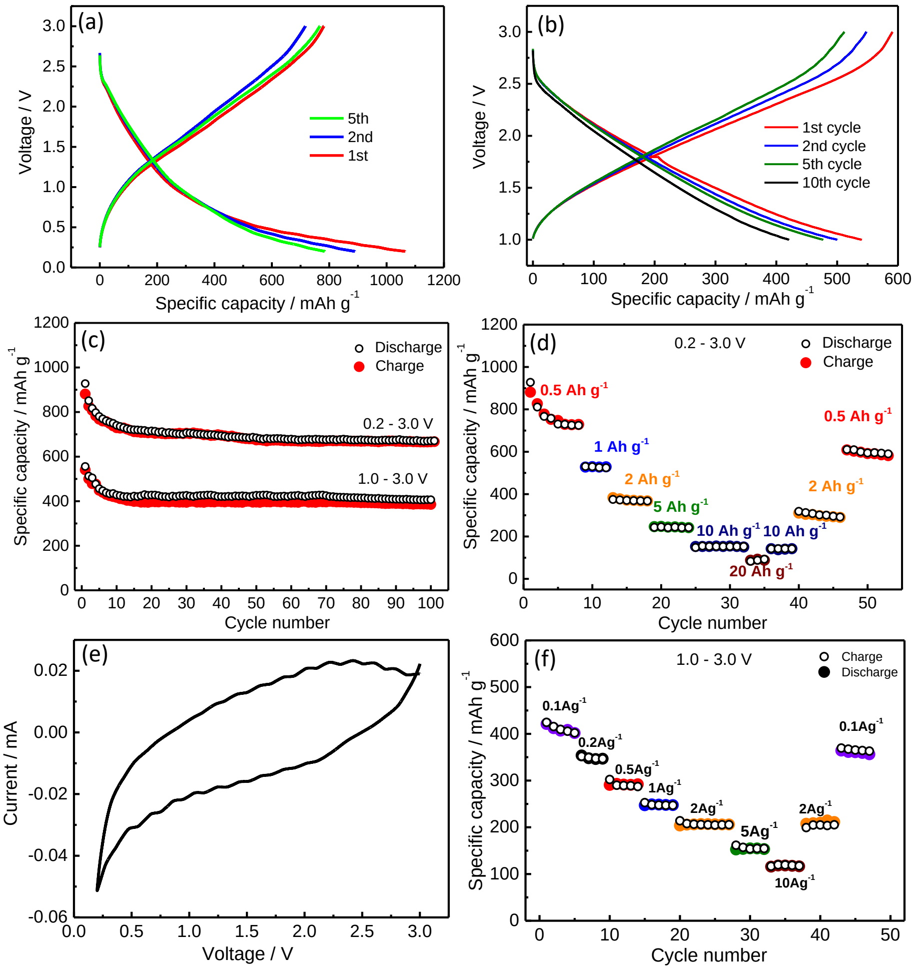

Figure 13. (a, b) Galvanostatic charge-discharge curves at different voltage ranges. (c) Cycling stability at 0.5 Ag^{-1} and (d) rate capability of ALD-grown MoS_2 versus Na for 0.2 – 3.0 V. (e) CV of MoS_2 nanowall versus Na (f) rate capability of MoS_2 nanowall versus Na for 1 – 3 V.

shows remarkable rate capability performance (Figure 13 d and f) and specific capacities of 728, 525, 367, 241, 152 and 85 mAhg^{-1} for the current density range, 0.5-20 Ag^{-1}. On reverting once again back to low current values, the initial capacities could be obtained. In the 1.0–3.0 V range (Figure 13f), a specific capacity of 120 mAhg^{-1} at 10 Ag^{-1} is obtained and which is comparable to that obtained in the voltage range of 0.2 – 3.0 V. The MoS_2 nanowall network performed extremely well even with regard to Li (**Figure 14**). A specific capacity value of 2726 mAhg^{-1} is observed in the 1st discharge cycle. This is followed by a gradual decrease to 2078 mAhg^{-1} in the 10th cycle (Figure 14a) stabilization at the 25th cycle. The MoS_2 nanowall network delivered a capacity of 1710 mAhg^{-1} after 100 cycles. In the voltage regime 1.2-3.0 V the cell exhibits stable capacity values of 980 mAhg^{-1} in the first cycle and 590 mAhg^{-1} even at 100 cycles (Figure 14b and c). Stable capacities of 2170, 1880, 1440, 1095,

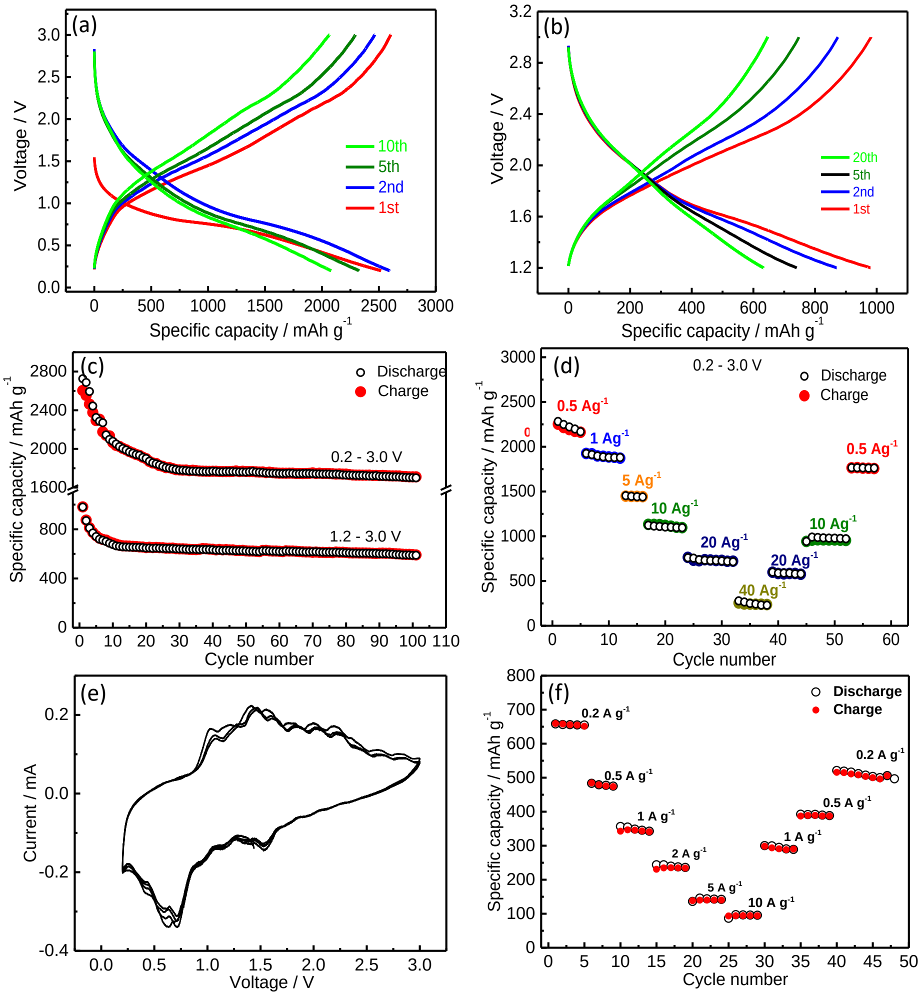

Figure 14. (a, b) Galvanostatic charge-discharge curves at different voltage ranges. (c) Cycling stability at 0.5 Ag-1 and (d) rate capability of ALD-grown MoS$_2$ versus Li for 0.2 – 3.0 V. (e) CV of MoS$_2$ nanowall versus Li for 0.2 – 3.0 V (f) rate capability of MoS$_2$ nanowall versus Li for 1.2 – 3.0 V.

715 and 230 mAhg^{-1} are obtained in the current density 0.5-40 Ag^{-1}. Nearly similar values are achieved (Figure 14d and f) on reverting to lower current densities. The theoretical capacity of MoS$_2$ is calculated to be 670 mAh/g upon consideration of a 4electron reduction processes. However, if the number of intercalating ions becomes more than or equal to 4, the cell in its deep discharge state starts acting as a Li-S/Na-S battery. The extremely high cycling capacity for Li-ion intercalation (~1710 mAhg^{-1}) can be attributed to Li-ion adsorption on the surface and edges of the MoS$_2$ layers. FESEM images and the EDAX spectrum of the MoS$_2$ thin film electrode after battery cycling shown in **Figure 15**, indicate that the MoS$_2$ network is smeared under the electrolyte which gets solidified during drying. The EDAX spectrum shows characteristic signals of MoS$_2$ and electrolyte.

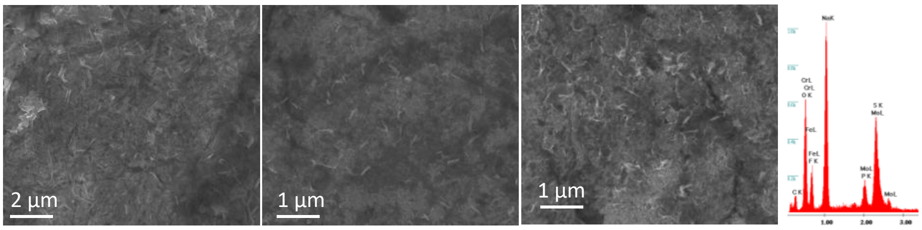

Figure 15. FESEM images of the surface of the MoS$_2$ thin films electrode after 100 cycles of Na battery test.

The superior performance of the Na -ion battery with the ALD grown MoS$_2$ nanowall network can be attributed to several favorable factors. ALD grown MoS$_2$ layers

Table 1. Comparison of the reported MoS$_2$ anode capacities depending on the method of synthesis.

Fabrication Method	Binder	Sp. capacity (mAh g^{-1})	Reference number
Chemical	Na-aliginate	~500 vs Na	42
Ultrasonic spray pyrolysis	Na-CMC	321 vs Na	29
Hydrothermal-freeze drying	-	300 vs Na	28
Exfoliation-in organic solvent	-	338 vs Na	43
Hydrothermal		500 vs Na	41
Exfoliation of bulk in NaOH	PAA	250 vs Na	44
Exfoliation of bulk in Formamide	PVDF	~500 vs Na	27
Ultrasonication	PVDF	320 vs Na	45
ALD- MoS$_2$ nanowalls network	No binder	667 vs Na	This work
Freeze drying-sintering	PVDF	900 vs Li (1A g^{-1})	46
Hydrothermal	PVDF	1000 vs Li	47
Hard template method	PVDF	500 vs Li	48
Hydrothermal	PTFE	700 (0.3-3V) 900 (0.01-3V)vs Li	49
MoS$_2$-CNT nanocomposite	PVDF	1000 vs Li	50
ALD- MoS$_2$ nanowalls network	No binder	1710 vs Li	This work

directly bind chemically with the current collector[51] and facilitates fast electron and ion transport and reduces resistance between the current collector and MoS_2.[52, 53]The orientation of the MoS_2 sufficiently reduces unwanted reactions leading to stable formation of SEI.[51] Unlike most of the reported MoS_2 battery work (Table 1), ALD grown MoS_2 nanowall network display extremely high cyclability over widely varying current values. The MoS_2 nanowall network exhibits superior mechanical strength and flexibility in accommodating the large sized Na-ion inside the layers. It is envisaged that the MoS_2 nanowall network and similar structures will be beneficial for other batteries chemistries including multivalent ions. Another important advantage of the ALD grown ultrathin MoS_2 layers is that it simplifies electrode assembly and rules out the usage of conducting and binder additives.

5. Conclusions

In summary, it is gratifying that we have been able to successfully grow crystalline MoS_2 consisting of epitaxial flat film along with vertical regions forming nanowalls without post-annealing on c-sapphire, at moderate temperatures by atomic layer deposition. The nanowalls form networks irrespective of the underlying substrate. The nanowalls networks grown directly on stainless steel current collector by ALD are conveniently exploited for fabricating the Na-ion battery, with desirable features including cyclic stability and rate capability. The capacity values obtained is superior to the values reported in the literature. Clearly, nanowall networks of ALD grown MoS_2 not only aid in suppressing mechanical instabilities but also provide facile transport pathways for both electrons and Na-ions, leading to efficient and stable electrochemical reaction. It should be noted that Li-ion batteries with excellent characteristics can also be fabricated with MoS_2 nanowall-network.

6. References

[1] K. S. Novoselov, A. K. Geim, S. V. Morozov, D. Jiang, Y. Zhang, S. V. Dubonos, I. V. Grigorieva, A. A. Firsov, *Science* **2004**, *306*, 666-669.

[2] A. K. Geim, K. S. Novoselov, *Nat Mater* **2007**, *6*, 183-191.

[3] A. K. Geim, I. V. Grigorieva, *Nature* **2013**, *499*, 419-425.

[4] K. S. Novoselov, A. Mishchenko, A. Carvalho, A. H. Castro Neto, *Science* **2016**, *353*, aac9439.

[5] Q. H. Wang, K. Kalantar-Zadeh, A. Kis, J. N. Coleman, M. S. Strano, *Nat Nano* **2012**, *7*, 699-712.

[6] S. Manzeli, D. Ovchinnikov, D. Pasquier, O. V. Yazyev, A. Kis, *Nat. Rev. Mater*. **2017**, 2, 17033.

[7] C. N. R. Rao, H. S. S. Ramakrishna Matte, U. Maitra, *Angew. Chem. Int. Ed.* **2013**, *52*, 13162-13185.

[8] H. S. S. Ramakrishna Matte, A. Gomathi, A. K. Manna, D. J. Late, R. Datta, S. K. Pati, C. N. R. Rao, *Angew. Chem. Int. Ed.* **2010**, *49*, 4059-4062.

[9] H. Li, J. Wu, Z. Yin, H. Zhang, *Acc. Chem. Res.* **2014**, *47*, 1067-1075.

[10] H. Schmidt, S. Wang, L. Chu, M. Toh, R. Kumar, W. Zhao, A. H. Castro Neto, J. Martin, S. Adam, B. Özyilmaz, G. Eda, *Nano Lett.* **2014**, *14*, 1909-1913.

[11] A. Splendiani, L. Sun, Y. Zhang, T. Li, J. Kim, C.-Y. Chim, G. Galli, F. Wang, *Nano Lett.* **2010**, *10*, 1271-1275.

[12] G. Eda, H. Yamaguchi, D. Voiry, T. Fujita, M. Chen, M. Chhowalla, *Nano Lett.* **2011**, *11*, 5111-5116.

[13] X. Wang, H. Feng, Y. Wu, L. Jiao, *J. Am. Chem. Soc.* **2013**, *135*, 5304-5307.

[14] Y. Li, Y. Yu, Y. Huang, R. A. Nielsen, W. A. Goddard, Y. Li, L. Cao, *ACS Catal.* **2015**, *5*, 448-455.

[15] R. L. Puurunen, *J. Appl. Phys.* **2005**, *97*, 121301.

[16] L. Wen, M. Zhou, C. Wang, Y. Mi, Y. Lei, *Adv. Energy Mater.* **2016**, *6*, 1600468.

[17] K. Vasu, M. B. Sreedhara, J. Ghatak, C. N. R. Rao, *ACS Appl. Mater. Interfaces* **2016**, *8*, 7897-7901.

[18] M. B. Sreedhara, J. Ghatak, B. Bharath, C. N. R. Rao, *ACS Appl. Mater. Interfaces* **2017**, *9*, 3178-3185.

[19] J. D. Emery, C. M. Schlepütz, P. Guo, R. P. H. Chang, A. B. F. Martinson, *Cryst. Growth Des.* **2016**, *16*, 640-645.

[20] N. P. Dasgupta, X. Meng, J. W. Elam, A. B. F. Martinson, *Acc. Chem. Res.* **2015**, *48*, 341-348.

[21] T. Jurca, M. J. Moody, A. Henning, J. D. Emery, B. Wang, J. M. Tan, T. L. Lohr, L. J. Lauhon, T. J. Marks, *Angew. Chem. Int. Ed.* **2017**, *56*, 4991-4995.

[22] M. Mattinen, T. Hatanpää, T. Sarnet, K. Mizohata, K. Meinander, P. J. King, L. Khriachtchev, J. Räisänen, M. Ritala, M. Leskelä, *Adv. Mater. Interfaces* **2017**, *4*, 1700123.

[23] L. K. Tan, B. Liu, J. H. Teng, S. Guo, H. Y. Low, K. P. Loh, *Nanoscale* **2014**, *6*, 10584-10588.

[24] J. J. Pyeon, S. H. Kim, D. S. Jeong, S.-H. Baek, C.-Y. Kang, J.-S. Kim, S. K. Kim, *Nanoscale* **2016**, *8*, 10792-10798.

[25] Z. Jin, S. Shin, D. H. Kwon, S.-J. Han, Y.-S. Min, *Nanoscale* **2014**, *6*, 14453-14458.

[26] S. Shin, Z. Jin, D. H. Kwon, R. Bose, Y.-S. Min, *Langmuir* **2015**, *31*, 1196-1202.

[27] D. Su, S. Dou, G. Wang, *Adv. Energy Mater.* **2015**, *5*, 1401205.

[28] Z. Hu, L. Wang, K. Zhang, J. Wang, F. Cheng, Z. Tao and J. Chen, *Angew. Chem. Int. Ed.* 2014, **126**, 13008-13012.

[29] S. H. Choi, Y. N. Ko, J.-K. Lee, Y. C. Kang, *Adv. Funct. Mater.* **2015**, *25*, 1780-1788.

[30] Y. Liu, Y. Li, H. Kang, T. Jin and L. Jiao, *Mater. Horiz* 2016, **3**, 402-421.

[31] Y. Liu, Y. Zhao, L. Jiao and J. Chen, *J. Mater. Chem. A* 2014, **2**, 13109-13115.

[32] T. Stephenson, Z. Li, B. Olsen, D. Mitlin, *Energy Environ. Sci.* **2014**, *7*, 209-231.

[33] J.-Y. Hwang, S.-T. Myung, Y.-K. Sun, *Chem. Soc. Rev.* **2017**, *46*, 3529-3614.

[34] V. Palomares, P. Serras, I. Villaluenga, K. B. Hueso, J. Carretero-Gonzalez, T. Rojo, *Energy Environ. Sci.* **2012**, *5*, 5884-5901.

[35] J. B. Goodenough, K.-S. Park, *J. Am. Chem. Soc.* **2013**, *135*, 1167-1176.

[36] C. Lee, H. Yan, L. E. Brus, T. F. Heinz, J. Hone, S. Ryu, *ACS Nano* **2010**, *4*, 2695-2700.

[37] H. Li, Q. Zhang, C. C. R. Yap, B. K. Tay, T. H. T. Edwin, A. Olivier, D. Baillargeat, *Adv. Funct. Mater.* **2012**, *22*, 1385-1390.

[38] H. Zeng, B. Zhu, K. Liu, J. Fan, X. Cui, Q. M. Zhang, *Phys. Rev. B* **2012**, *86*, 241301.

[39] K. Wang, J. Wang, J. Fan, M. Lotya, A. O'Neill, D. Fox, Y. Feng, X. Zhang, B. Jiang, Q. Zhao, H. Zhang, J. N. Coleman, L. Zhang, W. J. Blau, *ACS Nano* **2013**, *7*, 9260-9267.

[40] R. Sahu, D. Radhakrishnan, B. Vishal, D. S. Negi, A. Sil, C. Narayana, R. Datta, *J. Cryst. Growth* **2017**, *470*, 51-57.

[41] S. Zhang, X. Yu, H. Yu, Y. Chen, P. Gao, C. Li, C. Zhu, *ACS Appl. Mater. Interfaces* **2014**, *6*, 21880-21885.

[42] J. Wang, C. Luo, T. Gao, A. Langrock, A. C. Mignerey and C. Wang, *Small* **2015**, *11*, 473-481.

[43] L. David, R. Bhandavat and G. Singh, *ACS Nano* **2014**, *8*, 1759-1770.

[44] G. S. Bang, K. W. Nam, J. Y. Kim, J. Shin, J. W. Choi and S.-Y. Choi, *ACS Appl. Mater. Interfaces* **2014**, *6*, 7084-7089.

[45] X. Xie, Z. Ao, D. Su, J. Zhang and G. Wang, *Adv. Funct. Mater.* **2015**, *25*, 1393-1403.

[46] J. Zhou, J. Qin, X. Zhang, C. Shi, E. Liu, J. Li, N. Zhao and C. He, *ACS Nano* **2015**, *9*, 3837-3848.

[47] H. Hwang, H. Kim and J. Cho, *Nano Lett.* **2011**, *11*, 4826-4830.

[48] H. Liu, D. Su, R. Zhou, B. Sun, G. Wang and S. Z. Qiao, *Adv. Energy Mater.* **2012**, *2*, 970-975.

[49] C. Feng, J. Ma, H. Li, R. Zeng, Z. Guo and H. Liu, *Mater. Res. Bull.* **2009**, *44*, 1811-1815.

[50] Y. Shi, Y. Wang, J. I. Wong, A. Y. S. Tan, C.-L. Hsu, L.-J. Li, Y.-C. Lu and H. Y. Yang, *Sci. Rep.* **2013**, *3*, 2169.

[51] X. Meng, X.-Q. Yang, X. Sun, *Adv. Mater.* **2012**, *24*, 3589-3615.

[52] L. Ma, R. B. Nuwayhid, T. Wu, Y. Lei, K. Amine, J. Lu, *Adv. Mater. Interfaces* **2016**, *3*, 1600564.

[53] X. Wang, G. Yushin, *Energy Environ. Sci.* **2015**, *8*, 1889-1904.

Summary of the Thesis

2D ultrathin films of layered and non-layered materials exhibit promising applications in electronics, catalysis and energy devices. Graphene and MoS_2 are particularly prominent amongst the 2D materials in terms of the variety of novel properties. This thesis deals entirely with the ultrathin layers of metal oxides, nitrides and sulfides, prepared by different means including atomic layer deposition. Many properties of these materials with potential applications have been examined. Following is the summary of these studies.

Few-layer MoO_3 has been prepared by several methods including oxidation of few-layer MoS_2. These nanosheets have a higher band gap than bulk MoO_3 and exhibit higher catalytic activity for the photodegradation of methylene blue. It is noteworthy that composites of few-layer MoO_3 with borocarbonitride possess good characteristics as electrode supercapacitors. It is likely that many other applications will be found for few-layer MoO_3. We have also demonstrated successfully that few-layer MoO_3-reduced graphene oxide (rGO) composites have considerable potential as high-performance anode materials for Na-ion batteries. The 3D configuration of MoO_3-rGO is essentially due to Mo-O-C linkages between MoO_3 and rGO. The spatial configuration not only aids in suppressing the mechanical instabilities of MoO_3 taking place during repeated cycling but also provides facile transport pathways for both electrons and Na-ions leading to an efficient and stable electrochemical reaction. The amount of rGO in the composite is crucial, as this directly ascertains the structural stability and electrochemical performance of the MoO_3-rGO composite. The novel design of a 3D-composite comprising of a 2D-electroactive compound and its integration with an optimum amount of extended carbon structure is expected to pave way for design of many more 2D-electroactive materials based composites for prospective applications in sodium-ion batteries.

Reaction with n-butyllithium provides a satisfactory method of obtaining few-layer species of the members of the Aurivillius family of oxides ($Bi_2A_{n-1}B_nO_{3n+3}$, where A= Bi^{3+}, Ba^{2+} etc. and B= Ti^{4+}, Fe^{3+} with n= 3, 4, 5, 6 and 7) with the thickness corresponding to a fraction of the *c*-parameter. Since the bulk samples of these oxides are ferroelectrics, it may be possible to use the few-layer species as thin dielectric films in photovoltaics and other applications. Depositing the exfoliated nanosheets on various substrates and other layered materials can give rise to materials of interest.

The metal-insulator transition in V_2O_3 films at 150 K is markedly affected by nitrogen-substitution, the decrease in the transition temperature being ~30 degrees even with a modest substitution of nitrogen. Results of our first-principles density functional theory-based calculations on nitrogen substituted V_2O_3 reveal that N substitution in V_2O_3 makes the high-temperature metallic corundum phase lower in energy, leading to the observed reduction in Nèel temperature. This is also indicated in the electronic structure of r-$V_2O_{3-x}N_y$, where we see a dip in electronic density of states at the Fermi level and a wider sub-band of N(2*p*) states. In the monoclinic phase (m-$V_2O_{3-x}N_y$) too, N(2*p*) sub-band states of the less electronegative atom lies above the O(2*p*) states, but below the V(3*d*) states. Hybridization between N(2*p*) with the *d*-states of V results in the reduction of the *d*-*d* gap and a local magnetic moment of -1 μ_B/N on V atoms bonded to the N sites and in the vicinity of O-vacancies.

Few-layers of borocarbonitide (BCN) nanosheets of various compositions have been prepared using exfoliated graphene. Fluorescent labeling of surface species (FLOSS) has been employed to determin the surface concentrations of functional groups on 2-D materials such as graphene and BN. The method is successful in the case of BCN where both oxygen functionalities and amine groups respectively are quantitatively determined by FLOSS. The FLOSS results on amine functionalities suggest this method to be a good way to characterize surface amine groups on other 2D layered materials as well. Specific capacitance of supercapacitors is small in the case of graphene although its surface area and concentration of surface functionalities is high. In the case of BCN, the samples show reasonable specific capacitance, but we do not see any simple relation between specific capacitance and oxygen reduction reaction (ORR) onset potential with surface functionalities on these materials. The number of surface amine groups however, plays a crucial role on these properties. The study has demonstrates the potential applications of borocarbonitrides in catalysis and energy devices. Polymer matrix nanocomposites with BCN dispersed in PVA have been prepared and characterized in detail. Surface functionalities play a crucial role in the interfacial interaction between polymer and nanofiller. A 107% increment in hardness and 71% increment in elastic modulus were achieved by the addition of just 0.2 wt% of BCN to PVA. While the stiffness of the nanocomposites with varying chemical compositions of BCN is comparable with that of EG and BN nanocomposites, the hardness of the former is far superior. The substantial improvement in the mechanical properties upon addition of nanofiller can be attributed to effective load transfer between the polymer matrix and the nanofiller, aided by H-bonding. Moreover, the surface roughness of these nanosheets not only improves the interfacial adhesion but also benefit as nucleation centers for the crystalline domains in the polymer. Thus, BCN nanosheets are superior reinforcement materials for enhancing the mechanical properties of polymers as compared to well-studied graphene and BN. BCN can be produced economically compared to carbon nanotubes and other kind of nanocarbons.

Metal nitride nanosheets have been prepared by the chemical transformation of oxide and chalcogenide nanosheets. It is noteworthy that nanosheets of GaN are readily prepared by the ammonolysis of GaS and GaSe nanosheets. Preliminary studies have demonstrated success in preparing VN and MoN nanosheets from the oxide nanosheets. The simple methodology described here can be exploited to prepare good nanosheets of these and other metal nitrides. Ammonolysis of MoS_2 NSs also yields nitride NSs.

With the ever increasing demand for controllable and conformal films, atomic layer deposition (ALD) is one of the most effective methods possible with its sequential self-limiting reactions to meet the expectation of device community. ALD processes have been developed for a wide variety of materials, ranging from metals to metal oxides to complex ternary materials. However, the growth of pristine single phase material having preferred orientation with the underlying substrate has significant practical utility, however, most of ALD deposited materials are limited to polycrystalline or amorphous. Epitaxial thin films of anatase TiO_2 (001) have been successfully deposited on Al_2O_3 (001) substrates by atomic layer deposition at 300°C. N-doping of TiO_2 affects structural, optical, electrical and magnetic properties of the epitaxial films. Titanium vacancies seem to be the primary source of *p*-type conductivity and room temperature ferromagnetism in undoped and N-doped TiO_2 thin films. The observation of diode rectification from the TiO_2 based *p-n* homojunction has opened the way for using TiO_2 thin films for device applications.

We have been able to obtain ultrathin crystalline epitaxial films of V_2O_5 by using oxygen plasma with $VO(acac)_2$. The films show blue shift in the Raman spectra due to strain caused by epitaxial growth. It is also satisfying that making use of the n-type behavior of V_2O_5, we are able to fabricate a heterojunction diode with p-type TiO_2. It is noteworthy that the humidity sensor based on the V_2O_5 film has superior sensitivity relative to literature reports on other oxide-based sensors.

We have been able to successfully grow crystalline MoS_2 consisting of epitaxial flat film along with vertical regions forming nanowalls without post-annealing on c-sapphire, at moderate temperatures by atomic layer deposition. The nanowalls form networks irrespective of the underlying substrate. The nanowalls networks grown directly on stainless steel current collector by ALD are conveniently exploited for fabricating the Na-ion battery, with desirable features including cyclic stability and rate capability. The capacity values obtained is superior to the values reported in the literature. Clearly, nanowall networks of ALD grown MoS_2 not only aid in suppressing mechanical instabilities but also provide facile transport pathways for both electrons and Na-ions, leading to efficient and stable electrochemical reaction. It should be noted that Li-ion batteries with excellent characteristics can also be fabricated with MoS_2 nanowall-network.

The author hopes that the results reported in the thesis make valuable inputs to the area of 2D materials.

****